CHARACTERIZING SILVER ENGINEERED NANOPARTICLES IN A NATURAL WATER: ANALYTICAL CONSIDERATIONS FOR INSTRUMENTAL AND ENVIRONMENTAL FACTORS USING ASYMMETRIC FLOW FIELD FLOW FRACTIONATION

Anne Adelicia Galyean

A dissertation submitted to the faculty at the University of North Carolina at Chapel Hill in partial fulfillment of the requirements for the degree of Doctor of Philosophy in the Department of Environmental Sciences and Engineering in the Gillings School of Global Public Health.

Chapel Hill
2015

Approved by:

Howard S. Weinberg

Wyatt N. Vreeland

Michael C. Leopold

Rose M. Cory

Orlando Coronell

ABSTRACT

Anne Adelicia Galyean: Characterizing Silver Engineered Nanoparticles In A Natural Water: Analytical Considerations for Instrumental and Environmental Factors Using Asymmetric Flow Field Flow Fractionation
(Under the direction of Howard S. Weinberg)

With the likely release of engineered nanoparticles into the aquatic environment, developing appropriate analytical methods for occurrence surveys has become a priority. To this end, a method towards the quantification of silver nanoparticles (AgNP) in lake water samples using asymmetric flow field flow fractionation (AF^4) and inductively coupled plasma mass spectrometry (ICP-MS) is reported. Therefore, light scattering (LS) detection was used to develop an assessment metric to evaluate relative accuracy among AF^4 separations. This assessment metric is applied to optimization of cross flow (V_x) protocols in AF^4 separation interfaced with LS detection using mixtures of polystyrene beads. AF^4 has several instrumental parameters that may have a direct effect on separation performance. A sensitivity analysis utilizing orthogonal factional factorial design and graphical analysis was applied to ascertain the relative importance of five AF^4 primary/instrumental factor settings when analyzing synthetic freshwaters containing AgNPs. The most important and significant AF^4 primary/instrumental factors were buffer concentration and V_x velocity, while the least impacting was V_x ramp time. Optimal settings were also generated for each of the factors within the range of settings explored. A parallel orthogonal fractional factorial design was employed to evaluate the effects of five environmental factors, or water quality characteristics, on the separation. None of these water quality characteristic effects or interactions were found to be significant. Finally, the developed methodology was applied towards AgNP quantitation in a natural lake water sample using AF^4 followed by online inductively coupled plasma mass spectrometry (ICP-MS). The impacts of various AF^4 system components and natural organic matter (NOM) on AgNP quantitation were explored. Isotope enriched Ag ions (Ag^+) were used to identify Ag

speciation following AF^4 separation. Ag quantitation was achieved within 10% of a spiked “challenge” concentration of AgNP in lake water using the standard addition method to compensate for natural matrix and system complexity. Further investigations into potential Ag^+-NOM and AgNP-NOM interactions were performed using fluorescence spectroscopy. The corresponding results suggest that these interactions affect the molar mass and physical conformation of the NOM particles in the sample.

For MFD. Thank you for your patience and unwavering support.

ACKNOWLEDGEMENTS

I would like to thank: Drs. Wyatt Vreeland, R. David Holbrook, Jim Filliben, Dean Ripple, Mike Tarlov, Leona Scanlan, Donna (Omiatek) Konicek, Monique Johnson, and Abe Abouzeid for their mentorship, time, support, expertise, and friendship during my time at NIST; Dr. Monique Johnson, Karen Murphy, and Dr. Antonio Montoro Bustos for ICP-MS expertise and mentorship; Dongmei Wang at the Occoquan Watershed Monitoring Laboratory and Kirsten Studer from the University of North Carolina at Chapel Hill's Department of Environmental Sciences and Engineering for TOC measurements.

I would like to extend a special and sincere thank you to my committee members: Drs. Howard Weinberg, Wyatt Vreeland, Michael Leopold, Rose Cory, and Orlando Coronell. Thank you all for your commitment, time, dedication, and expertise.

This research was supported by funds from the National Institutes of Health (T32ES007018) and the National Science Foundation Graduate Research Fellowship Program under Grant No. (DGE-1144081), as well as from the Alliance for Graduate Education and the Professoriate (AGEP) and an Off-Campus Dissertation Research Fellowship from the University of North Carolina at Chapel Hill. Any opinions, findings, and conclusions or recommendations expressed in this material are those of the authors and do not necessarily reflect the views of the National Science Foundation. Certain commercial equipment, instruments, or materials are identified in this chapter in order to specify the experimental procedure adequately. Such identification is not intended to imply recommendation or endorsement by the National Institute of Standards and Technology, nor is it intended to imply that the materials or equipment identified are necessarily the best available for the purpose.

TABLE OF CONTENTS

LIST OF TABLES

LIST OF FIGURES

LIST OF ABBREVIATIONS

1FAT	One factor at a time
AF^4	Asymmetric flow field flow fractionation
AFM	Atomic force microscopy
Ag^+	Silver ions
Ag_2S NPs	Silver sulfide nanoparticles
AgNPs	Silver nanoparticles
ANOVA	Analysis of variance
CE	Capillary electrophoresis
DBPs	Disinfection byproducts
DEX or DOE	Design of experiment
DDT	Dichlorodiphenyltrichloroethane
DLS	Dynamic light scattering
DOE or DEX	Design of experiment
DOC	Dissolved organic carbon
EDA	Exploratory data analysis
EELS	Electron energy loss spectroscopy
EDS	Energy-disperseive spectroscopy
EIFFF	Electric field flow fractionation
ENPs	Engineered nanoparticles
ESEM	Environmental scanning electron microscopy
FFF	Field-flow fractionation
FIFFF	Flow field flow fractionation
F_{max}	Max fluorescence
HDC	Hydrodynamic chromatography
HPLC	High performance liquid chromatography
ICP-AES	Inductively coupled plasma atomic emission spectroscopy
ICP-MS	Inductively coupled plasma mass spectrometry

IR	Infra-red spectroscopy
ISO	International standards organization
LGW	Laboratory grade water, 18.2 MΩ
LIBD	Laser-induced breakdown detection
LS	Light scattering
MALS	Multi-angle light scattering
MM	Molar mass
MWCO	Molecular weight cutoff
NOM	Natural organic material
NPs	Nanoparticles
QELS	Quasi-elastic light scattering
RGD	Rayleigh-Gans-Debye
SAED	Selected area electron diffraction
SD	Standard deviation
SEC	Size-exclusion chromatography
SEM	Scanning electron microscopy
SR NOM	Suwannee River natural organic material
STEM	Scanning transmission electron microscopy
TEM	Transmission electron microscopy
TFFF	Thermal field flow fractionation
TOC	Total organic carbon
V_x	Cross flow velocity
XPS	X-ray photoelectron spectrometry
Y	Response variable

LIST OF SYMBOLS

A	Spherical radius
A_2	Second virial coefficient
B	Effects that can be estimated
β_o	Effect of Y when all main effects are equal to 0
c	Sample concentration
D	Diffusion coefficient
d_λ	Dydrodynamic particle diameter
$dn\ dc^{-1}$	Refractive index increment
f_{geom}	Geometrical calibration constant
l	Cloud thickness
I_o	Intensity of incident light
$I(\theta)$	Intensity of scattered light from the sample
$I_s(\theta)$	Intensity of scattered light from the solvent
$I(t)$	Intensity of scattered light at time t
k	Boltzmann constant or number of factors
K^*	Vertically polarized incident light constant
λ	Retention parameter
λ_o	Vertically polarized incident light
m	Refractive index of the solvated particle
m_i	Mass element
M_i	Molar mass of particle
M_w	Weight average molecular weight
n	Number of sample runs
η	Hydrodynamic viscosity of solvent or carrier solution
N_A	Avogadro's number
n_i	Particle of monodisperse size fraction, *i*, or the *i*th residual
n_o	Refractive index

p	Number of terms
$P(\theta)$	Angular dependence of scattered light
R	Retention ratio
r_i	Distance between center of mass of the particle to the mass element, m_i, or calculated R_h of the ith time slice
r_g or r_{rms}	Root mean square radius
r_g^2	Mean square radius
R_h	Hydrodynamic radius
r_{rms} or r_g	Root mean square radius
$R(\theta)$	Excess Rayleigh ratio
SD_{res}	Residual standard deviation
σ_{ri}	Uncertainty in the radius measurement
T	Absolute temperature in K
τ	Delay, amount that a duplicate intensity trace is shifted from the original
U	Cross flow induced velocity
V_c	Volumetric cross flow velocity
V_i	Particle volume
V^o	Void volume
V_r	Measured retention volume
w	Channel thickness

CHAPTER 1: INTRODUCTION AND STUDY OUTLINE

1.1 Background

1.1.1 What are engineered nanoparticles?

Engineered nanoparticles (ENPs) are anthropogenic particles less than 100 nm in more than one dimension and are a subset of all nanoparticles (NPs) but beyond their size, different ENPs may share little in common. They can exist as single particles or aggregated clusters, spheres, tubes, or irregular shapes but will fall somewhere in between traditional classifications of molecular pollutants and particulate materials (**Figure 1.1**). These diminutive dimensions provide ENPs with some unique physical properties. For example, particles less than 10 nm have more than 20% of their atoms at the surface, whereas the surface energy of particles in the micro scale is at least 3 orders of magnitude lower and the percentage of surface atoms is negligible [1].

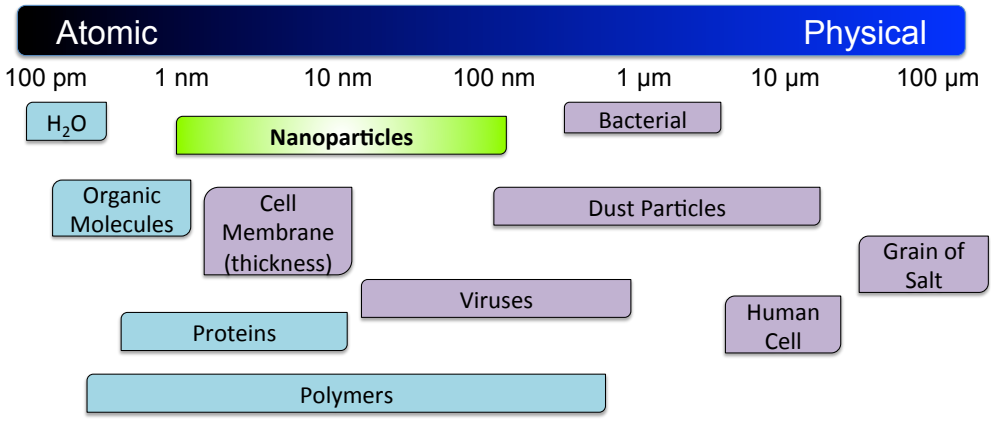

Figure 1.1. Size range of nanoparticles compared to other molecular and particulate materials [2].

In contrast to nanoparticles, natural colloids usually entertain a much broader definition, encompass a huge variety of materials, and are ubiquitously present in natural waters at high concentrations, the primary reason natural waters are such complex matrices. In aquatic systems, natural colloids range from 1 nm – 1 µm and include natural organic matter (NOM), dust particles, ash,

microbes biological and other materials [2, 3]. The fate, behavior, and occurrence of naturally occurring nanoparticles and colloids have been intensively studied for decades. However, the knowledge gained from these investigations is not complete enough to create a detailed model of ENP behavior and their fate in the environment. Whether existing knowledge can be applied to predict the fate and behavior of ENPs, or if ENPs demonstrate a unique fate and, therefore, occurrence, from natural nanoparticles, can only be addressed after more research into ENP fate and transport in the environment [3].

Nanotechnology began with the development of the atomic force microscope in the early 1980s when the observation, physical manipulation, and the relative scale of atoms and molecules became possible. By 1991, engineered carbon nanotubes had yielded an arrangement of carbon atoms that was six times lighter than steel and one hundred times stronger. The current use of nano-enabled consumer products and nanoparticle-producing industries is producing nano-waste at a rate that outpaces the scientific research necessary to understand their potential environmental implications. Approximately 79 % of publications in the field of NPs focus primarily on their synthesis, presenting a significant lack of literature addressing the potential environmental impact [4]. As of 2013, ENPs have been included in a wide range of over 1,600 consumer products from over 30 countries [5], with the single largest number in the health and fitness sector. The most common material listed in the product descriptions is silver (383 products). The next most abundant is titanium (179), including titanium dioxide (TiO_2), followed by carbon (87), including fullerenes, then silica (52), zinc (including zinc oxide) (36), and gold (19) [5]. Production estimates of common ENPs range from 270,000 to 320,000 metric tons per year, including estimates that suggest 17 % might be released into soils, 21% into water, and 2.5 % into air, with the balance entering landfills [6]. The estimation for a product value of $1 trillion by 2015, of which $800 billion would be in the US, appears to be holding [7]. A summary of some common nanoparticles, their respective applications, and some estimates of their potential environmental concentrations are presented in Table 1 [4, 8, 9].

1.1.2 Release of ENPs into environment and their persistence

Due to the rapid rise of ENP use in manufacturing, science, and, industry, their release into the environment will likely follow several possible pathways to the water/sediment interface (**Figure 1.2**).

Table 1.1. Some common nanoparticles, their respective applications, and some estimates of their potential environmental size concentrations (adapted from references [4,8,9]).

ENP Classification	ENP Type	Applications	Reported Particle Size for Distributions in Water (nm)	*Predicted Modeled Concentrations*		
				Water (µg/L)	Soil (µg/kg)	Air (µg/m^3)
Metals	Ag	Antimicrobials, paint, coatings, medical uses, food packaging	26.6 ± 8.8, 20-30	0.01-0.03	0.02-0.43	0.0017-0.0014
	Al	Metallic and optical coatings, plating, cosmetic filler	41.7 ± 8.1, 41			
	Au	Nanomedicine, electronics		0.14	5.99	
	Ca	Health supplements				
	Cu	Microelectronics	15-45, 26.7 ± 7.1			
	Fe	Water treatment				
	Mg	Health supplements				
	Pt-group	Catalysts				
	Se	Health supplements				
	Sn	Paints				
Metal Oxides	Al_2O_3	Usually substrate-bound, paint	60	0.0002	0.01	
	CeO_2	Fuel catalyst, sintering additives, UV absorbent, alloy coatings		<0.0001	<0.01	
	Fe_2O_3	Environmental remediation, biomedical applications, semiconductors	5-25, 9.2, <10			
	SiO_2	Paints, coatings	10, 14	0.0007	0.03	
	TiO_2	Cosmetics, paint, coatings, air purification, semiconductors, solar cells	4-5, 11, 15-27, 15-40, 50, 66	0.7-24.5	0.4-1030	0.0015-0.042
	ZnO	Cosmetics, paint pigments, coatings, flame retardants, dental cement	13, 20, 50-70, 60	76	3194	
Carbon	Carbon Black	Usually substrate bound, vehicular tires				
	Fullerenes	Cosmetics, nanomedicine		0.31	13.1	
	Nanotubes	Composite materials		0.0005-0.0008	0.001-0.02	0.0015-0.0023

This includes release into the air when powdered ENPs are agitated or during accidental spills and improper transportation. Release into surface water could possibly occur due to inadequate disposal practices or less than optimal removal at wastewater treatment facilities.

Ideally, closed systems and special waste processing techniques would minimize ENP release during production. The majority of ENP release into the environment would then likely occur during the use and disposal of ENP-containing consumer products; for example, applied sunscreen containing TiO_2 washing off into recreational waters or during showering into wastewater or the abrasion of nano-textiles. ENPs in fluids, suspensions, or aerosols are more easily and completely released during use than those embedded in solids, which are intended to remain within the matrix and are only released slowly as this matrix degrades. The majority of unintentional release will be into wastewater and, thus, wastewater treatment facilities are an important point source of ENP release into natural waters. Septic tanks may be a nonpoint source in groundwater or, if and when these tanks fail, could cause runoff into nearby surface waters. Risk assessment studies of ENPs containing silver have identified wastewater treatment plants as important intermediate barriers to controlling the release of ENPs from consumer products into the aquatic environment [11]. Unfortunately, the removal of ENPs from wastewater during the treatment process is still poorly understood [12].

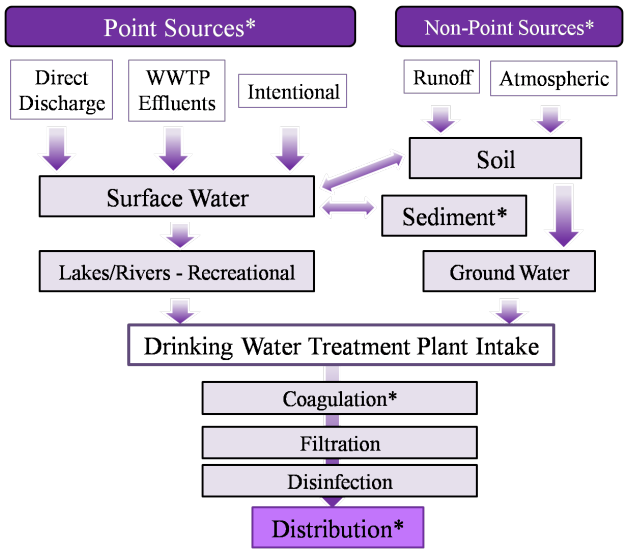

Figure 1.2. Pathways by which engineered nanoparticles enter the water column (* indicates steps where nanoparticles could enter; WWTP – wastewater treatment plant). Figure adapted from [13].

The inevitable release of ENPs into the environment has, however, prompted the rapid development of research into their potential environmental and public health implications. In fact, the majority of such research has focused on hazard assessment, whereas investigations into potential human exposure have lagged behind [14]. Once the hazard has been identified, both hazard assessment and exposure assessment can be considered. Finally, adequate data can then be combined into an associated risk characterization [15]. As risk is quantified as the product of exposure and hazard, an adequate risk assessment has yet to be performed for ENPs in the environment. While the impact of bare, model particles is an essential step in the systematic approach to understanding ENP environmental fate and transport, there is an urgent need to investigate commercialized nanoproducts and environmentally persistent ENP forms. Similarly, ecotoxicological studies focusing on a single type of ENP in contact with a single biological target should be considered a scientific stepping stone, but environmentally relevant concentrations combined with the influence of a complex environment and trophic transfer mechanisms are necessary to begin establishing appropriate risk profiles [14]. There are many ecotoxicological reviews discussing the toxicity of ENPs on individual species and cell lines available [16-27] to cite just a few recent works. Accordingly, the International Council of Nanotechnology identified the development of robust analytical characterization methods to track nanomaterials released into the environment as the main priority for the eco-responsible use of nanomaterials [28], a goal still listed in their 2014 progress review on the national nanotechnology initiative research strategy [29].

The form of ENPs released into the environment is similarly important in determining release quantities. As ENPs may be released as single particles, aggregates, or embedded in a product matrix, the fate and transport of each ENP type must be investigated. ENPs in mixtures are likely to be released both as single particles and in larger forms, such as carbon nanotubes in tires or brake pads [12]. TiO_2 was discharged into natural waters as individual particles from façade paint runoff due to normal weathering [30]. In an investigation of TiO_2 release from commercial sunscreen, Botta and co-workers [31] identified nanoparticle aggregates that represented up to 38 w/w% of the product released after artificial aging. These aggregates tended to sediment in seawater-like conditions. From this study, it was estimated that the average nano-TiO_2 containing sunscreen contains 4.6% TiO_2, thus yielding a release

of between 36 and 56 tonnes of TiO_2 into recreational reef areas based on a laboratory study using prepared salt waters.

Benn et al. [32] investigated the release of silver nanoparticles (AgNPs) from consumer products that were washed in tap water and identified released silver in quantities up to 45 μg g^{-1} product in the water. Although these findings do not take into consideration how variable water quality parameters will affect silver release, they do have important implications for future nano-enabled consumer product regulation, such as measures to better control the potential release of loosely-bound nanoparticles. The amount of silver released was highly dependent on product type. For example, less than 0.01% of the silver contained in medical masks was released from the original 27 w/w% of silver, whereas athletic shirts released about 2% of its initial silver content. It was assumed that 100% of silver was released from the personal care products (toothpaste, shampoo, and detergent). A select summary of the findings from this study is shown in **Table 1.2**. Reported findings of the environmental dispersion of silver and AgNPs from consumer products show that significant amounts of silver are released from AgNP impregnated clothing already after a few laundry cycles, both as particles and ionic species [33-36]. A recent release study by Hedberg and co-workers [37] investigated sequential contact with synthetic sweat, laundry detergent solutions, and freshwater, simulating a possible transport path through different aquatic media. Silver in sequential exposures was found to be approximately a factor of two lower than the sum of each separate exposure.

Investigations at full- and pilot-scale wastewater treatment facilities have identified nanoscale silver sulfide particles in final sludge and effluent. Using analytical high-resolution transmission electron microscopy, Kim and co-workers [38] determined that the reduced, sulfur-rich environment of wastewater treatment plants transforms influent AgNPs into nanosized silver sulfide (Ag_2S) particles. Similarly, the behavior of AgNPs was investigated in a pilot-scale wastewater treatment plant, where x-ray absorption spectroscopy identified that most silver in sludge and effluent was present as Ag_2S [39]. The transformation to Ag_2S can affect AgNP surface charge and dissolution that may ultimately affect reactivity, transport, and toxicity [40]. Sulfidation of Ag has been shown to significantly reduce toxicity due to lower solubility [41] and is likely to occur with other ENPs, such as CuO, Fe, and Pb, given the low solubility product constant for metal sulfides [42]. Westerhoff and coworkers [43] investigated the

presence and morphology of TiOx ENPs in WWTP effluent, and determined raw sewage titanium concentrations ranged from 181 to 1233 μg L^{-1}. Further exploration indicated the presence of titanium oxide ENPs (4 to 30 nm in diameter) in WWTP effluents. These studies have recognized relevant, transformed, and persistent species of ENP that are being directly released into the environment.

Table 1.2. Silver released from consumer products after a 1h wash time in 500 mL tap water. (Adapted from [32]).

Product	Advertised Form of Silver	Mass of Product Washed (g)	Silver content (μg Ag g^{-1} pdt)	*Released silver*		
				Total silver (μg Ag g^{-1} pdt)	Particles <100 nm (μg)	Particles <20 nm (μg)
Athletic shirt (3 samples)	Nanosilver	41 ± 9.6	30 ± 5.4	0.56 ± 0.01	20 ± 0.5	11 ± 1.2
Medical mask	Silver	1.4	270,000 ± 67,000	11	14.8	14.8
Medical cloth	Silver	0.3	230,000 ± 69,000	46	13.3	13.3
Toothpaste	Colloidal	2.1	7.6 ± 9.8	18	14.8	4.3
Shampoo	Colloidal, ionic	13.2	1.4 ± 0.02	0.9	4.8	3.8
Detergent	Colloidal	23.9	3.4 ± 0.06	1.8	6.8	1.7
Towel	Nanosilver	5	270 ± 80	< 1.0	< 5	< 5
Teddy Bear (stuffing)	Nanosilver	26	70 ± 30	< 0.2	< 5	< 5

pdt = products

The ultimate fate and persistence of ENPs in the environment depends primarily on various physicochemical properties, such as ENP size, aggregation state, or surface functionalization, which vary relative to ENP material and water quality characteristics. NPs have inherently very high surface areas and are, therefore, unusually surface reactive compared to their bulk counterparts. In particular, interactions between natural water components and ENPs may cause aggregates to form if the particles become destabilized. These interactions may also result in the breakup of aggregates if the particles are subsequently stabilized. For example, the presence of 0.5 mg L^{-1} of natural organic material (NOM) in a 10 mM KCl solution of pH 8 reduced the zeta potential of hematite particles from +19 mV to -37 mV [44]. The negative zeta potential suggests that these particles had become electrostatically stabilized from one

another since they all then carried a negative charge. Generally, metal and metal oxide ENPs become stabilized by negative zeta potentials in the presence of small amounts of NOM in natural aquatic matrices [45, 46]. On the other hand, ENPs containing metal oxides stabilized by NOM can be subsequently destabilized and thus aggregate in the presence of divalent cations, specifically Ca^{+2}, in the 0.04 M - 0.06 M range [45]. Carbonate-coated silver ENP agglomeration occurred within a few days of exposure to natural waters [47], which is consistent with previous studies in synthetic seawaters, natural freshwaters, and simulated estuarine waters [48].

While drinking water treatment processes have been optimized for the removal of biological and natural water constituents, it has not yet been determined if these processes are also effective at removing ENPs. No doubt their removal from surface waters during water treatment will depend heavily on the ability to induce particle aggregation. Natural nanomaterials include a mixture of polydispersed inorganic, organic, and biological colloidal and polymeric components. Inorganic colloids primarily comprise iron oxides and clays, while organic colloids are composed of humic and extracellular polymeric materials. Biological components include bacteria, viruses, fungi, femto, and picoplankton [49]. Primarily, water treatment plants utilize coagulation by chemical addition to destabilize particulate material, thereby inducing the formation of floc. Stabilized mixtures of ENPs with negative zeta potentials, however, may be resistant to aggregation. Zhang et al. reported that coagulation removal efficiencies of select metal oxide nanoparticles using jar tests with high electrolyte concentrations, only ranged between 20% and 60% [50].

By contrast, the addition of ions may compress the electric double layer and increase the zeta potential to near zero, allowing aggregated ENPs to be removed during the sedimentation and filtration processes. Alum (aluminum sulfate) has been shown to induce aggregation in TiO_2 and CdTe quantum dots, allowing up to 90% to be subsequently removed by 0.45 μm membrane filtration [44]. A study by Holbrook and co-workers [51] confirmed that multi-walled carbon nanotubes could be removed from the aqueous phase via coagulation using either ferric chloride or alum. While the addition of alum is used for conventional drinking water treatment, it is also becoming more popular in the preparation of wastewater for reuse. Granular activated carbon filters are often utilized in drinking water treatment but little information regarding ENP removal is available for this type of treatment. Oxidation, applied to control

taste, odor, and/or disinfection byproducts (DBPs) as well as final disinfection are processes that require more study relative to ENP persistence. Oxidation has been shown to modify the surfaces of carbon nanotubes, making them more hydrophilic and it can be assumed that a similar result would be expected in an oxidative treatment process [52]. NOM-stabilization may hinder ENP removal or detection, and ENPs that have reacted with added chemical disinfectants need to be carefully considered to identify any effects on the rate and type of DBP formation.

Nanoparticles, although not necessarily specifically engineered, may also enter drinking water through degraded distribution systems built of aging metal or concrete structures that could potentially be leaching metallic colloids. Wagner and co-workers determined that there was no change in the particle count in finished water leaving a plant when transported in either reinforced or pre-stressed concrete piping [53]. However, magnetite particles in the 3 nm - 5 nm range were identified in tap water distributed through cast iron pipes [54]. The presence and properties of biofilms within the distribution infrastructure can be influenced by contact with a residual disinfectant, the presence of DBPs, and the residence time and quality of the flowing water. The type and result of interactions between ENPs and these biofilms is unknown but it is possible that the disinfecting properties of silver in ENPs [55], if present in the distributed water, may bring more stability to the pipes. Therefore, the true occurrence of NPs, and especially ENPs, in drinking water relevant to human exposure can only be determined by characterizing water at every stage of the treatment and during distribution of water to consumers.

Once released into the environment, the ultimate fate and form of ENPs will depend primarily on several physical influences. For example, their aggregation state would dictate their mobility in the aqueous phase and will impact their presence and persistence in natural waters. Similarly, it is likely that ENPs will have contaminants adsorbed on their surfaces, potentially altering the toxicity of the particle [56]. The type and quality of the respective water will also play a significant role in the persistence of ENPs, for instance, recreational versus drinking water. Lake and reservoir water are not mixed well, have little flow, are usually periodically stratified, and are susceptible to runoff events. Therefore, pollution dilution may be less efficient in these natural systems compared to streams, rivers, and other moving bodies of natural water, suggesting that ENPs in lakes and reservoirs could potentially be present at higher concentrations than in moving bodies of water.

In order to establish a relevant and applicable risk profile, water quality parameters must be closely and regularly monitored. An analysis of currently available data for ENP risk characterization relative to the environment and human health recommended the modeling of reliable exposure scenarios as an important first step to adequate risk assessment [15]. These exposure models will require ENP characterization data, such as type, form, and surface characterization, as well as predictions of ENP fate and transport within the environment, including degradation and solubility, and finally, an occurrence study of ENP environmental concentrations. These types of models will allow for an appropriate relationship between ENP fate and water type to be developed. A summary of commonly studied environmental processes that directly affect ENP persistence is shown in **Table 1.3**.

Table 1.3. Potential fate of nanoparticles in aquatic systems (reproduced from [13, 20]).

Process	Implications for measurement
Dissolution	Loss of particle state as it becomes dissolved
Deposition	Loss on sample container surface; change in phase during sample processing
Sedimentation	Moving out of suspension; relevant during coagulation treatment
Agglomeration	Target single or clumped particles; Increase in surface area increases reactivity and sorption
Coated	Natural polymers may embed the particles; released before analysis
Association	Sorption to suspended matter could increase their removal during treatment
Reaction	Affected by photolysis, biological, or chemical mechanisms
Decomposition	Biodegradation or change of valence state

Colloidal behavior can offer insight into ENP fate. For instance, aggregation and subsequent settling occur naturally and can be exploited in wastewater and drinking water treatment processes to enhance ENP removal. Occurrence investigations, however, may require a modified approach compared to that used for natural colloids. Inherently, ENPs in either aggregated or individual form will likely have unique exposure profiles compared to each other and to natural colloids due to differences in physicochemical properties.

Analytical methods to distinguish ENPs of different forms and from natural particles should be developed for each targeted environmental matrix to adequately define whether or not the presence of

ENPs is a public health concern. The difficulty in defining the form of persistent ENPs in natural aquatic matrices presents a pressing need to design occurrence studies and sample handling methods that will be able to not only differentiate between natural and anthropogenic NPs, but also take into consideration the location of ENP introduction relative to sampling. Quantitative detection of ENPs is vital to establishing the potential risks to human health that will become increasingly relevant as ENPs are incorporated more and more into consumer products and used in industrialized settings. By correlating occurrence levels with identified risks and the associated environmental conditions, watershed protection and water treatment processes can be better evaluated for human and environmental safety.

Depending on the transportation of ENPs within the environment, it is likely that changing matrix qualities will directly affect the physicochemical properties of the particles. As metallic ENPs are inherently unstable in aqueous environments, it is common for the particles to be stabilized through surface functionalization during their synthesis and subsequent manufacturing [57,58]. Citrate, cysteine, carbonate, or surfactants are some examples of stabilizers used to minimize aggregation and preserve individual colloids, usually through electrostatic repulsion. This process has been shown to occur naturally, where the surface of mineral-based NPs can become functionalized during chemical or biological oxidation [57,58]. The complex and often undefined fate of ENPs in natural waters require extensive characterization including particle size, shape, and distribution, surface properties, redox potential, adsorbed or bound contaminants, catalytic properties, aggregation and dissolution potential, and original form which must be considered for any comprehensive analytical investigation [57, 58].

In order to adequately characterize the fate and transport behavior of ENPs in complex environmental matrices a combination of analytical techniques, rather than a single instrumental approach, will be required. The lack of widely accepted reference standards for quantitation and comparison presents a significant limitation to the development of such methods. According to the International Standards Organization (ISO), a measurement is only valid if the observed quantity is verified by comparison with a standard unit [59]. The potential for human exposure through natural and drinking waters dictates an evaluation of occurrence levels to elucidate a risk assessment and determine whether or not current treatment and watershed protection are maintaining this risk at a reasonable level.

1.1.3 Are ENPs a public health concern?

Nanotechnology initiatives have focused primarily on the synthesis of new ENPs and their subsequent incorporation into consumer products, rather than developing risk assessment for ecotoxicity and human exposure. In the case of other hazardous materials such as dichlorodiphenyltrichloroethane (DDT), lead paints, and asbestos, regulations have been established based on studies of human or environmental toxicity. These regulations have defined usage, containment, and disposal practices [60]. Until comprehensive studies investigating ENP fate, transport, and toxicity are completed, the relevant nano-specific regulation cannot be adequately established thus risking further and long-term exposure to humans and the environment. Most research and industrial processes have developed nano-specific handling and disposal procedures. However, these procedures generally do not extend into the commercial sector [60]. There are prohibitive unknowns and uncertainty in the assumptions required to quantitatively describe ENP fate and transport in natural waters [60] and thus develop an exposure profile to evaluate possible human health risks. In a comprehensive study by O'Brien and Cummins [50], it was concluded that surface water exposure potential rankings for metallic nanoparticles from nano-functionalized consumer products were severely limited by the assumptions required to apply a "best available method" approach.

While similar in size to viruses, natural NPs or ENPs might be erroneously considered benign, as they cannot replicate within a host. However, some NPs have been shown to interfere with cellular function and influence cell proliferation, metabolism, and even death. Conversely, some nanoparticles are being explored for medicinal purposes, able to target certain types of cells and deliver drugs, thereby fighting a disease at the cellular level [61]. Dermal contact, inhalation, and ingestion are possible points of entry for natural ENPs [62-67], which can also be injected or implanted for medicinal purposes. Inhalation of airborne ENPs is the most common human exposure route [68], as nanosized particles can rapidly and widely spread over long distances. Ingestion and dermal contact from liquid (e.g. water) or solid media (e.g. solid waste) is also likely [61].

Regardless of intent, the small size of NPs allows them to enter, translocate within, and even damage living cells by penetrating physiological barriers and travel within the circulatory system. For example, TiO_2 ENPs have been observed inducing DNA and chromosomal damage in the liver [65, 69].

While natural nanoparticles are ubiquitously present in the environment, ENPs are produced in a wide array of toxic materials, shapes, and sizes, yielding potentially very different physical and toxicological properties. Surface effects can affect NP chemical reactivity due to charges, functionalization, and the large fraction of atoms at the surface. As particle size shrinks, surface group's reactivity increases exponentially. NP surface charges can make them more reactive towards cells and proteins compared to their neutral counterparts [70], although a mechanistic correlation between ENP size, cellular uptake, and intercellular stability is still not fully understood [71]. One hypothesis is that, compared to larger particles, the small size ENPs allows them to translocate from entry portals into the circularity and lymphatic systems, and ultimately body tissues and organs, since they are typically smaller than cells and cellular organelles, and thus, potentially more toxic than larger particles [72, 73]. ENP material is also one of the key factors contributing to toxicity. It is well known that bulk materials have different toxic effects compared to their associated ENPs, which range from negligible to very high [71]. The extremely high reactivity of NPs compared to other materials can result in production of reactive oxygen species, and chain reactions can be expected within biological systems [71] making them more toxic than their bulk counterparts [74, 75]. For example, AgNPs were found more toxic than CeO_2 NPs for a range of toxicity measuring tests [76], and AgNPs induced higher toxicity to transparent embryos of zebrafish than gold NPs at the same size range and concentrations [77].

There are a large, and ever increasing, number of publications on ENP toxicity, resulting from the wide range of fields that encompass nanotechnology including chemistry, physics, material science and engineering, biology, medicine, and electronics. In just the last few months, a variety of ENP toxicity studies have been published. Gao and coworkers [78] explored TiO_2 exposure on human skin cells. Ahamed and coworkers [79] investigated dolomite NP toxicity in human larynx and liver cells. Brenner and coworkers [80] targeted occupational exposure to metal oxide ENPs in semiconductor wastewater treatment. Civardi and coworkers [81] performed a risk assessment study for copper-based ENPs, and, Valdiglesias and coworkers [82] explored the cytotoxicity, genotoxicity, developmental toxicity, and neurotoxicity of iron oxide ENPs. These examples just scratch the surface of the nanotoxicity research being performed today.

Unfortunately, a review of ENP toxicity studies [83] reveals varying experimental conditions, non-standardized methods, and a range of observed, exacerbating the already difficult process of obtaining data for systematic comparison and risk assessment. Traditional quantitative risk assessment frameworks cannot be used to draw definitive and comprehensive inferences due to the lack of sufficient data available regarding the environmental fate and transport of ENPs incorporated into commercial products. In a similar approach, Aschberger and coworkers [15] utilized a regulatory risk assessment methodology with assumptions to compensate for limited data. They concluded that a quantitative risk characterization on human exposure of metal and metal oxides from the environment was not possible with the lack of adequate fate and transport data. Possible risk conclusions were made only with the acceptance of high uncertainties and thus the authors recommended that results should not be used for any regulatory decision-making. Further, the generation of reliable data about ENP fate, transport, and occurrence in the environment is listed as the highest priority requirement for generating an effective risk assessment. It was emphasized that a major problem for deriving indicative human no-effect levels was the lack of nanomaterial standardization [15].

1.1.4 An environmentally relevant investigation: silver nanoparticles (AgNP)

Silver is the most abundantly incorporated material in consumer products containing ENPs [5]. AgNPs have at least one transformation product with observed persistence in natural waters [38, 39], and there is extensive literature on their toxicity, including aquatic [84, 85] and terrestrial [86] organisms, such as algae [87], plants and fungi [84], vertebrates (zebra fish) [88], invertebrates (*Caenorhabditis elegans*) [89], microorganisms *Escherichia coli* [90, 91] and *Pseudomonas putida* [92], and human skin keratinocytes, lung fibroblast cells, and glioblastoma cells [93, 94]. Studies reviewing the negative impact of AgNPs on the environment and, potentially, on humans are continually released [20, 41, 84, 95-100].

In 1889, M.C. Lea [101] reported the synthesis of citrate-stabilize silver colloids between 7 nm - 9 nm [102], and the stabilization of silver colloids with proteins followed in 1902 [103]. Since 1987, a commercially available nanosilver medicinal compound around 10 nm has been manufactured under the name “Collargol”. AgNPs have been incorporated into consumer products for over 100 years, being included in products such as antimicrobial biocides, photographics, pigments, wound treatment,

conductive composites, and catalysts [104]. Many common biocidal agents, such as organic compounds, are required at high concentrations and tend to fail at high temperatures. Metal inorganic agents, such as silver, overcome these limitations and can be applied diversely. The biocidal efficacy of silver is directly related to the additive's potential for releasing ionic silver, which falls within the two extremes of highly insoluble silver sulfide and completely soluble silver nitrate [104]. In a comprehensive study considering environmental risk assessments for ENPs, Tiede and coworkers predicted that the most likely route of human exposure to AgNPs was through surface and wastewaters [58]. Among the current estimate of 1600+ nano-enabled consumer products, approximately one in four contain AgNPs [5]. In Europe, silver is released into natural waters at an estimated 20-130 tons per year, yielding concentrations of 40 ng L^{-1} -320 ng L^{-1} [105]. Predicted environmental concentrations of silver nanomaterials are in the range < 0.03 μg L^{-1} – 0.32 μg L^{-1} [106].

Unlike other persistent aquatic pollutants, AgNPs are highly dynamic, reactive, and not thermodynamically stable in the natural environment [41, 107-110]. Several recent works [111-115] have explored the photoreduction of silver ions (Ag^{+}) into AgNPs in the presence of dissolved organic matter, which would likely improve AgNP persistence in sunlit, DOM-rich environments. These studies have recognized a relevant, transformed, and persistent species of ENP that is being directly released into the environment. It is assumed that metal ENPs persistent in the aquatic environment share particular aggregation and surface properties that are directly responsible for their environmental fate. For example, in order to be present in any measureable quantity, NOM-coated metal ENPs with a lower settling rate may persist where aggregated or dissolved particles might not. In the case of potential human exposure through natural waters, occurrence levels of environmentally relevant ENPs are necessary to help assign a toxicity index and determine whether existing watershed protection and subsequent treatments are meeting this objective. While not a surrogate for all possible ENPs, AgNP is a commonly used ENP in commercial products, is environmentally relevant with known toxicity, and commercially available for research use, making it an appropriate candidate for this study.

1.2 ENP Characterization

The diversity of shapes and composition, the various methods of fabrication, the use of assorted surface coatings, and the subsequent behavior of these nanomaterials all speak to the complexity of using engineered nanomaterials effectively and safely. An important, if not key, parameter in reducing this inherent complexity is in conducting proper nanomaterial characterization. Characterization is important for at least three main reasons. Quantifying critical properties of a specific nanomaterial is necessary to provide a comprehensive understanding of the starting material; to understand how these same properties are altered *in situ* by a specific environment; and to correlate these measured nanomaterial properties with a specific measured response. Yet, a major knowledge gap exists regarding the development of property-response relationships for a broad range of nanomaterials, and thus, identifying the key nanomaterial property (or properties) for a given behavior remains elusive.

The importance of proper nanomaterial characterization cannot be understated. Stefaniak et al. [116] argue that incomplete nanomaterial characterization limits the reliability (and perhaps validity) of conclusions drawn from scientific investigations, which may impede both future research in and commercialization of nanotechnology. By way of example, a review by Hansen et al. [117] of over 400 published nanotoxicology studies concluded that nanomaterial characterization was either poorly described or not at all conducted. Similarly, a review of the *in vitro* and *in vivo* genotoxicity literature indicated that comparing published data from disparate studies is difficult since detailed nanomaterial characterization is often missing [118]. Consequently, building a general consensus framework from different investigations without proper characterization is nearly impossible, even when similar nanomaterials are used [119]. Such uncertainly from the scientific community will also not favor timely environmental, health and safety guidelines from regulatory agencies.

A central question remains for nanomaterial characterization – what physiochemical parameter(s) should be measured for proper characterization? This question has been widely debated [116], and although the answer is somewhat dependent upon the application or purpose, there are several measurable parameters that are considered critical in providing an overall nanomaterial characterization description. Broadly speaking, analytical characterization techniques can be divided into three main areas: physical; chemical, and; behavioral. Physical characterization pertains to the nanomaterials'

architecture and includes the size, size distribution, crystal structure, morphology and/or surface area of a specific nanomaterial. Chemical and elemental characterization is focused on atomic compositions (including purity), bonding states and oxidation states, which could include bulk and surface measurements that provide information regarding atomic concentrations, specimen purity and/or reactivity. Behavioral characterization, where the measured property indicates how a nanomaterial responds to external factors, is strongly dependent on the ambient environment. Surface charge, zeta potential, and particle stability (both colloidal and dissolution potential) will all depend on the specific matrix. As such, behavioral characterization descriptors all *require* context (quantified descriptors of the ambient environment) for relevance. While the above list is by no means exhaustive, these parameters are most likely to be deemed important for a wide range of applications including human and environmental risk assessments. Tiede et al. [120] provide a comprehensive discussion of the importance of characterization parameters for developing a better understanding of nanomaterial behavior.

Although the difficulty in developing nanomaterial property-response relationships has been mentioned, nanomaterial characterization also poses a significant challenge. In theory, nanomaterial characterization appears to be very straightforward – obtain a sample, measure various parameters for that sample, analyze the measured data, and finally report analyzed data. Practically, however, there can be many technical and methodological nuances that can inadvertently introduce experimental bias during nanomaterial characterization measurements. A well-known example of such bias occurs when quantifying the average diameter of a heterogeneous particle mixture using dynamic light scattering (DLS) [121] the size distribution is shifted to the most efficient scatters (larger particles) thereby underrepresenting (or completely hiding) the population of smaller particles, which can also be an artifact of the parameters used in the software. This example serves to highlight that a thorough understanding of all issues that could influence a specific measurement for a given nanomaterial and instrument is a vital necessity for the successful analyst.

Regardless of whether ENPs are intentionally or unintentionally released into the environment, their potential as anthropogenic pollutants dictates that the ability to detect ENPs in natural aquatic matrices must be established for an effective risk assessment to be carried out. ENPs are manufactured

with the purpose of representing a wide range of particle sizes; therefore, a variety of structural and distribution analysis techniques must be applied to characterizing them. Since ENP fate and transport behaviors are directly correlated to their physicochemical properties, a full characterization will employ several analytical and separation techniques including microscopy, chromatography, spectroscopy, centrifugation, filtration, and others [122] in order to investigate the unique properties of the chosen ENPs. It is critical that independent characterization be carried out for each nanomaterial used, as there are currently no existing industrial standards for nanomaterial characterization. This is especially necessary since independent characterization data often differ significantly from data provided by the nanomaterial manufacturer [123].

A number of experimentally tested physical and chemical parameters are available for ENPs or can be calculated. These include particle size and number, electrical conductivity, steric properties, surface area, surface chemistry, functional groups, type of coating, quantum and charge parameters, aqueous solubility, hydrophobicity indices, topological and shape parameters, UV/visible absorption, fluorescence, dermal penetration, and physicochemical composition (e.g. free particles, agglomerates etc) [13]. These parameters may provide a basis for developing models to predict physicochemical properties and/or associated hazards.

A comprehensive study of techniques used for the characterization of ENPs was presented by Tiede and co-workers [120] who reiterated the need for combining techniques such as sample preparation and pre-concentration prior to mass spectrometric analysis for obtaining accurate and representative data.

The quantitative and qualitative analytical schemes that have demonstrated ability to analyze classic water-born contaminants (toxic metal ions like Pb^{+2} for example) are being applied to water samples containing ENPs. Techniques such as x-ray photoelectron spectrometry (XPS), energy-dispersive (x-ray) spectroscopy (EDS), infra-red spectroscopy (IR), and ICP-MS have been used to reveal chemical and elemental composition while the techniques of atomic spectroscopy, UV-Vis spectroscopy, and electrochemistry allow for more quantitative studies based on standard calibration comparisons. Reviews by Englert [124] and Wiesner et al. [125] have extensively detailed such approaches. Coupling quantitative analytical techniques with high-resolution microscopy is a promising characterization

approach. Electron microscopy has been successfully applied to observationally characterizing ENPs in a wide range of samples, from simple solutions to plant and other biological material [126]. A major limitation of such an approach is the potential that even several images of the same sample may not be representative of the actual ENP content or distribution. However, combining other analytical techniques with electron microscopy can be very effective for indirectly confirming the presence of ENPs in the sample and can provide information about the presence of other constituents in the sample. A more destructive instrumental technique is usually required to obtain individual component analysis.

In natural water, the detection of metallic ENPs might currently proceed with electron microscopy being used to visualize the presence of the electron dense object with the expected size and shape of the ENPs and atomic spectroscopy measuring the signal response of the metal atoms. The assumption made in this type of approach is that all the metal atoms originate from the ENPs. Ultimately, however, these traditional analytical chemistry approaches are fundamentally flawed in several ways. The ability to accurately determine the difference between targeted ENPs and naturally occurring NPs or the individual ENP components that almost certainly exist in actual environmental samples that contain the ENP has not yet been established [124]. Additionally, it is likely that nanoscale environmental pollutants in water samples are present at concentrations well below that of naturally occurring NPs or the targeted ENPs [127].

1.2.1 Separations

The aggregation state of ENPs in the environment depends heavily on their zeta potentials and is of particular importance in the development of extraction methods since the decision to target individual particles or larger aggregates will have an effect on recovery. In order to achieve measureable quantities of ENPs in natural water samples, high pre-concentration factors may be necessary to match the limitations of detector sensitivity. Following sample pretreatment, several separation techniques are applicable to ENP analysis including size-exclusion chromatography (SEC), high performance liquid chromatography (HPLC), capillary electrophoresis (CE), hydrodynamic chromatography (HDC) and field-flow fractionation (FFF). These techniques represent sensitive, non-destructive methods that can be combined with other characterization techniques for a more comprehensive analysis.

1.2.1.a Sample preparation and pre-treatment

Sample collection and preparation can present a significant source of bias and analytical uncertainty due to the unstable nature of ENPs in aquatic matrices. Their tendency to aggregate and/or become coated with NOM, for example, could significantly alter quantification results. Organic ligands may prevent complete atomization of metallic ENPs in an inductively coupled plasma (ICP), although samples are often digested in chromic or nitric acids prior to analysis and such pretreatment would likely address this issue [128]. Without careful storage, analyte losses could occur during sample processing as, for example, in the case of C_{60} fullerenes which were shown to irreversibly adsorb from solvent extracts onto glassware within four hours of contact [129]. Additionally, the presence of low level contamination may compete with the identity and detection of the similarly low concentration of ENPs. Preservation techniques must, therefore, be applied during sample collection and handling to ensure the stability of any ENPs present until they can be extracted and analyzed.

Low levels of ENPs in the environment will challenge existing methods used for other emerging contaminants in drinking water to adequately preconcentrate and analyze ENPs in natural waters. Approaches used for isolating NPs from water without distinguishing between natural and anthropogenic forms should be effective for targeting ENPs. Centrifugation from 330 g to 120,000 g for size fractionation of NPs in water collected after sedimentation during drinking water treatment [30] has achieved separation stages of 9000 nm, 750 nm, 180 nm, and 12 nm. The centrifuge tubes were designed to hold a transmission electron microscopy (TEM) grid or atomic force microscopy (AFM) mica sheet for further analysis. Ultracentrifugation at speeds up to 10^6g has been used similarly [130]. Using this approach, fibrous polysaccharide NPs and spherical black dots were characterized by AFM after being isolated from a drinking water treatment plant. Further analysis by TEM and elemental analysis also identified clay, iron oxide, and silica NPs and particle concentrations on the order of 10^7 NPs mL^{-1} were achieved [30]. Electrically assisted filtration has also been used to prepare NPs for AFM and scanning electron microscopy (SEM) with minimal changes to particle properties [131]. Membrane-, ultra-, and nanofiltration may be hindered by the precipitation or aggregation of some NPs at the membrane surface and subsequently removed if the filtration is performed in a step-wise fashion [132]. The significant limitation with filtration and centrifugation methods, however, is their inability to isolate both the dissolved and

suspended ENP forms, both of which are required for a total measure of ENP component concentration (e.g. AgNPs and silver ions). A promising method has been demonstrated by researchers in the Liu laboratory with the use of cloud point extraction using the surfactant Triton X-114 to selectively pre-concentrate trace amounts of AgNPs from spiked aqueous environmental samples [133].

1.2.1.b Size exclusion chromatography (SEC)

SEC is commonly interfaced with detection methods such as ICP-mass spectrometry (ICP-MS), voltammetry, multi-angle light scattering (MALS), and dynamic light scattering (DLS) in order to isolate and characterize ENPs. In order to achieve their effective isolation from water, the stationary phase must be properly chosen to ensure that particles larger than the defined ENPs are rejected. For example, a column of pore size 400 nm was used to separate gold ENPs between 10 nm and 80 nm with particle size correlated to retention time [134]. As industrial applications for noble metallic ENPs expand, however, the range of ENP surface functionalization becomes more diverse. Modified particles are usually stabilized by electrostatic repulsion or steric hindrance compared to their raw forms [135], rendering traditional SEC stationary phases inadequate for effective separation. In order to accommodate the variety in current and future ENP groups, specific SEC methods have been developed. For example, recycling SEC utilizing a porous hydrophobic microgel column has allowed for the high-resolution size-separation of alkanethiolate-stabilized gold ENPs below 3 nm [136]. The addition of anionic surfactants to the mobile phase allows the separation of water-soluble citrate-stabilized gold ENPs without analyte adsorption and coagulation effects [135]While most modern SEC columns can resolve particles between 5 nm -1200 nm independent of density, HDC columns containing non-porous beads can be used to separate particles by flow velocity and the velocity gradient [120], which help to reduce the effects of pore blockage experienced by typical SEC columns. HDC interfaced with ICP-MS was used to identify AgNP size distributions spiked into sewage sludge supernatant. The same setup was also able to separate, albeit with poor peak resolution, an ENP mixture and included effective analyte preconcentration and matrix removal using an on-line column method [122].

1.2.1.c Capillary electrophoresis (CE)

CE is an effective method for the size-based separation of water soluble and charged ENPs. The electrophoretic mobility of the particle is a function of the zeta potential, directly affected by the particle's surface charge, and can be controlled by adding modifying agents to the mobile phase buffer [136]. Comprehensive reviews of CE methods applied to ENPs demonstrate a consistent relationship between electrophoretic mobility and ENP diameter, taking into account particle-capillary surface interactions [137]. Buffer pH suppression and capillary surface modification have been shown to reduce or even prevent ENP retention.

Commercially available CE instruments allow for low sample volumes, but are limited by the low sensitivity of common online detectors, such as those utilizing spectrophotometric absorption. Although mass spectrometry is compatible as an interfaced detector for CE, no on-line applications have been established. CE analysis of gold nanoclusters followed by off-line analysis using matrix-assisted laser desorption/ionization MS [138] only further emphasizes the need for on-line characterization techniques. UV-Vis absorption and fluorescence spectroscopy methods are most commonly used with CE systems. CE-UV-Vis was applied to producing a population analysis of ENPs in the 57 nm - 992 nm range. A CE system interfaced with laser-induced fluorescence detection has been used to successfully analyze μm-sized particles and bio-conjugated CdSe/ZnS. Fluorescence detectors offer enhanced selectivity when compared with UV-Vis absorption for selected ENPs. Fluorescence spectra can identify structural information about single-walled carbon nanotubes. CE interfaced with other detection techniques, such as with light scattering which was used to separate polystyrene spheres and successfully identify individual particles greater than 110 nm, demonstrates the versatility and the compatibility on-line detection methods for CE systems [137].

1.2.1.d Field flow fractionation

Field flow fractionation (FFF) and specifically, flow field flow fractionation (FlFFF) are versatile methods for characterizing ENPs, due to their compatibility with a wide range of water quality parameters, the capability for rapid on-line pre-concentration, and the possibility of both additional on-line characterization with directly interfaced detectors and off-line characterization using collected size

fractions. Unlike chromatographic techniques, FlFFF does not require a stationary phase and instead, particle separation occurs in an open channel. The major advantages of FlFFF over other separation techniques are its ability to separate particles continuously, non-destructively, and at high resolution between 1 nm and 100 μm, depending on instrument setup. FlFFF is also incredibly versatile, as it is capable of being interfaced with several on- and off-line detectors, including elemental detectors such as ICP-MS and ICP-atomic emission spectroscopy (ICP-AES), scattering techniques such as light scattering, either multi-angle light scattering (MALS) and quasi-electric light scattering (QELS), or electron microscopy methods including TEM. FlFFF has been applied to particle separation of very small particles, such as humic substances in the 1 nm range, natural colloids in the 20 nm - 450 nm range, and larger particles, such as clay, in the 5 μm - 100 μm range [139]. Contado and Pagnoni [140] used FlFFF-ICP-AES to assess the presence and sizes of TiO_2 particles in commercial foundation cosmetic creams.

Asymmetric FlFFF (AF^4) utilizes hydrodynamic forces produced by an external field applied perpendicular to the channel flow through the fractionation channel [141]. AF^4 has been used to analyze some complex sample matrices such as soil suspensions and colloids in fresh and marine water samples [142], while simultaneously reducing sample complexity and fractionating colloidal materials by size. Due to the complexity of natural aquatic matrices and the need to preserve the physical state of ENPs within those samples, it is essential that interfaces between separation methods and characterization techniques continue to be developed. As increasingly complex AF^4 ENP studies progress, enhanced FFF techniques for other applications, such as thermal FFF (TFFF) and electric FFF (ElFFF), have been developed. Conventional TFFF and its new high-performance cousin, micro-TFFF, allow for particle separation by applying a temperature gradient perpendicular to the major flow direction to vary the diffusion and viscosity of the flow media, thereby separating sample particles by molecular weight and composition according to differences in the surface interaction with the flow media. ElFFF achieves separation by applying and electrical field perpendicular to the AF^4 flow, using differential electrophoretic mobilities and diffusional rates to separate particles at voltages three orders of magnitude lower than conventional electrophoretic methods [143].

AF^4-ICP-MS and AF^4-MALS/QELS-ICP-MS have recently emerged as versatile tools for the investigation of ENPs in environmental samples. FlFFF coupled with ICP-MS was proposed only in 1999,

but as of 2010 more than 90% of FFF and ICP techniques have been focused on environmental applications [144]. This multi-step approach allows for the pre-concentration and elemental characterization of size fractions or determination of ENP shape, and even quantitative analysis providing recovery and mass balance studies can be performed. As an example, AF^4-ICP-MS has been used to show the presence of natural nanoparticle populations in the 1-12 nm range with different trace-element binding characteristics at various depths in the Great Salt Lake, UT, USA [145]. AF^4-ICP-MS was also applied to the investigation of silver nanoparticle aggregation, which was determined to occur with increasing ionic strength, but decreased in the presence of NOM [146]. Poda and co-workers [147] used AF^4-ICP-MS to identify a significant increase in silver nanoparticle size, approximately 31 nm to 46 nm, after extraction from the tissue of the freshwater sediment-dwelling oligochaete, *Lumbriculus variegatus*, providing insight into the bioavailability and potential toxicity of silver nanoparticles in natural waters. Using this method, the group was able to separate and identify samples containing as low as 6.7 μg L^{-1} of 10 nm, 40 nm, and 70 nm silver nanoparticles, demonstrating the sensitivity and applicability of AF^4-ICP-MS for the analysis of ENPs at relevant environmental concentrations.

1.2.2 Microscopy

Techniques such as electron and scanning probe microscopy are commonly employed for characterization, detection and analysis of ENPs due to their nanometer resolution capabilities. These techniques include, but are not limited to, TEM, scanning transmission electron microscopy (STEM), SEM, environmental scanning electron microscopy (ESEM) and AFM. In general, the lateral resolution imaging capabilities of TEM, STEM and AFM surpass that of SEM and ESEM, thereby making the former techniques more suitable for characterization of individual particles. SEM and ESEM, however, may be more appropriate for imaging samples where physical characterization of structure, aggregation, size, and sorption are deemed important since the field of view can be much greater compared to, for example, TEM [122].

While electron and scanning probe microscopy techniques possess powerful imaging capabilities, by themselves they are unable to provide any compositional or elemental information about the sample. Consequently, these imaging techniques are frequently coupled with analytical devices that can detect

and measure various components generated during the electron beam-sample interaction. For example, EDS is often used to measure the characteristic x-rays in a SEM and/or ESEM [148], while electron energy loss spectroscopy (EELS) and selected area electron diffraction (SAED) are used to measure elemental and crystal structure, respectively, with TEM [149]. In EDS, the sample depth at which the x-rays are generated is based on many factors, including sample composition and incident electron beam voltage [148]. Subsequently, characteristic x-rays may be generated and measured from within the sample volume (> 1 μm depth) and, therefore, may not accurately reflect the true surface composition of the sample. If detailed surface-specific composition is required (< 3 nm depth), techniques such as Auger electron spectroscopy coupled to SEM [150] are required.

SEM and TEM imaging is conducted in a high-vacuum chamber, requiring samples to be dry prior to analysis. Environmental sample drying may significantly alter the ENP aggregation state, for example, or introduce other artifacts that are subsequently misinterpreted during analysis where there is a potential risk that even the analysis of several images of the same sample may not necessarily represent the accurate ENP content or distribution. This step of the analysis procedure, sample preparation, is often overlooked but remains a critical portion of proper ENP characterization, especially for aqueous ENP suspensions. Consequently, a number of electron microscopy techniques have been developed to provide images of fully-hydrated ENP samples: ESEM, WetSEM, and liquid TEM [151, 152].

The ESEM is an SEM that also makes use of a three-stage differential pumping system separated by apertures, a computer controlled gas introduction system and a patented gaseous secondary electron detector. The ESEM is able to operate with higher gas pressures in the specimen chamber compared to a conventional SEM, and the operator can choose the chamber gas composition but water vapor is the most common. With the use of a cooling stage, the ESEM is capable of maintaining liquid water under the electron beam [153]. The relaxed vacuum environment of the ESEM chamber opens electron microscopy to wet, oily, and dirty specimens that might not be considered appropriate for the higher vacuum of a conventional SEM specimen chamber. In viewing wet specimens in the hydrated state, the higher gas pressure in the specimen chamber makes high resolution imaging more challenging. In this instrument, it is possible to routinely view features tens to hundreds of nanometers in size in the hydrated state [154].

WetSEM was developed as an alternative to ESEM and uses a proprietary sealed capsule sample holder with an electron transparent membrane. This capsule can be filled with either liquid or wet solid samples, while the membrane allows *in situ* imaging in natural media. Tiede et al. [155] performed a comparison of conventional SEM and WetSEM for a series of ENP solutions and concluded that WetSEM may be a useful complimentary analytical technique in understanding the environmental behavior of ENPs in aqueous systems.

Both ESEM and WetSEM are limited in resolution due to their accelerating voltage; most conventional ESEM and SEM systems operate up to 30 kV. The accelerating voltage in a standard TEM, by contrast, is 300 kV, which suggests at least one order of magnitude resolution improvement and indicates the appeal of *in situ* TEM imaging of aqueous ENP solutions. A major difference between any liquid cell for TEM (liquid TEM) and WetSEM is in the position of the electron transparent membranes; liquid TEM requires the sample to be sandwiched in between the membranes while WetSEM requires a membrane on the top surface only. Williamson et al. [156] first reported nanoscale resolution with liquid TEM when imaging the nucleation and growth of nanoscale copper clusters during electrodepostion. Zheng et al. [157] imaged the growth of platinum nanocrystals and discovered two distinct growth processes. de Jonge et al. [158], Ring and de Jonge [159], and Klein et al. [152] used STEM and a novel microfluidic flow cell to image gold nanoparticles in various matrices. Although liquid STEM/TEM is still under development, this imaging modality offers a promising alternative to conventional electron microscopy imaging techniques since the introduction of sample artifacts during sample preparation is greatly reduced.

1.2.3 Scattering and Spectroscopic Techniques

The interaction between light and ENPs can be a powerful characterization tool, as the wave vector of the energy source can be modified relative to particle structures, size, and shape while the frequency remains unchanged or is changed as a result of absorption. The resulting signal can then be measured by x-ray, electron, or neutron diffraction and scattering techniques. Dynamic light scattering, or QELS, is commonly used for *in situ* ENP size analysis and physical characterization of aggregated ENPs. FFF-QELS, FFF-MALS, and/or FFF-UV-vis spectrophotometry, and hence the feasibility of pre-separation

of ENPs prior to detection, have demonstrated capabilities for complex characterization analyses of ENP samples. The structural properties of ENPs in solid and fluid materials, and in mono- or polydispersed systems, have also been studied using small angle x-ray scattering [120]. Scanning mobility particle sizing interfaced with electrospray atomization was able to elucidate the size distribution of AgNPs in an aqueous solution devoid of salt-impurities to within 2.0 nm ± 0.2 nm, subsequently confirmed by TEM [160].

Laser-induced breakdown detection (LIBD) is another example of a novel and highly sensitive technique for the non-destructive analysis of ENP concentration and number-weighted mean diameter in liquids [13]. LIBD is able to detect ENPs as small as those in the 10 nm range and has a limit of detection several orders of magnitude lower than other methods. In fact, a mobile LIBD device has been designed to allow on-site and online analysis of aqueous ENP suspensions [161]. LIBD has been used to analyze particles isolated by ultra-centrifugation from treated drinking water. The analysis provided a size "spectra" of the particles in the sample [30], determining that the mean particle size in the treated water prior to final disinfection was between 15 nm - 20 nm with a number density of 108 particles mL^{-1}. The determined number density by LIBD agreed with results from the permeate collected after a subsequent ultrafiltration step. Energy curves to calculate particle size and number density have been generated from samples collected at different drinking water treatment steps, ultimately showing that the ozonation process placed in between coagulation and filtration resulted in a decrease in the particle number density by a factor of 3 [161]. The particle diameters were found to be around 20 nm and did not appear to change significantly with the addition of ozonation. It follows that further study is needed to establish an occurrence profile of ENPs at environmental concentrations in various water treatment plants.

1.3. Study Approach

1.3.1 Instrumental Methods

The availability of existing particle characterization methods for application at the nanoscale has allowed for the development of a wide range of analytical techniques for NP characterization. Unfortunately, exploring ENP fate in the environment is more challenging than with larger particles, primarily due to the requirement of detecting trace amounts in complex natural matrices. While many of

the previously discussed analytical techniques are well suited for trace analysis, the complex, heterogeneous nature of environmental matrices may confound detection of environmentally relevant concentrations of ENPs (< μg L^{-1}) [162]. Therefore, commonly used techniques often used for particle size distribution and concentration analysis, such as microscopy [163], chromatography [164], centrifugation [165], laser light scattering [166], and filtration [167, 168], are typically inadequate for ENP characterization in natural systems. The primary disadvantage for most of these techniques is the limited method sensitivity, which is generally insufficient to distinguish environmentally relevant concentrations of ENPs) [169, 170]. Additionally, the challenges of differentiating between target ENPs from other, natural matrix constituents such as NOM is often too great for most techniques [171].

Microscopy is one of the most commonly used nanoparticle characterization techniques, since in theory, it allows for the detection of single NPs. However, the application of this approach is very difficult and is compounded by unrepresentative sampling, aggregation, and the ability to identify particles in very dilute samples [162].

Light scattering techniques, as stand-alone methods, are another example of a particle characterization method that is inadequate for the analysis of NPs in complex matrixes. Limitations include poor sensitivity in dilute solutions, failures to distinguish target ENPs from matrix components, and the inability to establish particle size distributions in polydisperse samples. Polydisperse distributions are particularly problematic, as scattering intensity scales with particle size, resulting in disproportionately large distributions, even if smaller sized particles predominate [162].

LIBD, while a promising technique, both as a stand-alone analyzer and interfaced with separation methods, is limited in several ways [172]. To begin with, LIBD is still a relatively young technique and instrumentation is not widely available. Similar to other scattering techniques, LIBD is not able to distinguish between target ENPs and matrix components. Finally, LIBD requires particle-specific external size calibrations, which is inhibited by the lack of NP standard materials and the wide variety of ENPs dispersed throughout the environment [172].

AF^4 was chosen as a separation technique to explore its application for AgNP analysis in natural waters because it is a promising technique, highly versatile for a wide range of ENP sizes, and is currently one of the most widely used methods for environmental ENP analysis. Further, AF^4 allows for

changes in a variety of instrumental settings to optimize the separation protocol, or combination of settings, for a target sample. These settings include, buffer concentration and composition, separation channel size, membrane type, hydrodynamic flow rate variations, and injection volumes. Comprehensive discussions of these settings, and their optimization for a variety of applications, are extensively discussed in the literature [139, 173-179] and a theoretical discussion of AF^4 is provided in section 1.3.1.a. Finally, AF^4 is well suited for on-line hyphenation with a wide range of detectors as well as collection of sample fractions for further off-line analysis [180-184]. The ability to serially couple, or hyphenate, more than two instruments is possible and increases the amount of information that can be confidently assigned to specific populations of nanoparticles as well as accommodating higher sample throughput compared to conventional methods [185].

In particular, AF^4-ICP-MS allows for elemental analysis at potentially environmentally relevant concentrations and [144, 186] due to the high plasma temperature, prevents interference from other components in a complex, natural sample. Further, multi-metal analysis is possible, providing a means to detect individual species in ENP mixtures comprised of several material types [162]. ICP-MS combines a high-temperature inductively coupled plasma (ICP) source with a mass spectrometer. The ICP source converts the resulting atoms to ions, which are then separated and detected by the mass spectrometer. There are several published reviews discussing environmental and NP applications of AF^4-ICP-MS [139, 144, 162, 170, 187, 188]. ICP-MS detection of target metal ENPs, when applied post-separation, is relatively straightforward and minimal optimization is required. AF^4-ICP-MS quantitation and elemental characterization of AgNPs in natural lake water samples are discussed in Chapter 4.

AF^4 separations of various natural, environmental, biological, or otherwise complex samples are less defined and contain a higher level of variability [181, 189-191] when compared to the separations of mixtures of monodisperse or distinct particle sizes. In order to establish a metric that determines if the separation optimization is complete and the separation is the best possible given the available experimental conditions, the inclusion of an online light scattering detector was used following separation. While light scattering detectors are inadequate for measuring AgNPs or other ENPs, AF^4-MALS-UV was used to monitor the molar mass distribution of NOM in synthetic freshwater samples as a method for understanding overall sample separation. The UV detector can respond to concentration that, in

combination with light scattering, produces NOM molar mass measurements. The output for this study is defined by minimizing the average molar mass of NOM following AF^4 separation. Further discussion of NOM can be found in Chapter 4. Theoretical discussions for AF^4 and light scattering are provided below in sections 1.3.1.a and 1.3.1.b, respectively. A demonstration of a light scattering separation metric using AF^4-QELS is discussed in detail in Chapter 2 using a model system of polystyrene beads. Extremely polydisperse mixtures, such as environmental or natural samples, may not yield sufficient resolution between sample components to judge separation quality by observing the raw data in fractograms alone. Therefore, the analysis of a single separation and its data may not provide adequate information about the accuracy of the measurement. A rigorous characterization requires multiple separation protocols and comparison among them. Therefore, prior to AF^4-ICP-MS quantitation and characterization of AgNPs in natural waters, AF^4-MALS was used to perform a sensitivity analysis of AF^4 instrument factors (e.g. "primary factors") and evaluated how they affected AF^4 separation of complex samples using the established separation metric. An introductory theoretical discussion and example of the sensitivity analysis and statistical methodology is provided in section 1.3.2 and described in Chapter 3. A schematic detailing the interfaced instruments used in this work is given in Chapter 4.

1.3.1.a Asymmetric flow field flow fractionation (AF^4)

AF^4 is a chromatography-like technique where particles are separated based upon hydrodynamic principles. Colloids, macromolecules, and particles are size-separated due to their interaction with a cross flow of carrier liquid applied, perpendicular to the main lateral laminar flow within the separation channel. FIFFF theory was established by J.C. Giddings and coworkers in 1966, after Giddings, an avid fisherman, observed that leaves in the center of a body of flowing water moved more quickly than those near the shores [192]. Similarly, the laminar flow in the separation channel creates a parabolic flow profile where the velocity near the channel walls is lower than in the center of the channel. To create the pseudo-perpendicular cross flow, the upper housing, forming the top of the separation channel, is impermeable while the bottom of the channel consists of an ultrafiltration membrane; the membrane's molecular weight cutoff is substantially lower than that of the analytes of interest to prevent them from

exiting the separation channel. In the case of AgNPs, which tend to release ionic Ag, the solid particles are retained while any unbound ionic fraction passes through the membrane.

Particle dispersion across the height (or thickness) of the channel when AF^4 is operating in its intended separation mode, is due to Brownian diffusion tending to equilibrate the particles across the channel height, and the cross-flow pushes the particles towards the ultrafiltration membrane. Smaller particles, with higher diffusion rates, tend to equilibrate into a "cloud" higher in the channel and sample a larger portion of the longitudinal flow profile where the velocity is higher. Contrarily, larger particles with lower diffusion rates tend to equilibrate towards the ultrafiltration membrane, where the longitudinal flow is slower. Smaller particles are, therefore, transported along the channel much faster than larger particles. Each equilibrium cloud is populated by particles of the same diffusion coefficient (*D*), where the thickness of the cloud (l) is dependent on the cross-flow-induced velocity (U) [139]:

$$l = \frac{D}{U} \tag{1.1}$$

Polydisperse samples, such as those analyzed in this project, contain populations of particles with varying diffusion coefficients and, thus, different values of l. Since particle retention is a function of the diffusion coefficient, particles of different sizes will be separated. The retention volume is related to D and the volumetric cross flow velocity (V_c) by [139]:

$$D = \frac{\lambda V_c w^2}{V^o} \tag{1.2}$$

where V^o is the void volume, or volume of the mobile phase, λ is the retention parameter, and w is the channel thickness. The retention parameter defines the distance between the accumulation wall of the channel and the mean cloud thickness of the analysis zone. Physical parameters related to the fractionation process can be extracted from λ. The retention parameter can be calculated by the ratio of cloud thickness to channel thickness [139]:

$$\lambda = \frac{l}{w} \tag{1.3}$$

Additionally, the retention parameter can be calculated from the measured retention volume (V_r), where the retention ratio (R) is given by [139]:

$$R = \frac{V^o}{V_r} = 6\lambda\left(\coth\frac{1}{2\lambda} - 2\lambda\right) \tag{1.4}$$

which can be approximated for very large particles that are strongly retained ($V_r > 6V^o$) to [139]:

$$\frac{V^o}{V_r} = 6\lambda \tag{1.5}$$

Finally, for normal Brownian mode, the retention parameter can be defined as [144]:

$$\lambda = \frac{kTV^o}{3\pi\eta V_c w^2 d_h} \tag{1.6}$$

where k is the Boltzman constant, T is the absolute temperature, η is the dynamic viscosity of the carrier solution, and d_h is the hydrodynamic particle diameter. The hydrodynamic diameter is defined as the diameter of a compact sphere with the same diffusion coefficient as the particle, can be determined by applying the Stokes-Einstein [139]:

$$d_h = \frac{kT}{3\pi\eta D} \tag{1.7}$$

In general, the intended separation mode predominates with particles in the nano range (1-500 nm). Transition to a different (and usually undesired) steric/hyperlayer elution mode occurs when colloid size with the presence of micro-sized particles and slip forces allow the larger particles to elute faster than the smaller ones.

The transition to steric mode, or steric inversion, depends on several primary instrument factors, such as flow rate, channel thickness, and field strength, and also sample parameters such as particle shape. Decreasing the cross flow, for example, shifts the steric inversion towards larger particle size [193]. Instrument factors (e.g. cross flow rates or ramp up/down) are optimized to avoid both modes occurring within the same separation, as co-elution of different sizes may occur. Typically, a size characterization method, like light scattering, is used as a detector to monitor particle elution. One of the working AF^4 instrument set-ups used in this work is shown in **Figure 1.3** and a schematic of the basic operation of a typical AF^4 separation channel is shown in **Figure 1.4**.

Figure 1.3 - An image of the AF^4-MALS/QELS instrument at the National Institute of Standards and Technology that was used in this research. The AF^4 separation channel is identified in red. The AF^4 is also interfaced online with a UV-Vis spectrophotometer.

To introduce the sample into the separation channel with minimal dispersion, AF^4 operates in a different flow configuration called focusing (**Figure 1.4b**). In this configuration the sample is injected into the separation channel through the sample inlet and focused below the injection site, allowing for the on-line pre-concentration of a theoretically unlimited volume of sample. Focusing occurs when the carrier solution is injected into the separation channel through both inlets on either end of the channel, which occurs by splitting the flow delivered through the pump. By adjusting the opposing flow rates, the area under the sample inlet has a lateral flow of essentially zero, and the flow vectors in the channel are

pointing at the focus point. This is particularly prudent for the investigation of ENPs in natural waters, as the ENP concentration will be very low and the ability to concentrate large volumes of sample will allow for increased detection capabilities.

After sample introduction is completed using the focusing configuration, the flow configuration is changed to elution mode; the mode described in the beginning of this section (**Figure 1.4c**). During this operation particles are separated by size. Carrier flow is injected into the flow inlet and exits the channel at both the channel outlet and through the membrane. The cross flow is generated by adjusting the pressure drop at the channel outlet (using flow measurement controlling motor-driven needle valves). In order to compensate for the loss of flow through the membrane and maintain axial flow velocity, the separation channel is trapezoidal in shape (**Figure 1.4a).**

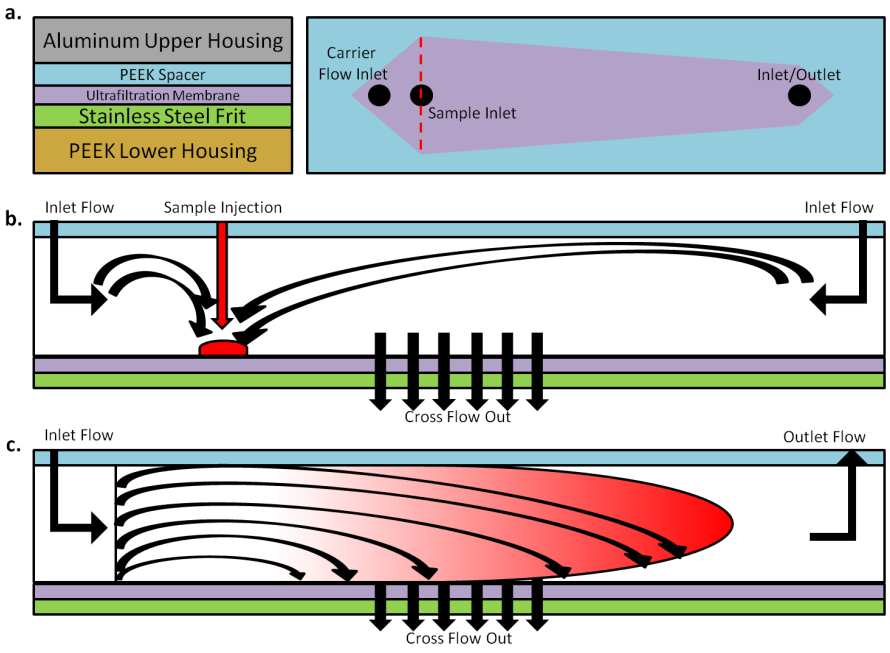

Figure 1.4 - Schematic showing a.) the design of a typical AF^4 separation channel looking from the side, illustrating the position of the channel within the housing, and the channel formed by the spacer and membrane; b.) a description of a typical sample focusing step, and; c.) a depiction of the laminar flow profile during a typical elution step when particles within the focused sample are separated. PEEK = polyether ether ketone. Components within figure are color coordinated with components labeled in a).

Although AF^4 is a powerful separation tool, it can be tedious and time-consuming to establish optimal conditions and good separation efficiency; therefore, method optimization through establishing appropriate separation protocols (i.e. combination of instrument factors and settings) and rigorous statistical analysis for a wide range of samples was the primary objective of this project. Instrumental factors include both hardware and software-controlled factors. Factors that require a physical hardware change include membrane type, spacer thickness, and buffer concentration or composition. Software-controlled factors include cross flow rate, cross flow ramp (increase or decrease rate over time), focus flow rate, focus time, elution time, and injection volume. For this work, software-controlled factors were targeted due to ease of adjusting factor settings. Buffer concentration was also selected, due to the expectation that changing buffer concentration, and in turn, the ionic strength within the separation channel, would result in a significant impact on the separation of ENPs in natural waters during the sensitivity analysis. In order to adequately characterize fractionated natural samples containing ENPs for the purposes of future occurrence surveys, the particles must retain their general shape and character. Therefore, careful consideration of the type of buffer and membrane composition was made to avoid the introduction of artifacts, a chemical change in sample components, or the loss of analyte to the membrane surface. Other hardware changes, including buffer composition and membrane type, were fixed based on preliminary experimentation (not shown).

1.3.1.b Light scattering

Light scattering was first described for macromolecular solutions and suspensions [121], but until separation techniques were established, light scattering measurements only produced weight average molecular weights and corresponding z-average square radii. The advent of separation techniques that can be directly interfaced into light scattering detectors has allowed for the distribution analysis of polydisperse mixtures of particles and identification of some molecular conformations. Both differential and cumulative molecular weight and mean square radii distributions can thus be produced. It is assumed that fractions eluted from an interfaced separation technique, in this case AF^4, each contain an essentially monodisperse particles. Since scattered light is proportional to a given concentration, relatively high concentrations of particles of low molecular weight are needed to produce an appreciable

signal. Light scattering itself has a particularly complex theory; however a brief review of multi-angle light scattering and its application will be covered here [121, 194].

Rayleigh scattering describes the elastic scattering of light or other electromagnetic radiation by objects much smaller than the wavelength of incident light. By definition, shorter wavelengths of light scatter more intensely than longer wavelengths, since Rayleigh scattering is inversely proportional to wavelength to the fourth power. Additionally, the longer wavelengths have a narrow spectral bandwidth and high coherence, which is essential for making analytical measurements of materials in the nanometer range. In order to accommodate larger particles, the theory was adjusted to minimize two major non-ideal effects: non-ideal solutions and large particles. The Rayleigh-Gans-Debye (RGD) approximation achieves this by extrapolating to zero concentration and to scattering at the 0^o angle of incident light. The intercept of this extrapolation yields the weight average molecular weight [121].

RGD calculations apply for dilute solutions, with negligible interactions between sample particles, solvent molecules, or each other, and for particles whose refractive index and size meet the following assumptions:

$$|m-1| \ll 1 \; and \; 2ka|m-1| \ll 1 \tag{1.8}$$

where 2a is a characteristic diameter of the particle and m is the refractive index of the solvated particle, $k = 2\pi\frac{n_o}{\lambda_o}$ and $m = \frac{n}{n_o}$, n_0 is the refractive index of the solvent, and λ_0 is the vacuum wavelength of the vertically polarized incident light. Essentially, the refractive index of the particle must be practically indistinguishable from that of the solvent, and the total phase shift of incident light is negligible as it passes through the molecule [121]. Each element of the overall particle is assumed to be a simple dipole scatterer with excitation and scattering independent of any other particle elements [195]. Therefore, in the absence of multiple scatter effects, the scatter pattern in a solution of particles is the same as that of a single particle, but amplified proportionally to the number of particles [194].

When the RGD assumptions are met, the excess Rayleigh ratio, R(θ), and the weight average molar weight, M_w, are related by the following [194]:

$$\frac{K*c}{R(\theta)} \approx \frac{1}{M_w P(\theta)} + 2A_2 c + \cdots \quad (1.9)$$

where c is the sample concentration, and M_w is the weight-average molecular weight. A_2 is the second virial coefficient, but it is ignored for colloidal and dilute solutions as it only applied for solvated systems. K* is a physical constant for vertically polarized incident light, dependent on the refractive index of the solvent (n_0), the vacuum wavelength of the vertically polarized incident light (λ_0), and the refractive index increment (dn/dc) of the solution [194]:

$$K^* = 4\pi^2 \left(dn/dc\right)^2 \frac{n_o^2}{(N_A \lambda_o^4)} \quad (1.10)$$

where N_A is Avogadro's number. The excess Rayleigh ratio, R(θ) describes the excess intensity of scattered light at a given angle [194]:

$$R(\theta) = f_{geom} \frac{[I(\theta) - I_S(\theta)]}{I_o} \quad (1.11)$$

where I_o is the intensity of incident light in ergs/cm^2-s, f_{geom} is a geometrical calibration constant that is a function of the solvent and, the refractive index and geometry of the scattering cell. $I(\theta)$ and $I_s(\theta)$ represents the intensity of scattered light from the sample and the pure solvent, respectively. I_o is the intensity of incident light per unit, projected area of volume. The angular dependence of scattered light, P(θ), is a function of the intensity of incident light, the solvent, and the refractive index and geometry of the scattering cell. P(θ) is represented as an alternating power series, where the coefficients ($\alpha_1, \alpha_2, \ldots$) depend on the mass distribution within the particle and can be determined from light scattering measurements [194]:

$$P(\theta) = 1 - \alpha_1 \sin^2 \frac{\theta}{2} + \alpha_2 \sin^4 \frac{\theta}{2} - \cdots \quad (1.12)$$

The molecular structure can be determined from light scattering measurements and the subsequent derivation of the coefficient (α_1). At $\theta = 0^o$, the first coefficient can be derived from the slope, $\frac{K^\theta c}{R(\theta)}$ and is given by [194]:

$$\alpha_1 = \left(\frac{4\pi n_o}{\lambda_o}\right)^2 \frac{\langle r_g^2 \rangle}{3} \tag{1.13}$$

where the mean square radius $\langle r_g^2 \rangle$ is measured as a light scattering average mean square radius as applied to a single particle. In each monodisperse particle size fraction (i) eluted from FFF, it is assumed that each particle (n_i) of molar mass (M_i) has the same $\langle r_g^2 \rangle$ and associated root mean square radius (r_g or r_{rms}). The $\langle r_g^2 \rangle$ is given by [194]:

$$\langle r_g^2 \rangle = \frac{\Sigma_i r_i^2 m_i}{\Sigma_i m_i} = \frac{1}{M} \int r^2 dm \tag{1.14}$$

where r_i represents the distance between the center of mass of the particle to the mass element (m_i). In the limit of $\theta \rightarrow 0$, $P(0^o)=1$ and concentration approaches zero [194]:

$$R_i(0^o) = K^* c_i M_i = K^* n_i M_i^2 \tag{1.15}$$

where $c_i = n_i M_i$. The number of particles per milliliter in each size fraction is proportional to [194]:

$$n_i \propto \frac{R(0^o)}{V_i^2} \tag{1.16}$$

where V_i is the volume of the particle. This proportionality holds if the particle of molar mass (M_i) is of uniform density and occupies a volume (V_i) [194].

The root mean square radius $\langle r_g \rangle$, for example, is calculated from the angular variation of scattered light intensity. By applying the RGD approximation, r_g is obtained by extrapolating the angular

dependence to zero degrees, but , it could also be defined by applying a parameter fit template (i.e. sphere, rod, etc.) if the shape of the particle is known [196]. Assuming the RGD approximation is valid, the differential number fraction ($\eta(r_g)dr_g$) of particles in a given peak region can be explicitly calculated by applying these templates, even if the mass concentration at each fraction is unknown. For example, for homogenous spheres, the spherical radius (a) is directly proportional to r_g by the following [194]:

$$a \equiv r_g\sqrt{\frac{5}{3}} \tag{1.17}$$

For small particles that fall within the valid range for the RGD approximation the error extrapolation for estimating the molar mass or $\langle r_g \rangle$ is relatively small and a first order linear fit can be applied. However, as the particle size increases, or the individual fractions become less resolved from each other, the first order fit incurs increasing error as the system nears the limits of the valid RGD range. The accuracy of the molar mass or r_g can be greatly improved by fitting a polynomial function and thereby minimizing error. With increasing order comes growing caution, as higher order polynomials can be applied to fit *any* data if not chosen wisely. Good quality data can be difficult to obtain if the sensitivity of lower angles results in saturated scattering detectors, thus a linear fit is preferred as it will minimize the effect of low angle errors [197]. The differential number fraction can then be obtained by sorting size fractions into bins. Corresponding cumulative distributions can be calculated from the differential number or mass fraction distributions.

In order to accommodate light scattering from non-ideal experimental conditions, there have been extensive investigations over several decades into the applicable range of the RGD approximation. Beginning with simple homogenous spheres in the 1960s, and expanding to include non-spehrical particles, fractal agglomerates, and biological particles. However, these reports have primarily focused on predicting integrative scattering, while largely ignoring the instrumentally practical angular scattering predictions [198]. There are three primary mathematical models that can be applied to extrapolate the relationship between light scattering intensity and scattering angle to compensate for non-ideal samples: the Debye, Zimm, and Berry methods [194, 197]. For small particles, extrapolation is simple due to the

linear association between the scattering angle and scattering intensity, however, the relationship becomes quite complex for larger molecules and the method of extrapolation must be carefully selected. While the angular dependence of scattered light can provide information about particle size as measured by MALS, QELS directly measures the translational diffusion coefficient through the time-dependent fluctuations in scattered light. Figure 1.5 shows a cartoon of these fluctuations in relation to particle size. These fluctuations are quantified using a second order correlation function [199]:

$$g^{(2)}(\tau) = \frac{\langle I(t)I(t+\tau)\rangle}{\langle I(t)\rangle^2} \tag{1.18}$$

where *I(t)* is the intensity of the scattered light at time *t*. The brackets indicate averaging over all *t*. The correlation function depends on the delay, *τ*, which represents the amount that a duplicate intensity trace is shifted from the original before averaging. The fluctuations are then directly related to the rate of diffusion of the molecule through the solvent, which, in turn, is related to the particles' hydrodynamic radii (R_h) using the Stokes-Einstein equation [199]:

$$r_h = \frac{kT}{6\pi\eta D} \tag{1.19}$$

where *k* is Boltzmann's constant, *T* is the temperature in K, and η is the solvent viscosity.

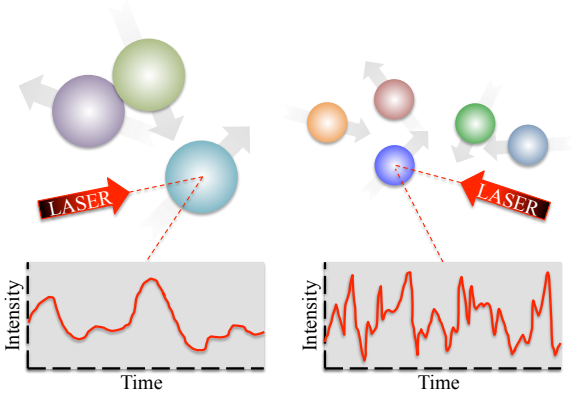

Figure 1.5 - The time-dependent fluctuations in scattered light, relative to particle size, as measured by QELS.

1.3.2 Statistical methodologies

1.3.2.a Experimental design

Statistical design of experiment (DEX) methodology requires rigorous problem solving to gain insight on an unknown response surface, the relationship between several explanatory variables and one or more response variables, of a given system containing a number of defined factors, *k*. With the correct design, the factorial dependencies of this system can be determined, subsequent conclusions can be validated, and the scientific experimental cost can be minimized [200, 201]. In particular, sensitivity analysis involves varying input parameter settings and assessing the subsequent changes in selected response variables in order to identify which input parameters yield the most significant influence on response behavior [202].

There are several commonly used experimental designs for sensitivity analysis, which aim to identify which experimental factors are most important (in this case, AF^4 instrumental factors), relative to the selected response output. The traditional approach is "one-factor-at-a-time" (1FAT), where all *k* factors are fixed and runs are made in which each factor is changed successively to another value. Though simple, logical, and inexpensive, the 1FAT design approach yields biased effect estimates and fails to correctly estimate potential factor interactions. In the case of a dynamic system, where the response surface might contain significant peaks or valleys, the bias can be particularly extreme as some of these topographical features may be missed without multiple factors being adjusted together [200, 203, 204]. A randomization Monte Carlo design randomly selects a combination of factors and settings from the complete population. Due to random sampling, the resulting conclusions will be unbiased; however, the necessary sample size must be very large to achieve a desired precision [200].

In order to increase accuracy and ensure both 1- and 2-dimensional design balance, orthogonal designs can be applied where every setting for each factor, and each pair of factors, appears an equal number of times across all observations [200, 202, 203]. Orthogonal designs require selected observations to be equally distributed across all possible parameter combinations, resulting in designs that are more accurate than the unbalanced designs often found in the literature [203]. Full factorial designs are intrinsically orthogonal and involve running every possible combination of factors and their levels, allowing for determination of the importance of all *k* factors without bias. While unbiased and

ensuring rigorous estimates about the relative importance of all *k* factors and potential interactions, full factorial designs are scientifically expensive. For a two-level design, the number of sample runs, *n*, is 2^k. For a three level design, $n = 3^k$, and quickly becomes prohibitive with increasing *k* values [200, 203, 204] In the case that a full factorial design is too expensive, a fractional factorial design can be applied. Therefore, a two-level orthogonal fractional factorial design was identified as a highly efficient and robust alternative. A detailed discussion of the two-level fractional factorial design used in this work is provided in Chapter 3.

As a hypothetical example, consider a *k*=3 factor experiment with two quantitative variables, particle size (*X1*) and concentration (*X2*), and a qualitative variable, the presence or absence of a ligand (*X3*) that absorbs to the particle surface and acts as a stabilizer to reduce particle dissolution. The response variable (*Y*) is the resulting number of stabilized particles. The 2-level experiment involves exploring two settings of each particle size (small and large), concentration (low and high), and ligand presence (none and ligand). The setting levels are denoted as "-" and "+", respectively. A full factorial design yields 2^3=8 sample runs, and an example is shown in **Table 1.4** and **Figure 1.6**.

Table 1.4 - Example of a 2^3 full factorial design. Effects data are artificially generated for demonstration purposes.

	X1: Size	*X2:* Concentration	*X3:* Stabilizer	*Y:* Number of Stabilized particles
1	-	-	-	20
2	+	-	-	40
3	-	+	-	10
4	+	+	-	30
5	-	-	+	50
6	+	-	+	80
7	-	+	+	60
8	+	+	+	70

The factor effect is defined by the change in response when the factor setting is switched from (−) to (+) while all other factors are fixed. The effects of increasing particle size from small (−) to large (+) yields 4 individual factors: Y_2-Y_1 = 40-20 = 20, Y_4-Y_3=20, Y_6-Y_5=30, and Y_8-Y_7=10. The *main effect* is

the average of all individual effects of a particular factor. The main effect of particle size is (20+20+30+10)/4 = 20. A *main effects plot* is a graphical tool (described in more detail in section 1.3.2.g) that shows the main effect for each factor setting, where the difference between the main effects for each of the two factor settings is graphically displayed.

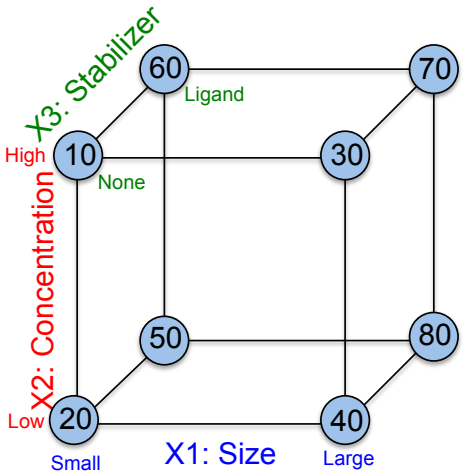

Figure 1.6 – Diagram showing relationship between the three factors: X1 (blue), X2 (red), and X3 (green); factor settings (small/large, low/high, and none/ligand, respectively), and the response factor effects (shown in blue bubbles).

The main effect of each factor can also be calculated as the difference between the average responses at each level. For particle size at the $(-)$ setting, the average response is (20+10+50+60)/4 = 35 and is (40+30+80+70)/4 = 55 at the $(+)$ setting. The difference in average response in factor levels for particle size is 20, which confirms the earlier calculation with the average of all individual factor effects. Therefore, since all observations are incorporated into the determination of all main effects, they are calculated with fourfold replicated precision [203]. A full linear model can be defined as:

$$Y = \beta_0 + \beta_1 X_1 + \beta_2 X_2 + \beta_3 X_3 + \beta_{12} X_1 X_2 + \beta_{13} X_1 X_3 + \beta_{23} X_2 X_3 + \beta_{123} X_1 X_2 X_3 + \epsilon \qquad (1.20)$$

where the β coefficients ($\beta_0,\ldots,\beta_{123}$) are effects that can be estimated with the full factorial design and then tested to determine if any are significantly different from 0, and ϵ is experimental error [205]. The

three *X* terms describes main effects, and β_0 is the response of *Y* when all main effects are equal to 0. There are also:

$$\frac{k(k-1)}{2} = \frac{3\times2}{2} = 3 \tag{1.21}$$

2-factor interaction terms and one 3-factor interaction term (often omitted) [205].

As an alternative, fractional factorial designs are a highly efficient subset of full factorial designs that maintain balance and orthogonality [200, 201, 203, 204, 206]. A two-level design is a simple and efficient way to obtain statistically unbiased estimates while maintaining a manageable number of *n* runs. 1FAT designs are by definition a fractional design, but lack orthogonality and result in biased estimates [200]. Though a subset of a full factorial design, a fractional factorial design often results in only a minimal decrease in statistical power due to the redundancy of factor effects and non-linear factor interactions becoming negligible when large numbers of fractions are used [203].

There are four major aspects of any experimental design [202]: 1.) Identify experimental factors (i.e. instrument parameters), 2.) Select factor levels and settings, 3.) Determine factor combinations, and 4.) Choose response variables. These four aspects are described in detail, below.

1.3.2.b Identify experimental factors

The maximum allowable number of experimental factors is all in a full factorial design. Fractional factorial designs can be used to reduce the number of factors if a full design is prohibitively expensive. Fixed control variables can be defined but are not factors to be investigated. Fixing parameters with less importance in order to investigate parameters with greater significance can further reduce the number of factors. Expertise and scientific knowledge can be applied in these cases, though care should be taken to avoid missing important system interactions while factors are fixed [202]. While 2-level designs are the most popular due to their simplicity and efficiency, it is often advantageous to include a center point level [205].

1.3.2.c Select factor levels and settings

Experimental levels should be determined so that the maximum number of combinations can be identified within cost and time restrictions. 2-level fractional factorial designs are simple, efficient, balanced, and orthogonal when used to reduce the number of factors from a costly full factorial design. Given two levels, the values for both levels at each factor must be defined, and are typically encoded as -1 and $+1$ or, just $(-)$ and $(+)$.

Field expertise and preliminary experimentation can be used to determine settings for the $(-)$ and $(+)$ levels of each factor. Settings should be realistic yet expected to yield differences in the response variable, since data analysis assumes that responses vary monotonically over all settings. In the event of non-monotonic responses, however, significant effects may be overlooked. Conclusions are only robust over the range of settings selected, so it is often recommended to perform additional sensitivity analyses using different setting levels to confirm.

1.3.2.d Determine factor combinations

When a full factorial design of $n=2^k$ is unfeasible due to the expense for a large number of factors, a fractional factorial design can be performed. The number of affordable runs can then be identified, and potential confounding effects should be considered. As an example, if 128 runs are determined to be affordable, then 2^7 combinations should be defined. Experiment design theory can be use to identify an applicable design, select appropriate combinations, and reveal confounding experiment structure [202, 207].

1.3.2.e Choose response variables

Selecting response variables that exaggerate particular model behaviors may lead to false conclusions. In particular, these errors become more prominent during careful exploration of the experimental space to understand response variables relative to changes in factor settings. A protocol, such as principal components analysis (PCA), a linear dimension reduction method, can be in place to determine which outputs correspond directly to each significant behavior [205].

1.3.2.f Exploratory data analysis

Experimental design conclusions will rely heavily on the chosen data analysis methodology, where exploratory data analysis (EDA) aims to maximize data set comprehension by revealing the basic structure of the data set. EDA therefore allows for the extraction of an appropriate model, outlier identification, conclusion robustness determination, parameter estimates and their associated uncertainties, a ranked list of influential factors and their statistical significance, and finally, the identification of optimal parameter and factor settings. Both quantitative and graphical data analysis techniques are available [207]. The classical Analysis of Variance (ANOVA) approach is commonly applied to sensitivity analyses. Quantitative methods tend to be far removed from the raw data and require many assumptions, resulting in conclusions that cannot be adequately tested for consistency [200]. The application of graphical analysis techniques provides insight into the data in a way that quantitative analogues cannot, by allowing for the analyst to utilize human comprehension and expertise across a series of well-chosen graphics [205].

1.3.2.g 10-Step graphical analysis

A 10-step, data-driven graphical analysis methodology has been developed at NIST, where each step generates a plot to expose information about model responses. Using multiple plots ensures various focus and interpretations; thereby yielding redundancies that increases conclusion confidence. Conflicting conclusions are also very helpful, revealing otherwise unseen relationships in the data [202, 205]. Descriptions of each of the 10-plots are given in the following sections, though not all are used in his work due to repetitious conclusions. The following discussions are a useful introduction to EDA and the types of plots, data, and conclusions that can be made. Examples are shown based on the full factorial design from **Table 1.4** and **Figure 1.6**, where the experimental goal was to maximize the response and number of stabilized particles.

Ordered data plot

The Ordered Data Plot uses the response data to identify the best average factor settings within predicted model values and the most important factor. The best settings can be recognized as the

settings corresponding to the best response value. Further, the most important factor is one in which changing the factor setting from $(-)$ to $(+)$ produces the greatest response. If a particular and consistent factor and level correspond to the best response and the near-best responses, then the factor can be deemed “most important”. Contrarily, if the same factor at the opposite level is associated with the worst and near-worst response, which is expected in a balanced design, then the factor is confirmed as “most important” [202, 205].

An example is given in **Figure 1.7**. The vertical axis contains the raw response value for each *n* experiments, ordered from smallest to largest. The horizontal axis is based on a coded index (1 to *n*) with defined *k* factor settings [205]. In this example, the best settings are $(+)(-)(+)$, corresponding to larger size, lower concentration, and the presence of stabilizer, respectively, since $Y = 80$ is the largest observed response. The most important factor is $X3$, since this corresponds to the largest response values when at the $(+)$ level, and to the smallest response when at the $(-)$ level.

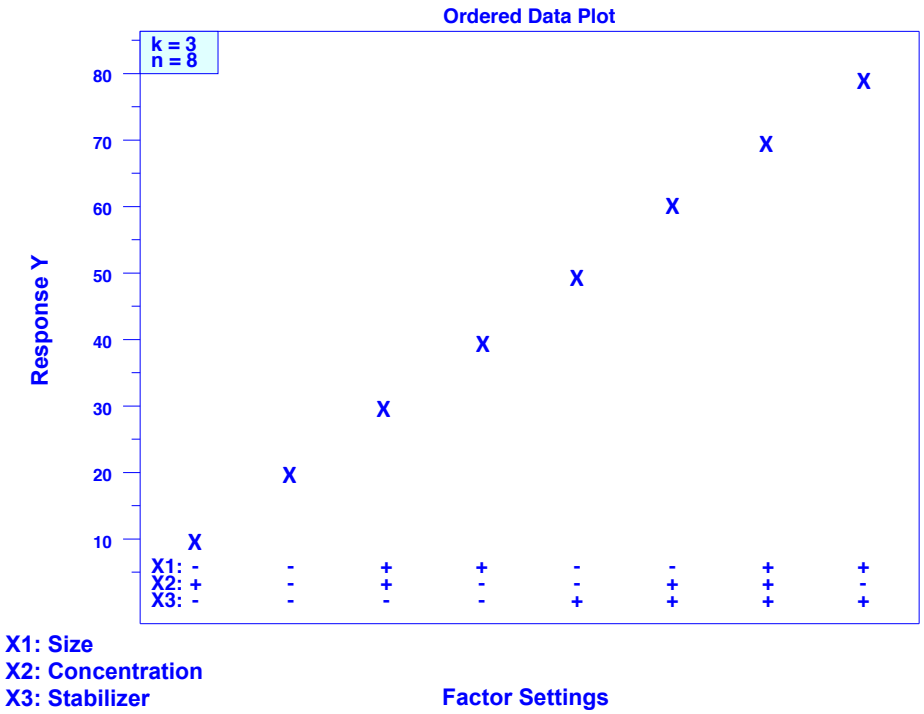

Figure 1.7. Ordered Data Plot.

Design of experiments (DOE) scatter plot

The DOE Scatter Plot aims to elucidate the important factors, the best settings for each of these factors, and finally, whether any data points can be classified as outliers. In this case, an important factor is one that results in a significant alteration for either the location or variation of the model response when the factor setting is changed from $(-)$ to $(+)$. The best factor setting is one that yields a response that is most accurate based on the experimental target, though this goal must be specified in the experimental design. Outliers are identified if the response falls into a different probability distribution than the rest of the data, which can be useful in determining which data points may potentially invalidate factor ranking conclusions by affecting other effects estimates. The DOE Scatter Plot is a simple way to isolate location changes, variation changes, and outliers, observations that can sometimes be missed in more advanced quantitative or graphical methodologies [202, 205].

An example is given in **Figure 1.8**. The vertical axis contains the raw data response for each of the *k* factors and setting ($-$ or $+$). The horizontal axis shows the k factors and settings. In this example, the most important factor is $X3$, since it yields the greatest difference in response when changing factor settings. The least important factor is $X2$, due to the location overlap between changing factor settings. The amount of overlap in the remaining factors often obscures the ranking beyond the extremes of “best’ and “worst”. The best settings are $(+)(-)(+)$, since they yield a response nearest the desired target. No outliers are seen in this analysis, though would be determined by identifying data that is far removed from the bulk data [205].

Main effects plot

The Main Effects Plot, or the DOE Mean Plot, is used to compile a ranked list of factors, and their best settings, in order of importance. The average is the simplest location estimator, and therefore a simple mean plot can be used to evaluate the importance of a single factor. The Main Effects Plot is a series of *k* plots, so each factor can be compared for relative importance. The best settings are chosen based on the averages, and the *k*-vector for the best settings should conform those identified with the DOE Scatter Plot [202, 205].

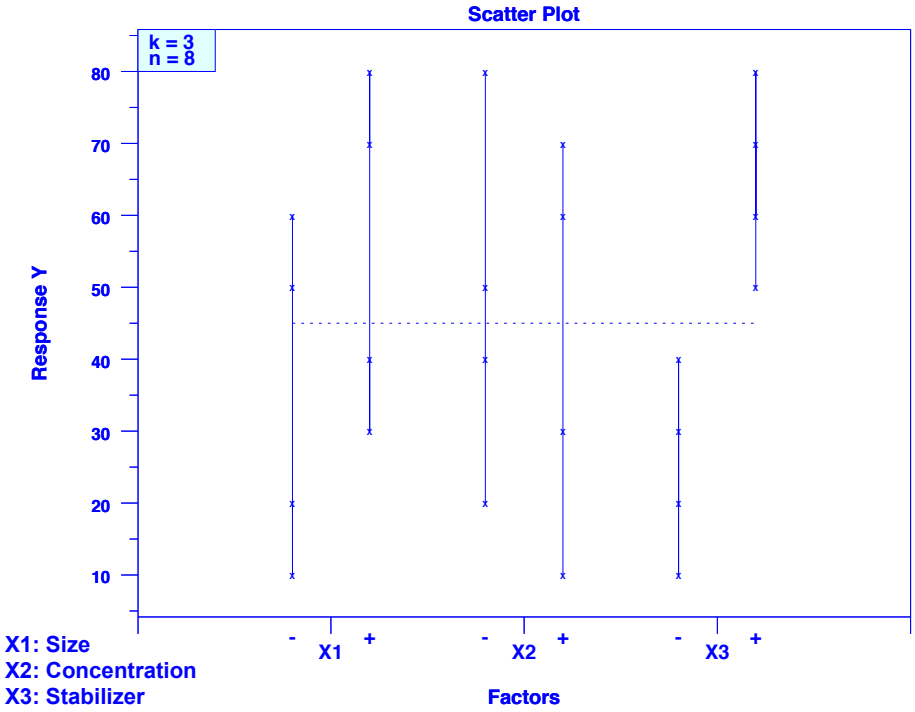

Figure 1.8. DOE Scatter Plot.

An example is given in **Figure 1.9.** The vertical axis represents the mean response for each *k* factor settings ($-$ and $+$). The horizontal axis lists the *k* factors and settings. The factor with the steepest line is categorized as the "most important", and the slope of the line indicates whether the effect is positive or negative when changing the factor settings from $(-)$ to $(+)$. Any significant effects (X3) are highlighted in red and correspond to one-way ANOVA f-test values of > 95.00%. The best average settings are defined by identifying which individual factor settings result in an average response nearest the desired target [205]. The qualitatively ranked list of important factors includes $X3, X1, \text{and } X2$. The best average settings are $(+)(-)(+)$. These conclusions are in good agreement with those made using the DOE Scatter Plot and the Ordered Data Plot.

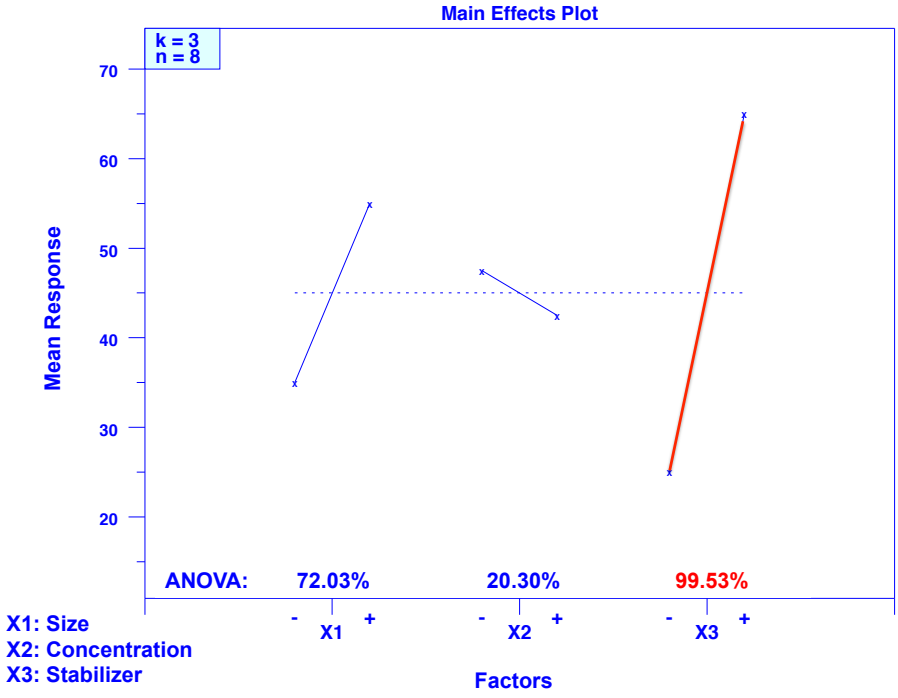

Figure 1.9. Main Effects Plot.

Interaction effects matrix

The interaction effects matrix plot includes the main effects and 2-factor interactions to explore a ranked list of important factors and the best settings for each of the *k* factors. While similar to the Main Effects Plot in this regard, the interaction effects matrix plot also takes the 2-factor interactions into account. As the number of k factors increases, the potential interactions also increase exponentially, where the total number of possible interactions $= 2^k - 1 - k$.

In this example, where $k = 4$, the number of potential interactions is 11. Since 2-factor interactions are the most important, while 3- and greater-factor interactions are often negligible, the number of potential 2-factor interactions can be given by:

$$\binom{k}{2} = \frac{k!}{2!(k-2)!} = \frac{k(k-1)}{2} \tag{1.22}$$

Again, using $k = 4$, the number of 2-factor interactions is 6. However, not all possible interactions are available to be incorporated into experimental conclusions, and the actual number of 2-factor interactions may be fewer, especially for fractional factorial designs.

In the case of fractional factorial designs, which typically contain confounding variables, the question arises as to whether a resulting effect is due to the main effect or a confounding interaction. It is prudent to consider these confounding effects when designing a fractional experiment, and chose a design that minimizes the main effect confounding. Poor designs containing 2-factor interactions result in ambiguous effects conclusions and factor rankings, while better designs with higher order interactions reduce main effect estimate biases [202, 205]. An example is given in **Figure 1.10**. The diagonal shows the mean plots for *k* main effects, and the 2-factor interactions are displayed in the off diagonal plots. The vertical axes display the mean response for each factor setting or 2-factor interaction. The horizontal axis holds the settings within each factor or interaction. The legend in each box includes the least-squares-estimate for each factor or interaction, which scales with the importance of that effect. The line slope is also an indication of effect importance, where larger slopes indicate greater importance [205]. The ranked factor list, from most to least important, is: $X3, X1, X2X3, (X2 \text{ and } X1X2), \text{and } X1X3$.

Block plot

The block plot is a multifactor analysis technique used to identify the relative importance of factors and 2-factor interactions, as well as the best settings for each important factor. The block plot is particularly useful in determining whether the factor importance is robust across all *k* factor settings, and therefore is also known as a DOE robustness plot. The ability to scan and compare factor effect blocks quickly is a strong advantage when using block plots, and the block height consistency can provide information about the factor robustness [202, 205]. An example is given in **Figure 1.11**. The vertical axis is the response, and the horizontal axis shows all 2^{k-1} combinations of robustness factors, or non-target factors. Each point in a block is associated with target factor settings. Internal block differences represent the relative importance of each factor, where larger blocks indicate greater effects. Important factors will also show consistent factor level settings ($-$ or $+$) [205]. Based on the $k = 4$ example, factors

and interactions $X3$ and $X1$ are important, and the best settings are $(+)(-)(+)$, which is in good agreement with previous plots.

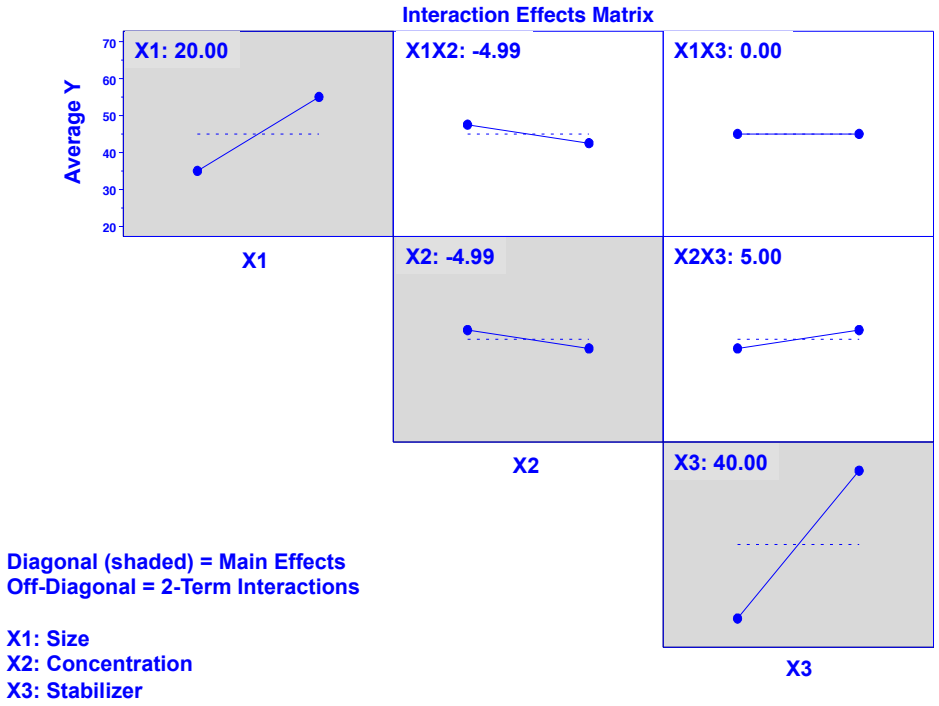

Figure 1.10. Interaction Effects Matrix.

Youden plot

The Youden Plot is a way to identify important factors and interactions, and is particularly appropriate for round-robin analysis when two variables are used. The plot generates a ranked list of factors and interactions, as well as sorts effects into "important" and "unimportant" categories. The Youden Plot is essentially a scatter plot of $(+)$ factors vs $(-)$ factors, where unimportant factors will cluster in the center while important factors will be farther away from the center. For each factor,

$$average\ (+) = \ c - average\ (-) \tag{1.23}$$

where *c* is a constant representing the grand mean. The ranked list of factor importance can be compared to the conclusions made with the previous plots, with more robust conclusions having greater consistency [202, 205]. An example is given in **Figure 1.12**.

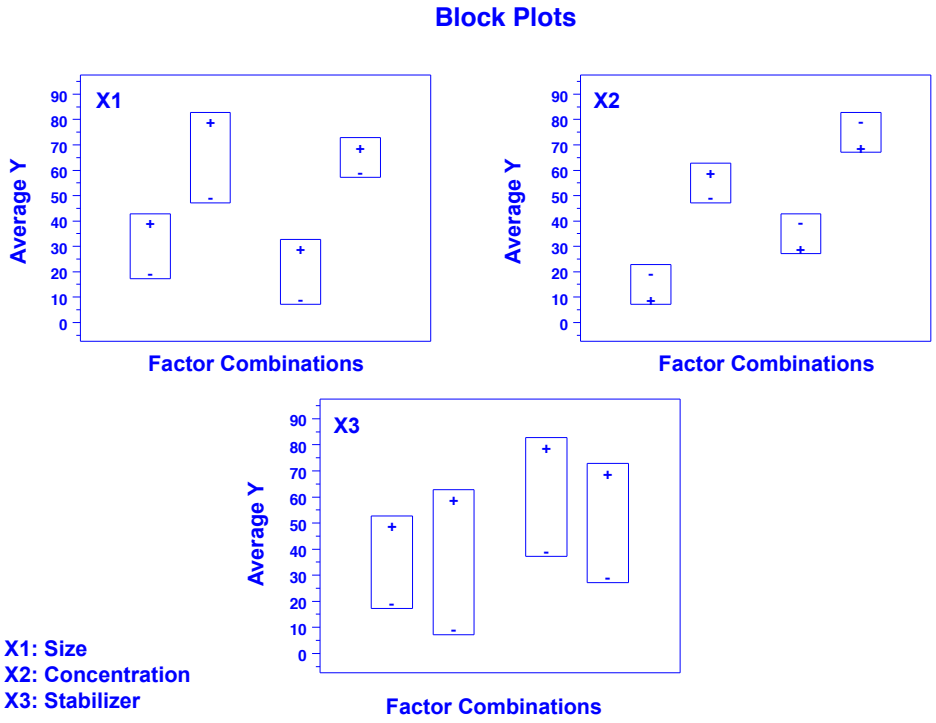

Figure 1.11. Block Plot.

The vertical axis represents the mean response at the $(+)$ factor setting. The horizontal axis shows the mean response at the $(-)$ factor setting. The $n/2$ response values are used to calculate each mean, (+) and (-). The factor farthest from the center point is defined as the "most important", and the "least important" factor is near the center point, the grand mean of all $n-1$ observations [205]. Continuing the $k=4$ example, the ranked list of factors and interactions includes *X3, X1, X2X3, (X2* and *X1X2),* and *X1X3.* The important factors are $X3$ and $X1$, which is in good agreement with previous conclusions.

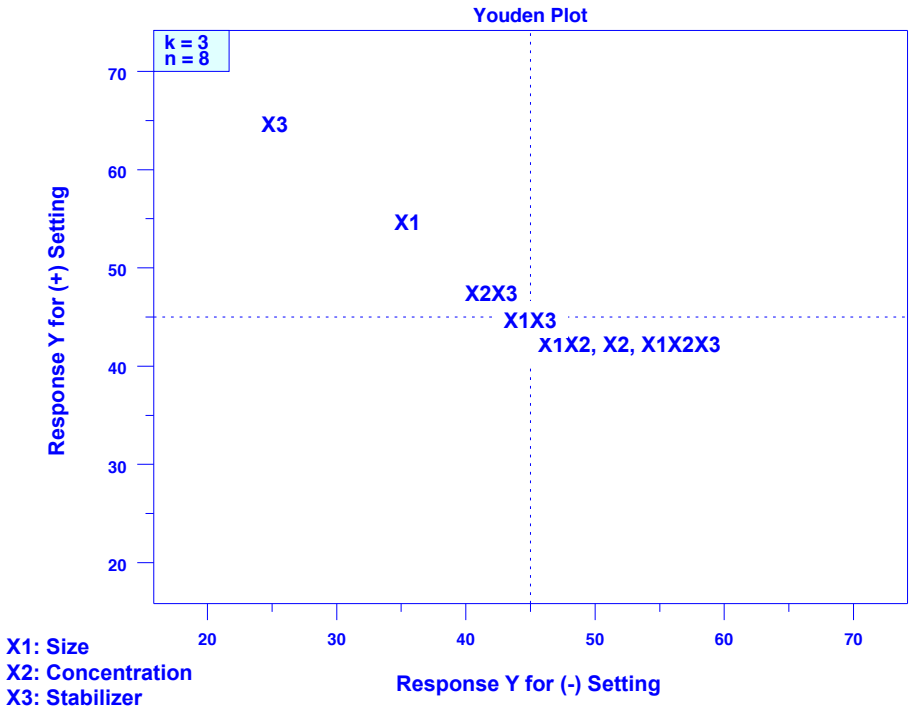

Figure 1.12. Youden Plot.

Absolute effects plot

The absolute effects plot, or |Effects| plot, graphically displays the ranked least squares estimated effect magnitude of each factor or interaction and their relative importance. For fractional factorial designs, additional information about confounding variables can be observed. For both full factorial and fractional factorial designs, the least squares estimate for each factor, 2-factor interaction, and multi-factor interaction effects is described as:

$$Effects = \bar{Y}(+) - \bar{Y}(-) \tag{1.24}$$

where $\bar{Y}(\pm)$ represents the average of all responses for each factor or interaction at either the $(+)$ or $(-)$ level setting. The graphical ranking or the factor and interaction effect magnitudes is given in the plot, and quantitatively provided in the upper right table, which also lists any confounding structure in the case of fractional factorial designs. The absolute value of the difference between the $(+)$ and $(-)$ averages indicates the importance of each factor or interaction, which larger differences being more important.

There are several ways to identify a bifurcation line to categorize effects as “important” or “unimportant”, including by statistical, engineering, numerical, or pattern significance [202, 205]. An example is given in **Figure 1.13**. The vertical axis lists the ordered absolute value of the estimated effects for each factor and interactions. The horizontal axis is the factor or interaction identification, with the ranked effects given in order of magnitude. The confounding structure for fractional factorial designs is provided, and the upper right table lists the ranked least squares effect estimates [205]. The ranked list of factors and interactions is *X3, X1, X2X3, (X2* and *X1X2), X1X2X3,* and *X1X3*. While this is a similar conclusion to those made with the other plots, the Absolute Effects Plot also includes a 3-factor interaction, $X1X2X3$.

Half-normal probability plot of absolute effects

The half-normal probability plot identifies the most important factors and interactions, based on the least squares estimate. The factors and interactions also categorized as either “important”, with effects in a normal distribution far removed from zero, or “unimportant”, where the normal distribution of effects is near zero. The arbitrary nature of assigning factor setting levels to $(+)$ and $(-)$ can be compensated for by using the magnitude of each effect, rather than the coded effect sign. Therefore, the absolute value of the effect magnitudes in a half-normal probability plot can be used to identify relative importance. Effects that lie near zero along a linear trend are classified as “unimportant”, while larger effects are “important” [202, 205]. An example is described in **Figure 1.13**. The vertical axis includes the ranked absolute value of each estimated effect for factors and interactions. The horizontal axis contains $n-1$ theoretical order statistic medians from the half-normal distribution. These median values are not data-dependent, but instead are based on the half-normal distribution and the $n-1$ number of observations where the median values are theoretical based on a typical ordered data set. The right margin indicates the factor and interaction identification. In the case of a fractional factorial design, the confounding structure is given [205]. The ranked list of important factors and interactions is: $X3, X1, X2X3, (X2 \text{ and } X1X2), \text{and } X1X3$. $X3 \text{ and } X1$ are important and $X1X3, X2, \text{and } X1X2$ are unimportant.

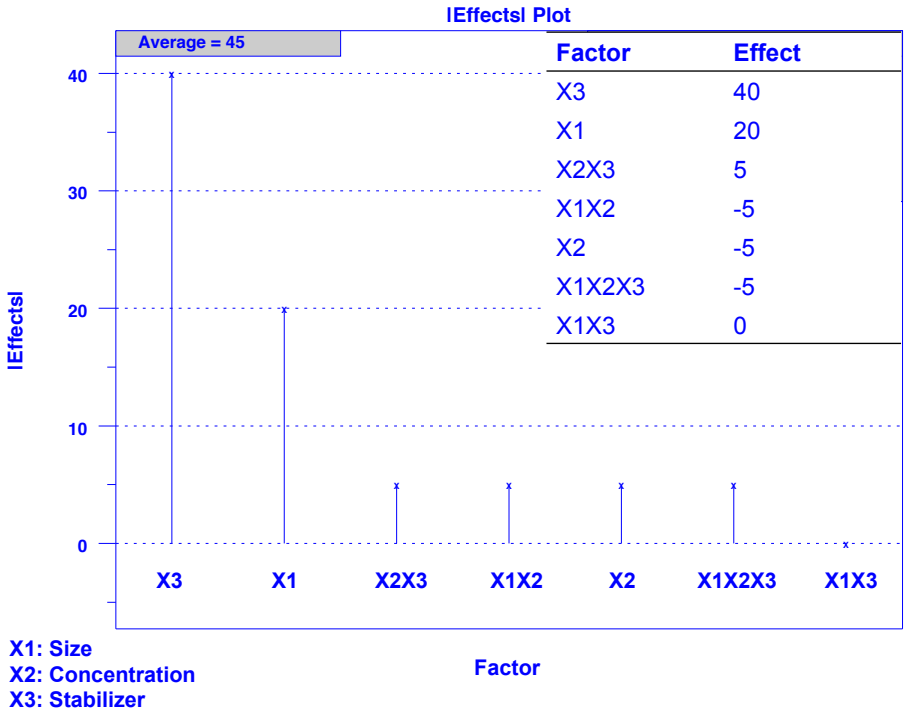

Figure 1.13. Absolute Effects Plot.

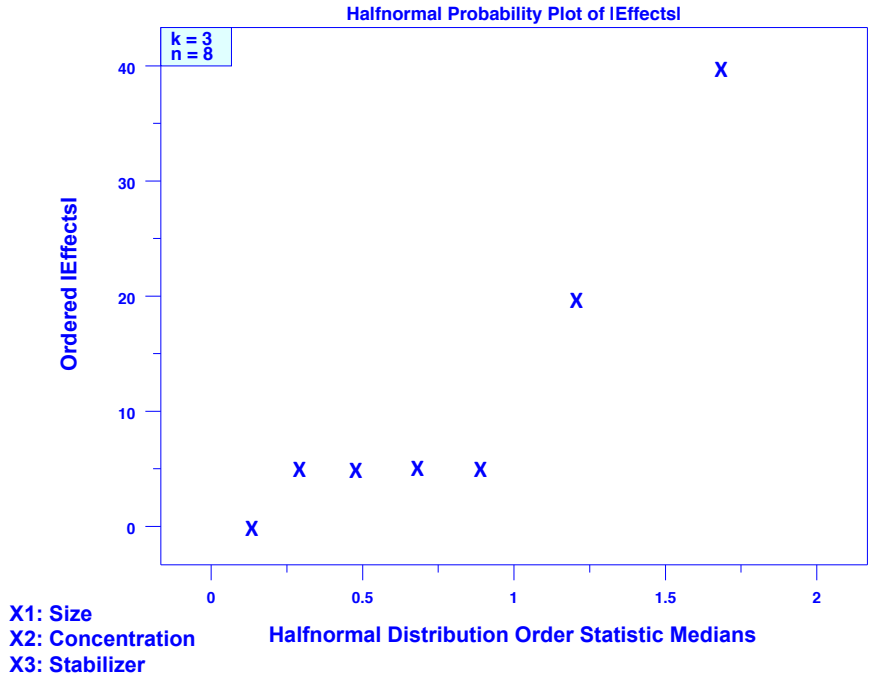

Figure 1.14. Half-Normal Probability Plot of Absolute Effects.

Cumulative residual standard deviation (SD) plot

The cumulative residual SD plot is used to determine an appropriate model for the data set. While the previous plots are used to rigorously identify the most important factor and interaction effects, as well as the best factor settings. A suitable model is one that can be used to predict the relationship between the response variable (*Y*) with the main effects and interactions. This is particularly useful for factors that are continuous and in-series, rather than discrete. The model equation can then be utilized to predict response values at observed points, at unobserved points within the design, and at unobserved points outside the design. The objectives are to determine a good function and subsequent estimates for coefficients within the function so that the resulting model values $(\hat{Y})$ are as accurate as possible in estimating the true *Y* and the residuals $(Y - \hat{Y})$ will be near zero. The residual SD SD_{res} describes the quality of the model fit,

$$SD_{res} = \sqrt{\frac{\sum_{i=1}^{n} r_i^2}{n-p}} \tag{1.25}$$

where *r* represents the *i*th residual and *p* designates the number of terms, including the constant. When models with a constant are fit using least squares, the assumption is that the mean residual is zero. For a good model fit, SD_{res} is small, but is large if the fit is poor. For a series of proposed models, the Cumulative Residual SD plot is a compilation of each individual SD_{res} for each model and identifies good models from poor, as well as classifying good models as "simple" or "complicated [202, 205]. The construction of these models is beyond the scope of this project, but has been described elsewhere [205].

An example of this plot is shown in **Figure 1.15**. The vertical axis contains the ranked SD_{res} from a sequence of fitted models with increasing complexity. The horizontal axis lists the factor and interaction identification. Each factor or interaction is assimilated into the model in an additive way. The cumulative SD_{res} fit will decrease as more terms are added to the model, with diminishing returns character following the noticeable change in slope at the "elbow point". The SD_{res} for the baseline model is ~ 25. With the addition of each successfive term, SD_{res} decreases to approximately $12.5, 6.5, 6, 5.5, 5, \text{and finally}, 0$. The "elbow point" appears at the $X1$ term, and therefore the fitted model is

$$\hat{Y} = \bar{Y} + B_3 X_3 + B_1 X_1 \tag{1.26}$$

and the least squares coefficient estimates, based on the estimated effects from the absolute effects plot, are:

$$\bar{Y} = (45), B_3 = (20), B_1 = (10) \tag{1.27}$$

The resulting model can subsequently be applied to predicting the values of $\hat{Y}$ and calculating the residuals $(Y - \hat{Y})$. The SD_{res} can then be calculated, and in this case found to be $SD_{res} = 6$ when $n = 8$ and $p = 3$ estimated coefficients. This value is in good agreement with that found on the plot above the "elbow point" at $X2X3$ [205].

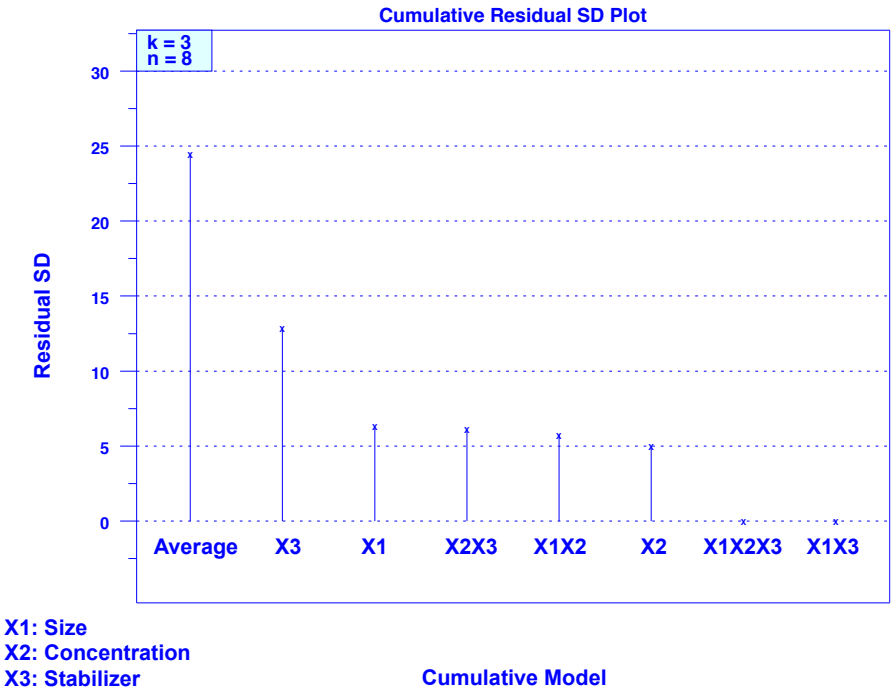

Figure 1.15. Cumulative Residual SD Plot.

Contour plot

The contour plot seeks to explore whether the response could be better optimized from the experimental input. Based on the previous EDA steps, the best settings have been identified relative to the *n* data points within the experiment. The contour plot aims to identify which settings would optimize the response. The two most important factors are selected to be contour Plot axes, while the remaining factors are fixed at their best settings based on conclusions made in the previous EDA steps, specifically, the ordered data plot, the main effects plot, and the interaction effects matrix plot. For *k* experimental factors,

$$number\ of\ potential\ contour\ plots = \binom{k}{2}\frac{k!}{2!(k-2)!} = \frac{k(k-1)}{2} \tag{1.28}$$

in the continuing example of $k = 4$, the possible contour plots include $X_1\ and\ X_2$, $X_1\ and\ X_3$, $X_1\ and\ X_4$, $X_2\ and\ X_3$, $X_2\ and\ X_4$, and $X_3\ and\ X_4$. Typically only one contour plot is generated based on the two most important main effects factors. Only the main effects are used as they can be directly related to instrument/experiment settings, whereas interactions cannot be controlled. The contour curves produce a visual projection of the response surface, or plot of responses based on multiple variables, and are based on the fitted model from the Cumulative Residual SD plot. The graphical response surface also allows for the determination of the best theoretical response value [202, 205]. An example is given in **Figure 1.16**, though there is no direction of steepest descent identified. The vertical axis is the second most important factor while the horizontal axis contains the most important factor. The four corners represent the combinations of the two most important factors, each with an average response value. The optimal theoretical settings can be found from the interaction of the steepest ascent or decent of the response surface (depending on target) direction with the optimal curve [205]. In our example, the steepest ascent would lead to the optimal theoretical settings, since the target response is a maximization of the number of stabilized particles.

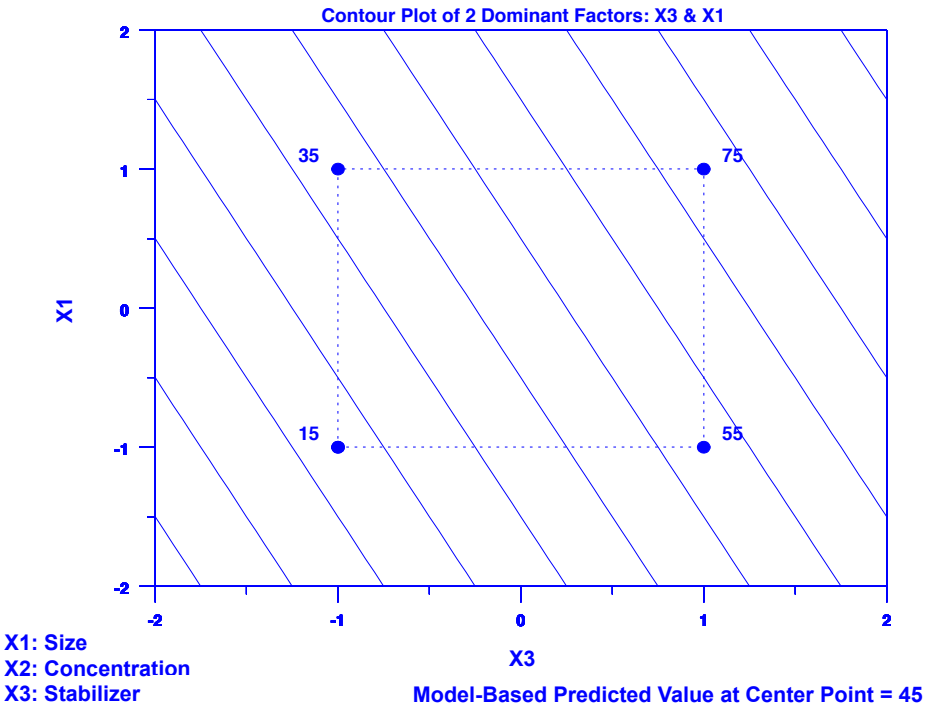

Figure 1.16. Contour Plot.

1.3.3 Applications to Natural Waters

Once the important instrumental factors have been identified, the method can be applied to quantitation and characterization of AgNPs in natural waters. The biggest challenge is accounting and compensating for the matrix complexity and low target analyte concentrations. NOM is a particularly complex environmental mixture, containing supramolecular assemblies of a wide range of molecular weights and chemical properties [135, 208-211]. NOM is generally categorized as either particulate or dissolved organic matter, where the dissolved fraction will pass through a 0.45 μm filter [212]. NOM experiences changes in structure, molar mass, and aggregation with varying aquatic chemistry and water quality characteristics [208], and smaller components can form aggregated clusters by hydrogen bonds, hydrophobic interactions, cation bridges, and dipole-dipole interactions [208, 210, 213-215]. AF^4-ICP-MS is well suited for this task, providing high Ag sensitivity, even in complex matrixes containing NOM. In fact, signal enhancement of many elements in ICP-MS is often caused by the presence of carbon-containing compounds [216]. Further, applying a standard addition quantitative analysis to compensate for matrix effects, dilution, and analyte loss during separation by adding AgNP concentration standards

directly to the analyzed sample. A more detailed discussion of AgNP-NOM and Ag-NOM interactions, AgNP quantification with AF^4-ICP-MS in the literature, including limitations of current methods, and the standard addition quantitative approach is discussed in depth in Chapter 4.

While heterogeneous NOM is ill defined and contains a large number of diverse chemical functionalities, there is no single analytical method capable of elucidating definitive structural or complete functional information about it. Fluorescence spectroscopy, however, is able to reveal important information about the chemical nature of NOM, since fluorescence is a function of NOM structure and functional groups [217]. Fluorescence intensity is strongly dependent on NOM molecular structure and decreases with increasing molar mass [218-220]. In an exploration of AgNP and humic acids, Philippe and Schaumann [211] determined that fluorescence peak areas of the humic substance did not vary in the presence or absence of nanoparticles. They suggested that the amount of humic acid absorbed on the particles was negligible compared to the dissolved amount.

Preliminary fluorescence measurements of collected AF^4 cross flow lake water fractions (i.e. fractions collected from material passing through AF^4 membrane) revealed there was no measureable fluorescence signal at the highest integration time allowed. This is primarily due to the AF^4 dilution factor (~100x) and the very low fluorescence found in the lake water raw sample. As a result, Suwannee River NOM (SR NOM) in laboratory-prepared freshwater was used. We acknowledge that SR NOM is not a representative surrogate for understanding all potential NOM-AgNP interactions in natural waters. However, fluorescence measurements are still able to reveal important information about SR NOM since fluorescence intensity is strongly dependent on NOM molecular structure and decreases with increasing molar mass.

1.4 Study outline

The undertaking of this research is relevant to understanding the science, fundamental chemistry, fate and transport of ENPs in the aquatic environment. Existing studies often lack robust experimental design and environmentally relevant conditions, two major targets of the described work. The combined use of chemical separations with physicochemical characterization and quantitation techniques is the

basis of this thesis with the goal of establishing an approach for new risk assessment tools of NPs in aquatic environments. The primary knowledge gap that this project will address is the lack of quantitative methods for detection of ENPs in natural waters. Currently the tools for simultaneously characterizing and quantifying ENPs in natural waters have limited effectiveness. Therefore, the project outputs will include the development of a practical, effective, and rigorously explored method for application in occurrence surveys including quantitation and detection of AgNPs in natural water. Although this project sets out to develop an analytical strategy for measuring environmental levels of AgNPs, this will provide the foundation for future applications that will generate occurrence data needed by regulators, utilities, and consulting engineers to demonstrate the effectiveness of current water treatment technology towards complete removal of AgNPs from water and confirm the ability of conventional treatment or make adjustments to processes to protect consumers from adverse health effects related to unplanned exposure to these pollutants. A perspective on the levels and types of ENPs present in aquatic systems will help designers engineer treatments to improve removal if occurrence levels suggest an unacceptable risk of exposure and provide for the dissemination of such information to the public.

The assumptions made in traditional approaches to characterizing ENPs in natural waters are fundamentally flawed: the ability to accurately determine the difference between targeted ENPs and naturally occurring NPs or the individual ENP components that almost certainly exist in actual environmental samples that contain the ENP has not yet been established [124]. Not only will this work demonstrate the versatility of AF^4, but it will also put the analytical technology at the forefront of environmental assessments and in particular for obtaining new knowledge relating to the potential human exposure to AgNPs and possible mechanisms to reduce exposure risk.

It is essential that interfaces between separation and detection or characterization techniques continue to be developed and utilized for the study of ENPs in the environment so as to minimize sample handling and its impact on NP physical state, and to provide comprehensive characterization on the same sample. This research investigated the use of AF^4 integrated with ICP-MS to separate and quantify AgNPs in natural lake and synthetic waters using a standard addition analysis. The addition of online UV and MALS detectors was used to monitor NOM separation. Offline fluorescence spectroscopy was utilized to better understand potential AgNP-NOM and Ag-NOM interactions using SR NOM and

laboratory-prepared freshwaters. Furthermore, a rigorous sensitivity analysis was used to identify which AF^4 primary/instrument variables had the most influence on NOM separation in laboratory freshwater samples containing SR NOM and AgNP. Overall, this project will define and optimize an exhaustive on-line analytical process for characterizing and quantifying AgNPs in aquatic samples.

This project considered three primary research questions:

***1.4.1 Research Question #1*:** How can AF^4 separations of AgNPs in aquatic matrices be assessed to determine separation quality so that subsequent characterization methods will be as accurate as possible?

1.4.1.a Objectives

- Develop a separation metric for determining relative AF^4 separation protocol success.
- Demonstrate separation metric using a polystyrene bead mixture as a model system for polydisperse samples such as AgNPs in natural waters.

1.4.1.b Approach

The analysis of natural and otherwise complex samples is challenging and yields uncertainty about the accuracy and precision of measurements. A practical tool assessed relative accuracy among AF^4 separation protocols for techniques using light scattering detection. Due to the highly non-linear relationship between particle size and the intensity of scattered light, a few large particles may obfuscate greater numbers of small particles. Therefore, insufficiently separated mixtures may result in an overestimate of the average measured particle size. Complete separation of complex samples is needed to mitigate this challenge. One separation protocol can be considered improved if the average measured particle size is smaller than the previous separation protocol. Further, the protocol resulting in the smallest average measured particle size yields the best separation among those explored. If the differential in average measured size between protocols is less than the measurement uncertainty, then the selected protocols are of equivalent precision. As a demonstration, this assessment metric is applied

to optimization of cross flow protocols in asymmetric flow field flow fractionation (AF^4) separation interfaced with online quasi-elastic light scattering (QELS) detection using mixtures of polystyrene beads spanning a large size range. Using this assessment metric, the cross flow factor was modulated to improve separation until the average measured size of the mixture was in statistical agreement with the calculated average size of particles in the mixture. While this metric was demonstrated by improving AF^4 cross flow factor settings, it can be applied to any given separation parameters for separation techniques that employ dynamic light scattering detectors. Additional discussion, methods, and results are provided in Chapter 2.

1.4.2 Research Question #2: Which AF^4 instrument variables are most important in influencing AF^4 separation of laboratory-prepared freshwater samples containing AgNP?

1.4.2.a Objectives

- Evaluate and rank the various separation protocols on their ability to minimize the average measured molar mass of NOM – in each sample to ultimately establish the optimization recommendations.
- Develop and perform a sensitivity analysis using AF^4-MALS-UV to identify AF^4 instrument factors with the highest impact on separation of AgNPs in laboratory-prepared freshwater samples containing SR NOM.

1.4.2.b Approach

AF^4 has several instrumental parameters that may have a direct effect on separation performance. A sensitivity analysis was applied to ascertain the relative importance of AF^4 primary instrument factor settings for the separation of AgNPs in laboratory-prepared synthetic water. The analysis evaluated the impact of instrumental factors namely, cross flow, ramp time, focus flow, injection volume, and run buffer concentration on the multi-angle light scattering measurement of NOM molar mass. A $2^{(5-1)}$ orthogonal fractional factorial design was used to minimize analysis time while preserving

the accuracy and robustness of the main effects and 2-way interactions. By assuming that separations resulting in the ability to measure smaller molar mass (MM) measurements would be more accurate, the analysis produced a ranked list of effects estimates for factors and interactions based on their relative importance in minimizing the MM when changed from low to high settings. Additional discussion, methods, and results are provided in Chapter 3.

***1.4.3 Research Question #3*:** Are AF^4-ICP-MS and AF^4 methods with offline fluorescence analysis appropriate tools to adequately separate, characterize, and quantify AgNPs in natural lake water samples

1.4.3.a Objectives

- Interface AF^4 -ICP-MS systems for online analysis
- Quantify AgNPs in natural lake water using AF^4-ICP-MS by applying a standard addition analysis.
- Explore potential AgNP-NOM and Ag^+-NOM interactions within the AF^4 separation channel using offline fluorescence spectroscopy.

1.4.3.b Approach

With the likely release of engineered nanoparticles into the aquatic environment, developing appropriate analytical methods for occurrence surveys has become a priority. To this end, the quantification of AgNP in lake water samples using AF^4 -ICP-MS is reported. The contribution of various AF^4 system components such asthe AF^4 membrane and focusing step and the presence of NOM are explored to determine how these affect the quantitation of Ag by ICP-MS. A standard addition method, described in Chapter 4, was applied by adding standard AgNPs for ICP-MS concentration calibration directly to the lake water samples prior to AF^4-ICP-MS analysis. Standard addition was used to compensate for natural matrix and system complexity, and ^{109}Ag isotope-enriched Ag ions (Ag^+) are used to identify Ag speciation in the ICP-MS fractogram following AF^4 separation. Further investigations into the amount of NOM retained within the AF^4 separation channel as a factor of potential Ag^+-NOM and AgNP-NOM interactions were performed using fluorescence spectroscopy, by measuring the fluorescent fraction of SR NOM in

laboratory–prepared freshwater samples containing either AgNP or Ag^{+}. Offline fractions were collected from the AF^{4} cross flow waste, or the sample fraction that passes through the AF^{4} membrane, for offline analysis to explore changes in intensity occurring with the addition of AgNP or Ag^{+}. Additional discussion, methods, and results are provided in Chapter 4.

REFERENCES

1. Adamson, A.W. and Gast, A.P. *Physical Chemistry of Surfaces.* John Wiley & Sons Inc.: New York, NY, 1997.

2. Walker, N. Current knowledge on nanomaterial toxicity: Implications for assessing product safety at the end of the life-cycle. 2009, Environmental Health Collaborative, Research Triangle Park, NC.

3. Wagner, S.; Gondikas, A.; Neubauer, E.; Hofmann, T.; von der Kammer, F. Spot the difference: engineered and natural nanoparticles in the environment-release, behavior, and fate. *Angew. Chem. -Int. Edit.* **2014,** *53,* 12398-12419.

4. Brar, S.K.S. Engineered nanoparticles in wastewater and wastewater sludge – Evidence and impacts. *Waste management (Elmsford)* **2010,** *30,* 504-520.

5. Woodrow Wilson International Center for Scholars Project on Emerging Nanotechnology. **2010,** http://www.nanotechproject.org/

6. Keller, A.A. and Lazareva, A. Predicted releases of engineered nanomaterials: From global to regional to local. *Environ. Sci. Technol. Lett.* **2014,** *1,* 65-70.

7. Roco, M.C. The long view of nanotechnology development: the National Nanotechnology Initiative at 10 years. *J. Nanopart. Res.* **2011,** *13,* 427-445.

8. Lin, D.; Tian, X.; Wu, F.; Xing, B. Fate and transport of engineered nanomaterials in the environment. *J. Environ. Qual.* **2010,** *39,* 1896-1908.

9. Ferreira da Silva, B.; Perez, S.; Gardinalli, P.; Singhal, R.K.; Mozeto, A.A.; Barcelo, D. Analytical chemistry of metallic nanoparticles in natural environments. *TrAC-Trends Anal. Chem.* **2011,** *30,* 528-540.

10. Maynard, A.D. Nanotechnology: managing the risks. *Nano Today* **2006,** *1,* 22-23.

11. Morones, J.; Elechiguerra, J.; Camacho, A.; Holt, K.; Kouri, J.; Ramirez, J.; Yacaman, M. The bactericidal effect of silver nanoparticles. *Nanotechnology* **2005,** *16,* 2346-2353.

12. Gottschalk, F. and Nowack, B. The release of engineered nanomaterials to the environment. *J. Environ. Monit.* **2011,** *13,* 1145-1155.

13. Weinberg, H.; Galyean, A.; Leopold, M. Evaluating engineered nanoparticles in natural waters. *TrAC-Trends Anal. Chem.* **2011,** *30,* 72-83.

14. Auffan, M.; Bottero, J.; Chaneac, C.; Rose, J. Inorganic manufactured nanoparticles: how their physicochemical properties influence their biological effects in aqueous environments. *Nanomedicine* **2010,** *5,* 999-1007.

15. Aschberger, K.; Micheletti, C.; Sokull-Kluettgen, B.; Christensen, F.M. Analysis of currently available data for characterising the risk of engineered nanomaterials to the environment and human health - Lessons learned from four case studies. *Environ. Int.* **2011,** *37,* 1143-1156.

16. Kahru, A. and Dubourguier, H. From ecotoxicology to nanoecotoxicology. *Toxicology* **2010,** *269,* 105-119.

17. Handy, R.D.; Owen, R.; Valsami-Jones, E. The ecotoxicology of nanoparticles and nanomaterials: current status, knowledge gaps, challenges, and future needs. *Ecotoxicology* **2008,** *17,* 315-447.

18. Handy, R.D.; von der Kammer, F.; Lead, J.R.; Hassellov, M.; Owen, R.; Crane, M. The ecotoxicology and chemistry of manufactured nanoparticles. *Ecotoxicology* **2008,** *17,* 287-314.

19. Handy, R.D.; Cornelis, G.; Fernandes, T.; Tsyusko, O.; Decho, A.; Sabo-Attwood, T.; Metcalfe, C.; Steevens, J.A.; Klaine, S.J.; Koelmans, A.A.; Horne, N. Ecotoxicity test methods for engineered nanomaterials: Practical experiences and recommendations from the bench. *Environ. Tox. Chem.* **2012,** *31,* 15-31.

20. Klaine, S.J.; Alvarez, P.J.J.; Batley, G.E.; Fernandes, T.F.; Handy, R.D.; Lyon, D.Y.; Mahendra, S.; McLaughlin, M.J.; Lead, J.R. Nanomaterials in the environment: Behavior, fate, bioavailability, and effects. *Environ. Toxicol. Chem.* **2008,** *27,* 1825-1851.

21. Kwak, J.I. and An, Y. Ecotoxicological effects of nanomaterials on earthworms: A review. *Hum. Ecol. Risk Assess.* **2015,** *21,* 1566-1575.

22. Taylor, U.; Tiedemann, D.; Rehbock, C.; Kues, W.A.; Barcikowski, S.; Rath, D. Influence of gold, silver and gold-silver alloy nanoparticles on germ cell function and embryo development. *Beilstein J. Nanotechnol.* **2015,** *6,* 651-664.

23. Roy, R.; Das, M.; Dwivedi, P.D. Toxicological mode of action of ZnO nanoparticles: Impact on immune cells. *Mol. Immunol.* **2015,** *63,* 184-192.

24. von Moos, N. and Slaveykova, V.I. Oxidative stress induced by inorganic nanoparticles in bacteria and aquatic microalgae - state of the art and knowledge gaps. *Nanotoxicology* **2014,** *8,* 605-630.

25. Minetto, D.; Libralato, G.; Ghirardini, A.V. Ecotoxicity of engineered TiO2 nanoparticles to saltwater organisms: An overview. *Environ. Int.* **2014,** *66,* 18-27.

26. Oh, N. and Park, J. Endocytosis and exocytosis of nanoparticles in mammalian cells. *Int. J. Nanomed.* **2014,** *9,* 51-63.

27. Baun, A.; Hartmann, N.B.; Grieger, K.; Kusk, K.O. Ecotoxicity of engineered nanoparticles to aquatic invertebrates: a brief review and recommendations for future toxicity testing. *Ecotoxicology* **2008,** *17,* 387-395.

28. Alvarez, P.J.J.; Colvin, V.; Lead, J.; Stone, V. Research Priorities to Advance Eco-Responsible Nanotechnology. *ACS Nano* **2009,** *3,* 1616-1619.

29. Subcommittee on Nanoscale Science, Engineering, and Technology. Progress review on the coordinated implementation of the national nanotechnology initiative 2011 environmental, health, and safety research strategy. *National Science and Technology Council Committee on Technology* **2014.**

30. Kaegi, R.; Wagner, T.; Hetzer, B.; Sinnet, B.; Tzuetkov, G.; Boller, M. Size, number and chemical composition of nanosized particles in drinking water determined by analytical microscopy and LIBD. *Water Res.* **2008,** *42,* 2778-2786.

31. Botta, C.; Labille, J.; Auffan, M.; Borschneck, D.; Miche, H.; Cabie, M.; Masion, A.; Rose, J.; Bottero, J. TiO(2)-based nanoparticles released in water from commercialized sunscreens in a life-cycle perspective: Structures and quantities. *Environ. Pollut.* **2011,** *159,* 1543-1548.

32. Benn, T.; Cavanagh, B.; Hristovski, K.; Posner, J.D.; Westerhoff, P. The release of nanosilver from consumer products used in the home. *J. Environ. Qual.* **2010,** *39,* 1875-1882.

33. Geranio, L.; Heuberger, M.; Nowack, B. The behavior of silver nanotextiles during washing. *Environ. Sci. Technol.* **2009,** *43,* 8113-8118.

34. Quadros, M.E.; Pierson, R.; Tulve, N.S.; Willis, R.; Rogers, K.; Thomas, T.A.; Marr, L.C. Release of Silver from Nanotechnology-Based Consumer Products for Children. *Environ. Sci. Technol.* **2013,** *47,* 8894-8901.

35. von Goetz, N.; Lorenz, C.; Windler, L.; Nowack, B.; Heuberger, M.; Hungerbuehler, K. Migration of Ag- and TiO_2-(nano)particles from textiles into artificial sweat under physical stress: experiments and exposure modeling. *Environ. Sci. Technol.* **2013,** *47,* 9979-9987.

36. Benn, T.M. and Westerhoff, P. Nanoparticle silver released into water from commercially available sock fabrics. *Environ. Sci. Technol.* **2008,** *42,* 4133-4139.

37. Hedberg, J.; Skoglund, S.; Karlsson, M.; Wold, S.; Wallinder, I.O.; Hedberg, Y. Sequential studies of silver released from silver nanoparticles in aqueous media simulating sweat, laundry detergent solutions and surface water. *Environ. Sci. Technol.* **2014,** *48,* 7314-7322.

38. Kim, B.; Park, C.; Murayama, M.; Hochella, M.F., Jr. Discovery and characterization of silver sulfide nanoparticles in final sewage sludge products. *Environ. Sci. Technol.* **2010,** *44,* 7509-7514.

39. Kaegi, R.; Voegelin, A.; Sinnet, B.; Zuleeg, S.; Hagendorfer, H.; Burkhardt, M.; Siegrist, H. Behavior of metallic silver nanoparticles in a pilot wastewater treatment plant. *Environ. Sci. Technol.* **2011,** *45,* 3902-3908.

40. Levard, C.; Reinsch, B.C.; Michel, F.M.; Oumahi, C.; Lowry, G.V.; Brown, G.E.,Jr. Sulfidation processes of PVP-coated silver nanoparticles in aqueous solution: Impact on dissolution rate. *Environ. Sci. Technol.* **2011,** *45,* 5260-5266.

41. Levard, C.; Hotze, E.M.; Lowry, G.V.; Brown, G.E.,Jr. Environmental transformations of silver nanoparticles: impact on stability and toxicity. *Environ. Sci. Technol.* **2012,** *46,* 6900-6914.

42. Stumm, W. and Morgan, J. *Aquatic chemistry: an introduction emphasizing chemical equilibria in natural waters.* Wiley: New York, 1981; Vol. 2nd Ed.

43. Westerhoff, P.; Song, G.; Hristovski, K.; Kiser, M.A. Occurrence and removal of titanium at full scale wastewater treatment plants: implications for TiO(2) nanomaterials. *J. Environ. Monit.* **2011,** *13,* 1195-1203.

44. Westerhoff, P.; Zhang, Y.; Crittenden, J.; Chen, Y. Properties of commercial nanoparticles that affect their removal during water treatment, In *Nanoscience and Nanotechnology,* Grassian, V.H., Ed.; Wiley: Hoboken, NJ, 2008; pp. 71-90.

45. Zhang, Y.; Chen, Y.; Westerhoff, P.; Crittenden, J. Impact of natural organic matter and divalent cations on the stability of aqueous nanoparticles. *Water Res.* **2009,** *43,* 4249-4257.

46. Keller, A.A.; Wang, H.; Zhou, D.; Lenihan, H.S.; Cherr, G.; Cardinale, B.J.; Miller, R.; Ji, Z. Stability and aggregation of metal oxide nanoparticles in natural aqueous matrices. *Environ. Sci. Technol.* **2010,** *44,* 1962-1967.

47. Piccapietra, F.; Sigg, L.; Behra, R. Colloidal stability of carbonate-coated silver nanoparticles in synthetic and natural freshwater. *Environ. Sci. Technol.* **2012,** *46,* 818-825.

48. Chinnapongse, S.L.; MacCuspie, R.I.; Hackley, V.A. Persistence of singly dispersed silver nanoparticles in natural freshwaters, synthetic seawater, and simulated estuarine waters. *Sci. Total Environ.* **2011,** *409,* 2443-2450.

49. Worms, I.A.M.; Szigeti, Z.A.; Dubascoux, S.; Lespes, G.; Traber, J.; Sigg, L.; Slaveykova, V.I. Colloidal organic matter from wastewater treatment plant effluents: Characterization and role in metal distribution. *Water Res.* **2010,** *44,* 340-350.

50. Zhang, Y.; Chen, Y.; Westerhoff, P.; Hristovski, K.; Crittenden, J.C. Stability of commercial metal oxide nanoparticles in water. *Water Res.* **2008,** *42,* 2204-2212.

51. Holbrook, R.D.; Kline, C.N.; Filliben, J.J. Impact of source water quality on multiwall carbon nanotube coagulation. *Environ. Sci. Technol.* **2010,** *44,* 1386-1391.

52. Bourlinos, A.B.; Georgakilas, V.; Boukos, N.; Dallas, P.; Trapalis, C.; Giannelis, E.P. Silicone-functionalized carbon nanotubes for the production of new carbon-based fluids. *Carbon* **2007,** *45,* 1583-1585.

53. Wagner, T.; Bundschuh, T.; Schick, R.; Koster, R. Detection of aquatic colloids in drinking water during its distribution via a water pipeline network. *Water Sci. Technol.* **2004,** *50,* 27-37.

54. Senftle, F.E.; Thorpe, A.N.; Grant, J.R.; Barkatt, A. Superparamagnetic nanoparticles in tap water. *Water Res.* **2007,** *41,* 3005-3011.

55. Nangmenyi, G.; Xao, W.; Mehrabi, S.; Mintz, E.; Economy, J. Bactericidal activity of Ag nanoparticle-impregnated fibreglass for water disinfection. *J. Water Health* **2009,** *07,* 657-663.

56. Gilbert, B.; Lu, G.; Kim, C.S. Stable cluster formation in aqueous suspensions of iron oxyhydroxide nanoparticles. *J. Colloid Interface Sci.* **2007,** *313,* 152-159.

57. Balbus, J.M.; Maynard, A.D.; Colvin, V.L.; Castranova, V.; Daston, G.P.; Denison, R.A.; Dreher, K.L.; Goering, P.L.; Goldberg, A.M.; Kulinowski, K.M.; Monteiro-Riviere, N.A.; Oberdoerster, G.; Omenn, G.S.; Pinkerton, K.E.; Ramos, K.S.; Rest, K.M.; Sass, J.B.; Silbergeld, E.K.; Wong, B.A. Meeting report: Hazard assessment for nanoparticles - Report from an interdisciplinary workshop. *Environ. Health Perspect.* **2007,** *115,* 1654-1659.

58. Tiede, K.; Hassellöv, M.; Breitbarth, E.; Chaudhry, Q.; Boxall, A.B.A. Considerations for environmental fate and ecotoxicity testing to support environmental risk assessments for engineered nanoparticles. *J. Chromatogr. A* **2009,** *1216,* 503-509.

59. Ichimura, S. Current activities of ISO TC229/WG2 on purity evaluation and quality assurance standards for carbon nanotubes. *Anal. Bioanal. Chem.* **2010,** *396,* 963-971.

60. O'Brien, N.J. and Cummins, E.J. A risk assessment framework for assessing metallic nanomaterials of environmental concern: Aquatic exposure and behavior. *Risk Analysis* **2011,** *31,* 706-726.

61. Buzea, C.; Pacheco, I.I.; Robbie, K. Nanomaterials and nanoparticles: Sources and toxicity. *Biointerphases* **2007,** *2,* MR17-MR71.

62. Lam, C.W.; James, J.T.; McCluskey, R.; Arepalli, S.; Hunter, R.L. A review of carbon nanotube toxicity and assessment of potential occupational and environmental health risks. *Crit. Rev. Toxicol.* **2006,** *36,* 189-217.

63. Dankovic, D.; Kuempel, E.; Wheeler, M. An approach to risk assessment for TiO_2. *Inhal. Toxicol.* **2007,** *19,* 205-212.

64. Liao, C.; Chiang, Y.; Chio, C. Model-based assessment for human inhalation exposure risk to airborne nano/fine titanium dioxide particles. *Sci. Total Environ.* **2008,** *407,* 165-177.

65. Trouiller, B.; Reliene, R.; Westbrook, A.; Solaimani, P.; Schiestl, R.H. Titanium dioxide nanoparticles induce dna damage and genetic instability *in vivo* in mice. *Cancer Res.* **2009,** *69,* 8784-8789.

66. Biskos, G. and Schmidt-Ott, A. Airborne engineered nanoparticles: Potential risks and monitoring challenges for assessing their impacts on children. *Paediatr. Respir. Rev.* **2012,** *13,* 79-83.

67. Morimoto, Y.; Kobayashi, N.; Shinohara, N.; Myojo, T.; Tanaka, I.; Nakanshi, J. Hazard assessments of manufactured nanomaterials. *J. Occup. Health* **2010,** *52,* 325-334.

68. Oberdorster, G.; Maynard, A.; Donaldson, K.; Castranova, V.; Fitzpatrick, J.; Ausman, K.; Carter, J.; Karn, B.; Kreyling, W.; Lai, D.; Olin, S.; Monteiro-Riviere, N.; Warheit, D.; Yang, H.; ILSI Research Foundation/Risk Science Institute Nanomaterial Toxicity Screening Working Group Principles for characterizing the potential human health effects from exposure to nanomaterials: elements of a screening strategy. *Part. Fibre.Toxicol.* **2005,** *2,* 8.

69. Bhattacharya, K.; Davoren, M.; Boertz, J.; Schins, R.P.F.; Hoffmann, E.; Dopp, E. Titanium dioxide nanoparticles induce oxidative stress and DNA-adduct formation but not DNA-breakage in human lung cells. *Part. Fibre. Toxicol.* **2009,** *6,* 17.

70. Deng, Z.J.; Liang, M.; Toth, I.; Monteiro, M.; Minchin, R.F. Plasma protein binding of positively and negatively charged polymer-coated gold nanoparticles elicits different biological responses. *Nanotoxicology* **2013,** *7,* 314-322.

71. Sajid, M.; Ilyas, M.; Basheer, C.; Tariq, M.; Daud, M.; Baig, N.; Shehzad, F. Impact of nanoparticles on human and environment: review of toxicity factors, exposures, control strategies, and future prospects. *Environ. Sci. Pollut. Res.* **2015,** *22,* 4122-4143.

72. Hsiao, I. and Huang, Y. Effects of various physicochemical characteristics on the toxicities of ZnO and TiO_2 nanoparticles toward human lung epithelial cells. *Sci. Total Environ.* **2011,** *409,* 1219-1228.

73. Shang, L.; Nienhaus, K.; Nienhaus, G.U. Engineered nanoparticles interacting with cells: size matters. *J. Nanobiotechnol.* **2014,** *12,* 5.

74. Stark, W.J. Nanoparticles in biological systems. *Angew. Chem. Int. Ed.* **2011,** *50,* 1242-1258.

75. Nel, A.; Xia, T.; Maedler, L.; and Li, N. Toxic potential of materials at the nanolevel. *Science* **2006,** *311,* 622-627.

76. Gaiser, B.K.; Fernandes, T.F.; Jepson, M.A.; Lead, J.R.; Tyler, C.R.; Baalousha, M.; Biswas, A.; Britton, G.J.; Cole, P.A.; Johnston, B.D.; Ju-Nam, Y.; Rosenkranz, P.; Scown, T.M.; Stone, V. Interspecies comparisons on the uptake and toxicity of silver and cerium dioxide nanoparticles. *Environ. Toxicol. Chem.* **2012,** *31,* 144-154.

77. Bar-Ilan, O.; Albrecht, R.M.; Fako, V.E.; Furgeson, D.Y. Toxicity assessments of multisized gold and silver nanoparticles in zebrafish embryos. *Small* **2009,** *5,* 1897-1910.

78. Gao, X.; Wang, Y.; Peng, S.; Yue, B.; Fan, C.; Chen, W.; Li, X. Comparative toxicities of bismuth oxybromide and titanium dioxide exposure on human skin keratinocyte cells. *Chemosphere* **2015,** *135,* 83-93.

79. Ahamed, M.; Alhadlaq, H.A.; Ahmad, J.; Siddiqui, M.A.; Khan, S.T.; Musarrat, J.; Al-Khedhairy, A.A. Comparative cytotoxicity of dolomite nanoparticles in human larynx HEp2 and liver HepG2 cells. *J. App. Toxicol.* **2015,** *35,* 640-650.

80. Brenner, S.A.; Neu-Baker, N.M.; Caglayan, C.; Zurbenko, I.G. Occupational exposure to airborne nanomaterials: an assessment of worker exposure to aerosolized metal oxide nanoparticles in semiconductor wastewater treatment. *J. Occup. Environ. Hyg.* **2015,** *12,* 469-481.

81. Civardi, C.; Schwarze, F.W.M.R.; Wick, P. Micronized copper wood preservatives: An efficiency and potential health risk assessment for copper-based nanoparticles. *Environ. Pollut.* **2015,** *200,* 126-132.

82. Valdiglesias, V.; Kilic, G.; Costa, C.; Fernandez-Bertolez, N.; Pasaro, E.; Teixeira, J.P.; Laffon, B. Effects of iron oxide nanoparticles: Cytotoxicity, genotoxicity, developmental toxicity, and neurotoxicity. *Environ. Mol. Mutagen.* **2015,** *56,* 125-148.

83. Kumar, A.; Kumar, P.; Anandan, A.; Fernandes, T.F.; Ayoko, G.A.; Biskos, G. Engineered nanomaterials: Knowledge gaps in fate, exposure, toxicity, and future directions. *J. Nanomater.* **2014,** 130198.

84. Navarro, E.; Baun, A.; Behra, R.; Hartmann, N.B.; Filser, J.; Miao, A.; Quigg, A.; Santschi, P.H.; Sigg, L. Environmental behavior and ecotoxicity of engineered nanoparticles to algae, plants, and fungi. *Ecotoxicology* **2008,** *17,* 372-386.

85. Gubbins, E.J.; Batty, L.C.; Lead, J.R. Phytotoxicity of silver nanoparticles to Lemna minor L. *Environmental Pollution* **2011,** *159,* 1551-1559.

86. Yin, L.; Cheng, Y.; Espinasse, B.; Colman, B.P.; Auffan, M.; Wiesner, M.; Rose, J.; Liu, J.; Bernhardt, E.S. More than the ions: The effects of silver nanoparticles on lolium multiflorum. *Environ. Sci. Technol.* **2011,** *45,* 2360-2367.

87. Angel, B.M.; Batley, G.E.; Jarolimek, C.V.; Rogers, N.J. The impact of size on the fate and toxicity of nanoparticulate silver in aquatic systems. *Chemosphere* **2013,** *93,* 359-365.

88. Asharani, P.V.; Wu, Y.L.; Gong, Z.; Valiyaveettil, S. Toxicity of silver nanoparticles in zebrafish models. *Nanotechnology* **2008,** *19,* 255102.

89. Roh, J.; Sim, S.J.; Yi, J.; Park, K.; Chung, K.H.; Ryu, D.; Choi, J. Ecotoxicity of silver nanoparticles on the soil nematode caenorhabditis elegans using functional ecotoxicogenomics. *Environ. Sci. Technol.* **2009,** *43,* 3933-3940.

90. Sondi, I. and Salopek-Sondi, B. Silver nanoparticles as antimicrobial agent: a case study on E. coli as a model for Gram-negative bacteria. *J. Colloid Interface Sci.* **2004,** *275,* 177-182.

91. Dror-Ehre, A.; Mamane, H.; Belenkova, T.; Markovich, G.; Adin, A. Silver nanoparticle-E. coli colloidal interaction in water and effect on E-coli survival. *J. Colloid Interface Sci.* **2009,** *339,* 521-526.

92. Fabrega, J.; Renshaw, J.C.; Lead, J.R. Interactions of silver nanoparticles with pseudomonas putida biofilms. *Environ. Sci. Technol.* **2009,** *43,* 9004-9009.

93. Lu, W.; Senapati, D.; Wang, S.; Tovmachenko, O.; Singh, A.K.; Yu, H.; Ray, P.C. Effect of surface coating on the toxicity of silver nanomaterials on human skin keratinocytes. *Chem. Phys. Lett.* **2010,** *487,* 92-96.

94. AshaRani, P.V.; Mun, G.L.K.; Hande, M.P.; Valiyaveettil, S. Cytotoxicity and genotoxicity of silver nanoparticles in human cells. *ACS Nano* **2009,** *3,* 279-290.

95. Ratte, H.T. Bioaccumulation and toxicity of silver compounds: A review. *Environ. Toxicol. Chem.* **1999,** *18,* 89-108.

96. Quadros, M.E. and Marr, L.C. Environmental and human health risks of aerosolized silver nanoparticles. *J. Air Waste Manage. Assoc.* **2010,** *60,* 770-781.

97. Panyala, N.R.; Maria Pena-Mendez, E.; Havel, J. Silver or silver nanoparticles: a hazardous threat to the environment and human health? *J. App. Biomed.* **2008,** *6,* 117-129.

98. Marambio-Jones, C. and Hoek, E.M.V. A review of the antibacterial effects of silver nanomaterials and potential implications for human health and the environment. *J. Nanopart. Res.* **2010,** *12,* 1531-1551.

99. Fabrega, J.; Luoma, S.N.; Tyler, C.R.; Galloway, T.S.; Lead, J.R. Silver nanoparticles: Behaviour and effects in the aquatic environment. *Environ. Int.* **2011,** *37,* 517-531.

100. Khaydarov, R.R.; Khaydarov, R.A.; Estrin, Y.; Evgrafova, S.; Scheper, T.; Endres, C.; Cho, S.Y. Silver nanoparticles environmental and human health impacts. *Nato. Sci. Peace Secur.* **2009,** 287-297.

101. Lea, M.C. On allotropic forms of silver. *Am. J. Sci.* **1889,** *37,* 476-491.

102. Frens, G. and Overbeek, J.T. Carey Lea's Colloidal Silver. *Kolloid-Zeitschrift and Zeitschrift Fur Polymere* **1969,** *233,* 922-&.

103. Paal, C. Ueber colloïdales Silber. *Berichte der deutschen chemischen Gesellschaft* **1902,** *35,* 2224-2236.

104. Nowack, B.; Krug, H.F.; Height, M. 120 Years of nanosilver history: Implications for policy makers. *Environ. Sci. Technol.* **2011,** *45,* 1177-1183.

105. Blaser, S.A.; Scheringer, M.; MacLeod, M.; Hungerbühler, K. Estimation of cumulative aquatic exposure and risk due to silver: Contribution of nano-functionalized plastics and textiles. *Sci. Total Environ.* **2008,** *390,* 396-409.

106. Batley, G.E.; Kirby, J.K.; McLaughlin, M.J. Fate and Risks of Nanomaterials in Aquatic and Terrestrial Environments. *Acc. Chem. Res.* **2013,** *46,* 854-862.

107. Wiesner, M.R.; Lowry, G.V.; Casman, E.; Bertsch, P.M.; Matson, C.W.; Di Giulio, R.T.; Liu, J.; Hochella, M.F.,Jr. Meditations on the ubiquity and mutability of nano-sized materials in the environment. *ACS Nano* **2011,** *5,* 8466-8470.

108. Glover, R.D.; Miller, J.M.; Hutchison, J.E. Generation of metal nanoparticles from silver and copper objects: nanoparticle dynamics on surfaces and potential sources of nanoparticles in the environment. *ACS Nano* **2011,** *5,* 8950-8957.

109. Yu, S.; Yin, Y.; Chao, J.; Shen, M.; Liu, J. Highly dynamic PVP-coated silver nanoparticles in aquatic environments: Chemical and morphology change induced by oxidation of Ag-0 and reduction of Ag+. *Environ. Sci. Technol.* **2014,** *48,* 403-411.

110. Li, Y.; Zhang, W.; Niu, J.; Chen, Y. Surface-coating-dependent dissolution, aggregation, and reactive oxygen species (ROS) generation of silver nanoparticles under different irradiation conditions. *Environ. Sci. Technol.* **2013,** *47,* 10293-10301.

111. Yin, Y.; Shen, M.; Zhou, X.; Yu, S.; Chao, J.; Liu, J.; Jiang, G. Photoreduction and stabilization capability of molecular weight fractionated natural organic matter in transformation of silver ion to metallic nanoparticle. *Environ. Sci. Technol.* **2014,** *48,* 9366-9373.

112. Yin, Y.; Liu, J.; Jiang, G. Sunlight-induced reduction of ionic Ag and Au to metallic nanoparticles by dissolved organic matter. *ACS Nano* **2012,** *6,* 7910-7919.

113. Adegboyega, N.F.; Sharma, V.K.; Siskova, K.; Zboril, R.; Sohn, M.; Schultz, B.J.; Banerjee, S. Interactions of aqueous Ag+ with fulvic acids: Mechanisms of silver nanoparticle formation and investigation of stability. *Environ. Sci. Technol.* **2013,** *47,* 757-764.

114. Akaighe, N.; Depner, S.W.; Banerjee, S.; Sohn, M. Transport and deposition of Suwannee River Humic Acid/Natural Organic Matter formed silver nanoparticles on silica matrices: The influence of solution pH and ionic strength. *Chemosphere* **2013,** *92,* 406-412.

115. Hou, W.; Stuart, B.; Howes, R.; Zepp, R.G. Sunlight-driven reduction of silver ions by natural organic matter: formation and transformation of silver nanoparticles. *Environ. Sci. Technol.* **2013,** *47,* 7713-7721.

116. Stefaniak, A.B.; Hackley, V.A.; Roebben, G.; Ehara, K.; Hankin, S.; Postek, M.T.; Lynch, I.; Fu, W.; Linsinger, T.P.J.; Thuenemann, A.F. Nanoscale reference materials for environmental, health and safety measurements: needs, gaps and opportunities. *Nanotoxicology* **2013,** *7,* 1325-1337.

117. Hansen, S.F.; Larsen, B.H.; Olsen, S.I.; Baun, A. Categorization framework to aid hazard identification of nanomaterials. *Nanotoxicology* **2007,** *1,* 243-U369.

118. Magdolenova, Z.; Collins, A.; Kumar, A.; Dhawan, A.; Stone, V.; Dusinska, M. Mechanisms of genotoxicity. A review of in vitro and in vivo studies with engineered nanoparticles. *Nanotoxicology* **2014,** *8,* 233-278.

119. Warheit, D.B.; Sayes, C.M.; Reed, K.L.; Swain, K.A. Health effects related to nanoparticle exposures: Environmental, health and safety considerations for assessing hazards and risks. *Pharmacol. Ther.* **2008,** *120,* 35-42.

120. Tiede, K.; Boxall, A.B.A.; Tear, S.P.; Lewis, J.; David, H.; Hassellöv, M. Detection and characterization of engineered nanoparticles in food and the environment. *Food Addit. Contam.* **2008,** *25,* 795-821.

121. Wyatt, P.J. Light scattering and the absolute characterization of macromolecules. *Anal. Chim. Acta* **1993,** *272,* 1-40.

122. Tiede, K.; Boxall, A.B.A.; Tiede, D.; Tear, S.P.; David, H.; Lewis, J. A robust size-characterisation methodology for studying nanoparticle behaviour in 'real' environmental samples, using hydrodynamic chromatography coupled to ICP-MS. *J. Anal. At. Spectrom.* **2009,** *24,* 964-972.

123. Park, H. and Grassian, V.H. Commercially manufactured engineered nanomaterials for environmental and health studies: Important insights provided by independent characterization. *Environ. Toxicol. Chem.* **2010,** *29,* 715-721.

124. Englert, B.C. Nanomaterials and the environment: uses, methods and measurement. *J. Environ. Monit.* **2007,** *9,* 1154-1161.

125. Wiesner, M.R.; Lowry, G.V.; Jones, K.L.; Hochella, M.F., Jr.; Di Giulio, R.T.; Casman, E.; Bernhardt, E.S. Decreasing uncertainties in assessing environmental exposure, risk, and ecological implications of nanomaterials. *Environ. Sci. Technol.* **2009,** *43,* 6458-6462.

126. Wild, E. and Jones, K.C. Novel method for the direct visualization of in vivo nanomaterials and chemical interactions in plants. *Environ. Sci. Technol.* **2009,** *43,* 5290-5294.

127. Lowry, G.V. and Wiesner, M.R. Environmental considerations: occurrences, fate, and characterization of nanoparticles in the environment, In *Nanotoxicology: Characterization, Dosing and Health Effects,* Monteiro-Riviere NA, T.C., Ed.; Informa Healthcare USA, Inc: New York, NY, 2007; pp. 369-389.

128. Orbaek, A. and Barron, A.R. ICP-AES analysis of nanoparticles. **2009,** http://cnx.org/content/m22058/1.18/

129. Isaacson, C.; Trimpin, S.; Barofsky, D.; Remcho, V.T.; Field, J.A. Method development for nanoparticle analysis in biological and environmental samples by LC ESI-MS/MS and MALDI MS. **2006,** SETACNorth America 27th Annual Meeting; Montreal, Canada.

130. Balnois, E.; Papastavrou, G.; Wilkinson, K.J. Force microscopy and force measurements of environmental colloids, In *Environmnetal Colloids and Particles : Behavior, Structure and Characterization,* Wilkinson, K.J. and Lead, J.R., Ed.; Wiley: Chichester, pp. 405-468.

131. Doucet, F.J.; Maguire, L.; Lead, J.R. Size fractionation of aquatic colloids and particles by cross-flow filtration: analysis by scanning electron and atomic force microscopy. *Anal. Chim. Acta* **2004,** *522,* 59-71.

132. Alayemieka, E. and Lee, S.H. and Oh, J.G. Estimation of cake formation on microfiltration membrane surface using zeta potential. *Kor. Soc. Environ. Eng.* **2006,** *11,* 201-207.

133. Liu, F. Analysis and applications of nanoparticles in the separation sciences: A case of gold nanoparticles. *J.Chromatogr. A* **2009,** *1216,* 9034-9047.

134. Liu, F. SEC characterization of Au nanoparticles prepared through seed-assisted synthesis. *Chromatographia* **2007,** *66,* 791-796.

135. Ju-Nam, Y. and Lead, J.R. Manufactured nanoparticles: An overview of their chemistry, interactions and potential environmental implications. *Sci. Total Environ.* **2008,** *400,* 396-414.

136. Al-Somali, A.M.; Krueger, K.M.; Falkner, J.C.; Colvin, V.L. Recycling size exclusion chromatography for the analysis and separation of nanocrystalline gold. *Anal. Chem.* **2004,** *76,* 5903-5910.

137. Surugau, N. and Urban, P.L. Electrophoretic methods for separation of nanoparticles. *J. Sep. Sci.* **2009,** *32,* 1889-1906.

138. Lo, C.K.; Paau, M.C.; Xiao, D.; Choi, M.M.F. Application of capillary zone electrophoresis for separation of water-soluble gold monolayer-protected clusters. *Electrophoresis* **2008,** *29,* 2330-2339.

139. Baalousha, M.; Stolpe, B.; Lead, J.R. Flow field-flow fractionation for the analysis and characterization of natural colloids and manufactured nanoparticles in environmental systems: A critical review. *J.Chromatogr. A* **2011,** *1218,* 4078-4103.

140. Contado, C. and Pagnoni, A. TiO(2) nano- and micro-particles in commercial foundation creams: Field flow-fractionation techniques together with ICP-AES and SQW voltammetry for their characterization. *Anal. Method* **2010,** *2,* 1112-1124.

141. Al-Ammar, A.; Siripinyanond, A.; Barnes, R.M. Simultaneous sample preconcentration and matrix removal using field-flow fractionation coupled to inductively coupled plasma mass spectrometry. *Spectroc. Acta Pt. B-Atom. Spectr.* **2001,** *56,* 1951-1962.

142. Sermsri, W.; Jarujamrus, P.; Shiowatana, J.; Siripinyanond, A. Flow field-flow fractionation: a versatile approach for size characterization of alpha-tocopherol-induced enlargement of gold nanoparticles. *Anal. Bioanal. Chem.* **2010,** *396,* 3079-3085.

143. Gale, B.K. A decade of progress in microscale FFF. **2007,** Proc. SPIE Microfluidics, BioMEMS, and Medical Microsystems V ; San Jose, CA, USA.

144. Dubascoux, S.; Le Hecho, I.; Hassellöv, M.; Von der Kammer, F.; Gautier, M.P.; Lespes, G. Field-flow fractionation and inductively coupled plasma mass spectrometer coupling: History, development and applications. *J. Anal. At. Spectrom.* **2010,** *25,* 613-623.

145. Diaz, X.; Johnson, W.P.; Fernandez, D.; Naftz, D.L. Size and elemental distributions of nano- to micro-particulates in the geochemically-stratified Great Salt Lake. *Appl. Geochem.* **2009,** *24,* 1653-1665.

146. Delay, M.; Dolt, T.; Woellhaf, A.; Sembritzki, R.; Frimmel, F.H. Interactions and stability of silver nanoparticles in the aqueous phase: Influence of natural organic matter (NOM) and ionic strength. *J. Chromatogr. A* **2011,** *1218,* 4206-4212.

147. Poda, A.R.; Bednar, A.J.; Kennedy, A.J.; Harmon, A.; Hull, M.; Mitrano, D.M.; Ranville, J.F.; Steevens, J. Characterization of silver nanoparticles using flow-field flow fractionation interfaced to inductively coupled plasma mass spectrometry. *J. Chromatogr. A* **2011,** *1218,* 4219-4225.

148. Golstein, J.I.; Newbury, D.E.; Joy, D.C.; Lyman, C.; Echlin, P.; Lifshin, E.; Sawyer, L.; Michael, J. *Scanning electron microscopy and X-ray microanalysis.* Plenum Press: New York, NY, USA, 2003;

149. Mavrocordatos, D. Analysis of environmental particles by atomic force microscopy, scanning and transmission electron microscopy. *Water Sci. Technol.* **2004,** *50,* 9-18.

150. Burleson, D.J.; Driessen, M.D.; Penn, R.L. On the characterization of environmental nanoparticles. *J. Environ. Sci. Health Part A-Toxic/Hazard. Subst. Environ. Eng.* **2004,** *39,* 2707-2753.

151. de Jonge, N. and Ross, F.M. Electron microscopy of specimens in liquid. *Nat. Nano* **2011,** *6,* 695-704.

152. Klein, K.L.; Anderson, I.M.; De Jonge, N. Transmission electron microscopy with a liquid flow cell. *J. Microsc.* **2011,** *242,* 117-123.

153. Danilatos, G. Introduction to the ESEM instrument. *Microsc. Res. Tech.* **1993,** *25,* 354-361.

154. Holbrook, R.; Wagner, M.; Mahoney, C.; Wight, S. Investigating activated sludge flocs using microanalytical techniques: Demonstration of environmental scanning electron microscopy and time-of-flight secondary ion mass spectrometry for wastewater applications. *Water Environ. Res.* **2006,** *78,* 381-+.

155. Tiede, K.; Tear, S.P.; David, H.; Boxall, A.B.A. Imaging of engineered nanopartlicles and their aggregates under fully liquid conditions in environmental matrices. *Water Res.* **2009,** *43,* 3335-3343.

156. Williamson, M.J.; Tromp, R.M.; Vereecken, P.M.; Hull, R.; Ross, F.M. Dynamic microscopy of nanoscale cluster growth at the solid-liquid interface. *Nat. Mater.* **2003,** *2,* 532-536.

157. Zheng, H.; Smith, R.K.; Jun, Y.; Kisielowski, C.; Dahmen, U.; Alivisatos, A.P. Observation of single colloidal platinum nanocrystal growth trajectories. *Science* **2009,** *324,* 1309-1312.

158. de Jonge, N.; Peckys, D.B.; Kremers, G.J.; Piston, D.W. Electron microscopy of whole cells in liquid with nanometer resolution. *Proc. Natl. Acad. Sci. U. S. A.* **2008,** *106,* 2159-2164.

159. Ring, E.A. and de Jonge, N. Microfluidic system for transmission electron microscopy RID B-5677-2008. *Microsc. Microanal.* **2010,** *16,* 622-629.

160. Elzey, S. and Grassian, V.H. Agglomeration, isolation and dissolution of commercially manufactured silver nanoparticles in aqueous environments. *J. Nanopart. Res.* **2010,** *12,* 1945-1958.

161. Latkoczy, C.; Kägi, R.; Fierz, M.; Ritzmann, M.; Günther, D.; Boller, M. Development of a mobile fast-screening laser-induced breakdown detection (LIBD) system for field-based measurements of nanometre sized particles in aqueous solutions. *J. Environ. Monit.* **2010,**

162. Bednar, A.J.; Poda, A.R.; Mitrano, D.M.; Kennedy, A.J.; Gray, E.P.; Ranville, J.F.; Hayes, C.A.; Crocker, F.H.; Steevens, J.A. Comparison of on-line detectors for field flow fractionation analysis of nanomaterials. *Talanta* **2013,** *104,* 140-148.

163. Leppard, G.G.; Mavrocordatos, D.; Perret, D. Electron-optical characterization of nano- and micro-particles in raw and treated waters: an overview. *Water Sci. Technol.* **2004,** *50,* 1-8.

164. Song, Y.; Jimenez, V.; McKinney, C.; Donkers, R.; Murray, R.W. Estimation of size for 1-2 nm nanoparticles using an HPLC electrochemical detector of double layer charging. *Anal. Chem.* **2003,** *75,* 5088-5096.

165. Lyon, D.Y.; Adams, L.K.; Falkner, J.C.; Alvarez, P.J.J. Antibacterial activity of fullerene water suspensions: Effects of preparation method and particle size. *Environ. Sci. Technol.* **2006,** *40,* 4360-4366.

166. Powers, K.W.; Palazuelos, M.; Moudgil, B.M.; Roberts, S.M. Characterization of the size, shape, and state of dispersion of nanoparticles for toxicological studies. *Nanotoxicology* **2007,** *1,* 42-51.

167. Howell, K.A.; Achterberg, E.P.; Tappin, A.D.; Worsfold, P.J. Colloidal metals in the tamar estuary and their influence on metal fractionation by membrane filtration. *Environ. Chem.* **2006,** *3,* 199-207.

168. Akthakul, A.; Hochbaum, A.I.; Stellacci, F.; Mayes, A.M. Size fractionation of metal nanoparticles by membrane filtration. *Adv. Mater.* **2005,** *17,* 532-+.

169. Kennedy, A.J.; Hull, M.S.; Bednar, A.J.; Goss, J.D.; Gunter, J.C.; Bouldin, J.L.; Vikesland, P.J.; Steevens, J.A. Fractionating nanosilver: Importance for determining toxicity to aquatic test organisms. *Environ. Sci. Technol.* **2010,** *44,* 9571-9577.

170. Hassellöv, M.; Readman, J.W.; Ranville, J.F.; Tiede, K. Nanoparticle analysis and characterization methodologies in environmental risk assessment of engineered nanoparticles. *Ecotoxicology* **2008,** *17,* 344-361.

171. Lead, J.R. and Wilkinson, K.J. Aquatic colloids and nanoparticles: Current knowledge and future trends. *Environ. Chem.* **2006,** *3,* 159-171.

172. Lens, P.N.L.; Virkutyte, J.; Jegatheesan, V.; Kim, S.H.; AlAbed, S. *Nanotechnology for Water and Wastewater Treatment.* 2013; Integrated Environmental Technology Series.

173. Gigault, J.; Pettibone, J.M.; Schmitt, C.; Hackley, V.A. Rational strategy for characterization of nanoscale particles by asymmetric- flow field flow fractionation: A tutorial. *Anal. Chim. Acta* **2014,** *809,* 9-24.

174. Bolea, E.; Jimenez-Lamana, J.; Laborda, F.; Castillo, J.R. Size characterization and quantification of silver nanoparticles by asymmetric flow field-flow fractionation coupled with inductively coupled plasma mass spectrometry. *Anal. Bioanal. Chem.* **2011,** *401,* 2723-2732.

175. Hawe, A.; Romeijn, S.; Filipe, V.; Jiskoot, W. Asymmetrical flow field-flow fractionation method for the analysis of submicron protein aggregates. *J. Pharm. Sci.* **2012,** *101,* 4129-4139.

176. Thang, N.; Geckeis, H.; Kim, J.; Beck, H. Application of the flow field flow fractionation (FFFF) to the characterization of aquatic humic colloids: evaluation and optimization of the method. *Colloid Surf. A-Physicochem. Eng. Asp.* **2001,** *181,* 289-301.

177. Hupfeld, S.; Ausbacher, D.; Brandl, M. Asymmetric flow field-flow fractionation of liposomes: optimization of fractionation variables. *J. Sep. Sci.* **2009,** *32,* 1465-1470.

178. Loeschner, K.; Navratilova, J.; Legros, S.; Wagner, S.; Grombe, R.; Snell, J.; von der Kammer, F.; Larsen, E.H. Optimization and evaluation of asymmetric flow field-flow fractionation of silver nanoparticles. *J. Chromatogr. A* **2013,** *1272,* 116-125.

179. Lyven, B.; Hassellov, M.; Haraldsson, C.; Turner, D. Optimisation of on-channel preconcentration in flow field-flow fractionation for the determination of size distributions of low molecular weight colloidal material in natural waters. *Anal. Chim. Acta* **1997,** *357,* 187-196.

180. Baalousha, M. and Lead, J.R. Characterization of natural aquatic colloids (< 5 nm) by flow-field flow fractionation and atomic force microscopy. *Environ. Sci. Technol.* **2007,** *41,* 1111-1117.

181. Giddings, J. Field-flow fractionation - Analysis of macromolecular, colloidal, and particulate materials. *Science* **1993,** *260,* 1456-1465.

182. Isaacson, C.W. and Bouchard, D. Asymmetric flow field flow fractionation of aqueous C-60 nanoparticles with size determination by dynamic light scattering and quantification by liquid chromatography atmospheric pressure photo-ionization mass spectrometry. *J. Chromatogr. A* **2010,** *1217,* 1506-1512.

183. Hagendorfer, H.; Kaegi, R.; Parlinska, M.; Sinnet, B.; Ludwig, C.; Ulrich, A. Characterization of silver nanoparticle products using asymmetric flow field flow fractionation with a multidetector approach - A comparison to transmission electron microscopy and batch dynamic light scattering. *Anal. Chem.* **2012,** *84,* 2678-2685.

184. Ulrich, A.; Losert, S.; Bendixen, N.; Al-Kattan, A.; Hagendorfer, H.; Nowack, B.; Adlhart, C.; Ebert, J.; Lattuada, M.; Hungerbuehler, K. Critical aspects of sample handling for direct nanoparticle analysis and analytical challenges using asymmetric field flow fractionation in a multi-detector approach. *J. Anal. At. Spectrom.* **2012,** *27,* 1120-1130.

185. Wilson, I.D. and Brinkman, U.A.T. Hyphenation and hypernation - The practice and prospects of multiple hyphenation. *J.Chromatogr. A* **2003,** *1000,* 325-356.

186. Gimbert, L.J.; Andrew, K.N.; Haygarth, P.M.; Worsfold, P.J. Environmental applications of flow field-flow fractionation (FIFFF). *TrAC-Trend. Anal. Chem.* **2003,** *22,* 615-633.

187. Williams, S.K.R.; Runyon, J.R.; Ashames, A.A. Field-flow fractionation: Addressing the nano challenge. *Anal. Chem.* **2011,** *83,* 634-642.

188. Bouby, M.; Geckeis, H.; Geyer, F.W. Application of asymmetric flow field-flow fractionation (AsFlFFF) coupled to inductively coupled plasma mass spectrometry (ICPMS) to the quantitative characterization of natural colloids and synthetic nanoparticles. *Anal. Bioanal. Chem.* **2008,** *392,* 1447-1457.

189. Popovici, S.; Kok, W.; Schoenmakers, P. Band broadening in size-exclusion chromatography of polydisperse samples. *J. Chromatogr. A* **2004,** *1060,* 237-252.

190. Kammer, F.; Baborowski, M.; Friese, K. Field-flow fractionation coupled to multi-angle laser light scattering detectors: Applicability and analytical benefits for the analysis of environmental colloids. *Anal. Chim. Acta* **2005,** *552,* 166-174.

191. Filella, M.; Zhang, J.; Newman, M.E.; Buffle, J. Analytical applications of photon correlation spectroscopy for size distribution measurements of natural colloidal suspensions: capabilities and limitations. *Colloids Surf. A - Physicochem. Eng. Aspects* **1997,** *120,* 27-46.

192. Giddings, J.C. New separation concept based on a coupling of concentration and flow non-uniformities. *Sep. Sci.* **1966,** *1,* 123.

193. Williams, P.S. and Giddings, J.C. Theory of field-programmed field-flow fractionation with corrections for steric effects. *Anal. Chem.* **1994,** *66,* 4215-4228.

194. Wyatt, P.J. Submicrometer particle sizing by multiangle light scattering following fractionation. *J. Colloid Interface Sci.* **1998,** *197,* 9-20.

195. Barber, P.W. and Wang, D. Rayleigh-Gans-Debye applicability to scattering by nonspherical particles. *Appl. Opt.* **1978,** *17,* 797-803.

196. Fröse, D. Light scattering data evaluation using legendre polynomials. *Macromolecular Symposia* **2000,** *162,* 95-108.

197. Andersson, M.; Wittgren, B.; Wahlund, K. Accuracy in multiangle light scattering measurements for molar mass and radius estimations: Model calculations and experiments. *Anal. Chem.* **2003,** *75,* 4279-4291.

198. Zhao, Y. and Ma, L. Applicable range of the Rayleigh-Debye-Gans theory for calculating the scattering matrix of soot aggregates. *Appl. Opt.* **2009,** *48,* 591-597.

199. Wyatt Technology. Understanding Dynamic Light Scattering. *2015,* http://www.wyatt.com/library/theory/dynamic-light-scattering.html

200. Lee, Y.; Filliben, J.J.; Micheals, R.J.; Phillips, P.J. Sensitivity analysis for biometric systems: A methodology based on orthogonal experiment designs. *Comput. Vision Image Understanding* **2013,** *117,* 532-550.

201. Scott, J.H.J. Accuracy issues in chemical and dimensional metrology in the SEM and TEM. *Meas. Sci. Technol.* **2007,** *18,* 2755-2761.

202. Sensitivity Analysis of MesoNet, In *Study of Proposed Internet Congestion Control Mechanisms,* Mills, K.M., Filliben, J.J., Cho, D.Y., Schwartz, E. and Genin, D., Eds.; U.S. Government Printing Office: Washington, D.C., 2010; pp. 71-135.

203. Filliben, J.J. and Simiu, E. Tall building response parameters: Sensitivity study based on orthogonal factorial experiment design technique. *J. Struct. Eng. -ASCE* **2010,** *136,* 160-164.

204. Kurosaki, H.; Radford, R.; Filliben, J.; Inn, K.G.W. An orthogonal design of experiment/exploratory data analysis for plutonium contamination. *J. Radioanal. Nucl.* **2008,** *276,* 323-328.

205. National Institute of Standards and Technology An EDA Approach to Experimental Design. *NIST/SEMATECH e-Handbook of Statistical Methods* **2013,** *2014,* http://www.itl.nist.gov/div898/handbook/pri/section5/pri59.htm

206. Wetzel, S.; Guttman, C.; Flynn, K.; Filliben, J. Significant parameters in the optimization of MALDI-TOF-MS for synthetic polymers. *J. Am. Soc. Mass Spectrom.* **2006,** *17,* 246-252.

207. Box, G.E.P.; Hunter, W.G.; Hunter, J.S. *Statistics for Experimenters: An Introduction to Design, Data Analysis and Model Building.* Wiley: New York, 1978.

208. Louie, S.M.; Tilton, R.D.; Lowry, G.V. Effects of molecular weight distribution and chemical properties of natural organic matter on gold nanoparticle aggregation. *Environ. Sci. Technol.* **2013,** *47,* 4245-4254.

209. Filella, M. Freshwaters: which NOM matters? *Environ. Chem. Lett.* **2009,** *7,* 21-35.

210. Piccolo, A. The supramolecular structure of humic substances. *Soil Sci.* **2001,** *166,* 810-832.

211. Philippe, A. and Schaumann, G.E. Interactions of dissolved organic matter with natural and engineered inorganic colloids: A review. *Environ. Sci. Technol.* **2014,** *48,* 8946-8962.

212. Chow, A.T.; Guo, F.; Gao, S.; Breuer, R.; Dahlgren, R.A. Filter pore size selection for characterizing dissolved organic carbon and trihalomethane precursors from soils. *Water Res.* **2005,** *39,* 1255-1264.

213. Jones, M.N. and Bryan, N.D. Colloidal properties of humic substances. *Adv. Colloid Interface Sci.* **1998,** *78,* 1-48.

214. Baalousha, M.; Motelica-Heino, M.; Le Coustumer, P. Conformation and size of humic substances: Effects of major cation concentration and type, pH, salinity, and residence time. *Colloids Surf. A - Physicochem. Eng. Aspects* **2006,** *272,* 48-55.

215. Avena, M.J. and Wilkinson, K.J. Disaggregation kinetics of a peat humic acid: Mechanism and pH effects. *Environ. Sci. Technol.* **2002,** *36,* 5100-5105.

216. Allain, P.; Jaunault, L.; Mauras, Y.; Mermet, J.; Delaporte, T. Signal enhancement of elements due to the presence of carbon-containing compounds in inductively coupled plasma mass-spectrometry. *Anal. Chem.* **1991,** *63,* 1497-1498.

217. Świetlik, J. and Sikorska, E. Application of fluorescence spectroscopy in the studies of natural organic matter fractions reactivity with chlorine dioxide and ozone. *Water Res.* **2004,** *38,* 3791-3799.

218. Hautala, K.; Peuravuori, J.; Pihlaja, K. Measurement of aquatic humus content by spectroscopic analyses. *Water Res.* **2000,** *34,* 246-258.

219. Peuravuori, J.; Koivikko, R.; Pihlaja, K. Characterization, differentiation and classification of aquatic humic matter separated with different sorbents: synchronous scanning fluorescence spectroscopy. *Water Res.* **2002,** *36,* 4552-4562.

220. Chen, J.; LeBoeuf, E.J.; Dai, S.; Gu, B. Fluorescence spectroscopic studies of natural organic matter fractions. *Chemosphere* **2003,** *50,* 639-647.

CHAPTER 2: USING LIGHT SCATTERING TO EVALUATE THE SEPARATION OF POLYDISPERSE NANOPARTICLES[1]

2.1 Introduction

Field flow fractionation (FFF) and specifically, flow field flow fractionation (FlFFF), has become one of the most favored methods for separating complex colloidal samples. FlFFF is a type of chromatography that does not require the use of a stationary phase and relies on hydrodynamic principles to separate particles in an open fluidic channel [1-4]. FlFFF can be directly interfaced with a wide variety of standard chromatography detectors, such as multi-angle light scattering (MALS) for particle sizing, quasi-elastic light scattering (QELS) for measuring particle diffusion coefficients, concentration detectors, fluorescence, or inductively coupled plasma-mass spectrometry for elemental analysis, among others [5]. FlFFF has been applied to particle separation of very small particles, such as humic substances in the 1 nm range, natural colloids in the 20 nm - 450 nm range, and larger particles, such as clay, in the 5 μm - 100 μm range [3]. FlFFF has been widely applied to nanoparticle analysis, such as metals, metal oxides, SiO_2, and carbon black. Additionally, it has been used to analyze complex sample matrices such as soil suspensions and colloids in fresh and marine water samples [6] while simultaneously reducing sample complexity and fractionating colloidal materials by size. There is a growing body of literature on how to optimize and define AF^4 separation parameters for various applications and types of nanomaterials, based on theory and experimental parameters that influence AF^4 [3, 7-13].

The development of separation techniques operated in tandem with MALS and QELS detectors allows for size and molar mass distribution measurements of arbitrary polydisperse mixtures of particles and in some cases, information about molecular conformation [14]. While the angular dependence of scattered light can provide information about particle size as measured by MALS, QELS directly measures the translational diffusion coefficient, and computes hydrodynamic radius (R_h) using the

[1] Galyean, A.A.; Vreeland, W.N.; Filliben, J.J.; Holbrook, R.D.; Ripple, D.C.; Weinberg, H.S. Using light scattering to evaluate the separation of polydisperse nanoparticles. *Anal. Chim. Acta* **2015,** 886**,** 207–213

Stokes-Einstein equation. When light scattering is combined with a non-destructive separation technique that presents the light scattering detector with scattering from an essentially monodisperse particle size at each measured fraction, the size distribution of the original sample can be calculated [15, 16]. Because the relationship between particle size and scattering intensity is highly non-linear ($I \propto r^6$, where *I* is the scattering intensity and *r* is the particle radius; light scattering theory has been described in detail elsewhere [15-17]), the measured size can be heavily biased to being erroneously large in insufficiently separated mixtures. In other words, a few large particles may obscure the detection and accurate measurement of much greater numbers of small particles. Therefore, obtaining an accurate measurement of a polydisperse distribution requires a separation of sufficient resolution, and the optimum separation will result in the smallest average size (**Figure 2.1**).

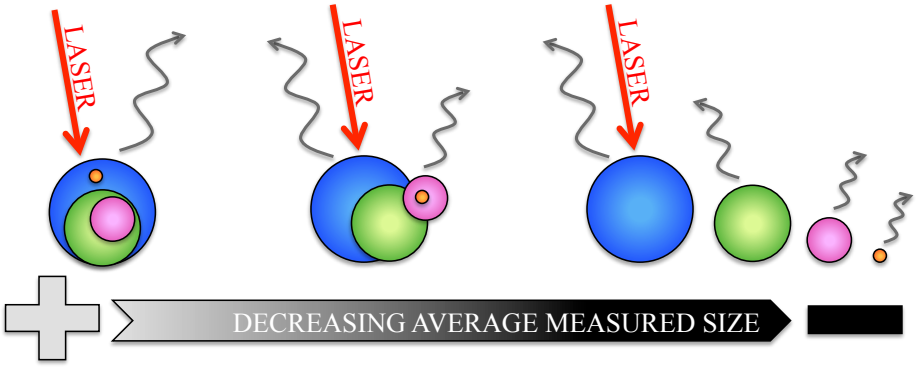

Figure 2.1. Cartoon depicting separation scenarios for a complex mixture of particles: (Left) insufficiently separated sample where large particles dominate the measurement and obscure smaller particles from detection, and (Right) a size-based separation of sufficient selectivity where both large and small particles are detected separately.

Separations of various natural, environmental, biological, or otherwise complex samples are less defined and contain a higher level of variability [14, 18-20] when compared to the separations of mixtures of monodisperse or distinct particle sizes. Currently, to our knowledge, there is no metric to establish whether the separation optimization is complete and the separation is the best possible given the available experimental conditions. Experience and FFF theory can provide tools for choosing separation conditions based on a certain range of particle sizes. However, in the case of unknown or complex

mixtures spanning a large size range, these conditions may be much less obvious. Similarly, extremely polydisperse mixtures, such as environmental or natural samples, may not yield sufficient resolution between sample components to judge separation quality by observing the raw data in fractograms alone. Therefore, the analysis of a single separation and its data may not provide adequate information about the accuracy of the measurement. Thus, a rigorous characterization requires multiple separation protocols and comparison among them.

To address the challenges described above, we compare the average measured particle size for a distribution of particles with various separation parameters, and demonstrate that the best separation possible is obtained when the average size is at a minimum. In this work, the separation parameter of cross flow in an AF^4-QELS system is used as a simplified example to represent changing separation conditions. This separation metric is described and subsequently applied to mixtures of polystyrene nanoparticles of several known mean sizes to mimic complex mixtures.

2.2 Materials and Methods

2.2.1 Instrumentation

AF^4 was performed using an Eclipse DualTec separation module (Wyatt Technologies Corp., Santa Barbara CA) with OpenLab CDS Chem Station edition software (Agilent Technologies, Santa Clara, CA). Injections were made with an Agilent 1260 Infinity series isopump and autosampler with a 900 µL injection loop. The run buffer was degassed by a Gastorr TG-14 (Flom USA, San Diego, CA, USA) at 10 kPa directly from solvent bottles, and filtered in series by a polytetrafluoroethylene frit (RESTEK Corp., Bellefontane, PA, USA) and a 0.1 µm Durapore® membrane filter (Millipore Inc., Billerica, MA, USA). Separation was performed with an outlet channel flowrate of 1 mL min^{-1} and a 1 min focusing time using a Wyatt Technologies "short channel" containing a 350 µm spacer and a regenerated cellulose ultrafiltration membrane with 5 kDa cutoff (Wyatt Technologies Corp.). AF^4 instrumental parameters held constant for each protocol are provided in **Table 2.1**

Quasi electric light scattering (QELS) measurements were made with a WyattQELS™ detector through a QELS fiber attached to the Wyatt DAWN® II MALS detector at a nominal angle of 140° with a 2.0 sec collection interval (Wyatt Technologies Corp.). Multi angle light scattering (MALS) measurements

were not included in this work. Polystyrene samples were prepared in ammonium nitrate buffer and placed in amber glass vials sealed with PTFE/silicone septa (Chemglass Life Sciences, Vineland, NJ, USA). Data were collected and analyzed with ASTRA™ Software version 6.1.1.17. ASTRA™ Software calculates the R_h using QELS data by measuring the time-dependent fluctuations in scattered light. The fluctuations are then directly related to the rate of diffusion of the molecule through the solvent, which, in turn, is related to the particles' hydrodynamic radii. In this work, the "average R_h" refers to the uncertainty-weighted average, determined in the ASTRA software by:

$$(R_h)_{avg} = \frac{\sum r_i \sigma_{r_i}^2}{\sum \sigma_{r_i}^2} \tag{1.1}$$

where r_i represents the calculated R_h of the *i*th time slice, and σ_{r_i} is the uncertainty in the radius measurement, defined as:

$$\sigma_{r_{avg}} = \frac{1}{\sum \sigma_{r_i}^2} \tag{1.2}$$

2.2.2 Materials

The AF^4 run buffer was prepared by dissolving ammonium nitrate (Sigma-Aldrich, St. Louis, MO, USA) in laboratory-grade 18.2 MΩ·cm water with 0.01% sodium azide (Ricca Chemical Company, Arlington, TX, USA) as an antimicrobial. Mixtures of spherical Nanosphere™ NIST-traceable polystyrene beads (Thermo Scientific, Waltham, MA, USA) of various sizes in laboratory-grade 18.2 MΩ·cm water were prepared. Two mixtures were prepared from bead suspensions of known bead size and concentration. Sample 1, prepared to represent a mixture containing a large amount of small particles and a small amount of large particles, consisted of a mixture of (21 ± 2) nm ([8.25 mg mL^{-1}]), (41 ± 4) nm ([0.47 mg mL^{-1}]), (57 ± 4) nm ([0.11 mg mL^{-1}]), (81 ± 3) nm ([0.05 mg mL^{-1}]) and (100 ± 3) nm ([0.03 mg mL^{-1}]) certified diameter beads with manufacturer specified size distribution. Sample 2, prepared to simulate polydisperse samples containing low scattering signal from small particles and large scattering

signal from large particles, consisted of a mixture containing spheres of (21 ± 2) nm, (41 ± 4) nm, (57 ± 4) nm, (81 ± 3) nm certified mean diameters, each at a particle concentration of 2.7×10^{12} mL^{-1}. Polystyrene bead mean diameters were provided by the supplier and confirmed in-house by both dynamic light scattering and AF^4-QELS (data not shown).

Table 2.1 - AF^4 operating conditions for each protocol where V_x and ramp time were varied.

AF^4 Operating Conditions	
Membrane	Regenerated cellulose, 10 kDa MWCO
Carrier liquid	1.0 mM NH_4NO_3 in 18.2 MΩ•cm nanopure water
Spacer thickness	350 µm
Detector flow	1.00 mL min^{-1}
Injection volume	50 µL (Sample 1) 60 µL (Sample 2)
Injection flow	0.20 mL min^{-1}
Focusing Regime	1.00 min focus 3.00 min focus + inject 2.00 min focus
Focusing Flow	1.50 mL min^{-1}

MWCO = molecular weight cutoff

2.2.3 Methods

Polystyrene sphere mixtures were separated with a range of low, medium, and high particle retention AF^4 separation protocols. Cross flow (V_x) for all protocols was ramped down linearly from the starting V_x rate to 0 mL min^{-1} over the period of elution. At a channel flow of 1 mL/min, the maximum V_x allowed with the instrument setup is 2.99 mL min^{-1}. From low to high retention, protocols were defined with initial V_x rates of 0.50 mL min^{-1}, 1.00 mL min^{-1}, 1.25 mL min^{-1}, 1.50 mL min^{-1}, 1.75 mL min^{-1}, 2.00 mL min^{-1}, 2.25 mL min^{-1}, 2.50 mL min^{-1}, 2.75 mL min^{-1}, and 2.99 mL min^{-1}, and linearly decreasing the V_x to 0 mL min^{-1} over the gradient duration. Duration of the V_x gradient from low to high retention were 10 min, 20

min, 30 min, 40 min, 50 min, and 60 min. **Figure 2.2** is a graphical representation of the initial V_x rate and ramp times for each protocol used in this work. Particle size analysis was performed at each data point across the entire elution window, from the point of injection through end of the separation. To assess the quality of a given separation relative to another, the average R_h of the measured sample distribution was calculated for each parameter setting using all data within the AF^4 elution window. Using the uncertainty-weighted average, points of lower accuracy with low signal to noise ratios are less influential in calculating $R_{h,}$ and no statistical manipulation was required. Further, all data were used to maintain consistency between protocols of different elution lengths and resolution. Each protocol was run in triplicate to ensure the reproducibility of the separation.

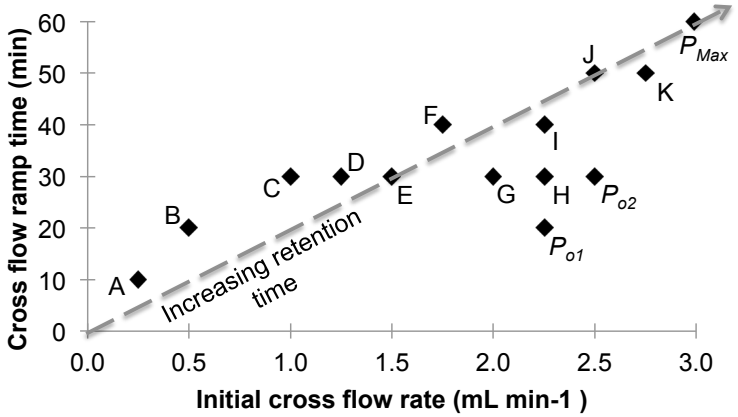

Figure 2.2. V_x and elution time of selected protocols using AF^4-QELS along the trend of increasing retention strength from *A-K*. P_{o1} and P_{o2} represent protocols that are orthogonal to protocol H in separation time and initial V_x. P_{max} represents the protocol of highest retention possible given instrumental or experimental limitations.

2.3 Results and Discussion

2.3.1 AF^4 Separation of Polystyrene Mixtures

The separation metric was applied to polystyrene bead mixtures spanning a wide dynamic range (20 nm -100 nm) in increments of 20 nm. While polystyrene beads are inherently less polydisperse than a complex natural sample, these mixtures mimic complex samples in that baseline resolution was not possible by adjusting the V_x and V_x gradient alone within the designated elution window. Polystyrene

beads (particles) are often used as model systems for AF^4 size calibration and system optimization prior to analysis with real, complex samples [2, 3, 21, 22] and polystyrene standards separated with AF^4 have been shown to have very good sample recoveries (up to 95%) [21]. The application of this metric to more complex samples, like environmental samples, would require additional characterization and recovery analysis to account for non-ideal behavior, such as the potential risk of particle-membrane and particle-particle interactions, to identify any sample changes that may occur with separation parameter modification. Recovery experiments are typically performed with the addition of a concentration detector, like refractive index or UV-Vis spectrophotometry.

Samples 1 and 2 were separated by AF^4-QELS using protocols of increasing retention time, shown in Figure 2.2 and described below. For demonstration purposes, the separation parameters chosen were V_x and V_x gradient time, as they are primary AF^4 separation parameters. While we have chosen two separation parameters out of a potentially larger set of instrument factors as a demonstration, the proposed methodology could be applied to any combination of other parameters or potentially all could be used simultaneously, depending on the desired application. In the case of all available parameters being applied, a broader optimized methodology of screening and optimization designs along with appropriate analysis would be required.

The analysis procedure chosen for this work is as follows: beginning with the protocol of very low retention time (protocol: "*A*"), the average measured size for each sample separated using each protocol of increasing retention time (protocols: "*B*" through "*K*") was compared with that of the previous protocol until increasing retention no longer produced a significant decrease in average measured size. At this point, a protocol of higher retention in an orthogonal direction of steepest descent to that of previous pair was selected (protocols: "P_{o1} and P_{o2}"). Exploring P_{o1} and P_{o2} better populates the experimental space in identifying a local minimum in average measured size. All values for each protocol were plotted for both mixtures, as shown in **Figure 2.3a** for Sample 1 and **Figure 2.3b** for Sample 2. In the event that increasing particle retention by turning up the V_x and elution ramp did not yield a significant decrease in average R_h compared to the previous protocol, the value was compared to that of P_{max} to ensure that an extreme increase in retention would not result in a significantly lower average R_h. If this comparison failed, then the retention was increased and the process repeated until the statistical minimum was identified.

The statistical details for a stepwise approach for selecting a successful separation protocol, and the determination as to whether the chosen protocol is sufficient for the intended application is shown via flowchart and a worked example in the Appendix 2.1 and 2.2, respectively.

2.3.2 Light Scattering Analysis

In both cases, protocol *H* was identified as being the optimal protocol of those tested, with the average measured R_h found to be (21.1 ± 0.5) nm and (26.3 ± 0.6) nm for the Samples 1 and 2, respectively (Figure 2.3). All uncertainties are defined at the 95% confidence interval. The average measured R_h and associated uncertainty for Samples 1 and 2 separated with protocols *A*-*K*, P_{o1}, P_{o2}, and P_{max} for n = 3 are given in Appendix 2.3 and shown relative to protocol selection in **Figure 2.4**.

The calculated average R_h of the polystyrene mixtures was (21.7 nm ± 1.0 nm) for Sample 1, and (23.6 nm ± 1.5) nm for Sample 2, based on the known particle size distribution and individual mean particle sizes for each polystyrene bead in the mixture as determined by light scattering. The calculations are provided in the Appendix 2.4. While separation expertise might suggest that the optimal parameters lies after the midpoint of increasing retention strength and could have been used as a more efficient initial starting point for either design or analysis, we chose to begin at low retention in order to better demonstrate the trend towards a minimum average measured size.

It is expected that the average measured size for Sample 1 is lower than that of the Sample 2, as the majority of QELS signal intensity in Sample 2 is of very low intensity compared to signal from large particles. The signal from the low amount of scatter attributed to the smaller particle sizes in Sample 2 might be too low to be distinguished from the larger particles and, therefore, the measured average size will be larger than the actual average size.

2.3.3 Separations of Polydisperse Mixtures

In the case of polydisperse samples with characteristics similar to Sample 2, it may not be possible to detect the smallest sizes within the constraints of the instrument; either due to detection limits from low scattering intensity of small particles, or further increases in retention time causes dispersive mechanisms to reduce the separation efficiency. In contrast, Sample 1 contains a relatively large amount

of small particles compared to large particles (approximately 98% of polystyrene mass concentration contains particles between ~20 nm and ~40 nm in diameter, whereas the remaining 2% of polystyrene mass concentration contains particles between ~60 nm and ~100 nm in diameter), thus, there is more scattering signal from the smaller particles relative to larger particles. In a complex mixture, achieving baseline resolution between particle species is unlikely. By minimizing the measured size, however, the ability to find the separation protocol that yields the best possible measurement is possible, considering the polydisperse sample distribution and the instrument operational limits. These observations are demonstrated in the representative fractograms and hydrodynamic radius distribution overlays, given in Figure 2.5, for Samples 1 and 2 using separation protocols *A*, *H*, and P_{max}.

While this paper identifies a local optimum protocol based on discrete data, the more rigorous approach would be to identify a global optimum based on a continuous surface design of measured particle size against separation parameters along a continuum of settings. The cost of global optimization would require significantly more data.

The point of optimal separation identified by statistically significant decreases in measured size may not in fact be the point of the very best separation. However, increasing retention time will not likely produce a statistically smaller average size than the protocol with shorter retention time, as demonstrated with Samples 1 and 2 beyond the local minimum of Protocol *H*, and will require an increase in analysis time with minimal improvement in separation. Furthermore, higher retention may also increase the average measured size as dispersive effects compromise the benefits of increased selectivity.

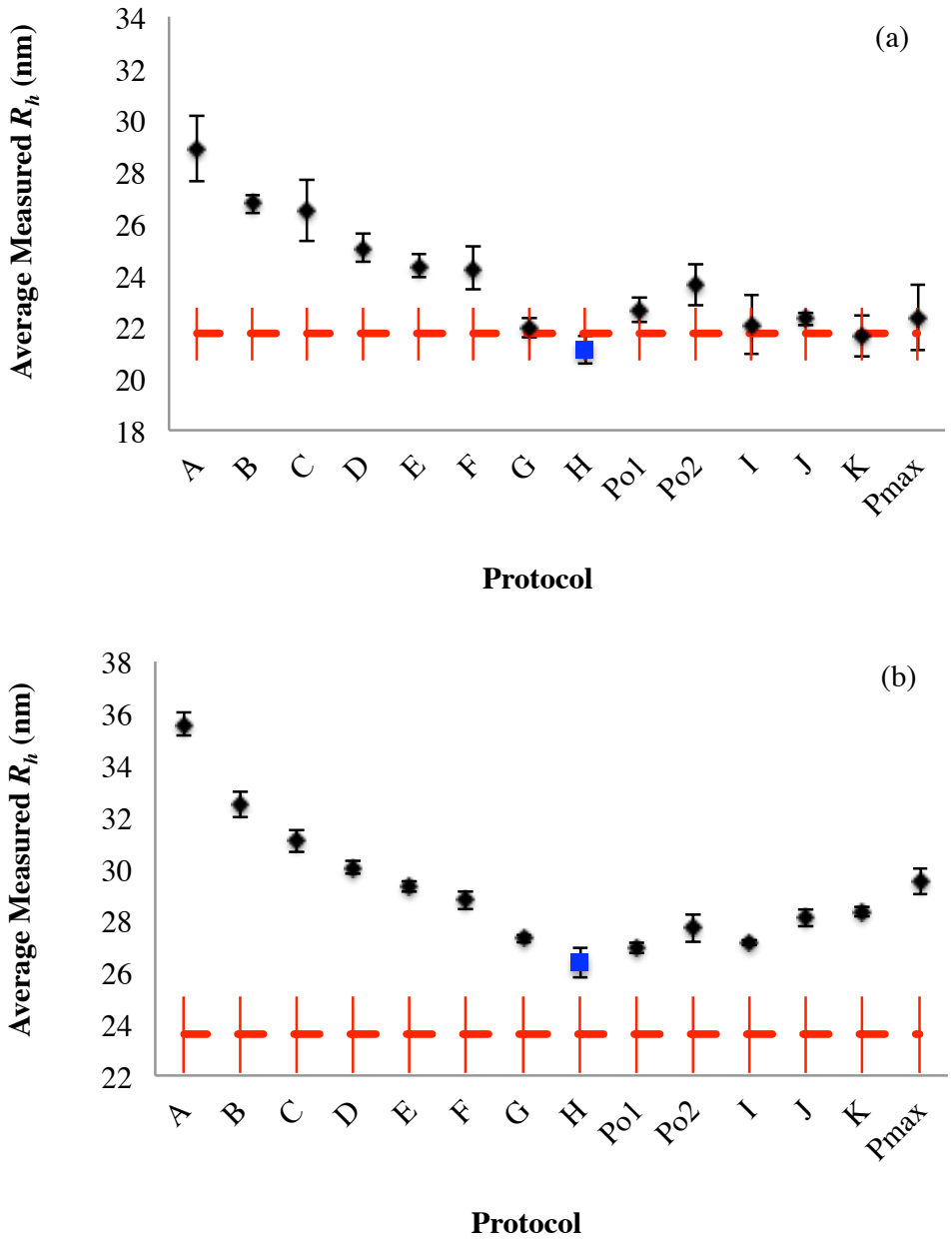

Figure 2.3. The combined average measured R_h (u) and associated uncertainty from (a) Sample 1 (b) Sample 2 with protocols *A*-*K*, P_{o1}, P_{o2}, and P_{max} for n = 3 using AF^4-QELS. The optimal protocol is "*H*" (n), where R_h is minimized. The calculated average R_h and associated uncertainty based on the actual size distribution for each sample are given as the dashed line. All uncertainties are defined at the 95% confidence interval. R_h = Hydrodynamic Radius (nm).

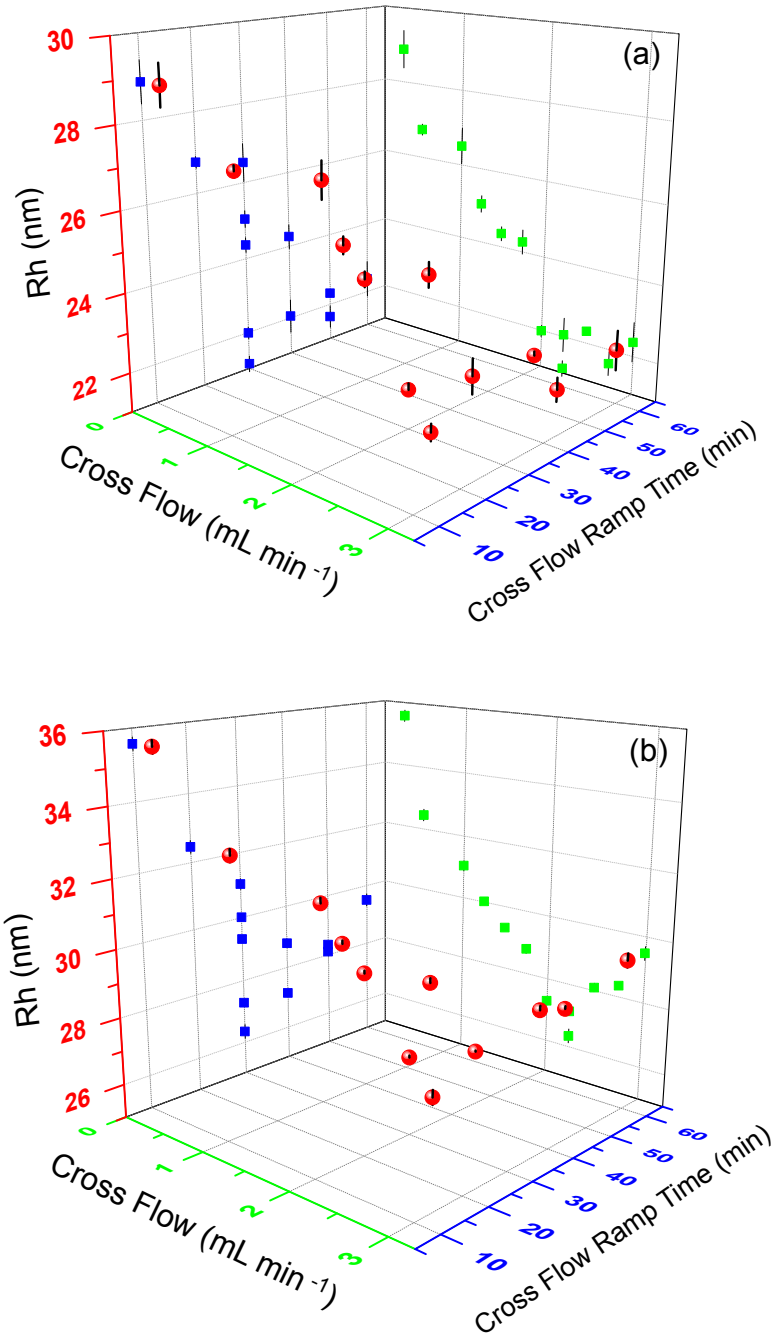

Figure 2.4. The average measured R_h and associated uncertainty for (*a*) Sample 1 and (*b*) Sample 2 separated with selected protocols, shown as initial cross flow vs. ramp time, for $n = 3$. R_h = Hydrodynamic Radius (nm).

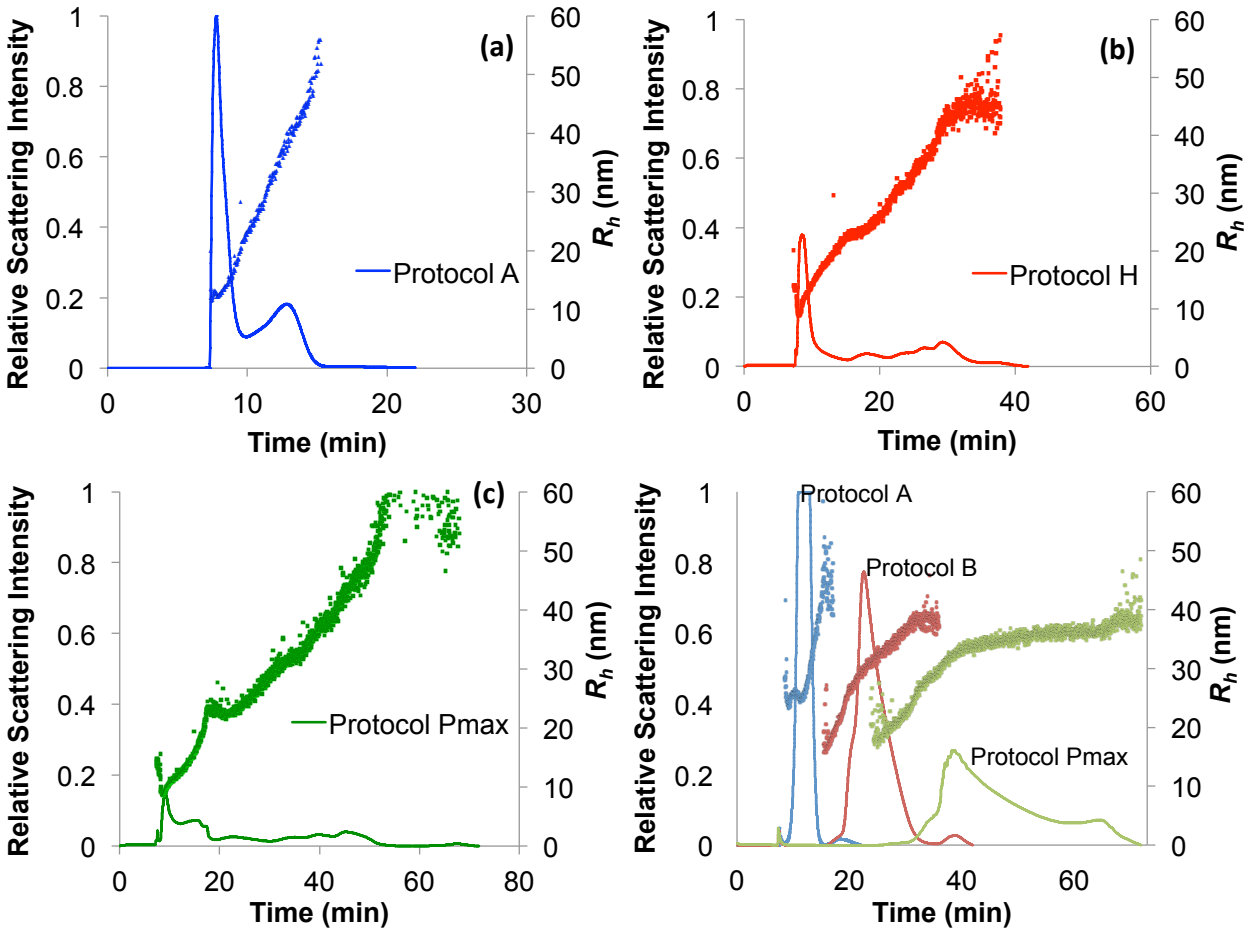

Figure 2.5. Representative fractograms from Sample 1 using separation protocol (a) *A*, (b) *H*, and (c) P_{max}. Fractograms from Sample 2 are also shown (d). Sample 2, Protocol A resulted in detector saturation. The solid line represents the relative light scattering signal intensity and the markers indicate the measured hydrodynamic radius (nm) at each time slice.

Optimization depends on the relative priority of retention time and separation selectivity. Depending on the sample properties and the intended application, a separation protocol can be selected that balances analysis time and separation resolution. The separation variables, V_x and ramp time, were chosen to linearly populate the domain of particle retention from the protocol of lowest retention (*A*) to one of highest retention (P_{max}), as shown in **Figure 2.2**. Simple separation theory predicts that the average measured size will decrease to an asymptote; beyond a certain separation, additional retention increases

do not yield a significant decrease in measured size. In reality, however, the average measured size will typically reach a minimum and then (with higher retention) likely increase due to dispersive effects.

2.3.4 Method Application

There are several options for the sequential choice of protocols. For a stepwise approach without making assumptions based on sample distribution, a protocol should be initially chosen with minimum retention, while the subsequent protocols of increasing retention should be selected so that the average measured size decreases significantly before reaching a minimum. Again, in situations where separation theory and experience are not sufficient for qualitatively determining the separation quality of complex, polydisperse mixtures, more objective and rigorous approaches should be applied. In most cases, a gradient method can be applied to best identify a local minimum within the experimental space, by analyzing protocols orthogonal to those identified as optimal in the direction of steepest descent [23, 24], *e.g.,* P_{o1} and P_{o2} for protocol *H* in **Figure 2.2**. The larger design issue in regard to choosing the number of parameters to investigate balanced with practical constraints of how many sample runs are affordable is the subject of further study. The next step is to perform a formal response surface optimization analysis, a methodology to explore the relationships between several independent variables and one or more response variable [25]. A response surface design would provide a more statistically rigorous way of identifying globally optimal parameters that yield the minimum average measured size, especially for the cases where the optimal set of parameters might not lie directly on the linear path between a set of parameters with very low retention and P_{max}.

REFERENCES

1. Messaud, F.A.; Sanderson, R.D.; Runyon, J.R.; Otte, T.; Pasch, H.; Williams, S.K.R. An overview on field-flow fractionation techniques and their applications in the separation and characterization of polymers. *Prog. Polym. Sci.* **2009,** *34,* 351-368.

2. von der Kammer, F.; Legros, S.; Hofmann, T.; Larsen, E.H.; Loeschner, K. Separation and characterization of nanoparticles in complex food and environmental samples by field-flow fractionation. *TrAC-Trends Anal. Chem.* **2011,** *30,* 425-436.

3. Baalousha, M.; Stolpe, B.; Lead, J.R. Flow field-flow fractionation for the analysis and characterization of natural colloids and manufactured nanoparticles in environmental systems: A critical review. *J. Chromatogr. A* **2011,** *1218,* 4078-4103.

4. Lattuada, M.; Olivo, C.; Gauer, C.; Storti, G.; Morbidelli, M. Application of asymmetric flow-field flow fractionation to the characterization of colloidal dispersions undergoing aggregation. *Langmuir* **2010,** *26,* 7062-7071.

5. Bednar, A.J.; Poda, A.R.; Mitrano, D.M.; Kennedy, A.J.; Gray, E.P.; Ranville, J.F.; Hayes, C.A.; Crocker, F.H.; Steevens, J.A. Comparison of on-line detectors for field flow fractionation analysis of nanomaterials. *Talanta* **2013,** *104,* 140-148.

6. Sermsri, W.; Jarujamrus, P.; Shiowatana, J.; Siripinyanond, A. Flow field-flow fractionation: a versatile approach for size characterization of alpha-tocopherol-induced enlargement of gold nanoparticles. *Anal. Bioanal. Chem.* **2010,** *396,* 3079-3085.

7. Gigault, J.; Pettibone, J.M.; Schmitt, C.; Hackley, V.A. Rational strategy for characterization of nanoscale particles by asymmetric- flow field flow fractionation: A tutorial. *Anal. Chim. Acta* **2014,** *809,* 9-24.

8. Bolea, E.; Jimenez-Lamana, J.; Laborda, F.; Castillo, J.R. Size characterization and quantification of silver nanoparticles by asymmetric flow field-flow fractionation coupled with inductively coupled plasma mass spectrometry. *Anal. Bioanal. Chem.* **2011,** *401,* 2723-2732.

9. Hawe, A.; Romeijn, S.; Filipe, V.; Jiskoot, W. Asymmetrical flow field-flow fractionation method for the analysis of submicron protein aggregates. *J. Pharm. Sci.* **2012,** *101,* 4129-4139.

10. Thang, N.; Geckeis, H.; Kim, J.; Beck, H. Application of the flow field flow fractionation (FFFF) to the characterization of aquatic humic colloids: evaluation and optimization of the method. *Colloid Surf. A-Physicochem. Eng. Asp.* **2001,** *181,* 289-301.

11. Hupfeld, S.; Ausbacher, D.; Brandl, M. Asymmetric flow field-flow fractionation of liposomes: optimization of fractionation variables. *J. Sep. Sci.* **2009,** *32,* 1465-1470.

12. Loeschner, K.; Navratilova, J.; Legros, S.; Wagner, S.; Grombe, R.; Snell, J.; von der Kammer, F.; Larsen, E.H. Optimization and evaluation of asymmetric flow field-flow fractionation of silver nanoparticles. *J. Chromatogr. A* **2013,** *1272,* 116-125.

13. Lyven, B.; Hassellov, M.; Haraldsson, C.; Turner, D. Optimisation of on-channel preconcentration in flow field-flow fractionation for the determination of size distributions of low molecular weight colloidal material in natural waters. *Anal. Chim. Acta* **1997,** *357,* 187-196.

14. Kammer, F.; Baborowski, M.; Friese, K. Field-flow fractionation coupled to multi-angle laser light scattering detectors: Applicability and analytical benefits for the analysis of environmental colloids. *Anal. Chim. Acta* **2005,** *552,* 166-174.

15. Wyatt, P.J. Submicrometer Particle sizing by multiangle light scattering following fractionation. *J. Colloid Interface Sci.* **1998,** *197,* 9-20.

16. Wyatt, P.J. Light scattering and the absolute characterization of macromolecules. *Anal. Chim. Acta* **1993,** *272,* 1-40.

17. Fabelinskiĭ, I.L. *Molecular Scattering of Light.* Plenum Press: New York, 1968.

18. Popovici, S.; Kok, W.; Schoenmakers, P. Band broadening in size-exclusion chromatography of polydisperse samples. *J. Chromatogr. A* **2004,** *1060,* 237-252.

19. Filella, M.; Zhang, J.; Newman, M.E.; Buffle, J. Analytical applications of photon correlation spectroscopy for size distribution measurements of natural colloidal suspensions: capabilities and limitations. *Colloids Surf. A- Physicochem. Eng. Aspects* **1997,** *120,* 27-46.

20. Giddings, J. Field-flow fractionation - Analysis of macromolecular, colloidal, and particulate materials. *Science* **1993,** *260,* 1456-1465.

21. Otte, T.; Bruell, R.; Macko, T.; Pasch, H.; Klein, T. Optimisation of ambient and high temperature asymmetric flow field-flow fractionation with dual/multi-angle light scattering and infrared/refractive index detection. *J. Chromatogr. A* **2010,** *1217,* 722-730.

22. Makan, A.C.; Otte, T.; Pasch, H. Analysis of high molar mass branched polybutadienes by SEC-MALLS and AF4-MALLS. *Macromolecules* **2012,** *45,* 5247-5259.

23. Bortz, D.M. and Kelley, C.T. The simplex gradient and noisy optimization problems, In *Computational Methods for Optimal Design and Control,* 24th ed.; Borggaard, J., Burns, J., Cliff, E. and Schreck, S., Eds.; Birkhauser Boston: Cambridge, MA, 1998; Vol.24 pp. 77.

24. Snyman, J. *Practical Mathematical Optimization: An Introduction to Basic Optimization Theory and Classical and New Gradient-Based Algorithm**s**.* Springer Science + Business Media, Inc: New York, NY, 2005.

25. Box, G.E.P.; Hunter, W.G.; Hunter, J.S. *Statistics for Experimenters: An Introduction to Design, Data Analysis and Model Building*. Wiley: New York, 1978.

CHAPTER 3: ASYMMETRIC FLOW FIELD FLOW FRACTIONATION OF COMPLEX AQUATIC MATRICES CONTAINING SILVER NANOPARTICLES - A SENSITIVITY ANALYSIS USING ORTHOGONAL FACTORIAL EXPERIMENT DESIGN

3.1 Introduction

With the increased use of engineered nanoparticles (ENPs) in industrial processes and consumer products, the International Council of Nanotechnology has identified the development of robust analytical characterization methods to investigate the occurrence and fate of ENPs in the environment as one of their highest priority goals for the ecoresponsible use of nanomaterials [1]. These methods have been difficult to achieve as they require a combination of analytical techniques in order to characterize their behavior in complex environmental matrices [2, 3]. Field flow fractionation and specifically, asymmetric flow field flow fractionation (AF^4), has become one of the most favored and common methods for separating ENPs in complex matrices prior to various online detection methods, such as inductively coupled plasma – mass spectrometry (ICP-MS) or UV-Visible spectrophotometry (UV-Vis). However, there appears to be no comprehensive understanding of the relationship between various environmental factors and how they affect the ability of AF^4 to separate ENPs in natural systems prior to further characterization.

AF^4 is a chromatography-like technique that does not require the use of a stationary phase but instead relies on hydrodynamic principles to separate a wide range of particles by diffusion in an open channel. AF^4 has been described elsewhere in detail [4-7], but briefly, it can be used to separate complex samples that may damage, or be damaged by, typical chromatography columns [8, 9]. Colloids, macromolecules, and particles are separated due to their interaction with a cross flow of run buffer applied perpendicularly to the longitudinal laminar flow within a separation channel. The upper housing, forming the top of the separation channel, is impermeable while the bottom of the channel consists of an ultrafiltration membrane. The laminar flow in the channel creates a parabolic flow profile, with lower flow velocities near the channel walls than in the center. With the application of a cross flow perpendicular to the laminar channel flow, the average particle position will shift towards the membrane. Diffusion (or

Brownian motion) presents a counteracting force to the applied cross flow. Smaller particles, with higher diffusion rates, tend to equilibrate over a greater height of the channel and sample a larger portion of the longitudinal flow profile resulting in a higher average velocity. In contrast, larger particles, with lower diffusion rates, tend to equilibrate towards the accumulation wall where the longitudinal flow is slower. Smaller particles are therefore transported along the channel faster than larger particles. **Figure 3.1** presents a schematic of a typical AF^4 separation.

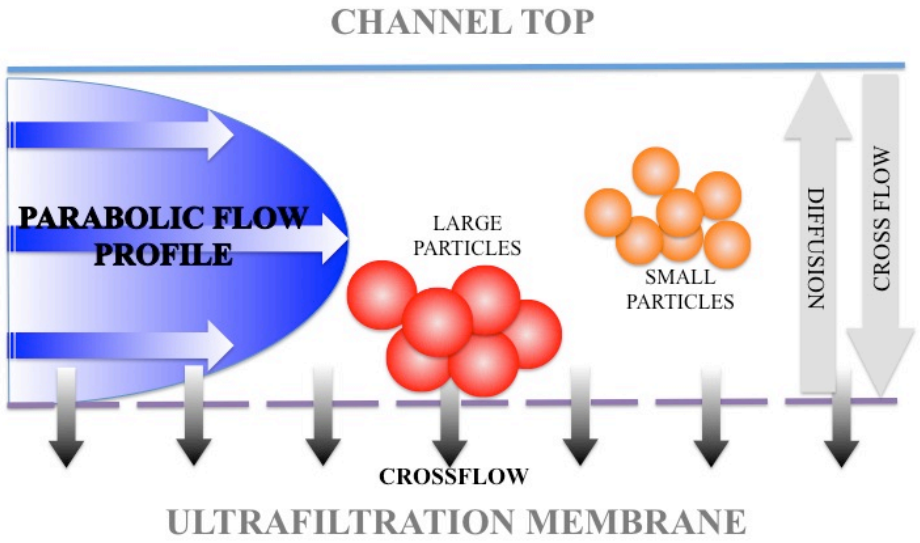

Figure 3.1. Schematic showing large and small particles being separated in an AF^4 channel by hydrodynamic forces.

AF^4 is compatible with a wide range of matrix compositions and is capable of rapid on-line pre-concentration, which is particularly useful for highly complex matrices containing analytes of low concentration, including ENPs, in environmental samples [10-12]. Finally, AF^4 can be directly interfaced with a wide variety of standard chromatography detectors, such as light scattering (LS) for particle sizing and molar mass (MM) measurements [10].

Little is known about the separation of particles suspended in complex, non-reproducible matrices containing a continuum of similar species that differ from each other by an infinitesimal amount, such as in environmental samples. Natural organic matter (NOM) is a particularly complex environmental material containing supramolecular assemblies of a wide range of molecular weights and chemical properties [13].

It is generally categorized as particulate or dissolved organic matter, with the latter defined as passing through a 0.45 μm filter [14]. NOM experiences changes in structure, MM, and aggregation with varying aquatic chemistry and water quality characteristics [13], and smaller components can form aggregated clusters by hydrogen bonds, hydrophobic interactions, cation bridges, and dipole-dipole interactions [13, 15-18]. The chemistry and character of an environmental matrix including particles, as well as type and concentration of NOM, directly control potential NOM-ENP behavior if they co-occur in the environment. While the most significant NOM-ENP interaction is adsorption of dissolved NOM to the particle surface, cation bridging and other flocculation mechanisms can induce ENP aggregation into NOM-ENP complexes [19]. Louie and coworkers investigated how different MM components of NOM interact with metal or metal oxide ENPs. They concluded that higher MM fractions, primarily comprised of >100,000 g mol^{-1} humic acid aggregates, disproportionately dominated aggregation behavior of sample components compared to lower MM fractions that tend to enhance ENP stability. Therefore, small differences in NOM molecular weight distribution can alter ENP aggregation and potential fate in the aquatic environment [13].

It is important to consider that a major difficulty in comparing or combining conclusions of ENP interactions in the environment is the lack of standardization. Therefore, any optimization conclusions directly depend on the instrument as well as the sample characteristics, all of which vary between laboratories and their methodologies. Further, it is very important that the technique itself does not impart changes to the sample. The optimization of AF^4 separation parameters based on instrument theory and fractogram observation has been extensively studied [20-27]. However, a significant challenge to using optimization schemes for developing methods for separating ENPs in complex natural systems is the limited understanding of the relationship between various primary/instrumental and robustness/environmental factors and how they affect the ability of AF^4 to separate nanoparticles.

Complex samples such as natural waters, yield fractograms that are less defined and contain a higher level of variability [5, 28-30] when compared to the separations of mixtures of monodisperse or distinct particle sizes. This difficulty in interpretation constitutes an obstacle to investigating ENP fate and transport with respect to the complexity of environmental samples. Loeschner and co-workers [25] recently identified that run buffer composition, membrane type, cross flow rates, and channel spacer thickness all significantly influenced nanoparticle recoveries and retention times in simple aqueous

suspensions. To our knowledge, there have been no attempts to explore the relationship between factors and AF^4 separation of natural waters.

In order to address this knowledge gap, this work investigates AF^4 optimization by applying statistical design of experiment (DEX) in concert with appropriate exploratory data analysis (EDA). This approach aims to better understand how the AF^4 separation output is affected by changing input, specifically AF^4 instrument parameters. Compared to trial-and-error method development, DEX is a cost-effective and systematic approach to system optimization, using both instrument knowledge and experimental data to determine the effects of multiple factors and factor interactions on a given response. In the past, Kuklenyik and co-workers [31] used multivariate DEX to optimize AF^4 instrumental parameters for maximum channel recovery and size resolution of lipoproteins in human serum. Racamonde and co-workers [32] demonstrated the applicability of sensitivity DEX analysis for environmental samples by using a mixed factorial design to identify significant parameters affecting the fabric phase sorptive extraction of pollutants in natural water samples.

With the correct design, factorial dependencies of the AF^4 system can be rigorously determined; the subsequent conclusions can be robustly validated, while simultaneously minimizing analysis time [33, 34]. In particular, sensitivity analysis involves varying input parameter settings and assessing the subsequent changes in selected response variables in order to identify which input parameters have the most significant influence on response behavior [35]. The primary sensitivity analysis results in a ranked list of factors (and interactions), based on a least-squares-based estimation of their effects [34].

The target response, or output, for this study is defined by minimizing the average MM of NOM following AF^4 separation. The MM is measured inline by multi-angle light scattering (MALS) and UV detection [36]. Other examples of AF^4 system outputs are analyte recoveries or retention times [25]. In the case of environmentally relevant concentrations of ENPs, it is unlikely that they would be present above the detection limits for MALS and UV-Vis. However, since ENPs have been shown to interact with NOM in environmental samples [13, 19], this work assumes that adequately separating NOM will also result in effective separation of any ENPs present, though additional detectors suitable for characterizing ENPs would be required for future quantitative studies. Using this sensitivity analysis approach, the AF^4 system will be better understood, with respect to environmental sample characteristics, and the ranked

importance and robustness of separation parameters can be identified. Rather than applying directly to a specific environmental sample such as surface water, the use of a controlled synthetic matrix that simulates such a water allows for evaluating a wide range of water characteristics. Similarly, silver nanoparticles (AgNPs) were selected as a water sample characteristic to ensure that the methodology developed might be applicable for use in occurrence and quantification studies of ENPs in natural waters. AgNPs are an environmentally relevant target ENP because silver is the most abundantly incorporated material in consumer products containing ENPs [37] and AgNPs have at least one transformation product with observed persistence in natural waters [38, 39]. Hence, an orthogonal fractional factorial design is applied toward the sensitivity analysis of AF^4 separations of synthetic, environmentally relevant mixtures containing AgNPs to explore which primary/instrumental factors and interactions have the greatest effect on separation. To broaden the scope of the instrumental factor conclusions, a parallel analysis of both primary/instrumental and robustness/environmental factors is explored. This is the first application of orthogonal fractional factorial design and sensitivity analysis to AF^4 separations of complex environmental samples.

3.2 Experimental Methods

AF^4 separation was performed using a Wyatt Technologies Corp. (Santa Barbara, CA) Eclipse DualTec module whose separation protocol settings were controlled with OpenLab CDS Chem Station edition software (Agilent Technologies, Santa Clara, CA). Separation was performed using a Wyatt Technologies short channel containing a Wyatt Technologies regenerated cellulose membrane with a 10 kDa cutoff, an injector flow of 0.2 mL min^{-1}, and a detector flow of 1 mL min^{-1}. Sample injections were made with an Agilent (Santa Clara, CA) 1260 Infinity series isopump and autosampler. The AF^4 run buffer was prepared by dissolving ammonium nitrate (ACS Reagent ≥ 98%, Sigma-Aldrich, St. Louis, MO) in laboratory-grade 18.2 MΩ·cm water (LGW) with 0.01% sodium azide (Ricca Chemical Company, Arlington, TX) as an antimicrobial. Run buffer used for all experiments at target concentrations, was degassed with a Gastorr TG-14 unit at 100 hPa directly from solvent bottles, and then filtered first by a polytetrafluoroethylene frit (RESTEK Corp., Bellefontane, PA) and then a 0.1 μm Durapore membrane filter (Millipore Inc., Billerica, MA). Focus flow and cross flow were varied based on experimental

parameters. Bovine serum albumin (Fraction V, Sigma-Aldrich, St. Louis, MO) at 1 mg mL^{-1} was used as an internal standard reference to assess instrument drift and to calibrate the MALS detector. Water samples were analyzed from 1.5 mL amber glass autosampler vials with PTFE/silicone septa caps (Chemglass Life Sciences, Vineland, NJ) that were rinsed with LGW before use. Samples were analyzed immediately by AF^4-MALS-UV and randomized to compensate for run order wait time.

To assess the quality of a given separation relative to another, average MM of the NOM sample distribution was calculated for each separation protocol using standard online MALS techniques [40] . The differential refractive index of NOM was estimated to be 0.151 dn dc^{-1}, based on measurements for NOM in phosphate buffers from the literature [41, 42]. UV absorbance measurements were made at 254 nm (hereafter referred to as UV_{254}), a wavelength specific to NOM with no interference from AgNPs using an online Agilent 1260 Infinity diode array detector (model # LV G1315D) following AF^4-MALS. MALS and UV data were collected and analyzed with ASTRA™ Software version 6.1.1.17, and MALS data were also plotted with a Debye formalism and fit with a 2nd order polynomial. ASTRA™ Software calculates the weight average MM (MM_w) by relating excess scattering intensity to the NOM concentration from UV absorbance measurements using the Rayleigh-Debye-Gans light scattering model [43]:

$$\frac{K^* c}{R(\theta)} = \frac{1}{MM_w P(\theta)} + 2A_2 c \tag{3.1}$$

where K* is an optical parameter defined as:

$$K^* = 4\pi^2 n^2 (dn/dc)^2 / N_A \lambda_o^4 \tag{3.2}$$

R(θ) is the excess scattered light intensity at detector angle, θ; c is the sample concentration as determined by UV; MM_w is the weight-average MM; A_2 is the second virial coefficient; n is the solvent refractive index and dn dc^{-1} is the refractive index increment; N_A is Avogadro's number; and λ_o is the wavelength of scattering light in vacuum. The function P(θ) describes the angular dependence of scattered light.

Specific conductance measurements were made with a Wyatt Technologies Möbiuς using Dynamics Software version 7.2.4. EDA plots were generated with the NIST-developed analysis software, DATAPLOT [44]. The factors chosen for this sensitivity analysis are listed in **Table 3.1**.

Table 3.1 Chosen primary/instrumental factors, robustness/environmental factors, and their respective settings. [NP] and [NOM] refers to nanoparticle and NOM concentration, respectively. mg C L^{-1} refers to mg carbon per liter, as estimated by UV_{254} absorbance.

Primary/Instrumental Factors

Abbreviation	Factor	Low (-)	Midpoint	High (+)	(units)
X1	Cross Flow	0.5	1.5	2.5	mL min^{-1}
X2	Ramp	20	30	40	min
X3	Focus	1	2	3	min
X4	Injection volume	200	350	500	µL
X5	Buffer	0.1	1	5	mM NH_4NO_3

Robustness/Environmental Factors

Abbreviation	Factor	Low (-)	Midpoint	High (+)	(units)
R1	[NP]	3	50	100	µg L^{-1}
R2	[NOM]	1	5	10	mg C L^{-1}
R3	Ionic Strength	1029	2992	4781	µeq L^{-1}
R4	pH	6	7	8	
R5	NP Size	10	50	100	nm

Water samples, as well as their DEX factors and levels, were designed according to U.S. average freshwater measurements [45] as a guide for matrix composition. For example, the conductivities of Little Rock Lake, Vilas, CO., Harriet Lake, Minneapolis, MN., and Colorado River, AZ. were used as the basis for low (0.22 mS cm^{-1}), medium (0.40 mS cm^{-1}), and high (0.59 mS cm^{-1}) ionic strength waters,

respectively [45]. Hence, waters of corresponding character were prepared in LGW at concentrations of 1029 μeq L^{-1}, 2992 μeq L^{-1}, and 4781 μeq L^{-1}, respectively, from a combination of $MgSO_4*7H_20$, $NaHCO_3$, $KHCO_3$, $MgCl_2$, $CaCl_2$, $CaCO_3$, and NaCl (all analytical grade; Sigma-Aldrich, St. Louis, MO), as described in Appendix 2.1. These solutions were allowed to equilibrate for 24 hours before adding a Suwannee River NOM (International Humics Substances Society, St. Paul, MN, USA) solution, dissolved into LGW and allowed to equilibrate for 24 hours, which was pH-adjusted to 6, 7, or 8 by HCl (1 N, Sigma Life Sciences, St. Louis, MO) or NaOH (1 M, Fluka Analytical, St. Louis, MO) according to sample requirements. Organic carbon in NOM stock solutions was quantified as dissolved organic carbon (DOC) concentration [46] after filtration through 0.45 μm pore size nylon membranes (EMD Millipore, Billerica, MA). UV_{254} absorbance measurements (Nanodrop, Thermo Scientific, Wilmington, DE) were then used to estimate NOM concentration for sample preparation from a calibration of absorbance versus NOM concentration in a series of diluted NOM solutions. This estimate was not used for MM calculations. NanoXact™ citrate-stabilized AgNPs were diluted from a manufacturer supplied 0.02 mg mL^{-1} stock in 2 mM sodium citrate solution (Nanocomposix, San Diego, CA) and were introduced to each sample 1-12 hours prior to AF^4 separation, depending on sample analysis randomization. Stock AgNP stability was monitored with UV-vis spectrophotometry at 400 nm. AgNP size range was confirmed by quasi electric light scattering (QELS) with a WyattQELS™ detector at a nominal angle of 140°, and was in good agreement with those reported by the manufacturer [47]. All salt stock solutions and NOM samples were stored in the dark at 4°C prior to analysis and held no longer than one week or 48 hours, respectively.

3.3 Experimental Design Methodology

Statistical design of experiment (DEX) methodology is a rigorous problem-solving approach to gain detailed insight on the characteristics of a complex and unknown response surface of a given system containing a number of defined factors *k*. With the correct design, factorial dependencies of this system can be rigorously determined; the subsequent conclusions can be robustly validated, while simultaneously minimizing analysis [33, 34]. In particular, sensitivity analysis involves varying input parameter settings and assessing the subsequent changes in selected response variables in order to identify which input parameters have the most significant influence on response behavior [35]. The

primary sensitivity analysis results in a ranked list of factors (and interactions), based on a least-squares-based estimation of their effects [33].

There are many primary/instrumental and robustness/environmental factors that can affect AF^4 system output, NOM, and MM each with varying degrees of importance along a continuum of settings, depending on optimization goals [21-27, 48]. Instrumental factors represent instrument settings that can be "dialed" up or down depending on the separation protocol, such as AF^4 cross flow or injection volume. Environmental factors refer to water quality characteristics, variables that are defined when a natural water sample is collected such as pH or NOM concentration. The number of factors, *k*, and the reasonable/affordable number of sample runs, *n*, are the key pair of values that quantitatively describe a chosen experimental design. Some designs, even with the same *k* and *n*, are statistically superior to others. The class of fractional designs defined as "orthogonal", balanced in every factor and every pair of factors, have known superior qualities in that they adequately sample the *k* dimensions, reduce the bias in the factor estimates, and reduce the variation in the effect estimates [49]. For this current work, appropriate (and affordable) orthogonal designs were chosen for both the examination of the effect of the primary/instrumental factors and simultaneously for the examination of the robustness/environmental factors.

Beyond the general characteristics of the formal experimental plan, there are many obstacles to executing a large experimental sample set. These include, but are not limited to, hardware or software malfunctions, human error in sample preparation or sample run execution, unexpected or anomalous data, and statistical analysis challenges. With these considerations, and acknowledging the inclusion of blank and reference samples, it was determined that approximately 400 hours of AF^4 instrument time was needed as the affordable practical upper time limit for this specific DEX.

Given this $n \approx 400$ background constraint, a subset of potential factors was identified and selected. To achieve the desired broad scientific scope for our yet-to-be-computed conclusions, the constructed experimental design consisted of $k = 5$ primary/instrument factors to be examined and optimized. In addition, $k = 5$ robustness/environmental factors were identified, based on a combination of non-statistical preliminary experiments and prior instrumental expertise which indicated that some factors may cause a more significant change in system output than others.

It should be noted that even a full factorial two-level design to test every combination of these factors and settings (a $2^5 \times 2^5$ design) would be experimentally prohibitive—resulting in $n = 1024$ runs, far exceeding the affordable 400-hour upper limit for the experimental effort. Therefore, a two-level orthogonal fractional factorial design was identified as a highly efficient and robust alternative. Specifically, a $2^{5-1} \times -2^{5-2}$ orthogonal fractional factorial design was chosen; that is, the chosen 5 primary/instrumental factors were examined in $n = 2^{5-1} = 16$ runs, while the chosen 5 robustness/environmental factors were examined in $n = 2^{5-2} = 8$ runs. Note that the use of orthogonal fractional factorial designs—especially 2-level orthogonal fractional factorial designs—is efficient, and must be constructed with caution. The "price to be paid" for fractional factorial designs, or any design with fewer runs than *k*-factor full factorial design, is that confounding will necessarily exist. Confounding indicates the bias that occurs when the value of a main effect estimate might result from both the main effect itself and higher order interactions. For a given *k* and *n*, the goal is to construct and choose those designs which minimize such confounding.

The 2^{5-1} design chosen for the primary/instrumental factors fulfills this goal, and is a strong, "Resolution V" design. Resolution V indicates that the estimates of the $k = 5$ main factors are completely unconfounded, or uncontaminated, by any of the 15 potential 2-term interactions as well as the 10 potential 3-term interactions. Further, the 15 2-term interactions are unconfounded with one another. This design thus yields 5 + 10 = 15 unconfounded least-squares estimates of the 5 main effects and the 10 2-term interactions, all at an extremely affordable $n = 16$ experimental cost [50] .

For the 5 robustness/environmental factors, the 2^{5-1} design was deemed too expensive at 16 runs. The expected variability in the instrument was such that replication was deemed to be necessary, which would have thus increased the experimental effort to 256 x 2 = 512 runs, beyond our experimental limit of 400 runs, where each run is approximately 1 hour. For this reason, the effect of the 5 robustness/environmental factors was explored via a 2^{5-2} design. The virtue of this orthogonal design is that it is economical, but still requires caution as it has lower resolution. This design is Resolution III, meaning that the resulting estimates for the main effects will be confounded with (some pre-determinable) 2-term interactions, and some 2-term interactions will be confounded with one another. Given this confounding structure, the resulting estimates were assessed to determine the practical likelihood of the

2-term interactions in fact being real. Further, the flexibility afforded to the robustness/environmental factors was deemed to be a fair trade for the afforded replication, since the prime focus of this AF^4 study was the effect of the controllable primary/instrumental parameters, as opposed to the uncontrollable robustness/environmental factors. The goal for using an orthogonal fractional design—even a highly-fractionated one (k = 5, n = 8), was to maximize the likelihood of generating external robustness conditions that could potentially affect the primary/instrumental factors. This was achieved with the 2^{5-2} design, as it allowed for the conclusions to have a measure of robustness that would be missing via other experiment design approaches. The use of fractional orthogonal designs for both the primary instrumental factors and the robustness environmental factors was first developed by Genichi Taguchi, and was referred to as Taguchi Parameter Designs with "inner and outer arrays" [51] .

The resulting base design which jointly encompasses both the primary and robustness factors is thus a $2^{5-1} \times 2^{5-2}$ orthogonal fractional factorial design consisting of $2^4 \times 2^3$, or n =128 runs. This is well within the defined n = 400 upper limit. With extra budget, duplicate runs (a necessity) were allowed at a cost of 256 runs. Further, the 16 unique conditions for the primary/instrumental factors and the 8 unique conditions for the robustness/environmental factors could be affordable if augmented by control points to monitor instrument drift. With this in mind, the extra 2 points consisted of two center/control points within the 5 primary factor levels, and both a center point and reference within the 5 robustness factor levels, yielding,

$$2[(2^{5-1}+2)] \times (2^{5-2}+2) = n = 360 \tag{3.3}$$

where $n = 360$ falls within our prescribed upper experimental limit. **Table 3.1** summarizes the chosen factors and settings. The settings for each individual separation protocol (primary/instrumental factors) and sample (robustness/environmental factors) are given in Appendices 3.2 and 3.3, respectively.

3.4 Results

The best local factor settings as determined by statistical EDA are a direct result of the detector output and raw data. The range of factors and associated settings evaluated to arrive at these are given

in **Table 3.1**. **Figure 3.2** shows the MALS fractogram and UV_{254} response for both the best (**Figure 3.2a**) and worst (**Figure 3.2b**) factor settings, or combination of primary/instrumental and robustness/environmental factors that yields the smallest or largest MM measurements, respectively.

The main effects plot [52] in **Figure 3.3** is used to illustrate the ranked list of factors, and their best settings, in order of importance. The effects (difference in response value, mean MM) are the result of adjusting each primary/instrumental factor from low to high. Buffer concentration and cross flow are the factors considered statistically significant, since the one-way ANOVA F-test considers p-values < 5% to be significant. The ranked order of factor importance, according to decreasing effect magnitude, is buffer concentration, cross flow, focus flow, injection volume and ramp time. The Main Effects Plot is a series of *k* mean plots (associated with *k* factors), all on the same scale, so each factor can be compared for relative importance. Factor effects are determined by the difference in response value achieved when changing the factor setting from low to high.

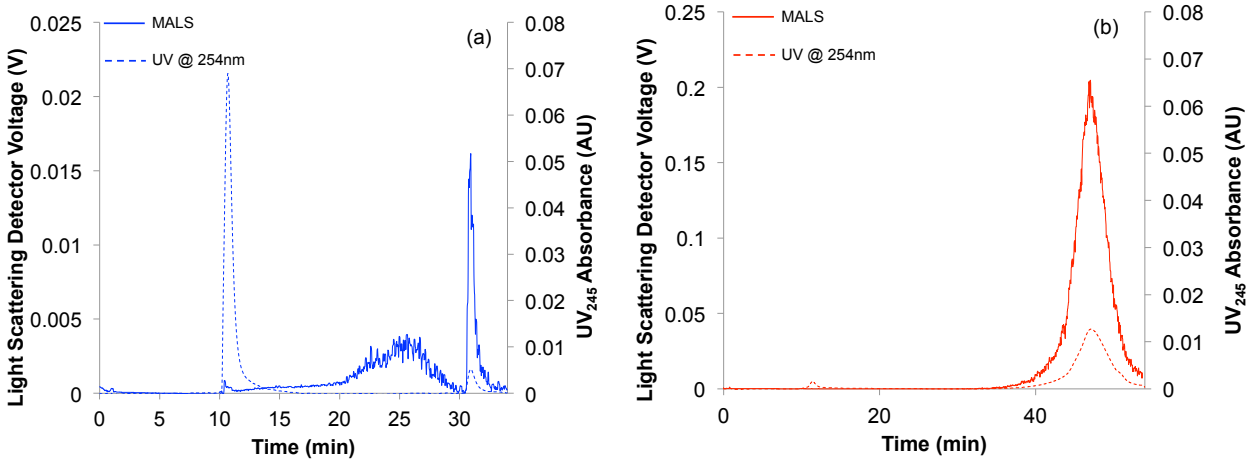

Figure 3.2. AF^4-MALS-UV fractogram representing the (a) best and (b) worst combinations of primary/instrumental and robustness/environmental factor settings.

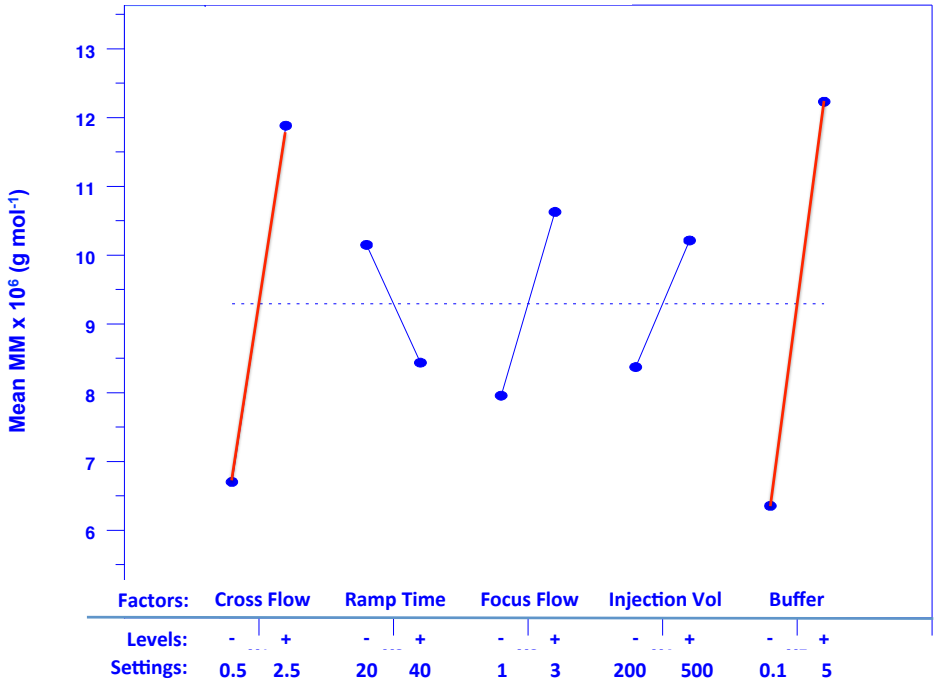

Figure 3.3. Main Effects Plot for the mean target response (MM) across all separation protocols. Significant effects, buffer and cross flow, are highlighted in red and correspond to ANOVA f-test p-values of 1.35% and 3.42%, respectively. Settings, units, and levels are detailed in 3.1. Factor units: Cross flow (mL min^{-1}), ramp time (min), focus flow (mL min^{-1}), injection volume (µL), and buffer concentration (mM NH_4NO_3).

Of the various factor design combinations considered in the design, the best settings yielding the smallest mean response (average MM across all separation protocols) are (- + - - -), where (-) represents "low" and (+) represents "high" for each of the five factors described in **Table 3.1**. This corresponds to low cross flow = 0.5 mL min^{-1}, high ramp time = 40 minutes, low focus flow = 1 mL min^{-1}, low injection volume = 200 µL, and low buffer concentration = 0.1 mM NH_4NO_3. In contrast, the worst settings are (+ - + + +), corresponding to high cross flow = 2.5 mL min^{-1}, short ramp time = 20 minutes, high focus flow = 3 mL min^{-1}, high injection volume = 500 µL, and high buffer concentration = 5 mM NH_4NO_3.

In a similar fashion, a main effects plot for the 5 robustness/environmental factors is shown in **Figure 3.4**. The Main Effects Plot using response means reveals the ranked order of factor importance as

AgNP concentration, AgNP size, NOM concentration, ionic strength, and finally, pH. No factors were identified as statistically significant after adjusting each robustness/environmental factor from low to high.

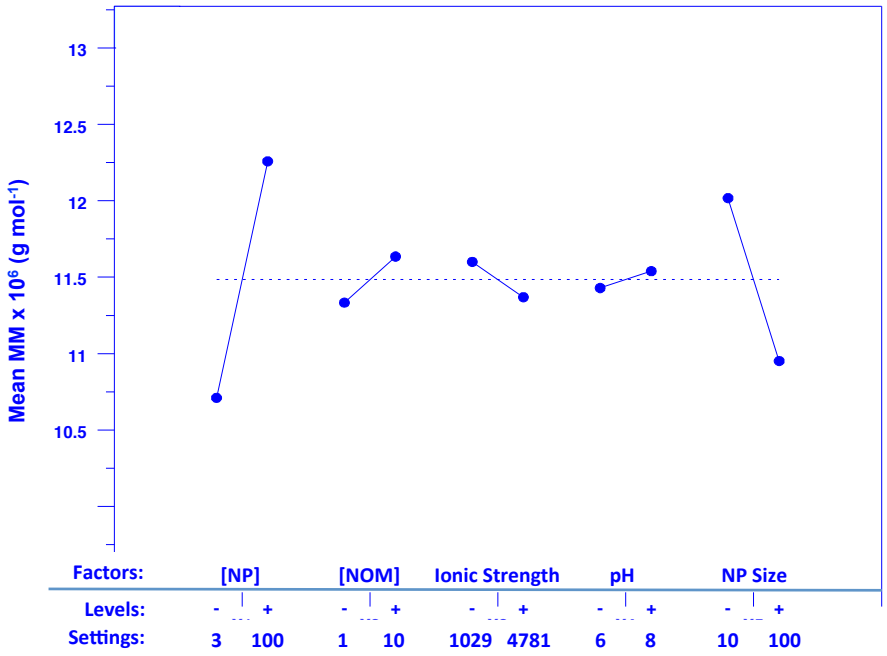

Figure 3.4. Main Effects Plot for the mean target response (MM) across all separation protocols for robustness/environmental factors. Factor units: [NP] (μg L^{-1}), [NOM] (mg C L^{-1}), ionic strength (μeq L^{-1}), and NP size (nm).

The ordered data plot [53] is used on the response data primarily to identify the best factor settings (optimization analysis) and, secondarily, the most important factor (sensitivity analysis). The nature of the ordered data plot's ascending response surface over the various factor settings is also of interest. The vertical axis contains the mean of replicated average MM measurements for *n=16* experiments, ordered from smallest to largest. The horizontal axis lists factor settings defined in **Table 3.1**. Buffer concentration (green box) and cross flow trends (red box) are highlighted as significant factors and discussed in the next section. The plot is given in **Figure 3.5** and shows that the best-observed settings are low cross flow, low ramp time, low focus flow, high injection volume, and low buffer concentration. These settings correspond to (- - - + -) respectively. The second best combination is nearly as good, or

even equivalent by observation, (- + - - -). The worst settings are (+ + + + +). The environmental/robustness factor ordered data plot is given in Appendix 3.5.

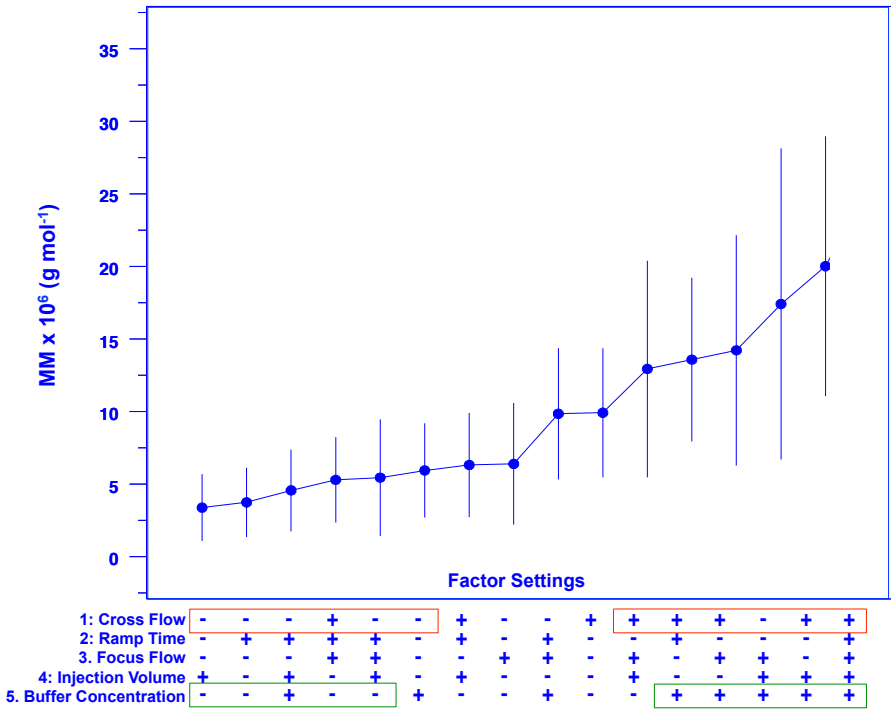

Figure 3.5. Ordered data plot of primary/instrumental factors and settings. Error bars represent the 95% confidence interval for the mean value across 8 replicated samples.

Finally, the contour plot [54] shown in **Figure 3.6** is used to explore whether the response could have been better optimized beyond the experimental input and, specifically, which settings would improve the response. The vertical axis (cross-flow) is the second most important factor, while the horizontal axis contains the most important factor, buffer concentration. The four corners represent the combinations of the two most important factors, each with an average response value (MM). The remaining factors are fixed at their best settings based on conclusions made in the main effects plots and ordered data plots for both primary/instrumental (**Figures 3.3** and **3.5**, respectively) and robustness/environmental (**Figure 3.4**) factors. Only the main effects are used in the contour plot, as they can be directly related to primary/instrumental factor settings, whereas interactions cannot be controlled.

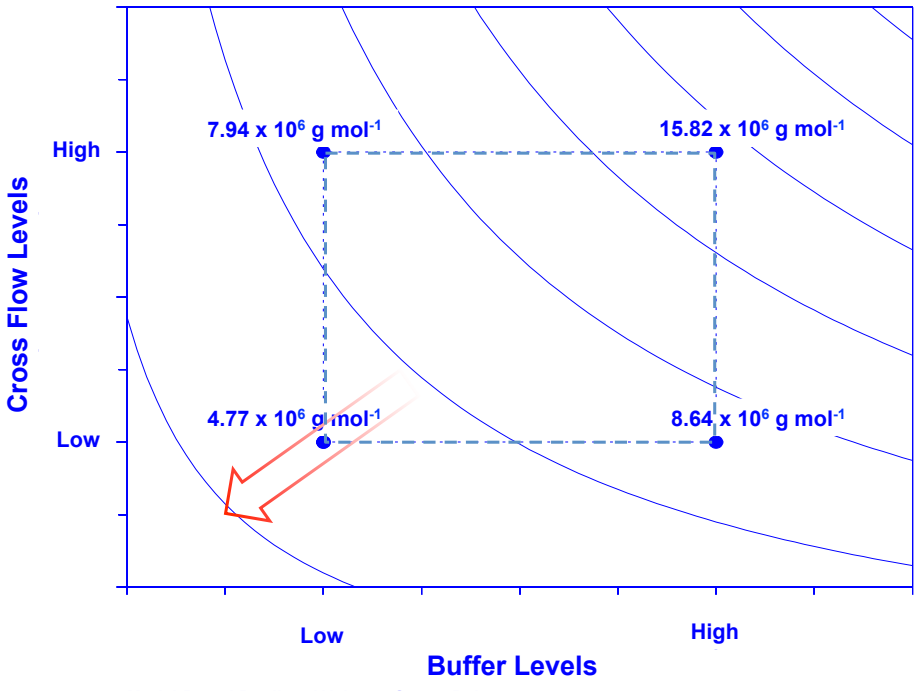

Figure 3.6. Contour Plot. The red arrow signifies the direction of steepest descent.

The contour curves produce a visual projection of the response surface and allow for the determination of the best theoretical response value [35, 55]. Improved optimal theoretical settings can be found from the interaction of the steepest descent direction with the optimal curve [54, 55], demonstrating that further optimizing the AF^4 system towards a minimized average MM would require (in this case) decreasing both the buffer concentration and the cross flow.

3.5 Discussion

While perfect separations of complex samples are likely not tenable due to matrix complexity, separation optimization will result in the most accurate analysis possible. This research analyzes relative separation improvement on the assumption that a separation protocol can be deemed better if the average range of MM measurement of NOM is smaller than that of another separation protocol. Further, the separation protocol yielding the smallest average range of MM measurements can be identified as the best among those explored. To reinforce and to illustrate the degree of confidence in the sensitivity analysis conclusions, a heavily statistical graphics approach (EDA) has been applied. The conclusions

were corroborated via a quantitative approach (e.g., ANOVA, data not shown). Further, modeling prediction and residual analysis (Appendix 3.6) were explored based on four basic data assumptions; randomness, fixed location, fixed variation, and fixed distribution.

The best AF^4 instrument settings yielded a fractogram (**Figure 3.2a**) showing the majority of organic material, as represented by UV_{254} absorbance, eluting near the beginning of the elution period as small NOM particles or aggregates. In the plot representing the worst settings (**Figure 3.2b**), most material detected by MALS and absorbing at UV_{254} is co-eluting at the end of the separation, suggesting larger material. The light scattering signal detects all particles in the sample regardless of material but it is unlikely that individual AgNPs are contributing any significant light scattering signal, as their low concentrations are difficult for MALS to detect. For investigations into AgNP fate and transport in the presence of NOM, an additional detector, such as ICP-MS, would need to be interfaced with AF^4 in order to adequately monitor AgNP elution and is the subject of Chapter 4.

The main effects plot in **Figure 3.3** identifies the ranked order of factor importance, according to decreasing effect magnitude, as buffer concentration, cross flow, focus flow, injection volume and ramp time. This conclusion differs slightly from the observations in **Figure 3.5**, which included low ramp time. However, ramp time was found to be a non-significant factor, so the difference between low and high ramp time has negligible effect on the response value, MM. The main effects plot in **Figure 3.3** takes all trends across all *k* factor settings into consideration to display the average best settings, whereas the ordered data plot in **Figure 3.5** only lists factor settings and individually ranked responses. Note (see highlighting, **Figure 3.5**) that buffer concentration and cross flow are generally low at the smaller MM end of **Figure 3.5**'s ordered data plot and generally high at the larger MM end of the plot. This reinforces that these are the two most important factors; the difference, or effect, between the low and high settings for each results in a significant change in measured MM.

The orthogonality of the underlying experimental design ensures that the main effects' estimates are identical to the least-squares effects' estimates. The identification of buffer concentration and cross flow as the two most important factors suggests that higher buffer concentrations and cross flows may contribute to or encourage sample aggregation within the robustness conditions tested, potentially reducing the confidence of subsequent sample analysis following AF^4 separation. The identification of

important factors is in good agreement with a scatter plot analysis (Appendix 3.7), which is used to recognize data outliers. The scatter plot identified one potential outlier. In order to retain design balance, the outlier was not simply removed, but instead replaced with the global average for all mean MM values, with the assumption that it would minimize any bias of local means (Appendix 3.7).

The main effects plot for the 5 robustness/environmental factors (**Figure 3.4**) provides insight into the relative importance of robustness/environmental factors, independent of primary/instrumental factors, and enhances the robust nature of the primary/instrumental factor conclusions. The robustness/environmental factors effects, as measured by the mean MM range, are all very small compared to those of the primary/instrumental factors, and none were identified as significant by the ANOVA f-test ($p > 0.05$). This suggests that the primary/instrumental factor settings are valid across the range of water quality characteristics explored. Although not shown, the robustness factor main effects were also explored using medians, rather than means, as the estimator for a “typical” response of a factor at a certain level. The median main effects were in good agreement with the mean main effects and emphasize the robustness of the experimental design. Medians are useful for reinforcing effects conclusions because they are less affected by outliers.

An interaction effects matrix is provided in Appendix 3.8 and reveals that the cross flow/buffer concentration interaction was the fourth most important effect. The remaining 2-factor interactions are insignificant, illustrating the quality of the fractional factorial design utilized in combination with the relative linearity of the AF^4 components. Further exploration of the effects and interactions is also included in Appendix 3.9 with an absolute effects plot. The primary/instrumental and robustness/environmental factors and their associated settings, were predetermined as suitable for this study because they were simple to adjust between separation protocols as well as deemed likely to result in NOM MM distribution changes. There are several other factors that were not considered such as membrane type, buffer composition, focus time, channel flow rate, and spacer thickness. Therefore, this work does not identify a complete optimization of all possible parameters but, instead, the best possible separation conditions for the factors and settings tested.

A replication analysis matrix is provided in Appendix 3.10 and explores the most consistent and precise primary/instrumental and robustness/environmental factor settings across each of the two

replicates relative to the experiment day. Of interest, there does not appear to be any significant instrument drift as variability between replicates is a consequence of factor settings and noise (Appendix 3.6).

While the most significant NOM-ENP interaction is adsorption of dissolved NOM to the particle surface, cation bridging and other flocculation mechanisms can induce ENP aggregation into NOM-ENP complexes [19], producing larger particles that will increase the light scattering signal and likely increase the measured MM response value. The relationship between particle size and light scattering intensity is highly non-linear; light scattering intensity scales with particle radius to the 6^{th} power [40, 43]. This non-linearity is seen in **Figure 3.2**, where the LS signal from larger particles (eluting later) is far greater than that of smaller particles (eluting more quickly). The presence of these larger aggregates is likely a combination of the sample characteristics and an interaction between NOM and AgNP, or the limits of the AF^4 separation protocol.

Since the separation metric used in this work is based on the observation that minimizing average measured MM produces a better separation of polydisperse particles [36], higher MM measurements could result from either aggregation or losses of lower MM NOM components. Losses of lower MM NOM molecules could occur due to increasing buffer concentration, which would reduce the electric double layer of NOM functional groups, potentially causing a coiling effect and a smaller effective particle size. This would then allow some particles larger than the membrane molecular weight cutoff of the ultrafiltration membrane in the AF^4 apparatus to potentially pass through the membrane [56]. Several studies have also shown that the loss of humic acid in AF^4 separations was proportional to ionic strength [57, 58]. This corroborates the conclusion that buffer concentration is the most important primary/instrumental factor affecting measured MM. Unfortunately, the experimental design does not differentiate between the source of these effects, but can conclude which combination of AF^4 settings results in the lowest average MM over all samples tested—thus demonstrating a robustness regardless of sample characteristics. An exploration into potential NOM-AgNP interactions using AF^4 separation is discussed in Chapter 4.

It is important to note that although the goal of this work was to minimize the average sample MM, the average MM measurements were approximately two or three orders of magnitude higher than many

of those reported in the literature for different NOMs [23, 41, 59, 60], though there is a large degree of variability in measurements depending on NOM type, optical properties defined, and analytical approaches reported. Light scattering studies, compared to traditional humics sizing methods like atomic force microscopy, transmission electron microscopy, and fluorescence correlation spectroscopy, typically result in the detection of larger molecules ranging from 10,000 g mol^{-1}- 100,000 g mol^{-1} and larger [41, 42]. For example, Caceci and Billon [61] reported evidence of large organic scatterers (50 nm - 200 nm) in humic acid samples. This suggests that NOM complex molecules may be extensively associated into large, light scattering aggregates. The presence of AgNP, resulting in potential NOM-Ag and NOM-AgNP complexes, may also contribute to larger aggregates. The AF^4 setup used for the measurements in this study included 10 kDa membrane molecular weight cutoff. Most small MM or dissolved NOM (< 0.45 μm) passes through the AF^4 membrane removing it during separation, resulting in an elevated average MM compared to the unfractionated sample. According to Christman and co-workers [42], light scattering measurements should be made on samples containing very high NOM concentrations to ensure adequate detector signal to noise, while the NOM samples in this current work contained only 1 mg C L^{-1} - 10 mg C L^{-1}. Lower analyte concentrations are more difficult to separate and analyze (i.e. quasi-elastic light scattering signal was insufficient for any measurements), but this range is more environmentally relevant for surface waters.

REFERENCES

1. Alvarez, P.J.J.; Colvin, V.; Lead, J.; Stone, V. Research priorities to advance eco-responsible nanotechnology. *ACS Nano* **2009,** *3,* 1616-1619.

2. Weinberg, H.; Galyean, A.; Leopold, M. Evaluating engineered nanoparticles in natural waters. *TrAC-Trends Anal. Chem.* **2011,** *30,* 72-83.

3. Tiede, K.; Boxall, A.B.A.; Tear, S.P.; Lewis, J.; David, H.; Hassellöv, M. Detection and characterization of engineered nanoparticles in food and the environment. *Food Addit. Contam.* **2008,** *25,* 795-821.

4. Schimpf, M.E.; Caldwell, K.; Giddings, J.C. *Field Flow Fractionation Handbook.* Wiley, New York **2000,** 616.

5. Giddings, J. Field-flow fractionation - Analysis of macromolecular, colloidal, and particulate materials. *Science* **1993,** *260,* 1456-1465.

6. Giddings, J.C.; Yang, F.J.; Myers, M.N. Flow field-flow fractionation: A versatile new separation method. *Science* **1976,** *193,* 1244.

7. Giddings, J.C. New separation concept based on a coupling of concentration and flow non-uniformities. *Sep. Sci.* **1966,** *1,* 123.

8. Messaud, F.A.; Sanderson, R.D.; Runyon, J.R.; Otte, T.; Pasch, H.; Williams, S.K.R. An overview on field-flow fractionation techniques and their applications in the separation and characterization of polymers. *Prog. Polym. Sci.* **2009,** *34,* 351-368.

9. Pasch, H.; Makan, A.C.; Chirowodza, H.; Ngaza, N.; Hiller, W. Analysis of complex polymers by multidetector field-flow fractionation. *Anal. Bioanal. Chem.* **2014,** *406,* 1585-1596.

10. Bednar, A.J.; Poda, A.R.; Mitrano, D.M.; Kennedy, A.J.; Gray, E.P.; Ranville, J.F.; Hayes, C.A.; Crocker, F.H.; Steevens, J.A. Comparison of on-line detectors for field flow fractionation analysis of nanomaterials. *Talanta* **2013,** *104,* 140-148.

11. Hassellöv, M.; Readman, J.W.; Ranville, J.F.; Tiede, K. Nanoparticle analysis and characterization methodologies in environmental risk assessment of engineered nanoparticles. *Ecotoxicology* **2008,** *17,* 344-361.

12. von der Kammer, F.; Ferguson, P.L.; Holden, P.A.; Masion, A.; Rogers, K.R.; Klaine, S.J.; Koelmans, A.A.; Horne, N.; Unrine, J.M. Analysis of engineered nanomaterials in complex matrices (environment and biota): General considerations and conceptual case studies. *Environ. Toxicol. Chem.* **2012,** *31,* 32-49.

13. Louie, S.M.; Tilton, R.D.; Lowry, G.V. Effects of molecular weight distribution and chemical properties of natural organic matter on gold nanoparticle aggregation. *Environ. Sci. Technol.* **2013,** *47,* 4245-4254.

14. Chow, A.T.; Guo, F.; Gao, S.; Breuer, R.; Dahlgren, R.A. Filter pore size selection for characterizing dissolved organic carbon and trihalomethane precursors from soils. *Water Res.* **2005,** *39,* 1255-1264.

15. Piccolo, A. The supramolecular structure of humic substances. *Soil Sci.* **2001,** *166,* 810-832.

16. Jones, M.N. and Bryan, N.D. Colloidal properties of humic substances. *Adv. Colloid Interface Sci.* **1998,** *78,* 1-48.

17. Baalousha, M.; Motelica-Heino, M.; Le Coustumer, P. Conformation and size of humic substances: Effects of major cation concentration and type, pH, salinity, and residence time. *Colloid Surf. A-Physicochem. Eng. Asp.* **2006,** *272,* 48-55.

18. Avena, M.J. and Wilkinson, K.J. Disaggregation kinetics of a peat humic acid: Mechanism and pH effects. *Environ. Sci. Technol.* **2002,** *36,* 5100-5105.

19. Philippe, A. and Schaumann, G.E. Interactions of dissolved organic matter with natural and engineered inorganic colloids: A review. *Environ. Sci. Technol.* **2014,** *48,* 8946-8962.

20. Gigault, J.; Pettibone, J.M.; Schmitt, C.; Hackley, V.A. Rational strategy for characterization of nanoscale particles by asymmetric- flow field flow fractionation: A tutorial. *Anal. Chim. Acta* **2014,** *809,* 9-24.

21. Hawe, A.; Romeijn, S.; Filipe, V.; Jiskoot, W. Asymmetrical flow field-flow fractionation method for the analysis of submicron protein aggregates. *J. Pharm. Sci.* **2012,** *101,* 4129-4139.

22. Bolea, E.; Jimenez-Lamana, J.; Laborda, F.; Castillo, J.R. Size characterization and quantification of silver nanoparticles by asymmetric flow field-flow fractionation coupled with inductively coupled plasma mass spectrometry. *Anal. Bioanal. Chem.* **2011,** *401,* 2723-2732.

23. Thang, N.; Geckeis, H.; Kim, J.; Beck, H. Application of the flow field flow fractionation (FFFF) to the characterization of aquatic humic colloids: evaluation and optimization of the method. *Colloid Surf. A-Physicochem. Eng. Asp.* **2001,** *181,* 289-301.

24. Baalousha, M.; Stolpe, B.; Lead, J.R. Flow field-flow fractionation for the analysis and characterization of natural colloids and manufactured nanoparticles in environmental systems: A critical review. *J. Chromatogr. A* **2011,** *1218,* 4078-4103.

25. Loeschner, K.; Navratilova, J.; Legros, S.; Wagner, S.; Grombe, R.; Snell, J.; von der Kammer, F.; Larsen, E.H. Optimization and evaluation of asymmetric flow field-flow fractionation of silver nanoparticles. *J. Chromatogr. A* **2013,** *1272,* 116-125.

26. Qureshi, R.N. and Kok, W.T. Optimization of asymmetrical flow field-flow fractionation. *Lc. Gc. N. Am.* **2011,** *29,* 76.

27. Lyven, B.; Hassellov, M.; Haraldsson, C.; Turner, D. Optimisation of on-channel preconcentration in flow field-flow fractionation for the determination of size distributions of low molecular weight colloidal material in natural waters. *Anal. Chim. Acta* **1997,** *357,* 187-196.

28. Popovici, S.; Kok, W.; Schoenmakers, P. Band broadening in size-exclusion chromatography of polydisperse samples. *J. Chromatogr. A* **2004,** *1060,* 237-252.

29. Kammer, F.; Baborowski, M.; Friese, K. Field-flow fractionation coupled to multi-angle laser light scattering detectors: Applicability and analytical benefits for the analysis of environmental colloids. *Anal. Chim. Acta* **2005,** *552,* 166-174.

30. Filella, M.; Zhang, J.; Newman, M.E.; Buffle, J. Analytical applications of photon correlation spectroscopy for size distribution measurements of natural colloidal suspensions: capabilities and limitations. *Colloid Surf. A-Physicochem. Eng. Asp.* **1997,** *120,* 27-46.

31. Kuklenyik, Z.; Gardner, M.S.; Parks, B.A.; Schieltz, D.M.; Rees, J.C.; McWilliams, L.G.; Williamson, Y.M.; Pirkle, J.L.; Barr, J.R. Multivariate DOE optimization of asymmetric flow field flow fractionation coupled to quantitative LC-MS/MS for analysis of lipoprotein subclasses. *Chromatography* **2015,** *2,* 96-117.

32. Racamonde, I.; Rodil, R.; Benito Quintana, J.; Jose Sieira, B.; Kabir, A.; Furton, K.G.; Cela, R. Fabric phase sorptive extraction: A new sorptive microextraction technique for the determination of non-steroidal anti-inflammatory drugs from environmental water samples. *Anal. Chim. Acta* **2015,** *865,* 22-30.

33. Lee, Y.; Filliben, J.J.; Micheals, R.J.; Phillips, P.J. Sensitivity analysis for biometric systems: A methodology based on orthogonal experiment designs. *Comput. Vision Image Understanding* **2013,** *117,* 532-550.

34. Scott, J.H.J. Accuracy issues in chemical and dimensional metrology in the SEM and TEM. *Meas Sci Technol* **2007,** *18,* 2755-2761.

35. Sensitivity Analysis of MesoNet, In *Study of Proposed Internet Congestion Control Mechanisms,* Mills, K.M., Filliben, J.J., Cho, D.Y., Schwartz, E. and Genin, D., Eds.; U.S. Government Printing Office: Washington, D.C., 2010; pp. 71-135.

36. Galyean, A.A.; Vreeland, W.N.; Filliben, J.J.; Holbrook, R.D.; Ripple, D.C.; Weinberg, H.S. Using light scattering to evaluate the separation of polydisperse nanoparticles. *Anal. Chim. Acta* **2015,** *Accepted.*

37. Woodrow Wilson International Center for Scholars Project on Emerging Nanotechnology. **2010,** http://www.nanotechproject.org/

38. Kaegi, R.; Voegelin, A.; Sinnet, B.; Zuleeg, S.; Hagendorfer, H.; Burkhardt, M.; Siegrist, H. Behavior of metallic silver nanoparticles in a pilot wastewater treatment plant. *Environ. Sci. Technol.* **2011,** *45,* 3902-3908.

39. Kim, B.; Park, C.; Murayama, M.; Hochella, M.F., Jr. Discovery and characterization of silver sulfide nanoparticles in final sewage sludge products. *Environ. Sci. Technol.* **2010,** *44,* 7509-7514.

40. Wyatt, P.J. Submicrometer particle sizing by multiangle light scattering following fractionation. *J. Colloid Interface Sci.* **1998,** *197,* 9-20.

41. Wagoner, D. and Christman, R. Molar mass and size of Norwegian aquatic NOM by light scattering. *Environ. Int.* **1999,** *25,* 275-284.

42. Christman, R.; Shi, J.; Wagoner, D.; Sharpless, C.; Fischer, E.; Schupbach, J. *A new method for characterizing aquatic organic matter.* University of North Carolina at Chapel Hill: Chapel Hill, NC, 1998; Vol. WRRI Project No. 70 142.

43. Wyatt, P.J. Light scattering and the absolute characterization of macromolecules. *Anal. Chim. Acta* **1993,** *272,* 1-40.

44. Filliben, J.J. DATAPLOT-an interactive high-level language for graphics, non-linear fitting, data analysis, and mathematics. *ACM SIGGRAPH Comput.Graph.* **1981,** *15,* 199-213.

45. Brezonik, Patrick L., Arnold,William A., *Water chemistry : an introduction to the chemistry of natural and engineered aquatic systems.* Oxford University Press: New York, 2011.

46. American Public Health Association. *Standard Method 5310C-2011.* Standard Methods Online - Standard Methods for the Examination of Water and Wastewater: Washington D.C., USA, 2000.

47. nanoComposix NanoXact. **2015**, http://nanocomposix.com/collections/silver-spheres/products/10-nm-silver-nanospheres

48. Dubascoux, S.; Von Der Kammer, F.; Le Hecho, I.; Gautier, M.P.; Lespes, G. Optimisation of asymmetrical flow field flow fractionation for environmental nanoparticles separation. *J. Chromatogr. A* **2008,** *1206,* 160-165.

49. Box, G.E.P.; Hunter, W.G.; Hunter, J.S. *Statistics for Experimenters: An Introduction to Design, Data Analysis and Model Building*. Wiley: New York, 1978.

50. Box, G.E.; Hunter, J.S.; Hunter, W.G. *Statistics for Experimenters: Design, Innovation, and Discovery.* John Wiley & Sons, Inc.: Hoboken, NJ, 2005; Vol. 2nd Edition, pp. 664.

51. Taguchi, G. and Konishi, S. *Orthogonal Arrays and Linear Graphs.* ASI press: Dearborn, MI, USA, 1987.

52. National Institute of Standards and Technology DOE Mean Plot. *NIST/SEMATECH e-Handbook of Statistical Methods* **2013,** http://www.itl.nist.gov/div898/handbook/pri/section5/pri593.htm

53. National Institute of Standards and Technology Ordered Data Plot. *NIST/SEMATECH e-Handbook of Statistical Methods* **2013,** http://www.itl.nist.gov/div898/handbook/pri/section5/pri591.htm

54. National Institute of Standards and Technology DOE Contour Plot. *NIST/SEMATECH e-Handbook of Statistical Methods* **2013,** http://www.itl.nist.gov/div898/handbook/pri/section5/pri59a.htm

55. National Institute of Standards and Technology An EDA Approach to Experimental Design. *NIST/SEMATECH e-Handbook of Statistical Methods* **2013,** http://www.itl.nist.gov/div898/handbook/pri/section5/pri59.htm

56. Neubauer, E.; v.d. Kammer, F.; Hofmann, T. Influence of carrier solution ionic strength and injected sample load on retention and recovery of natural nanoparticles using Flow field-flow fractionation. *J. Chromatogr. A* **2011,** *1218,* 6763-6773.

57. Schimpf, M.E. and Petteys, M.P. Characterization of humic materials by flow field-flow fractionation. *Colloids Surf. Physicochem. Eng. Aspects* **1997,** *120,* 87-100.

58. Manh Thang, N.; Geckeis, H.; Kim, J.I.; Beck, H.P. Application of the flow field flow fractionation (FFFF) to the characterization of aquatic humic colloids: evaluation and optimization of the method. *Colloid Surf. A-Physicochem. Eng. Asp.* **2001,** *181,* 289-301.

59. Hassellöv, M.; Von der Kammer, F.; Beckett, R. Characterisation of aquatic colloids and macromolecules by field-flow fractionation, In *Environmental Colloids and Particles: Behaviour, Separation and Characterisation,* Volume 10 of Series on Analytical and Physical Chemistry of Environmental Systems ed.; Wilkinson, K.J. and Lead, J.R., Eds.; John Wiley & Sons: 2007; pp. 224.

60. Guéguen, C. and Cuss, C.W. Characterization of aquatic dissolved organic matter by asymmetrical flow field-flow fractionation coupled to UV–Visible diode array and excitation emission matrix fluorescence. *J. Chromatogr. A* **2011,** *1218,* 4188-4198.

61. Caceci, M. and Billon, A. Evidence for large organic scatterers (50-200nm Diameter) in humic-acid samples. *Org. Geochem.* **1990,** *15,* 335.

CHAPTER 4: QUANTIFICATION OF SILVER NANOPARTICLES IN LAKE WATER BY ASYMMETRIC FLOW FIELD FLOW FRACTIONATION AND INDUCTIVELY-COUPLED PLASMA MASS SPECTROMETRY

4.1 Introduction

Engineered nanoparticles (ENPs) are increasingly being incorporated into industrial processes and consumer products. The International Council of Nanotechnology has identified that one of their highest priority goals is the development of robust analytical characterization methods to investigate ENPs in the environment as the first step towards understanding any potential human exposure risks [1]. The current use of nano-enabled consumer products and nanoparticle-producing industries is producing nano-waste at a rate that outpaces the scientific research necessary to understand their potential environmental implications. Regardless of whether ENPs are intentionally or unintentionally released into the environment, their potential as anthropogenic pollutants dictates that the ability to characterize and quantify ENPs in natural aquatic matrices must be established for an effective risk assessment to be carried out. Among the most recent estimate of 1600+ consumer products containing nano materials, more than 438 contain silver ENPs [2] making them one of the most commonly used ENP materials. Tiede and coworkers predicted that the most likely route of human exposure to silver ENPs (AgNPs) was through surface and wastewaters [3]. Predicted freshwater concentrations of AgNPs based on a substance flow analysis from products to water in Switzerland are in the range < 0.03 μg L^{-1} – 0.32 μg L^{-1}. These models contained estimated worldwide production volume, allocation of the production volume to product categories, particle release from products, and flow coefficients within the environmental compartments [4, 5].

Once in surface waters or wastewater, AgNPs are expected to interact with naturally occurring organic matter (NOM) [6-18]. This is because of the high concentrations of NOM in the environment relative to persistant ENPs [19], as well as a wide range of functional groups within NOM molecules, though the specific interaction mechanisms are still being debated [18], Because NOM is ubiquitous in natural and engineered waters, and is well known to be important for fate and transport of natural

inorganic colloids, there has been a recent push to investigate interactions between NOM and AgNPs [6, 12, 13, 15-18, 20]. Generally, metal and metal oxide ENPs become electrostatically stabilized by in the presence of small amounts of NOM in natural aquatic matrices [21, 22]. NOM results from the breakdown of plant and microbial organic matter, and is a heterogeneous and polydisperse complex environmental mixture, containing supramolecular assemblies of a wide range of molecular weights and chemical properties [6, 7, 23-25]. NOM falls into two major categories: the non-humic, hydrophobic fraction containing aliphatic carbon and nitrogen, and the humic, hydrophilic fraction, composed aromatic carbon, phenolic structures, and conjugated double bonds. Operationally, humic acids are insoluble at low pH, while low molecular weight fulvic acids are soluble over a wide range of pH values [18].

NOM is generally categorized as either particulate or dissolved organic where the dissolved fraction will pass through a 0.45 μm filter [26]. NOM changes in structure, molar mass, and aggregation with varying aquatic chemistry and water quality characteristics [7], and smaller components can form aggregated clusters by hydrogen bonds, hydrophobic interactions, cation bridges, and dipole-dipole interactions [7, 24, 27-29]. Similarly, it is expected that NOM-ENP interactions are controlled by the chemistry and characteristics of the matrix , ENPs, and NOM [30-35]. NOM-ENP interactions that have been studied include the adsorption of dissolved NOM to the particle surface, cation bridging and other flocculation mechanisms can induce ENP aggregation into NOM-ENP complexes [6].

Louie and coworkers [7] investigated how different molecular weight components of NOM interact with metal or metal oxide ENPs. They concluded that higher molar mass fractions, primarily comprised of >100,000 g mol^{-1} humic acid aggregates, disproportionately dominate aggregation behavior of sample components compared to lower molar mass fractions that tend to enhance ENP stability. Therefore, small differences in NOM molecular weight distribution can alter ENP stability and potential fate in the aquatic environment because. NOM-coated metal ENPs with a lower settling rate may persist in the aquatic environment where aggregated or dissolved particles may not. However, Bae et al. [10] demonstrated that potential NOM-ENP interactions are less likely to be based on adsorption of NOM to ENPs, but, instead, on the adsorption of NOM-ENP complexes to humic acids or NOM aggregates. Despite both theoretically- and experimentally-based predictions, the implication is that larger and

potentially unstable aggregates will be formed in waters containing ENPs at environmental concentrations and heterogeneous mixtures of NOM.

Building on the previous work, Sánchez-Cortés et al. [8] concluded that higher molecular weight humic substances absorbed preferentially through H-bonding, while smaller molecules absorbed through electrostatic and hydrophobic forces. By studying adsorption of humic and fulvic acids on citrate-stabilized AgNPs, Sánchez-Cortés et al. [8] observed that the sorption takes place through NOM carboxyl groups at acidic pH. In contrast, Litvin et al. [9] suggested that chelation can occur between humic acids and silver ions present at the surface. Using a different approach, Lau et al. [11] determined through nuclear magnetic resonance (NMR) that both humic and fulvic acids can replace citrate ions on the surface of citrate stabilized-AgNPs.

Heterogeneous NOM is poorly characterized at the level needed to predict how it may control or stabilize ENPs in natural or engineered waters, because it contains a large number of diverse chemical functionalities. Thus, there is no single analytical method capable of elucidating definitive structural or functional information for all moieties in NOM that may interact with ENPs. However, many analytical approaches have been used to characterize average or trace chemical characteristics of different fractions of NOM. For example, fluorescence spectroscopy provides information on three general types of carbon within NOM [36] and therefore, fluorescence intensities of NOM can be strongly dependent on NOM molecular structure and molar mass [37-43]. Using fluorescence of NOM to characterize interactions between AgNP and humic acids, Philippe and Schaumann [6] determined that fluorescence peak areas of the humic substance did not vary in the presence or absence of nanoparticles. They suggested that the amount of humic acid absorbed on the particles was negligible compared to the dissolved amount.

A recent report by the European Commission on requirements for NP measurements [45] concluded that asymmetric flow field flow fractionation (AF^4) interfaced with inductively coupled plasma mass spectrometry (ICP-MS) was one of the most appropriate and promising approaches for quantification of AgNPs in a variety of environmental matrices. ICP-MS signal is correlated with the number of ions produced as nanoparticles enter the plasma chamber will be atomized completely [46].

Therefore, the number of ICP-MS counts is proportional to the mass of the particles, allowing for concentration determination of metal-based ENPs.

Several groups have recently used AF^4-ICP-MS to quantify AgNP in complex matrices. For example, AF^4-ICP-MS reported in the literature. AF^4-spICP-MS (single particle ICP-MS) was used to quantify AgNP spiked into chicken meat [47]while Ramos and coworkers [48] quantified AgNP in nutraceuticals and beverages. Of the studies that have used AF4 to investigate AgNPs, there are several key differences in their approach. For instance, some studies have attempted the quantification of AgNP using AF^4-ICP-MS by calibrating with post-channel injection (introduced into the system after AF^4 separation) of ionic silver standards [48, 49]. Yet, other studies have applied AF^4-ICP-MS towards NP mass-determination using analyte recovery methods [30, 50] and pre-channel injections of AgNP calibration standards [51]. In contrast to post-channel calibration, pre-channel injections (introduced prior to AF^4 separation) account for recovery differences due to particle-system interactions, such as material loss through the membrane. Hoque et al. [49] developed a method for AF^4-ICP-MS quantification of AgNP in wastewater using external pre-channel calibration with polyacrylate particles. It is difficult to compare findings across these studies, as there is a lack of consistency in application, system and matrix complexity, and environmental relevance (i.e. low AgNP concentration). Furthermore, these studies are not directly applicable to environmental studies, given that they were conducted using AgNP concentrations much greater than expected in surface waters.

Therefore, a primary challenge to AgNP quantification in natural systems is the lack of standardized methodologies that account for the effects of the matrix and instrumental on the results. To address this challenge, Ranville et al. [53] described a detailed method for symmetric field flow fractionation (FFF)-ICP-MS signal correction and element calibration that has since been applied to similar studies [54-56]. Linear signal drifts are corrected for using standard solutions run at the beginning and end of each analysis sequence. Detector signal conversion to concentration is achieved by external calibration using matrix matched standard solutions measured directly with ICP-MS prior to analyzing samples with the symmetric FFF interface. Attribution of elemental Ag concentration to colloidal or ionic species is achieved by peak integration. However, these methods are only applicable under constant output channel flow, such as during symmetric FFF. In contrast, during AF^4 separation, the output flow

fluctuates slightly and can take time to achieve a steady rate after or during the application of cross flows. Bouby and coworkers [57] determined that AF^4 channel outflow was not constant and experienced a decrease in ICP-MS signal of their internal standard throughout the flow regime. However, the identified flow variations and subsequent fractograms in Bouby et.al. [57] were reproducible and, therefore, signals were normalized to the internal standard to compensate for drift [57]. This quantification approach is well-suited for a standard addition calibration approach using normalized signal, which would compensate for these potential flow variations.

The quantification of AgNPs, is further complicated, due in part to their inherent instability and subsequent release of ionic Ag+. This presents a challenge for ensuring accurate and reproducible measurements [58-60]. In addition to elemental analysis, ICP-MS can also determine stable isotope mass ratios in speciation studies [46, 61] and provide a means to discriminate between isotopically enriched and non-enriched Ag species (Ag+ or AgNP). For example, Gigault and Hackley [61] doped estuarine sediment with isotopically enriched ^{109}AgNP to investigate AgNP-sediment behavior. Isotopically enriched Ag^+ or AgNP are, therefore, very useful in determining speciation and will likely influence quantification results in occurrence surveys, as speciation may affect potential environmental and human exposure and toxicity risks.

Taking into account the complexity of NOM, the measurement challenges of quantifying AgNP in natural matrices, instrument complexity, and the inconsistency in applied quantification methods, this work presents the combined use of AF^4 separations coupled online with ICP-MS elemental characterization and standard addition quantitation of AgNPs in a natural water to establish the basis for new risk assessment measurement methods. In the case of synthetic or natural freshwater matrices, precipitation, aggregation, and dissolution effects are expected [62-69]. A standard addition quantification approach is intended to compensate for these losses and matrix effects, ultimately providing a more accurate determination of environmental persistence than studies attempting to control these factors. Multiple standard addition analyses might be required to monitor analyte losses that might occur in the sample over time. Finally, iotoppically-enriched 109Ag+ are used to differentiate between the ionic and AgNP silver fractions in the ICP-MS following AF4 separation. An offline fluorescence detector was used to corroborate Ag-NOM and AgNP-NOM interactions occurring within the samples, and trends were

confirmed using dialysis at a molecular weight cutoff below that of the AF^4 membrane. This additional exploration was used to better understand how molecular weight distribution of NOM changes upon addition of Ag^+ or AgNPs.

4.2 Experimental Methods

4.2.1 Water Samples and Handling

The synthetic freshwater matrix (**Table 4.1**) was established using U.S. average freshwater measurements [70] as a guide for matrix composition. For example, measurements from Little Rock Lake, Vilas, CO., Harriet Lake, MN., and Colorado River, AZ. were used to design compositions so that the matrix contained 3 meq L^{-1} each of both anions and cations from a combination of $MgSO_4*7H_20$, $NaHCO_3$, $KHCO_3$, $MgCl_2$, $CaCl_2$, $CaCO_3$, and NaCl (all analytical grade; Sigma-Aldrich, St. Louis, MO) in 18.2 MΩ□cm laboratory grade water (LGW) providing a total conductivity of 0.40 mS cm^{-1} of the final working sample. The synthetic freshwater matrix was allowed to equilibrate for 24 hours prior to experiments. Suwannee River NOM (SR NOM) (International Humics Substances Society, St. Paul, MN) was dissolved in LGW for 24 hours, in the dark at 4°C, prior to sample preparation. No pH adjustments or mixing was performed at this time. Aliquots of dissolved NOM were added to the synthetic freshwater matrix, filtered by vacuum at 0.45 µm (mixed cellulose esters, MF-Millipore, Billerica, MA), and pH adjusted to 7 with HCl (1 N solution, Sigma Life Sciences, St. Louis, MO) or NaOH (1 M, Fluka Analytical, St. Louis, MO).

In order to explore the applicability of our instrumental approach towards future AgNP occurrence surveys in the environment, a natural lake water sample was selected as the matrix for AgNP quantification studies by AF^4-ICP-MS. As a first step in the AgNP quantification process, Ag speciation following an AF^4 separation was explored with online ICP-MS. Mixtures of lake water, AgNP, and isotopically enriched $^{109}Ag^+$ taken through the entire AF^4-ICP-MS interface using protocol A or B (**Table 4.1**). AF^4 separation Protocol A was optimized for the separation selectivity of NOM based on the UV absorbance signal at 254nm. The consequence of this is that the ICP-MS Ag signal peaks are not as well resolved. The ramped cross flow velocity was insufficient to adequately separate the Ag in the sample,

and, therefore, a steady cross flow (Protocol B) was applied to impart more hydrodynamic force on the sample during separation, and to increase elution time and resolution.

Lake water samples (Gaithersburg, MD) were collected by grab sampling in triplicate into nitric acid-cleaned, 40 mL amber glass vials that were rinsed with 18.2 MΩ water prior to use. Samples were vacuum filtered as described above and stored in the dark at 4°C until addition of Ag^+ or AgNP and analysis (within 48 hours). Lake water characteristics are given in **Table 4.1**.

Table 4.1. Water sample characteristics

Water Sample			Value
Synthetic Freshwater	Components	Ca^{2+}	684 µeq L^{-1}
		Mg^{2+}	297 µeq L^{-1}
		Na^+	1975 µeq L^{-1}
		K^+	36 µeq L^{-1}
		HCO_3^-	919 µeq L^{-1}
		SO_4^{2-}	247 µeq L^{-1}
		Cl^-	1826 µeq L^{-1}
	Characterization	pH	7.00
		Specific Conductance	0.40 mS cm^{-1}
		DOC (SR NOM)	10 or 5.0 mg C L^{-1}
Lake Water	Characterization	pH	7.60
		Specific Conductance	0.48 mS cm^{-1}
		TOC	4.88 mg C L^{-1}
		DOC	4.76 mg C L^{-1}

DOC = dissolved organic carbon; TOC = total organic carbon; SR NOM = Suwannee River natural organic material

4.2.2 Silver Nanoparticles and Ions

NanoXact™ citrate-stabilized AgNP (10 nm, Nanocomposix, San Diego, CA) were used at environmentally relevant concentrations diluted from 0.02 mg mL^{-1} stock. Ag^+ in synthetic freshwater and lake water samples was prepared by dilution from LGW containing silver nitrate (≥ 99.0%, Sigma Aldrich, St. Louis, MO). Isotope enriched $^{109}Ag^+$ was prepared by dilution in LGW (enrichment 99.97% ^{109}Ag, Oak Ridge National Laboratory, Oak Ridge, TN).

AgNPs, Ag^+, or $^{109}Ag^+$ were introduced to water samples by shaking by hand for 10 seconds, either synthetic freshwater matrix or raw lake water, 1 hour prior to AF^4 separation to allow for stabilization and equilibration. During this hour, the samples equilibrated in the dark at 4°C. AgNP size was confirmed by quasi-electric light scattering (QELS) with a WyattQELS™ detector at a nominal angle of 140°, and was in good agreement with those reported by the manufacturer [71]. All stock solutions and samples were stored in the dark at 4°C prior to analysis.

The natural isotropic ratio of $^{107}Ag/^{109}Ag$ is near 1:1 (Appendix 4.2) [82], so any deviation would provide a means to distinguish between ionic and AgNP in the ICP-MS signal. Further, the appropriate standard addition calibration was performed to mitigate system and matrix effects prior to quantification of the "challenge" AgNP spike (0.6 μg L^{-1}).

4.2.3 Characterization of the Source Waters

Specific conductance measurements of the final working samples for each of the two waters were made with a Wyatt Technologies Möbiuζ instrument using Dynamics Software version 7.2.4. Fractionation of the two water samples by AF^4 was observed by a UV detector (UVIS 204, Linear, Reno, NV) at 254 nm to monitor NOM absorbance. UV absorbance data was not collected for AgNPs due to limited absorbance at low concentrations. Total organic carbon (TOC) and DOC measurements were made using a Shimadzu TOC-V_{CPH} Analyzer (Shimadzu Corporation, Atlanta, GA) using Standard Method 5310 [72] following vacuum filtration at 0.45 μm (mixed cellulose esters, MF-Millipore, Billerica, MA).

Fluorescence excitation and emission measurements were performed by Aqualog (Horiba Instruments Inc., Kyoto, Japan) using quartz cuvettes (10 mm x 10 mm, 3-Q-10, Starna Cells) offline for both the collected AF^4 cross flow fractions and dialysis samples. Lake water samples did not contain a strong fluorescent fraction and, therefore, synthetic freshwater samples were used for analysis. AgNP and Ag^+ did not interfere with sample fluorescence or UV absorbance within the target ranges (Appendix 4.1). Daily water, Raman emission, and validation checks using a fluorescence intensity correction standard (SRM 2940, National Institute of Standards and Technology, Gaithersburg, MD) were performed to monitor instrument performance. An AF^4 system blank, collected as cross flow waste from an injection using identical conditions to sample, was subtracted from each sample of cross flow waste to account for

any potential fluorescence from the AF^4 hardware and run buffer. Similarly, dialyzed blanks containing synthetic freshwater matrix without SR NOM were used. All samples were allowed to come to room temperature before analysis. Fluorescence data is reported as F_{max}, or the maximum fluorescence < 250 nm excitation and at 441 nm emission, corresponds to the relative amount of the humic-like NOM sample [73, 74]. Fluorescence trends were confirmed using dialysis at a molecular weight cutoff below that of the AF^4 membrane.

Fluorescence measurements of collected AF^4 lake water fractions from the 50:50 AF^4 elution flow split prior to the ICP-MS detector in 3 minute fractions (1.5 mL) revealed there was no measureable fluorescence signal with a 6 second integration time. The instrument averages the number of lamp pulse-cycles for the specified integration time. While longer integration time reduces the signal-to-noise ratio for the sample fluorescence intensity, it also allows more light to reach the detector. In this case, increasing the integration time resulted in detector saturation before adequate sample signal was achieved. This is primarily due to the AF^4 dilution factor (~100x) and the very low fluorescence found in the lake water raw sample. As a result, SR NOM in synthetic freshwater was used for fluorescence experiments.

4.2.4 Dialysis

Dialysis experiments were performed on each of three separate aliquots of synthetic freshwater samples containing 5 mg C L^{-1} SR NOM. Samples were distributed into 5 mL Spectra/Por® Float-a-Lyzer® G2 3.5 kDa – 5 kDa dialysis tubing made from Biotech-grade Cellulose Ester (Spectrum Labs, Rancho Dominguez, CA). Dialysis tubes were prepared for sample dialysis as directed by the manufacturer. Deionized (DI) water was used as the dialysis buffer and was replaced with fresh DI water at 2 hours, 6 hours, and 14 hours before sample was removed after 20 hours. Samples were transferred to fluorescence cuvettes directly from dialysis tubes for immediate analysis.

4.2.5 Instrumentation

AF^4 was performed using a Wyatt Technologies Corp. Eclipse (Santa Barbara, CA) separation module with manufacturer-supplied Eclipse software. Separation was performed using a Wyatt Technologies long channel containing a vendor-supplied 250µm spacer to define the flow channel

thickness and a 10kDa regenerated cellulose membrane (Wyatt Technologies) membrane. Sample injections were made using a manual sample injector with a 900µL injection loop that was flushed with AF^4 run buffer continuously during analysis. The run buffer was prepared by dissolving ammonium nitrate (0.5 mM, ACS Reagent ≥ 98%, Sigma-Aldrich, St. Louis, MO) in LGW containing 0.01% sodium azide (Ricca Chemical Company, Arlington, TX) as an antimicrobial. Run buffer was degassed with a Gastorr TG-14 unit at 100 hPa directly from solvent bottles and then filtered sequentially by a polytetrafluoroethylene frit (Restek Corp., Bellefontane, PA) followed by a 0.1 µm Durapore® membrane filter (EMD Millipore, Billerica, MA). The AF^4 separation module was interfaced online with a UV detector (UVIS 204, Linear, Reno, NV) and quadrupole ICP-MS (ThermoFisher X Series 7, Waltham, MA) equipped with a C-Type Concentric Quartz Nebulizer (Analytical West Inc., Lebanon, PA). Fractions of AF^4 cross flow waste were collected for offline analysis. The elution flow from the AF^4 passed through the UV detector before being split 50:50 to waste and ICP-MS, respectively. The flow was pumped through a peristaltic pump at 30 rpm before being combined with a 1 ppb internal standard, Indium (^{115}In) (SRM 3124a, National Institute of Standards and Technology, Gaithersburg, MD) in 1.5% nitric acid (69% Veritas® double distilled, GFS Chemicals, Powell, OH). ICP-MS data were collected and exported to Origin graphing software (OriginLab Corp, Northampton, MA) for peak area integration. Total peak areas correspond directly to the concentration of Ag in each respective fraction. An instrument setup schematic is shown in **Figure 4.1**. Fluorescence measurements were made offline with collected AF^4 cross flow fractions using a bench top Aqualog Fluorometer (Horiba Instruments Inc., Kyoto, Japan). Separation protocol and instrumental parameters are listed in **Table 4.2**.

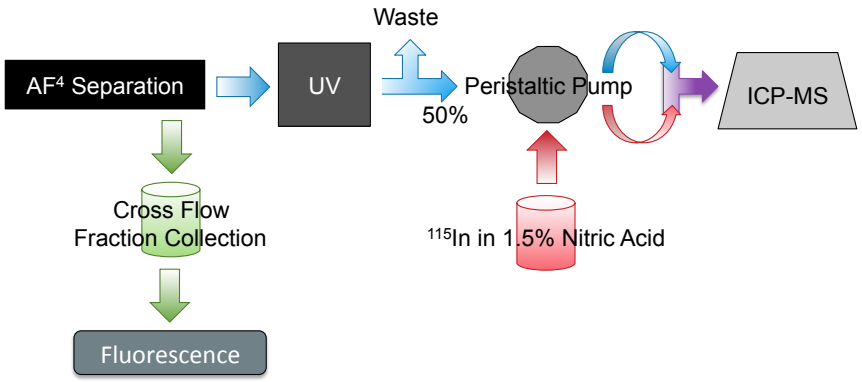

Figure 4.1. Schematic showing AF^4-UV-ICP-MS instrumental setup.

Table 4.2. Summary of instrumental conditions and parameters. (Conditions not listed for protocol B are the same as protocol A).

Instrumentation				
AF4			Protocol A	Protocol B
	Channel	Injection volume	400 µL	
		Membrane	10 kDa regenerated cellulose	
		Spacer	250 µm	
	Flow	Channel Flow	1.00 mL min^{-1}	
		Cross Flow	1.00 mL min^{-1}	1.50 mL min^{-1}
		Cross Flow ramp	to 0.00 mL min^{-1}	none
		Injector Flow	0.2 mL min^{-1}	
		Focus Flow	2.00 mL min^{-1}	
	Elution	Focus + inject	4 min	
		Focus	1 min	
		Elution	30 min	20 min
UV-Vis		Wavelength	254 nm	
ICP-MS		Nebulizer flow rate	1.0 mL min^{-1}	
		Dwell time	300 ms	
		Mode	Transient Time Resolved Analysis	
		Targeted isotopes	^{115}In, ^{107}Ag, ^{109}Ag	
Fluorescence		CCD Gain	Medium	
	Excitation	Wavelength	< 250 nm	
	Emission	Wavelength	441 nm	
	Integration time	Cross Flow samples	5 sec	
		Dialysis samples	1 sec	

CCD = charge coupled device

4.3 Results

The stabilizing effects of NOM on Ag^+ and AgNP were explored using AF^4-ICP-MS by analyzing total Ag concentrations with and without the presence of SR NOM in the synthetic samples (**Figure 4.2**). These experiments were performed with Ag^+ or AgNP in synthetic freshwater, both with and without the addition of SR NOM. The addition of NOM greatly improves stability (**Figures 4.2b** and **4.2d**), compared to Ag+ or AgNP alone (**Figures 4.2a** and **4.2c**), resulting in an observed increased amount of Ag reaching the ICP-MS detector. Calibration curves were generated total Ag from the peak area of the normalized

signal relative to the known concentration of AgENPs. These calibration curves generated are linear and reproducible, with peak area standard deviation less than 5% of the mean between triplicate injections.

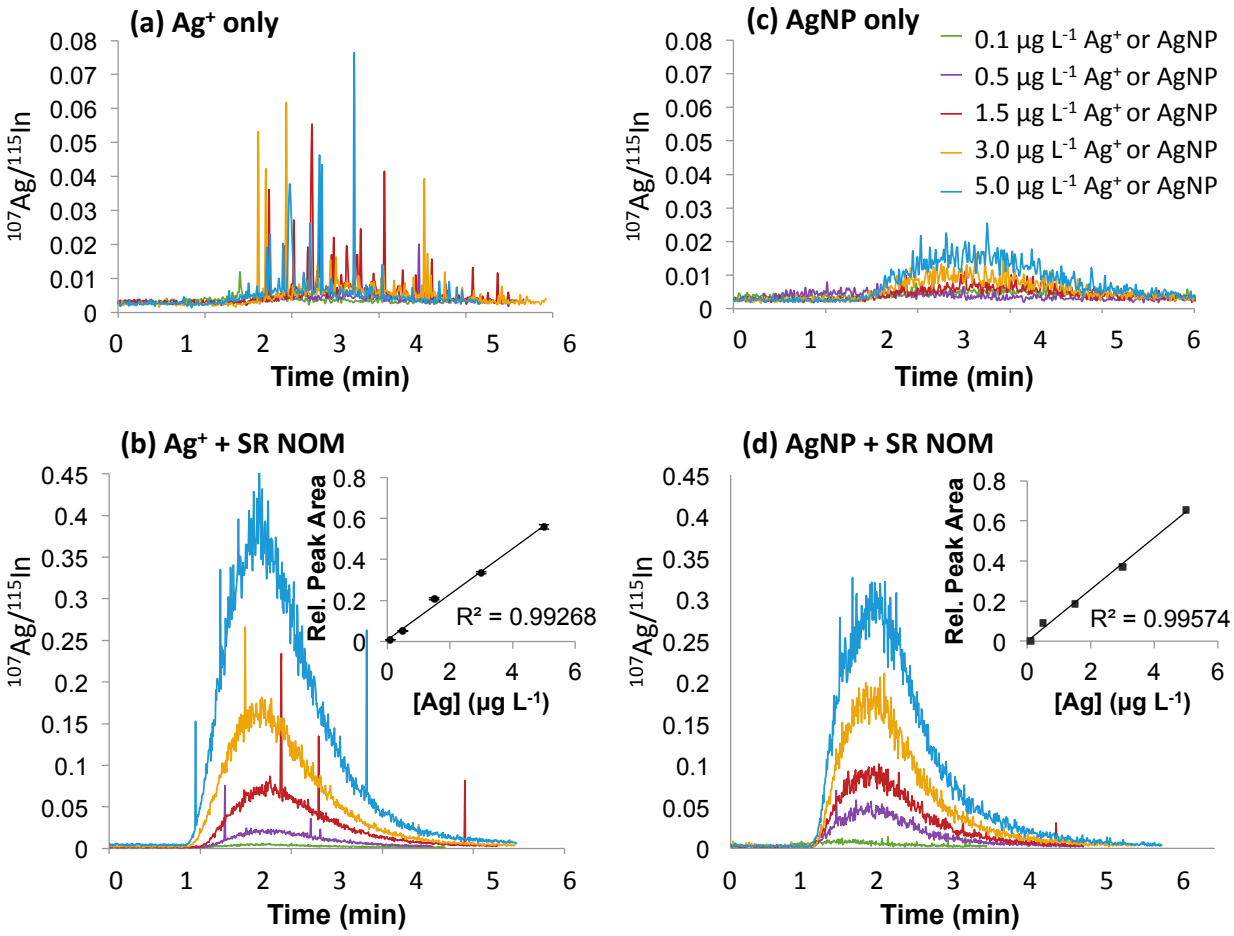

Figure 4.2. ICP-MS signal counts following AF^4 separation with membrane removed for ^{107}Ag normalized to ^{115}In internal standard of increasing concentrations of (a, b) Ag^+ and (c, d) 10 nm AgNP in synthetic freshwater. (b, d) contain 10 mg C L^{-1} SR NOM. Inlay shows calibration curve generated from relative (rel.) peak area and known Ag concentration for n=3 with SD < 5%.

Figure 4.3 shows linear regressions of varying calibration conditions under the step-wise addition of several AF4 system components. Calibration for associated Ag^+ concentrations in synthetic freshwater (red) containing 10 µg C L^{-1} SR NOM with the AF^4 membrane removed is also provided for comparison. A

significant decrease ($p < 0.05$) in the regression slope was identified with the inclusion of the AF^4 focusing step.

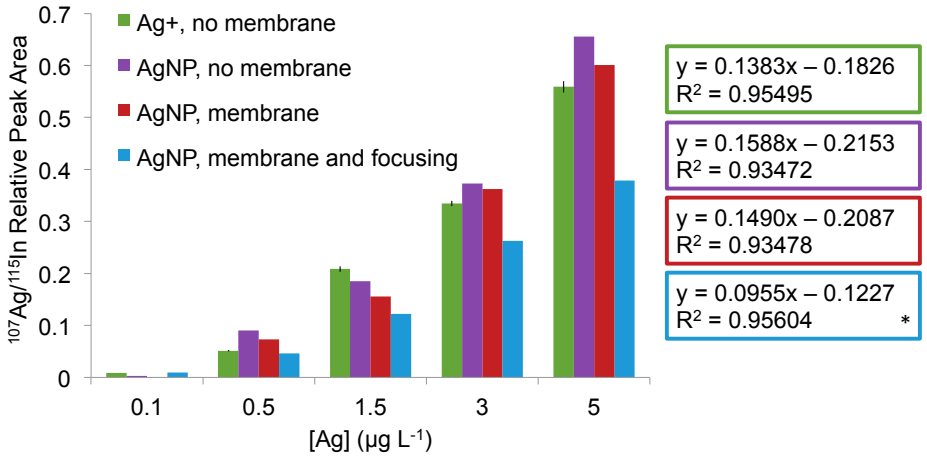

Figure 4.3. Calibration curves for normalized ^{107}Ag ICP-MS peak area against increasing concentrations of Ag^+ and AgNP containing 10 mg C L^{-1} SR NOM. Error bars represent standard error for n = 3, and (*) indicates significant difference in regression slope.

Ag speciation following an AF^4 separation was explored with online ICP-MS. Mixtures of lake water, AgNP, and isotopically enriched $^{109}Ag^+$ were separated by AF4 using protocol A or B (**Table 4.1**), and analyzed online by ICP-MS, generating the fractograms in Figure 4.4. An overlay of a typical UV_{254} absorbance is included in **Figure 4.4**, indicating the presence and elution profile of NOM. No differences were observed in UV_{254} between samples. Compared to the Lake water spiked with ^{109}Ag (red trace) in **Figures 4.4b** and **4.4d**, the addition of higher concentrations of AgNP (yellow, purple, and teal traces, respectively) primarily result in an increase in the second signal peak around 12min. The first peak at 9 min increases in height, but not to the same extent as the second peak at 12 min.

Figure 4.5 shows the standard addition quantification of the "challenge" AgNP spike in lake water with both separation Protocols A and B and calibration samples of 0.05 µg L^{-1}, 0.5 µg L^{-1}, and 1.0 µg L^{-1} AgNP. Peak area integration and quantification using separation Protocol A resulted in a 7.9% overestimation, whereas separation Protocol B yielded a 9.1% underestimation of the 0.6 µg L^{-1} "challenge" AgNP spike though linearity was improved (R^2 = 0.99776 *vs.* 0.93907) for Protocols A and B,

respectively. Taking the average between the two estimates resulted in 0.60 µg L^{-1} +/- 0.04 µg L^{-1} Ag quantification in the AgNP peak.

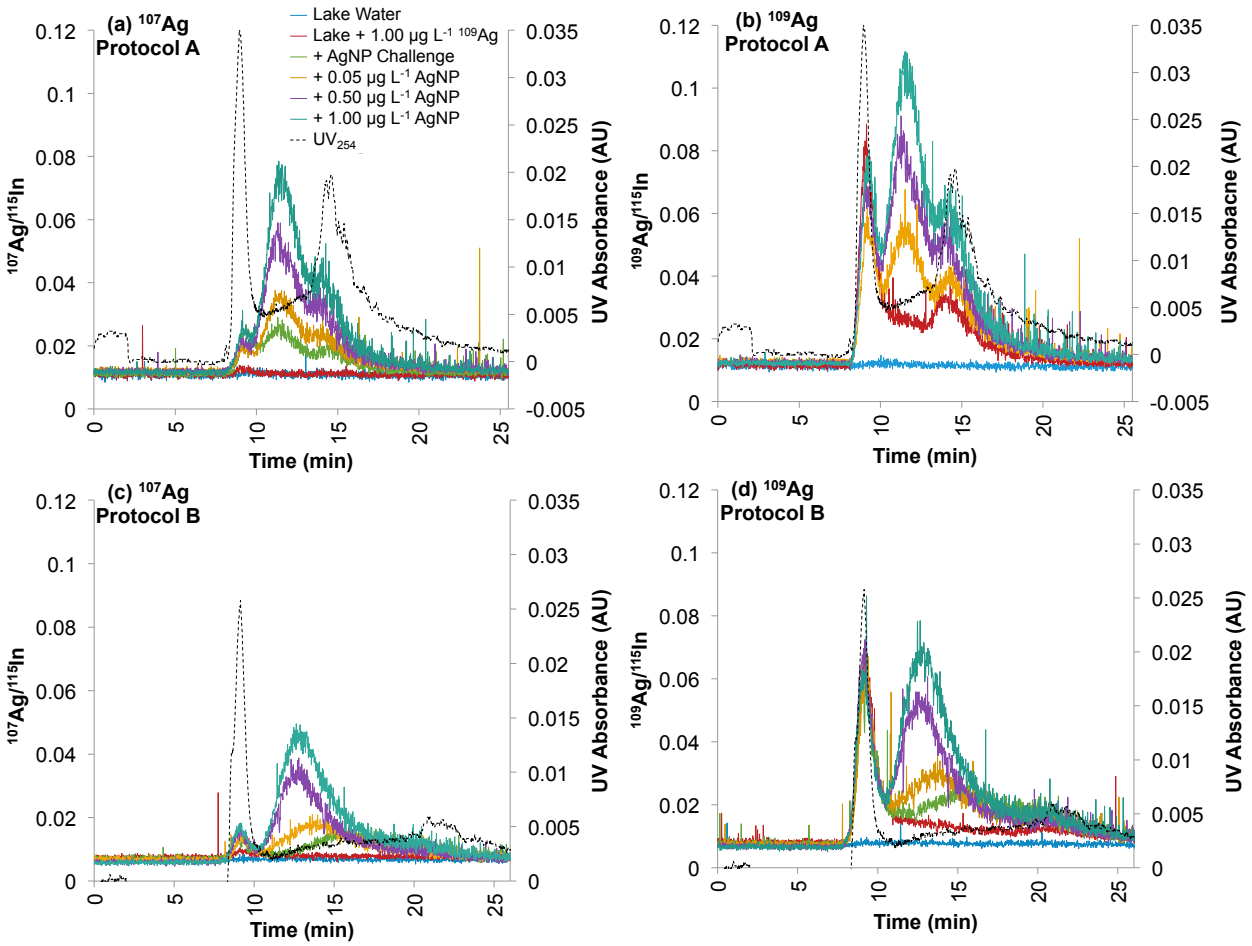

Figure 4.4. ICP-MS relative ion response for (a,c) ^{107}Ag and (b,d) ^{109}Ag signal normalized to ^{115}In for lake water samples. Samples undergo either AF^4 separation (a,b) protocol A or (c,d) B. Ag signal is normalized to the internal standard, ^{115}In. All samples, excluding raw lake water, contain the same concentration of isotope-enriched $^{109}Ag^+$. A typical UV absorbance trace at 254 nm is overlaid with dashed line for each protocol.

An offline fluorescence detector was used to further investigate potential Ag-NOM and AgNP-NOM interactions occurring within the samples, The fluorescence analysis used to probe how molecular weight distribution of NOM may change upon addition of Ag^+ or AgNP showed a significant change in

fluorescence signal of SR NOM in synthetic freshwater after the addition of Ag^+ or AgNP. **Figure 4.6a** shows max fluorescence (F_{max}) measurements in the humic-like region for excitation wavelengths < 250 nm and an emission wavelength of 441 nm of collected AF^4 cross flow waste following an injection of 10 mg C L^{-1} SR NOM in synthetic freshwater. F_{max} measured in SR NOM cross flow waste fractions significantly decreased ($p < 0.01$) upon the addition of both Ag^+ and AgNP. The difference in F_{max} between samples containing Ag^+ and AgNP are not statistically significant. The relative standard deviation of F_{max} values between triplicate sample analysis ranged from 1.1% to 5.5%, with an average of 3.2%. AgNPs do not display fluorescence and no quenching or signal enhancement of SR NOM was observed in the presence of 1.0 µg L^{-1} AgNP or Ag^+ (Appendix 4.3). A corollary experiment was performed using dialysis tubing smaller than the molecular weight cutoff of the AF^4 membrane (3.5 kDa – 5 kDa *vs.* 10 kDa, respectively), to represent the material retained within the AF^4 separation channel and analyzed by ICP-MS (**Figure 4.6b**). An increase of F_{max} signal results from the addition of Ag^+ and AgNP, corroborating the AF^4 cross flow results.

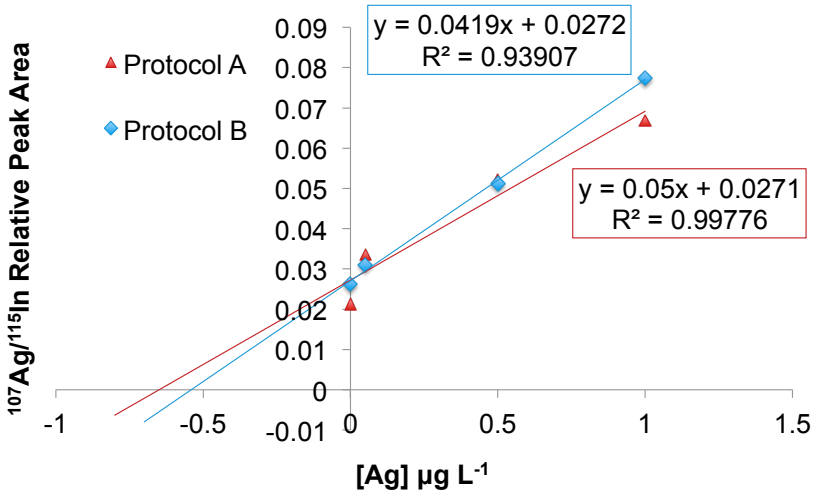

Figure 4.5. Standard addition calibration curve of AgNP in lake water samples using signal peak area of ICP-MS counts for ^{107}Ag normalized to ^{115}In using AF^4 separation protocols (red) A and (blue) B. The "challenge" spike was 0.6 µg L^{-1} AgNP.

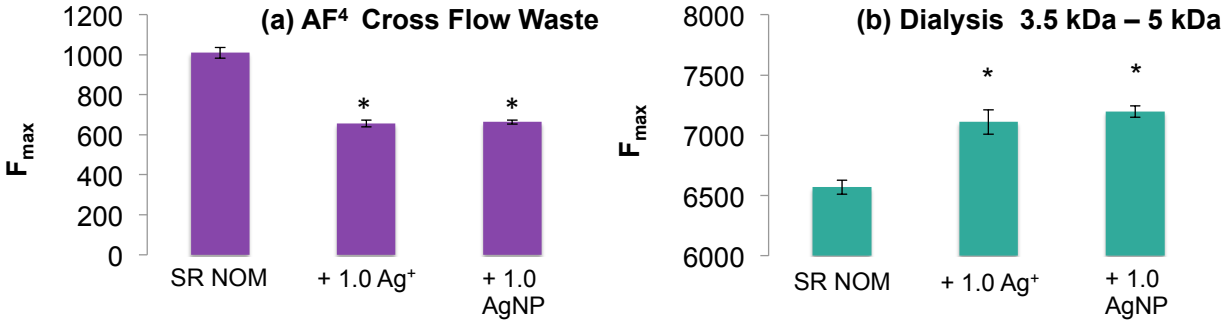

Figure 4.6. Max fluorescence (F_{max}) in Raman units measured for synthetic freshwater containing 5 mg C L^{-1} SR NOM from (a) AF^4 cross flow waste after separation with Protocol A and (b) after dialysis at 3.5 kDa – 5 kDa with the addition of 1.0 µg L^{-1} Ag^+ or 1.0 µg L^{-1} AgNP. Significant differences (*) in F_{max} from SR NOM were determined at $p < 0.01$ for n=3. Error bars represent standard error for n=3.

4.4 Discussion

4.4.1 Stabilizing Effect of NOM on Ag^+ and AgNP

Ag^+ or AgNP injected into AF^4-ICP-MS would be expected to reach the ICP-MS detector with the AF^4 separation channel (including membrane) removed, because analyte loss through the membrane or from particle-membrane interactions would be avoided (**Figure 4.2a**). However, **Figures 4.2a** and **4.2c,** showed that insufficient Ag, as either injected Ag+ or AgNP, respectively, is reaching the ICP-MS detector with the separation channel removed. This stabilization observed upon the addition of SR NOM corroborates Ag-NOM complexation and AgNP-NOM interactions proposed in the literature [6-11].

The instability of AgNP, combined with dilution effects and interactions with the AF^4 tubing, may all be factors contributing to this Ag loss. In the case of synthetic or natural freshwaters, AgCl may have precipitated in the sample vial prior to injection, due to the presence of Cl^- in the synthetic freshwater sample or naturally occurring in the lake water, though, no visual precipitate was observed.

4.4.2. Calibration Variations and Influence of System Components

The differences in amount of Ag reaching the ICP-MS detector in the presence of SR NOM was explored with various system component configurations: with/without the AF^4 membrane present and

with/without a focusing step applied (**Figure 4.3**). Focusing is used to pre-concentrate sample within the AF4 channel prior to separation. Upon the addition of the AF^4 focusing step, a significant decrease in regression slope was observed, suggesting that the addition of an AF^4 flow regime results in a change in the amount of Ag reaching the ICP-MS. Calculations are provided in Appendix 4.1, and AF^4 operations are discussed in detail in Chapter 1 section 1.3.1.a. Over-focusing is known to cause aggregation of humic acids and potential sample loss through the membrane [75, 76], but typically, this focusing step is optimized to minimize sample loss while maximizing separation selectivity by pre-concentrating the sample prior to separation [77]. Combined with the NOM stability effects from **Figure 4.2**, the significant drop in slope with the addition of system components (**Figure 4.3**) emphasizes the need to run any calibration standards within the same system, matrix, and separation parameters as the complex analyte samples to avoid unnecessary variation in the amount of analyte reaching the ICP-MS. Standard addition fits these requirements. While the concentration range tested is at the high end to an order of magnitude higher than of modeled predicted concentrations of AgNP in the aquatic environment [5, 78], there is no a priori reason why these relative slopes might vary as a function of environmentally relevant concentration ranges.

The average recovery of AgNP after AF^4-ICP-MS with the AF^4 membrane installed and focusing step applied was 49.1% - 66.9% compared to that with the membrane removed using equation 4.1:

$$Recovery\ \% = \frac{S}{S_o} \times 100 \qquad (4.1)$$

where S_0 is the ICP-MS $^{107}Ag/^{115}In$ peak area obtained without the AF^4 channel/membrane and S is the peak area obtained with the channel/membrane installed and focusing step applied. Additional losses might be explained due to particle-system or particle-membrane interactions, aggregation behavior under additional flow conditions causing larger clusters to elute after the detection window, and flow fluctuations near the 50% flow split following AF^4 separation and prior to ICP-MS detection.

4.4.3. Ag Speciation in Lake Water and Identification of AgNP Peak in ICP-MS Fractogram

It was hypothesized that, of the three visible ICP-MS Ag signal peaks in **Figure 4.4**, the first peak was primarily Ag^+ and the latter two were more likely to be AgNP or Ag-NOM and AgNP-NOM aggregates. In order to test this hypothesis, Ag^+ enriched with ^{109}Ag was spiked into the lake water samples containing added AgNP. **Figures 4.4a** and **4.4c** are showing only the ^{107}Ag trace, whereas **Figures 4.4b** and **4.4d** are showing the ^{109}Ag trace. The lake water spiked with ^{109}Ag (red trace) in **Figure 4.4a** does not show any measurable ^{107}Ag signal above that of the unspiked raw lake water. However, **Figure 4.4b** shows a strong ^{109}Ag signal around 9 min with increased ^{109}Ag signal throughout the following two peaks (~12 min and ~14min) compared to **Figure 4.4a**. The associated fractograms for Protocol B, with a different cross flow regime, are given in **Figures 4.4c** and **4.4d**, and result in better ICP-MS Ag signal resolution, though the third "peak" (~14 min), more defined in **Figures 4.4a** and **4.4b**, is diminished with the increased cross flow.

The dimished peak ~14min in **Figures 4.4c** and **4.4d**, compared to **Figures 4.4a** and **4.4b**, suggests that the peak at ~14 minutes is comprised of larger aggregates that feel the effects of the cross flow more strongly and are retained longer in the separation channel, broadening the signal and reducing the peak height. Further, the implication is that the first eluting peak (9 min) is almost entirely Ag^+ or small Ag-NOM complexes, since that signal peak responds to $^{109}Ag^+$, while the second peak (12 min) is primarily AgNP, because that signal peak responds to the addition of AgNP. To identify the concentration of Ag as AgNP, this AgNP peak (12 min) was selected for quantification in the next section.

4.4.4 AgNP Quantification

As identified in section 4.4.3 and **Figure 4.4**, the second ^{107}Ag ICP-MS peak is to be used for quantification of AgNP by standard addition in Figure 4.5. It is possible that replicate quantitative analyses with different separation protocols produces a more accurate quantification than using only one separation protocol, compensating for resolution biases and variations in peak selection. However, the regression slopes are not statistically different for $p < 0.05$. While this quantitative analysis is only a preliminary first step towards standard addition application to AgNPs in a natural water, further

experimentation with a wider range of concentrations should be explored to ascertain if the quantitative uncertainty is consistent or if any concentration effects occur, resulting in non-linearity.

4.4.5 Using fluorescence and dialysis to explore sample changes due to potential Ag-NOM and AgNP-NOM interactions

The cross flow waste fraction from AF^4 analysis, containing species less than 10 kDa in molar mass (the molecular weight cutoff of the AF^4 membrane), was expected to contain the unbound dissolved DOM and/or Ag^+, where the NOM material retained in the AF^4 channel is of higher molar mass or aggregated, possibly in Ag-NOM or AgNP-NOM clusters. The decrease in F_{max} observed in **Figure 4.6** upon the addition of Ag^+ or AgNP implies that the Ag^+-NOM and AgNP-NOM interactions affect the size and physical conformation of the NOM particles in the sample, resulting in more material retained within the separation channel and not passing through the membrane. This is in good agreement with the stabilizing effect of NOM discussed in **Figure 4.2**, and could result in more Ag reaching the ICP-MS detector. If quantitation is performed without taking this increased NOM and enhanced Ag signal into account, the resulting concentration might be overestimated. This change in F_{max} signal indicates that the molar mass of NOM within the channel is increasing, perhaps due to Ag-NOM and AgNP-NOM interactions.

REFERENCES

1. Alvarez, P.J.J.; Colvin, V.; Lead, J.; Stone, V. Research Priorities to Advance Eco-Responsible Nanotechnology. *ACS Nano* **2009,** *3,* 1616-1619.

2. Woodrow Wilson International Center for Scholars Project on Emerging Nanotechnology. **2010,** http://www.nanotechproject.org/

3. Tiede, K.; Hassellöv, M.; Breitbarth, E.; Chaudhry, Q.; Boxall, A.B.A. Considerations for environmental fate and ecotoxicity testing to support environmental risk assessments for engineered nanoparticles. *J. Chromatogr. A* **2009,** *1216,* 503-509.

4. Batley, G.E.; Kirby, J.K.; McLaughlin, M.J. Fate and Risks of Nanomaterials in Aquatic and Terrestrial Environments. *Acc. Chem. Res.* **2013,** *46,* 854-862.

5. Mueller, N.C. and Nowack, B. Exposure modeling of engineered nanoparticles in the environment. *Environ. Sci. Technol.* **2008,** *42,* 4447-4453.

6. Philippe, A. and Schaumann, G.E. Interactions of Dissolved Organic Matter with Natural and Engineered Inorganic Colloids: A Review. *Environ. Sci. Technol.* **2014,** *48,* 8946-8962.

7. Louie, S.M.; Tilton, R.D.; Lowry, G.V. Effects of Molecular Weight Distribution and Chemical Properties of Natural Organic Matter on Gold Nanoparticle Aggregation. *Environ. Sci. Technol.* **2013,** *47,* 4245-4254.

8. Sanchez-Cortes, S.; Francioso, O.; Ciavatta, C.; Garcia-Ramos, J.V.; Gessa, C. pH-dependent adsorption of fractionated peat humic substances on different silver colloids studied by surface-enhanced Raman spectroscopy. *J. Colloid Interface Sci.* **1998,** *198,* 308-318.

9. Litvin, V.A.; Galagan, R.L.; Minaev, B.F. Kinetic and mechanism formation of silver nanoparticles coated by synthetic humic substances. *Colloids Surf. A: Physiochem. Eng. Asp.* **2012,** *414,* 234-243.

10. Bae, E.; Park, H.; Yoon, J.; Kim, Y.; Choi, K.; Yi, J. Bacterial uptake of silver nanoparticles in the presence of humic acid and AgNO3. *Korean J. Chem. Eng.* **2011,** *28,* 267-271.

11. Lau, B.L.T.; Hockaday, W.C.; Ikuma, K.; Furman, O.; Decho, A.W. A preliminary assessment of the interactions between the capping agents of silver nanoparticles and environmental organics. *Colloids Surf. A: Physiochem. Eng. Asp.* **2013,** *435,* 22-27.

12. Zou, X.; Shi, J.; Zhang, H. Morphological evolution and reconstruction of silver nanoparticles in aquatic environments: The roles of natural organic matter and light irradiation. *J. Hazard. Mater.* **2015,** *292,* 61-69.

13. Gunsolus, I.L.; Mousavi, M.P.S.; Hussein, K.; Buehlmann, P.; Haynes, C.L. Effects of Humic and Fulvic Acids on Silver Nanoparticle Stability, Dissolution, and Toxicity. *Environ. Sci. Technol.* **2015,** *49,* 8078-8086.

14. Yin, Y.; Shen, M.; Zhou, X.; Yu, S.; Chao, J.; Liu, J.; Jiang, G. Photoreduction and Stabilization Capability of Molecular Weight Fractionated Natural Organic Matter in Transformation of Silver Ion to Metallic Nanoparticle. *Environ. Sci. Technol.* **2014,** *48,* 9366-9373.

15. Yin, Y.; Shen, M.; Tan, Z.; Yu, S.; Liu, J.; Jiang, G. Particle Coating-Dependent Interaction of Molecular Weight Fractionated Natural Organic Matter: Impacts on the Aggregation of Silver Nanoparticles. *Environ. Sci. Technol.* **2015,** *49,* 6581-6589.

16. Kanel, S.R.; Flory, J.; Meyerhoefer, A.; Fraley, J.L.; Sizemore, I.E.; Goltz, M.N. Influence of natural organic matter on fate and transport of silver nanoparticles in saturated porous media: laboratory experiments and modeling. *J. Nanopart. Res.* **2015,** *17,* 154.

17. Cupi, D.; Hartmann, N.B.; Baun, A. The Influence of Natural Organic Matter and Aging on Suspension Stability in Guideline Toxicity Testing of Silver, Zinc Oxide, and Titanium Dioxide Nanoparticles with Daphnia Magna. *Environ. Toxicol. Chem.* **2015,** *34,* 497-506.

18. Grillo, R.; Rosa, A.H.; Fraceto, L.F. Engineered nanoparticles and organic matter: A review of the state-of-the-art. *Chemosphere* **2015,** *119,* 608-619.

19. Wagner, S.; Gondikas, A.; Neubauer, E.; Hofmann, T.; von der Kammer, F. Spot the Difference: Engineered and Natural Nanoparticles in the Environment-Release, Behavior, and Fate. *Angew. Chem. - Int. Edit.* **2014,** *53,* 12398-12419.

20. Khaksar, M.; Jolley, D.F.; Sekine, R.; Vasilev, K.; Johannessen, B.; Donner, E.; Lombi, E. In Situ Chemical Transformations of Silver Nanoparticles along the Water-Sediment Continuum. *Environ. Sci. Technol.* **2015,** *49,* 318-325.

21. Zhang, Y.; Chen, Y.; Westerhoff, P.; Crittenden, J. Impact of natural organic matter and divalent cations on the stability of aqueous nanoparticles. *Water Res.* **2009,** *43,* 4249-4257.

22. Keller, A.A.; Wang, H.; Zhou, D.; Lenihan, H.S.; Cherr, G.; Cardinale, B.J.; Miller, R.; Ji, Z. Stability and Aggregation of Metal Oxide Nanoparticles in Natural Aqueous Matrices. *Environ. Sci. Technol.* **2010,** *44,* 1962-1967.

23. Filella, M. Freshwaters: which NOM matters? *Environ. Chem. Lett.* **2009,** *7,* 21-35.

24. Piccolo, A. The supramolecular structure of humic substances. *Soil Sci.* **2001,** *166,* 810-832.

25. Ju-Nam, Y. and Lead, J.R. Manufactured nanoparticles: An overview of their chemistry, interactions and potential environmental implications. *Sci. Total Environ.* **2008,** *400,* 396-414.

26. Chow, A.T.; Guo, F.; Gao, S.; Breuer, R.; Dahlgren, R.A. Filter pore size selection for characterizing dissolved organic carbon and trihalomethane precursors from soils. *Water Res.* **2005,** *39,* 1255-1264.

27. Jones, M.N. and Bryan, N.D. Colloidal properties of humic substances. *Adv. Colloid Interface Sci.* **1998,** *78,* 1-48.

28. Baalousha, M.; Motelica-Heino, M.; Le Coustumer, P. Conformation and size of humic substances: Effects of major cation concentration and type, pH, salinity, and residence time. *Colloids Surf. A: Physiochem. Eng. Asp.* **2006,** *272,* 48-55.

29. Avena, M.J. and Wilkinson, K.J. Disaggregation kinetics of a peat humic acid: Mechanism and pH effects. *Environ. Sci. Technol.* **2002,** *36,* 5100-5105.

30. Unrine, J.M.; Colman, B.P.; Bone, A.J.; Gondikas, A.P.; Matson, C.W. Biotic and Abiotic Interactions in Aquatic Microcosms Determine Fate and Toxicity of Ag Nanoparticles. Part 1. Aggregation and Dissolution. *Environ. Sci. Technol.* **2012,** *46,* 6915-6924.

31. Bone, A.J.; Colman, B.P.; Gondikas, A.P.; Newton, K.M.; Harrold, K.H.; Cory, R.M.; Unrine, J.M.; Klaine, S.J.; Matson, C.W.; Di Giulio, R.T. Biotic and Abiotic Interactions in Aquatic Microcosms

Determine Fate and Toxicity of Ag Nanoparticles: Part 2-Toxicity and Ag Speciation. *Environ. Sci. Technol.* **2012,** *46,* 6925-6933.

32. El Badawy, A.M.; Silva, R.G.; Morris, B.; Scheckel, K.G.; Suidan, M.T.; Tolaymat, T.M. Surface Charge-Dependent Toxicity of Silver Nanoparticles. *Environ. Sci. Technol.* **2011,** *45,* 283-287.

33. Dasari, T.P. and Hwang, H. The effect of humic acids on the cytotoxicity of silver nanoparticles to a natural aquatic bacterial assemblage. *Sci. Total Environ.* **2010,** *408,* 5817-5823.

34. Gondikas, A.P.; Morris, A.; Reinsch, B.C.; Marinakos, S.M.; Lowry, G.V.; Hsu-Kim, H. Cysteine-Induced Modifications of Zero-valent Silver Nanomaterials: Implications for Particle Surface Chemistry, Aggregation, Dissolution, and Silver Speciation. *Environ. Sci. Technol.* **2012,** *46,* 7037-7045.

35. Fabrega, J.; Luoma, S.N.; Tyler, C.R.; Galloway, T.S.; Lead, J.R. Silver nanoparticles: Behaviour and effects in the aquatic environment. *Environ. Int.* **2011,** *37,* 517-531.

36. Cory, R.M.; Boyer, E.W.; McKnight, D.M. Spectral Methods to Advance Understanding of Dissolved Organic Carbon Dynamics in Forested Catchments. *Ecol. Stud.* **2011,** *216,* 117-135.

37. Hautala, K.; Peuravuori, J.; Pihlaja, K. Measurement of aquatic humus content by spectroscopic analyses. *Water Res.* **2000,** *34,* 246-258.

38. Peuravuori, J.; Koivikko, R.; Pihlaja, K. Characterization, differentiation and classification of aquatic humic matter separated with different sorbents: synchronous scanning fluorescence spectroscopy. *Water Res.* **2002,** *36,* 4552-4562.

39. Chen, J.; LeBoeuf, E.J.; Dai, S.; Gu, B. Fluorescence spectroscopic studies of natural organic matter fractions. *Chemosphere* **2003,** *50,* 639-647.

40. Coble, P.G.; Green, S.A.; Blough, N.V.; Gagosian, R.B. Characterization of Dissolved Organic-Matter in the Black-Sea by Fluorescence Spectroscopy. *Nature* **1990,** *348,* 432-435.

41. McKnight, D.M.; Boyer, E.W.; Westerhoff, P.K.; Doran, P.T.; Kulbe, T.; Andersen, D.T. Spectrofluorometric characterization of dissolved organic matter for indication of precursor organic material and aromaticity. *Limnol. Oceanogr.* **2001,** *46,* 38-48.

42. Del Vecchio, R. and Blough, N.V. On the origin of the optical properties of humic substances. *Environ. Sci. Technol.* **2004,** *38,* 3885-3891.

43. Boyle, E.S.; Guerriero, N.; Thiallet, A.; Del Vecchio, R.; Blough, N.V. Optical Properties of Humic Substances and CDOM: Relation to Structure. *Environ. Sci. Technol.* **2009,** *43,* 2262-2268.

44. Świetlik, J. and Sikorska, E. Application of fluorescence spectroscopy in the studies of natural organic matter fractions reactivity with chlorine dioxide and ozone. *Water Res.* **2004,** *38,* 3791-3799.

45. Linsinger, T.; Roebben, G.; Gilliland, D.; Calzolai, L.; Rossi, F.; Gibson, N.; Klein, C. Requirements on measurements for the implementation of the European Commission definition of the term "nanomaterials", In *JRC Reference Reports,* Anonymous ; European Commission Joint Research Center, Institute for Reference Materials and Measurements: 2012; pp. 52.

46. Dubascoux, S.; Le Hecho, I.; Hassellöv, M.; Von der Kammer, F.; Gautier, M.P.; Lespes, G. Field-flow fractionation and inductively coupled plasma mass spectrometer coupling: History, development and applications. *J. Anal. At. Spectrom.* **2010,** *25,* 613-623.

47. Loeschner, K.; Navratilova, J.; Kobler, C.; Molhave, K.; Wagner, S.; von der Kammer, F.; Larsen, E.H. Detection and characterization of silver nanoparticles in chicken meat by asymmetric flow field flow fractionation with detection by conventional or single particle ICP-MS. *Anal. Bioanal. Chem* **2013,** *405,* 8185-8195.

48. Ramos, K.; Ramos, L.; Camara, C.; Gomez-Gomez, M.M. Characterization and quantification of silver nanoparticles in nutraceuticals and beverages by asymmetric flow field flow fractionation coupled with inductively coupled plasma mass spectrometry. *J. Chromatogr. A* **2014,** *1371,* 227-236.

49. Hoque, M.E.; Khosravi, K.; Newman, K.; Metcalfe, C.D. Detection and characterization of silver nanoparticles in aqueous matrices using asymmetric-flow field flow fractionation with inductively coupled plasma mass spectrometry. *J. Chromatogr. A* **2012,** *1233,* 109-115.

50. Poda, A.R.; Bednar, A.J.; Kennedy, A.J.; Harmon, A.; Hull, M.; Mitrano, D.M.; Ranville, J.F.; Steevens, J. Characterization of silver nanoparticles using flow-field flow fractionation interfaced to inductively coupled plasma mass spectrometry. *J. Chromatogr. A* **2011,** *1218,* 4219-4225.

51. Geiss, O.; Cascio, C.; Gilliland, D.; Franchini, F.; Barrero-Moreno, J. Size and mass determination of silver nanoparticles in an aqueous matrix using asymmetric flow field flow fractionation coupled to inductively coupled plasma mass spectrometer and ultraviolet-visible detectors. *J. Chromatogr. A* **2013,** *1321,* 100-108.

52. Dubascoux, S.; Le Hecho, I.; Gautier, M.P.; Lespes, G. On-line and off-line quantification of trace elements associated to colloids by As-Fl-FFF and ICP-MS. *Talanta* **2008,** *77,* 60-65.

53. Ranville, J.F.; Chittleborough, D.J.; Shanks, F.; Morrison, R.J.S.; Harris, T.; Doss, F.; Beckett, R. Development of sedimentation field-flow fractionation-inductively coupled plasma mass-spectrometry for the characterization of environmental colloids. *Anal. Chim. Acta* **1999,** *381,* 315-329.

54. Hassellov, M.; Lyven, B.; Haraldsson, C.; Sirinawin, W. Determination of continuous size and trace element distribution of colloidal material in natural water by on-line coupling of flow field-flow fractionation with ICPMS. *Anal. Chem.* **1999,** *71,* 3497-3502.

55. Lyven, B.; Hassellov, M.; Turner, D.R.; Haraldsson, C.; Andersson, K. Competition between iron- and carbon-based colloidal carriers for trace metals in a freshwater assessed using flow field-flow fractionation coupled to ICPMS. *Geochim. Cosmochim. Acta* **2003,** *67,* 3791-3802.

56. Stolpe, B.; Hassellöv, M.; Andersson, K.; Turner, D.R. High resolution ICPMS as an on-line detector for flow field-flow fractionation; multi-element determination of colloidal size distributions in a natural water sample. *Anal. Chim. Acta* **2005,** *535,* 109-121.

57. Bouby, M.; Geckeis, H.; Geyer, F.W. Application of asymmetric flow field-flow fractionation (AsFlFFF) coupled to inductively coupled plasma mass spectrometry (ICPMS) to the quantitative characterization of natural colloids and synthetic nanoparticles. *Anal. Bioanal. Chem.* **2008,** *392,* 1447-1457.

58. Liu, J.; Yu, S.; Yin, Y.; Chao, J. Methods for separation, identification, characterization and quantification of silver nanoparticles. *Trac-Trend. Anal. Chem.* **2012,** *33,* 95-106.

59. Zook, J.M.; Long, S.E.; Cleveland, D.; Geronimo, C.L.A.; MacCuspie, R.I. Measuring silver nanoparticle dissolution in complex biological and environmental matrices using UV-visible absorbance. *Anal. Bioanal. Chem.* **2011,** *401,* 1993-2002.

60. MacCuspie, R.I.; Rogers, K.; Patra, M.; Suo, Z.; Allen, A.J.; Martin, M.N.; Hackley, V.A. Challenges for physical characterization of silver nanoparticles under pristine and environmentally relevant conditions. *J. Environ. Monitor.* **2011,** *13,* 1212-1226.

61. Gigault, J. and Hackley, V.A. Differentiation and characterization of isotopically modified silver nanoparticles in aqueous media using asymmetric-flow field flow fractionation coupled to optical detection and mass spectrometry. *Anal. Chim. Acta* **2013,** *763,* 57-66.

62. Levard, C.; Mitra, S.; Yang, T.; Jew, A.D.; Badireddy, A.R.; Lowry, G.V.; Brown, G.E., Jr. Effect of Chloride on the Dissolution Rate of Silver Nanoparticles and Toxicity to E. coli. *Environ. Sci. Technol.* **2013,** *47,* 5738-5745.

63. Li, X.; Lenhart, J.J.; Walker, H.W. Dissolution-Accompanied Aggregation Kinetics of Silver Nanoparticles. *Langmuir* **2010,** *26,* 16690-16698.

64. Li, X. Aggregation Kinetics and Dissolution of Coated Silver Nanoparticles. *Langmuir* **2012,** *28,* 1095-1104.

65. Liu, J. and Hurt, R.H. Ion Release Kinetics and Particle Persistence in Aqueous Nano-Silver Colloids. *Environ. Sci. Technol.* **2010,** *44,* 2169-2175.

66. Badawy, A.M.E.; Luxton, T.P.; Silva, R.G.; Scheckel, K.G.; Suidan, M.T.; Tolaymat, T.M. Impact of Environmental Conditions (pH, Ionic Strength, and Electrolyte Type) on the Surface Charge and Aggregation of Silver Nanoparticles Suspensions. *Environ. Sci. Technol.* **2010,** *44,* 1260-1266.

67. Elzey, S. and Grassian, V.H. Agglomeration, isolation and dissolution of commercially manufactured silver nanoparticles in aqueous environments. *J. Nanopart. Res.* **2010,** *12,* 1945-1958.

68. Chinnapongse, S.L.; MacCuspie, R.I.; Hackley, V.A. Persistence of singly dispersed silver nanoparticles in natural freshwaters, synthetic seawater, and simulated estuarine waters. *Sci. Total Environ.* **2011,** *409,* 2443-2450.

69. Delay, M.; Dolt, T.; Woellhaf, A.; Sembritzki, R.; Frimmel, F.H. Interactions and stability of silver nanoparticles in the aqueous phase: Influence of natural organic matter (NOM) and ionic strength. *J. Chromatogr. A* **2011,** *1218,* 4206-4212.

70. Brezonik, Patrick L., Arnold,William A., *Water chemistry : an introduction to the chemistry of natural and engineered aquatic systems.* Oxford University Press: New York, 2011;

71. nanoComposix NanoXact. *2015,* http://nanocomposix.com/collections/silver-spheres/products/10-nm-silver-nanospheres

72. APHA (American Public Health Association); American Water Works Association; Water Environmental Federation In *Standard Methods for the Examination of Water and Wastewater,* 20th ed.; Anonymous ; American Public Health Association: Washington, D.C., 1999;

73. Stedmon, C. and Markager, S. Resolving the variability in dissolved organic matter fluorescence in a temperate estuary and its catchment using PARAFAC analysis. *Limnol. Oceanogr.* **2005,** *50,* 686-697.

74. Lakowicz, J.R. *Principles of Fluorescence Spectroscopy.* Springer: New York, 2006;

75. Wahlund, K. Flow field-flow fractionation: Critical overview. *J. Chromatogr. A* **2013,** *1287,* 97-112.

76. Schimpf, M.E. and Wahlund, K. Asymmetrical flow field-flow fractionation as a method to study the behavior of humic acids in solution. *J. Microcolumn Sep.* **1997,** *9,* 535-543.

77. Schimpf, M.E.; Caldwell, K.; Giddings, J.C. Field Flow Fractionation Handbook. *Wiley, New York* **2000,** 616.

78. Boxall, A.B.A.; Tiede, K.; Chaudhry, Q. Engineered nanomaterials in soils and water: How do they behave and could they pose a risk to human health? *Nanomedicine* **2007,** *2,* 919-927.

79. Giddings, J.C.; Yang, F.J.; Myers, M.N. Flow Field-Flow Fractionation: A Versatile New Separation Method. *Science* **1976,** *193,* 1244.

80. Giddings, J.C. New separation concept based on a coupling of concentration and flow non-uniformities. *Sep. Sci.* **1966,** *1,* 123.

81. Giddings, J. Field-Flow Fractionation - Analysis of Macromolecular, Colloidal, and Particulate Materials. *Science* **1993,** *260,* 1456-1465.

82. De Laeter, J.; Bohlke, J.; De Bievre, P.; Hidaka, H.; Peiser, H.; Rosman, K.; Taylor, P. Atomic weights of the elements: Review 2000 - (IUPAC technical report). *Pure Appl. Chem.* **2003,** *75,* 683-800.

CHAPTER 5: CONCLUSIONS

Determining the fate, form, and concentration of an unknown ENP pollutant in an environmental matrix is a very complex objective that requires a complex approach. Efforts to evolve new product and removal treatment technologies are hindered by the uncertainty of ENP fate and transport in the environment. Scientists and engineers must come together to develop effective methods to target ENPs and make accurate quantitative conclusions, as a perspective on the levels and types of ENPs present in aquatic systems will help designers engineer treatments to improve removal if occurrence levels suggest an unacceptable risk of exposure. Moreover, the dissemination of such information is needed to allay public fears related to the risk from use of products containing ENPs and risk from exposure. It is essential that interfaces between separation and detection or characterization techniques continue to be developed and utilized for the study of ENPs in the environment so as to minimize sample handling and its impact on NP physical state, and to provide comprehensive characterization on the same sample. The research presented in this dissertation was a first step towards these goals by selecting an environmentally relevant ENP, AgNP, with known persistence and toxicity. The lack in overall understanding of how AgNPs in freshwaters may affect human and environmental health represents an important opportunity for researchers to develop analytical strategies that specifically target AgNPs once they are released into the environment. To this end, an optimized and rigorously explored multi-step analytical strategy was presented, providing the foundation for obtaining AgNP occurrence data in complex aquatic matrices needed by regulators, utilities, and engineers. Existing methods often lack robust experimental design and environmentally relevant conditions, two major targets of the described work. The combined use of chemical separations with physicochemical characterization and quantitation techniques was the basis of this thesis.

The use of AF^4 integrated with ICP-MS was evaluated to separate and quantify AgNPs in natural lake and synthetic waters using a standard addition analysis. The addition of online UV and MALS detectors was used to monitor NOM separation. Offline fluorescence spectroscopy was utilized to better

understand potential AgNP-NOM and Ag-NOM interactions in SR NOM- and laboratory-prepared freshwaters. Furthermore, a rigorous sensitivity analysis was used to identify which AF^4 primary/instrument variables had the most influence on NOM separation in laboratory freshwater samples containing SR NOM and AgNPs. Overall, this project defined and optimized an exhaustive on-line analytical process for characterizing and quantifying AgNPs in aquatic samples. These investigations provide a methodology for measurement of the release of AgNPs into the aquatic environment and, thereby, a scientific basis for adequate and reasonable regulation of these and potentially other ENPs.

Chapter 2 objectives:

- Develop a separation metric for determining relative AF^4 separation protocol success.
- Demonstrate separation metric using a polystyrene bead mixture as a model system for polydisperse samples such as AgNPs in natural waters.

The analysis of natural and otherwise complex samples is challenging and yields uncertainty about the accuracy and precision of measurements. A practical tool was developed that assessed the relative accuracy among AF^4 separation protocols for techniques using light scattering detection. Due to the highly non-linear relationship between particle size and the intensity of scattered light, a few large particles may obfuscate greater numbers of small particles. Therefore, insufficiently separated mixtures may result in an overestimate of the average measured particle size. Complete separation of complex samples is needed to mitigate this challenge. As a demonstration, this assessment metric was applied to optimization of cross flow protocols in AF^4 separation interfaced with online QELS detection using mixtures of polystyrene beads spanning a large size range. Using this assessment metric, the cross flow factor was modulated to improve separation until the average measured size of the mixture was in statistical agreement with the calculated average size of particles in the mixture.

Chapter 2 introduced a new metric for optimizing separations of polydisperse samples through a demonstration using AF^4-QELS with a model system of polystyrene bead mixtures in order to mimic complex samples. The comparison of average measured size between separation parameters provides an analytical means for objectively converging to the optimal combination of instrumental parameters and identifying a separation protocol that sufficiently separates a polydisperse mixture of nanoparticles,

especially when separation theory and observations of the raw data become difficult to apply to complex samples. By identifying a separation protocol that is of sufficient selectivity, large and small particles are separated in such a way that they are detected distinctly, resulting in an overall lower average particle size measurement. One separation protocol can be considered improved if the average measured particle size is smaller than the previous separation protocol. Further, the protocol resulting in the smallest average measured particle size yields the best separation among those explored. If the differential in average measured size between protocols is less than the measurement uncertainty, then the selected protocols are of equivalent precision. Additionally, this metric established a methodology of identifying a quality separation while minimizing unnecessary analysis time. Although demonstrated by improving AF^4 cross flow factor settings using AF^4-QELS, the separation metric and step-wise approach are applicable to any chromatography technique coupled with dynamic light scattering detection.

Chapter 3 Objectives:

- Evaluate and rank the various separation protocols on their ability to minimize the average measured molar mass of NOM – in each sample to ultimately establish the optimization recommendations.
- Develop and perform a sensitivity analysis using AF^4-MALS-UV to identify AF^4 instrument factors with the highest impact on separation of AgNPs in laboratory-prepared freshwater samples continuing SR NOM.

AF^4 has several instrumental parameters that likely have a direct effect on separation performance. Any AF^4 separation and subsequent analysis directly depends on the primary/instrumental factors and their settings, which vary between instruments and sample requirements. Therefore, a structured methodology of statistical DEX and sensitivity analysis is useful to better understand how the system output is affected by the system inputs. To this end, a sensitivity analysis was applied to ascertain the relative importance of AF^4 primary/instrumental factor settings towards the separation of a laboratory-prepared synthetic freshwater containing AgNPs and SR NOM. Chapter 3 described a systematic investigation of the impact of primary/instrumental factors: cross flow, ramp time, focus flow, injection volume, and run buffer concentration on the MALS measurement of NOM molar mass. A $2^{(5-1)}$ orthogonal

fractional factorial design, with parallel $2^{(5-2)}$ design for environmental/robustness factors, was used to minimize analysis time while preserving the accuracy and robustness of the main effects and 2-way interactions. By assuming that separations resulting in the ability to measure smaller MM measurements would be more accurate, the analysis produced a ranked list of effects estimates for factors and interactions based on their relative importance in minimizing the MM when changed from low to high settings.

The sensitivity analysis and extensive EDA analysis concluded that two primary/instrument factors, buffer and cross flow, are important, within the range of robustness factor conditions explored, and make a difference to the system output, minimizing measured MM range of NOM, when changed. These conclusions make experimental sense and were expected, as buffer ionic strength and hydrodynamic flows are known to have a major impact on NP separations. The methodology and approach are not specific to AgNPs, however, and can be applied to any natural matrix containing ENPs, though their effects on the separation of natural samples as a function of NOM MM still needs to be explored. Optimization that follows the path of steepest descent suggests smaller values for both to minimize sample aggregation or separations of limited selectivity. The robustness/environmental factors were found to be insignificant compared to the primary/instrumental factors, suggesting that the separation protocols tested were valid across the range of water quality characteristics explored. In order to obtain consistent, robust, and reproducible results, it is critically important to explore and fully understand the system as a whole, relative to the robustness/environmental characteristics, an approach not often explored. Future studies for improved modeling and prediction should evaluate both primary/instrumental and robustness/environmental factors. Ultimately, identifying important instrumental factors and their best settings saves time in optimization studies, which then simply require modification from a rigorously defined starting point.

Chapter 4 Objectives:

- Interface AF^4 -ICP-MS systems for online analysis
- Quantify AgNPs in natural lake water using AF^4-ICP-MS by applying a standard addition analysis.

- Explore potential AgNP-NOM and Ag^+-NOM interactions within the AF^4 separation channel using offline fluorescence spectroscopy.

With the likely release of ENPs into the aquatic environment, developing appropriate analytical methods for occurrence surveys has become a priority. Chapter 4 aimed to explore, and to an extent validate, standard addition quantification of AgNPs in lake water with the combined use of AF^4 separations coupled online with ICP-MS elemental characterization. The contribution of various AF^4 system components, such as the AF^4 membrane and focusing step, and the presence of NOM were explored to determine how these affect the quantitation of Ag by ICP-MS. A standard addition method was applied by adding standard AgNPs for ICP-MS concentration calibration directly to the lake water samples prior to AF^4-ICP-MS analysis. The standard addition approach is useful in that it compensates for both matrix and system complexity, where analyte recovery and potential interactions within the sample are not yet fully explored. For example, the effects of NOM on Ag and AgNP stability in the form of AgNP-NOM and Ag-NOM interactions would be accounted for. This methodology and characterization approach allows for accurate quantification of AgNPs in complex natural water matrices, as the basis for new risk assessment tools and occurrence surveys in aquatic environments. Isotope-enriched $^{109}Ag^+$ was used to identify Ag speciation in the ICP-MS fractogram following AF^4 separation. Further investigations into the amount of NOM retained within the AF^4 separation channel as a factor of potential Ag^+-NOM and AgNP-NOM interactions were performed using fluorescence spectroscopy, by measuring the fluorescent fraction of SR NOM in laboratory–prepared freshwater samples containing either AgNPs or Ag^+. Offline fractions were collected from the AF^4 cross flow waste, or the sample fraction that passed through the AF^4 membrane, for offline analysis to explore changes in intensity occurring with the addition of AgNP or Ag^+.

The concentration of a “challenge” AgNP spike (0.6 µg L^{-1}) was measured with AF^4-ICP-MS to within 0.04 µg L^{-1} Ag. Offline fluorescence results suggest that the addition of either Ag^+ or AgNPs increases the physical conformation and molar mass of NOM particles in the sample. High molecular weight organic material, which is not always biodegradeable, can be difficult for water treatment processes, and might require additional treatment steps in order to remove of a wide organic material MM range. Inadequately removed high molecular weight NOM complexes containing ENPs might increase the

risk of ENP persistence in the aquatic environment. This study demonstrates proof of principle that AF^4-ICP-MS with a standard addition analysis quantitative approach is a promising technique for the quantification of AgNPs in real natural water samples, though the methodology can be extended to examine both Ag^+ and AgNP phases and their transformations. Similarly, this approach is not specific to AgNPs and can be extrapolated to other ENPs systems containing inorganic metal that can be detected by ICP-MS.

Final Reflections

Overall, the primary goal of this work was establishing an approach for new risk assessment tools of AgNPs in aquatic environments by developing a practical, effective, and rigorously explored method for application in occurrence surveys, including their quantitation and detection in natural water. Risk assessments are required to develop adequate environmental protection policy that continues to encourage nanotechnology, but these assessments cannot be developed without thorough occurrence data. Such data can then be used to assess the effectiveness of, or make adjustments to, conventional water treatment processes to protect public and environmental health related AgNP exposure and provide for the dissemination of such information to the public. This work provides the foundation for future applications that will generate occurrence data needed by regulators, utilities, and consulting engineers to demonstrate the effectiveness of current water treatment technology towards complete removal of AgNPs. However, while AgNPs were used in this work to ensure environmentally relevant matrix complexity, the methods developed in this research are not specific to AgNPs alone, and can be applied towards the separation and quantitation of other metal-containing ENPs that can be detected by ICP-MS. Future work should explore the applicability of these methods to other ENPs in natural waters. While a full sensitivity analysis for each instrumental combination is not required to perform successful quantitative experiments, it can be used to better understand the relationship between instrumental factors and experimental output and ultimately reduce optimization time for each target analyte by establishing these relationships for natural matrices. The quantitative analysis performed in this work was only a preliminary first step towards standard addition application to AgNPs and other ENPs in natural waters. Further experimentation with a wider range of concentrations should be explored to ascertain if the quantitative

uncertainty is consistent and if concentration effects occur. Additionally, quantitation needs to be performed with a variety of natural freshwater types and compositions, before the methodology can be confirmed for use in occurrence surveys.

APPENDIX 2.1: FLOWCHART SHOWING STATISTICAL APPROACH TO OPTIMIZING SEPARATION

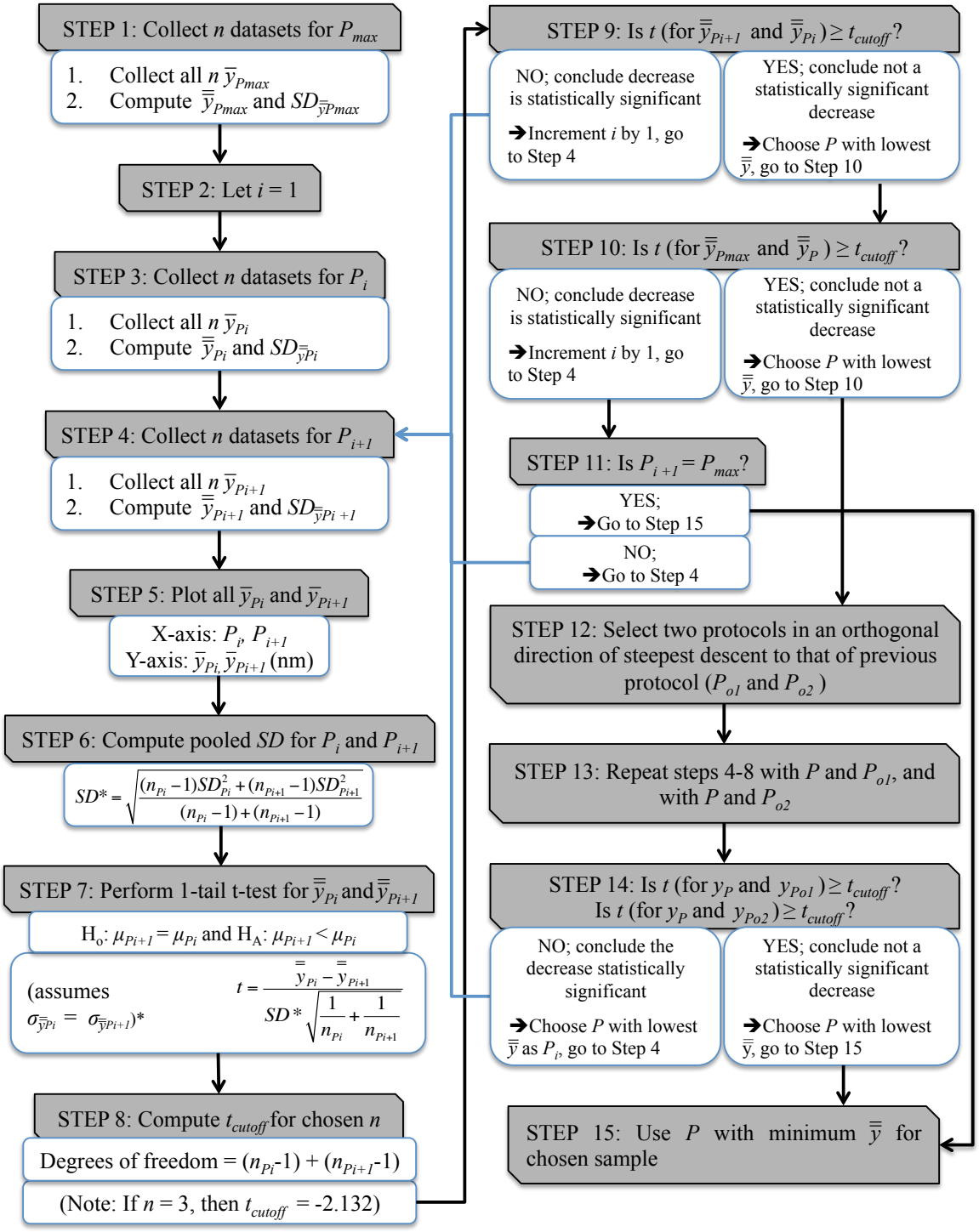

APPENDIX 2.3: Flowchart showing statistical approach to optimizing separation of polydisperse samples by minimizing the average measured radius. *A Levene's/F-Test can be performed to determine if the population variances are equal.

APPENDIX 2.2: STATISTICAL APPROACH WORKED EXAMPLE

Appendix 2.2: Detailed description of each step in statistical approach and worked example using Sample 2 polystyrene mixture based on Figures S-3, and Figures 3, and 4.

Procedure	***Example: Sample 2***
Step 1: select a protocol (*P*) of the highest retention practical for its application (i.e. maximum analysis time), such as a protocol with high cross flow and a long elution time. This protocol is designated P_{max}, and is used to evaluate whether or not the optimized P is the best possible in the limit of high retention. The average measured size, $\bar{y}$ ($\bar{y}_{Pmax}$), should be collected for n datasets. Finally, compute the combined average, $\bar{\bar{y}}$ ($\bar{\bar{y}}_{Pmax}$) and standard deviation, *SD* ($SD_{\bar{\bar{y}}_{Pmax}}$). Continue to Step 2.	**(1)** P_{max}: Crossflow (V_x) = 2.99 mL min^{-1} Elution time = 60 min $\bar{y}_{Pmax}$ (n = 3): 29.6 nm, 29.6 nm, 29.3 nm $\bar{\bar{y}}_{Pmax}$ = 29.5 nm $SD_{\bar{\bar{y}}_{Pmax}}$ = 0.2 nm ➔Proceed to Step 2
Step 2: let i = 1. Continue to Step 3.	**(2)** i = 1. ➔Proceed to Step 3
Step 3: select P_i of low retention (i.e. low cross flow and short elution time). Collect all $\bar{y}_{Pi}$ for n repetitions, while ignoring SD_{Pi} under the assumption of statistical parsimony, where the standard deviation within each protocol will be insignificant when compared to the standard deviation between protocols. Compute $\bar{\bar{y}}_{Pi}$ and $SD_{\bar{\bar{y}}_{Pi}}$. Continue to Step 4.	**(3)** P_i (label A): V_x = 0.25 mL min^{-1} Elution time = 10 min $\bar{y}_{Pmax}$ (n = 3): 35.8 nm, 35.5 nm, 35.5 nm $\bar{\bar{y}}_{Pi}$ = 35.6 nm $SD_{\bar{\bar{y}}_{Pi}}$ = 0.2 nm ➔Proceed to Step 4
Step 4: select protocol of higher retention than P_i (P_{i+1}). Collect all $\bar{y}_{Pi+1}$ for n repetitions Compute $\bar{\bar{y}}_{Pi+1}$ and $SD_{\bar{\bar{y}}_{Pi+1}}$. Continue to Step 5.	**(4)** P_{i+1} (label B): Vx = 0.50 mL min^{-1} Elution time = 20 min $\bar{y}_{Pi+1}$ (n = 3): 32.3 nm, 32.4 nm, 32.7 nm $\bar{\bar{y}}_{Pi+1}$ = 32.5 nm $SD_{\bar{\bar{y}}_{Pi+1}}$ = 0.2 nm ➔Proceed to Step 5
Step 5: Plot all $\bar{y}_{Pi}$ and $\bar{y}_{Pi+1}$ to gain a visual representation of the difference in $\bar{\bar{y}}$ and better identify trend towards optimization. Continue to Step 6.	**(5)** 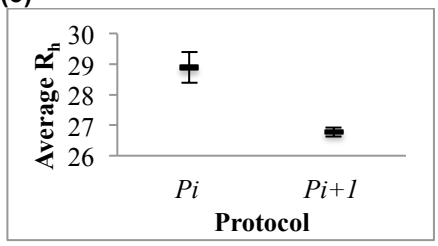 ➔ Proceed to Step 6

Step 6: Compute pooled *SD* (*SD**) for P_i and P_{i+1}. Continue to Step 7.

$$SD^* = \sqrt{\frac{(n_{Pi}-1)SD_{Pi}^2 + (n_{Pi+1}-1)SD_{Pi+1}^2}{(n_{Pi}-1)+(n_{Pi+1}-1)}}$$

(6) SD^* = 0.2 nm

➔ Proceed to Step 7

Step 7: A statistical 1-tailed t-test for $\bar{\bar{y}}_{Pi}$ and $\bar{\bar{y}}_{Pi+1}$ is performed, where t is calculated depending the assumptions that the true standard deviation (σ) is equal for P_i and P_{i+1}.

$$t = \frac{\bar{\bar{y}}_{Pi} - \bar{\bar{y}}_{Pi+1}}{SD^*\sqrt{\frac{1}{n_{Pi}} + \frac{1}{n_{Pi+1}}}}$$

(7) t = -13.8

F test showed $\sigma_{\bar{\bar{y}}_{Pi}} = \sigma_{\bar{\bar{y}}_{Pi+1}}$

➔ Proceed to Step 8

If the assumption $\sigma_{\bar{\bar{y}}_{Pi}} = \sigma_{\bar{\bar{y}}_{Pi+1}}$ fails, however, a Levene's/F Test can be performed to determine if the population variances are equal. If assume, $\sigma_{\bar{\bar{y}}_{Pi}} \neq \sigma_{\bar{\bar{y}}_{Pi+1}}$, then calculate,

$$t = \frac{\bar{\bar{y}}_{Pi} - \bar{\bar{y}}_{Pi+1}}{\sqrt{\frac{\left[SD_{\bar{\bar{y}}_{Pi}}\right]^2}{n_{Pi}} + \frac{\left[SD_{\bar{\bar{y}}_{Pi+1}}\right]^2}{n_{Pi+1}}}}$$

Our null hypothesis is that the actual average measured size from P_{i+1} (μ_{Pi+1}) is equal to that of P_i (μ_{Pi}), indicating that both protocols are statistically equal at separating the given sample. The alternative hypothesis is that $\mu_{Pi+1} < \mu_{Pi}$. Continue to Step 8.

Step 8: Compute t_{cutoff} for chosen n based on 1-tailed t-test. In the case of n = 3, there are (n_{Pi}-1) + (n_{Pi+1}-1) = 4 degrees of freedom, and t_{cutoff} = -2.132. Continue to Step 9.

(8) t_{cutoff} = -2.1

➔ Proceed to Step 9

Step 9: The calculated t from Step 6 is compared to t_{cutoff}. If the t-test confirms a statistically significant decrease between $\bar{\bar{y}}_{Pi+1}$ and $\bar{\bar{y}}_{Pi}$, increment i by 1 and return to Step 4 to repeat with a protocol of higher retention. However, if $t \geq t_{cutoff}$, then there is no significant decrease between $\bar{\bar{y}}_{Pi+1}$ and $\bar{\bar{y}}_{Pi}$, and the scientist should proceed to Step 10 by selecting the protocol with the lowest $\bar{\bar{y}}$.

(9) (Protocols A and B): t = -13.8
$t < t_{cutoff}$

[Increment i by 1, return to step 4 and repeat with protocol of higher retention until $t \geq t_{cutoff.}$]
…
(Protocols H and I): t = 4.9
$t \geq t_{cutoff}$

➔ Proceed to Step 10 with Protocol H

Step 10: If Step 9 concluded that there existed a statistically significant decrease between tested protocols, then a 1-tailed t-test should be performed between $\bar{\bar{y}}$ chosen in Step 9 and $\bar{\bar{y}}_{Pmax}$ from Step 1. This step ensures that $\bar{\bar{y}}$ from the chosen protocol is indeed the statistically significant minimum and that the scientist has reached the asymptote where increasing retention will no longer significantly lower $\bar{\bar{y}}$. If the t-test concludes there is not a significant difference, skip to Step 12. If the t-test concludes that the difference is significant, then $\bar{\bar{y}}$ is not statistically minimized. Increment *i* by 1 and continue to Step 11.

(10) (Protocols H and P_{max}): t = 12.0
t_{cutoff} = -2.132
$t \geq t_{cutoff}$

➔ Proceed to Step 12 with Protocol H

Step 11: Is $P_{i+1} = P_{max}$? If yes, then protocol retention cannot be increased. Skip to step 15. If no, then return to Step 4 and repeat with next protocol of higher retention.

(11) N/A

Step 12: Select two protocols in an orthogonal direction of steepest decent to that of previous pair (P_{o1} and P_{o2}). This step confirms the statistically significant minimum $\bar{\bar{y}}$ by exploring more of the experimental space in a gradient decent. Continue to Step 13.

(12) P_{o1}:
V_x = 2.25 mL min^{-1}
Elution time = 20 min

P_{o2}:
V_x = 2.50 mL min^{-1}
Elution time = 30 min

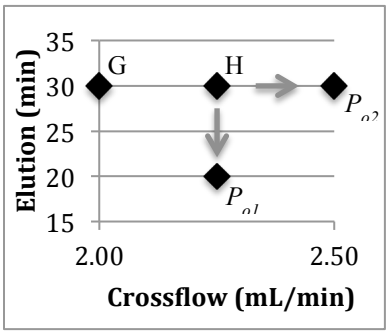

➔ Proceed to Step 13

Step 13: Repeat Steps 4-8 with P and P_o.

.

(13)
$\bar{y}_{Po1}$ (n = 3): 26.8 nm, 26.9 nm, 27.0 nm

$\bar{\bar{y}}_{Po1}$ = 26.9 nm
$SD_{\bar{\bar{y}}_{Po1}}$ = 0.1 nm

(Protocols H and P_{o1}): t = 3.3
t_{cutoff} = -2.132 for n = 3

$\bar{y}_{Po2}$ (n = 3): 27.6 nm, 27.9 nm, 27.5 nm

$\bar{\bar{y}}_{Po2}$ = 27.7 nm

$SD_{\bar{\bar{y}}_{Po2}}$ = 0.2 nm

(Protocols H and P_{o2}): t = 4.2
t_{cutoff} = -2.132 for n = 3

➔ Proceed to Step 14

Step 14: If the t-test confirms a statistically significant decrease between $\bar{\bar{y}}_P$ and $\bar{\bar{y}}_{Po1}$, and $\bar{\bar{y}}_P$ and $\bar{\bar{y}}_{Po2}$, then choose P with lowest y as P_i, go to Step 4 to repeat with a protocol of higher retention. However, if $t \geq t_{cutoff}$, then there is no significant decrease between $\bar{\bar{y}}_P$ and $\bar{\bar{y}}_{Po1}$, or $\bar{\bar{y}}_P$ and $\bar{\bar{y}}_{Po2}$, and the scientist should proceed to Step 15 by selecting the protocol with the lowest $\bar{\bar{y}}$

(14) $t \geq t_{cutoff}$ for $\bar{\bar{y}}_P$ and $\bar{\bar{y}}_{Po1}$
$t \geq t_{cutoff}$ for $\bar{\bar{y}}_P$ and $\bar{\bar{y}}_{Po2}$

➔ Proceed to Step 15

Step 15: Use the separation protocol with the minimum $\bar{\bar{y}}$ for desired application.

(15) Protocol H: $\bar{\bar{y}}$ = 26.4 nm

Protocol ***H*** selected as optimal.

APPENDIX 2.3: COMBINED AVERAGE MEASURED HYDRODYNAMIC RADIUS AND ASSOCIATED UNCERTAINTY

Appendix 2.3: Combined average ($\bar{\bar{y}}$) measured hydrodynamic radius (R_h) and associated uncertainty for n = 3 of the scatter- and particle number-matched samples run with separation protocols *A-K*, P_{o1}, P_{o2}, and P_{max}. The actual R_h was calculated based on the known particle size distributions and individually measured R_h of the polystyrene beads using AF^4-QELS. All uncertainties defined at the 95% confidence level.

	Sample 1	*Sample 2*
PROTOCOL	**Avg Radius (nm)**	**Avg Radius (nm)**
A	28.9 ± 1.3	35.6 ± 0.4
B	26.8 ± 0.4	32.5 ± 0.5
C	26.5 ± 1.2	31.0 ± 0.4
D	25.1 ± 0.5	30.0 ± 0.2
E	24.4 ± 0.5	29.3 ± 0.2
F	24.3 ± 0.8	28.8 ± 0.4
G	22.0 ± 0.4	27.3 ± 0.1
H	21.1 ± 0.5	26.4 ± 0.6
P_{o1}	22.6 ± 0.5	26.9 ± 0.2
P_{o2}	23.6 ± 0.8	27.7 ± 0.5
I	22.1 ± 1.1	27.1 ± 0.1
J	22.3 ± 0.3	28.1 ± 0.3
K	21.6 ± 0.8	28.3 ± 0.2
Pmax	22.4 ± 1.3	29.5 ± 0.5
Actual	21.7 ± 1.0	23.6 ± 1.5

APPENDIX 2.4: CALCULATIONS FOR DETERMINING ACTUAL HYDRODYNAMIC RADIUS OF POLYSTYRENE MIXTURES

Appendix 2.4: Calculations for determining actual R_h of polystyrene mixtures, Samples 1 and 2.

Measured R_h values for each individual particle size were determined by AF^4-QELS.

			Sample 1		Sample 2
Measured R_h (nm)	SD (nm)	particles mL^{-1}	**mL**	**Number of Particles**	**Number of Particles**
43.76	1.07	2.27E+15	0.003	6.81E+12	
36.34	1.01	2.83E+14	0.005	1.42E+12	2.70E+12
28.94	1.02	8.39E+13	0.010	8.39E+11	2.70E+12
19.80	0.96	3.54E+13	0.045	1.59E+12	2.70E+12
9.42	0.11	1.81E+13	0.787	1.42E+13	2.70E+12
		Total Particles		2.49E+13	1.08E+13
		SUM: # Particles * Measured R_h		5.39E+14	2.55E+14
		Average R_h (nm)		**21.7**	**23.6**
		Compound SD		0.5	0.8
		Uncertainty at 95% CI		**1.0**	**1.5**

APPENDIX 3.1: LOW, MEDIUM, AND HIGH IONIC STRENGTH WATER RECIPES

Appendix 3.1: The low (0.22 mS cm^{-1}), medium (0.40 mS cm^{-1}), and high (0.59 mS cm^{-1}) ionic strength water recipes containing 1029, 2992, and 4781 µeq L^{-1}, respectively, of both positive and negative ions from a combination of $MgSO_4*7H_20$, $NaHCO_3$, $KHCO_3$, $MgCl_2$, $CaCl_2$, $CaCO_3$, NaCl.

High (+)

µeq L^{-1}	Cl^-	SO_4^{2-}	C_T	ΣC^{z+}
Ca^{2+}	0	0	744	**744**
Mg^{2+}	6	235	0	**241**
Na^+	0	0	8	**8**
K^+	0	0	36	**36**
ΣA^{z-}	**6**	**235**	**788**	**1029**

Medium (0)

µeq L^{-1}	Cl^-	SO_4^{2-}	C_T	ΣC^{z+}
Ca^{2+}	0	0	684	**684**
Mg^{2+}	51	246	0	**297**
Na^+	1776	0	199	**1975**
K^+	0	0	36	**36**
ΣA^{z-}	**1827**	**246**	**919**	**2992**

Low (-)

µeq L^{-1}	Cl^-	SO_4^{2-}	C_T	ΣC^{z+}
Ca^{2+}	0	0	584	**584**
Mg^{2+}	0	262	0	**262**
Na^+	3500	0	399	**3899**
K^+	0	0	36	**36**
ΣA^{z-}	**3500**	**262**	**1019**	**4781**

APPENDIX 3.2: PRIMARY/INSTRUMENTAL FACTOR SETTINGS AND DESIGN

Appendix 3.2: Primary/Instrumental factors, 2^{5-1} design with 2 center points. +1, 0, and -1 refer to high, medium, and low settings, respectively, described in Table 1 of the main text.

Primary/Instrumental Factors (*k* = 5, *n* = 18 = 16 + 2)
2^{5-1} Design with 2 Center Points

	X1	X2	X3	X4	X5
Separation Protocol	Cross Flow	Ramp	Focus	Injection Vol	Buffer
1	-1	-1	-1	-1	+1
2	+1	-1	-1	-1	-1
3	-1	+1	-1	-1	-1
4	+1	+1	-1	-1	+1
5	-1	-1	+1	-1	-1
6	+1	-1	+1	-1	+1
7	-1	+1	+1	-1	+1
8	+1	+1	+1	-1	-1
9	-1	-1	-1	+1	-1
10	+1	-1	-1	+1	+1
11	-1	+1	-1	+1	+1
12	+1	+1	-1	+1	-1
13	-1	-1	+1	+1	+1
14	+1	-1	+1	+1	-1
15	-1	+1	+1	+1	-1
16	+1	+1	+1	+1	+1
17	0	0	0	0	0
18	0	0	0	0	0

APPENDIX 3.3: ROBUSTNESS/ENVIRONMENTAL FACTOR SETTINGS AND DESIGN

Appendix 3.3: Robustness/environmental factors, 2^{5-2} design with 1 center point and BSA reference. (+1, 0, and -1) refer to high, medium, and low settings, respectively, described in Table 1 of the main text.

Robustness/Environmental Factors (*k* = 5, *n* = 9 = 8 + 1)
2^{5-2} Design with Center Point and with Reference

	R1	R2	R3	R4	R5
Sample	[NP]	[NOM]	Ionic Strength	pH	NP Size
1	-1	-1	-1	+1	+1
2	+1	-1	-1	-1	-1
3	-1	+1	-1	-1	+1
4	+1	+1	-1	+1	-1
5	-1	-1	+1	+1	-1
6	+1	-1	+1	-1	+1
7	-1	+1	+1	-1	-1
8	+1	+1	+1	+1	+1
9	0	0	0	0	0
10	Ref	Ref	Ref	Ref	Ref

APPENDIX 3.4: PLOT DESCRIPTIONS

The **DOE scatter plot** aims to elucidate the important factors, the best settings for each of these factors, and finally, whether any data points can be classified as outliers. In this case, an important factor is one that results in a significant alteration for either the location or variation of the model response when the factor setting is changed from $(-)$ to $(+)$. The best factor setting is one that yields a response that is most accurate based on the experimental target, though this goal must be specified in the experimental design. Outliers are identified if the response falls into a different probability distribution than the rest of the data, which can be useful in determining which data points may potentially invalidate factor ranking conclusions by affecting other effects estimates [1].

The **main effects plot**, or the **DOE mean plot**, is used to compile a ranked list of factors, and their best settings, in order of importance. The average is the most effortless location estimator, and therefore a simple mean plot can be used to evaluate the importance of a single factor. The main effects plot is a series of *k* plots, so each factor can be compared for relative importance. Importance is ranked by the effect magnitude. The vertical axis represents the mean response for each *k* factor settings ($-$ and $+$). The horizontal axis lists the *k* factors and settings. The factor with the steepest line is categorized as the "most important", and the slope of the line indicates whether the effect is positive or negative when changing the factor settings from $(-)$ to $(+)$. The best average settings are defined by identifying which individual factor settings result in an average response nearest the desired target [1].

The **interaction effects matrix** includes the main effects and 2-factor interactions to explore a ranked list of important factors and the best settings for each of the *k* factors. While similar to the Main Effects Plot in this regard, the Interaction Effects Matrix plot also takes the 2-factor interactions into account. In the case of fractional factorial designs, which typically contain confounding variables, the question arises as to whether a resulting effect is due to the main effect or a confounding interaction. It is prudent to consider these confounding effects when designing a fractional experiment, and chose a design that minimizes the main effect confounding. Poor designs containing 2-factor interactions result in ambiguous effects conclusions and factor rankings, while better designs with higher order interactions reduce main effect estimate biases [1, 2].

The **absolute effects plot**, or |Effects| Plot, graphically displays the ranked least squares estimated effect magnitude of each factor or interaction and their relative importance. For fractional factorial designs, additional information about confounding variables can be observed. The graphical ranking or the factor and interaction effect magnitudes is given in the plot, and quantitatively provided in the upper right table, which also lists any confounding structure in the case of fractional factorial designs. The absolute value of the difference between the $(+)$ and $(-)$ averages indicates the importance of each factor or interaction, which larger differences being more important [1, 2].

The **ordered data plot** is used the response data to identify the best average factor settings, within predicted model values, and the most important factor, typically used for optimization analysis. The best settings can be recognized as the settings corresponding to the best response value. Further, the most important factor is one in which changing the factor setting from $(-)$ to $(+)$ produces the greatest response. If a particular, and consistent, factor and level that correspond to the best response and the near-best responses, then the factor can be deemed "most important". Contrarily, if the same factor at the opposite level is associated with the worst and near-worst response, which is expected in a balanced design, then the factor is confirmed as "most important" [1, 2].

The **block plot** is a multifactor analysis technique used to identify the relative importance of factors and 2-factor interactions, as well as the best settings for each important factor. The Block Plot is particularly useful in determining whether the factor importance is robust across all *k* factor settings, and therefore is also known as a DOE Robustness/environmental Plot. Each point in a block is associated with target factor settings. Internal block differences represent the relative importance of each factor, where larger blocks indicate greater effects. The ability to scan and compare factor effect blocks quickly is a strong advantage when using Block Plots, and the block height consistency can provide information about the factor robustness/environmental [1, 2]. The block plot continues exploring the question, "what are the best and worst primary/instrumental factor settings?"

The **replication analysis matrix** is used to identify the most consistent and precise primary/instrumental and robustness/environmental factor levels across two replicates. Replication analysis allows for insight into the robustness/environmental of factor settings and insight into instrument stability during large-scale optimization studies [1].

APPENDIX 3.5: THE ENVIRONMENTAL/ROBUSTNESS/ENVIRONMENTAL FACTOR ORDERED DATA PLOT

The ordered data plot using the robustness/environmental factors is given below. Robustness/environmental factor combination rankings can provide insight into how the sample water quality characteristics may affect separation independently from the primary/instrumental factors. The best settings are (- - - + +), corresponding to low NP concentration, low NOM concentration, low specific conductance, high pH, and high NP size, respectively. The worst settings are (+ + - + -). By observation, there is little difference between the best and worst settings, which is in good agreement with the mean-based results of the main effects plot in Figure 3.3.

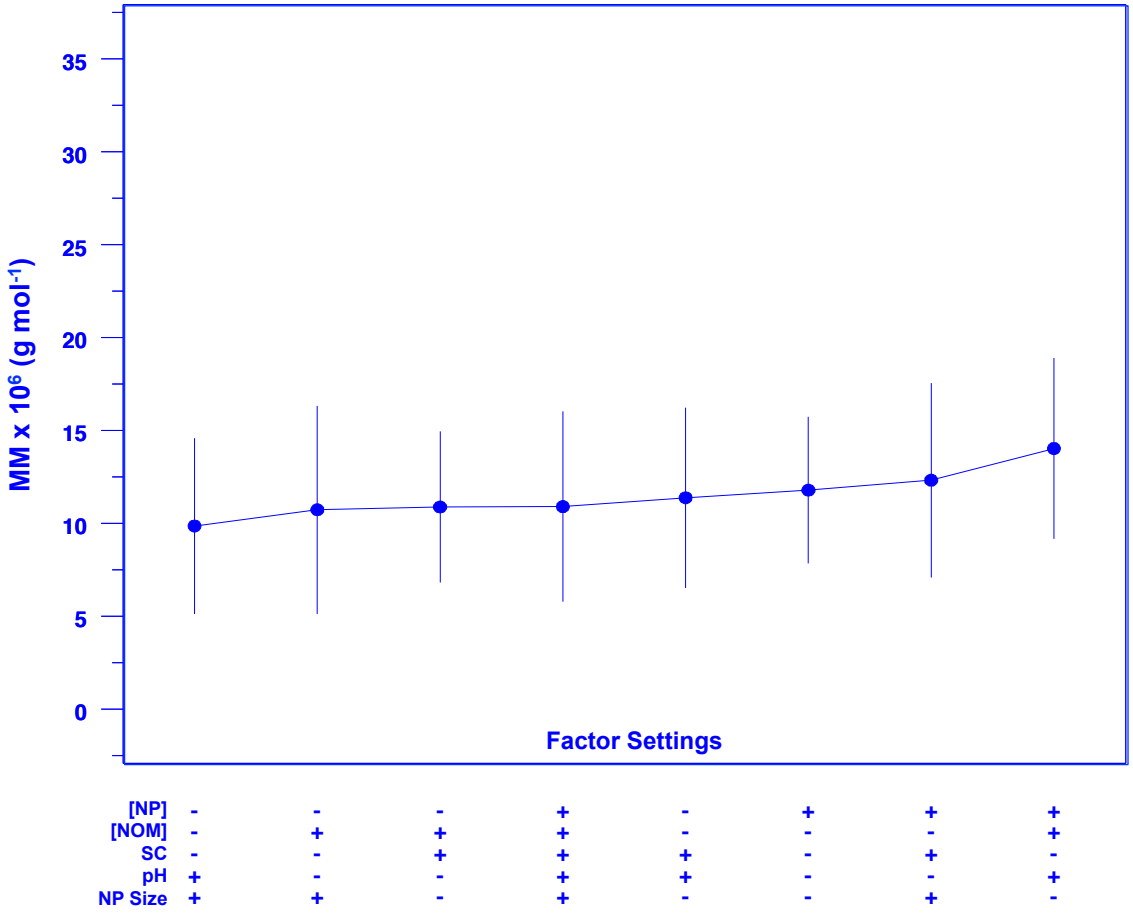

Appendix 3.5: Robustness/environmental factor ordered data plot. The vertical axis represents the mean of both average MM measurements from replicated data points. The horizontal axis lists factor settings defined in Table 3.1. Error bars represent the 95% confidence interval for the mean value.

APPENDIX 3.6: MODELING PREDICTION AND RESIDUAL ANALYSIS

Measurement processes are typically based on four basic data assumptions: randomness, fixed location, fixed variation, and fixed distribution. Identifying an appropriate model to fit a data set is an iterative process that requires empirical evidence in the data, expertise, and experimentation. Residual plots and repeated model improvement reveal the underlying details within datasets that are not always evident upon initial observations [3]. In the case of this work, a resolution V design ensures that all main effects and 2-factor interactions can be estimated without significant confounding interactions.

To begin the modeling prediction process, a basic univariate function equating response with a constant plus error is designated Model 0. This model assumes that no factors, primary/instrumental or robustness/environmental, are important. A 4-plot graphical analysis is generated to assess the model fit and given in Figure A3.6a.

The 4-Plot reveals information about the underlying assumptions, ultimately determining the validity of the model. Run Sequence plots present potential shifts in location and scale. If the fixed location assumption is valid, the run sequence plot will appear random and not contain drift. In the case of Model 0, a fixed location refers to the unknown constant. If the fixed variation assumption is valid, then the run sequence plot will contain a relatively flat vertical spread across all values of i [3]. The run sequence plot does seem to drift slightly at higher values of n, where shifts in the vertical spread are also evident.

The lag plot provides information about the randomness of the data, where random data should result in residuals with no discernable pattern, and suggests whether the errors are independent. Dependent errors will result in a biased standard deviation estimate and potentially flawed conclusions. Each residual value versus the value of the subsequent residual is plotted relative to the time of observation. For Model 0, no identifiable pattern is observed and therefore there is no significant dependence between errors. As randomness is an underlying assumption for most statistical techniques, the lag plot is a very useful tool for experimenters seeking a more detailed understanding of their data.

The histogram and normal probability plots reveal information about the final assumption, that the data have a fixed distribution. A histogram will describe the location, scale, and spread of the data, and identify the presence of any outliers or multiple modes. The normal probability plot reveals the normality

of the data by plotting against a theoretical normal distribution of corresponding normal order statistic medians. If the fixed distribution assumption is valid, the histogram will show data that are normally distributed and the normal probability plot will be near linear, though Model 0 fails both these tests.

It can be concluded that Model 0 is inadequate for describing this dataset, as the residuals have violated several of the underlying univariate assumptions. However, the univariate model can be easily improved by expanding the function to incorporate several variables that become additional deterministic constituents. The advantage of building from the univariate model is that using the residuals from each fitted model of increasing complexity to test the underlying assumptions is a useful tool for model validation and quality assessment.

The next step is to generate a 4-Plot using a model of increasing complexity, Model 1 shown in Figure A3.6b, which includes primary/instrumental factors as important contributors of the model response. The Run sequence plot contains much less drift and vertical spread than seen with Model 0, and the lag plot continues to display observably random data. The histogram is less skewed and is approaching a normally distributed bell-curve. The probability plot is still non-linear. Model 1, while an improvement from Model 0, does not yet satisfy the underlying assumptions.

For further improvement, another term is subsequently added to the univariate model, described as Model 2, which includes robustness/environmental factors instead of primary/instrumental factors as important model variables. The 4-Plot generated with Model 2 is given in Figure A3.6c. Unfortunately, this iteration is a step backwards compared to Model 1, where the run sequence plot increases in drift and vertically spread. The histogram and normal probability plots show that the data are less normally distributed using this model.

Finally, both primary/instrumental and robustness/environmental factors are added to the univariate base model as important variables in Model 3, given in Figure A3.6d. Model 3 is a clear improvement over the previous Models 0-2. The run sequence plot appears flat and non-drifting, and therefore the fixed-location assumption holds. Further, the run sequence plot has vertical spread that is generally consistent across all *i*, so the fixed-variation assumption is also satisfied. The lag plot again structureless and is in good agreement with the randomization assumption. Both the histogram and the normal probability plot shows approximately normally distributed data, with a nearly symmetrical bell-

curve and linear plot, respectively. Model 3 is therefore deemed “in statistical control”, and is an appropriate model to describe this dataset. Therefore, both the primary/instrumental and robustness/environmental factors are important variables, and the data reflect changes in factor settings. While the robustness/environmental factors were deemed important in this model, the main effects plot in Figure 3.4 revealed that the robustness/environmental factors were not statistically significant factors.

With a validated model identified, exploring residuals relative to instrument time can reveal further drift analysis. The residuals are plotted against a “start” and “end” day, corresponding to the day where the first and second replicate was performed. This plot is shown in Figure A3.6e. Due to the large number of experiments required for this design, several gaps in experimental run days occurred due to instrument maintenance and other obstacles. These gaps are reflected in the residuals plot, though no observable drift is present to indicate any pattern in instrument variability. The vertical spread appears to be random and therefore strengthens the conclusions made in the previous sections regarding changes due to primary/instrumental and robustness/environmental factor setting differences.

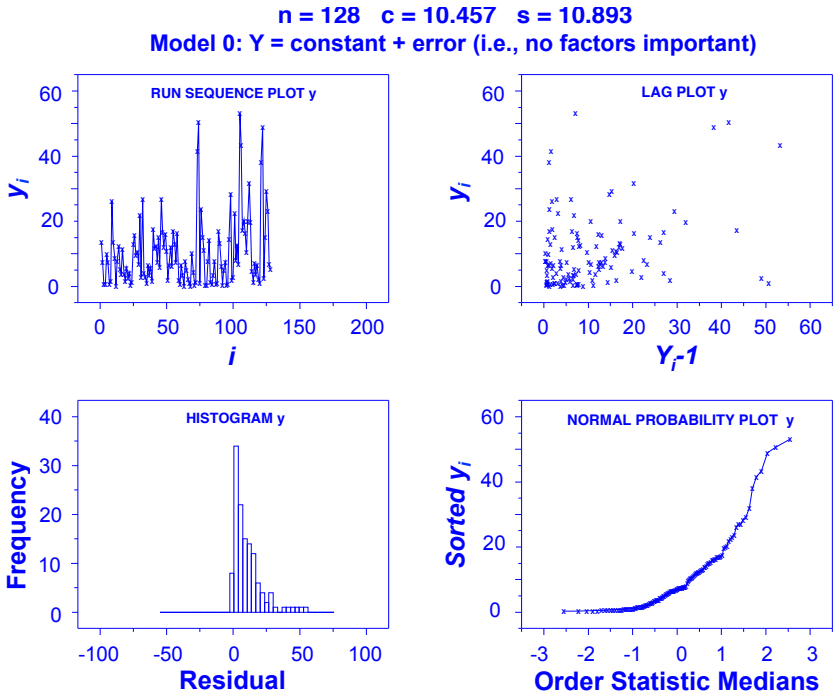

Figure A3.6a: 4-Plot for Model 0, where n is the number of observations as cell means, c is the predicted global mean, and s is the standard deviation of the residuals. Y_i represents the response variable, or average MM, across *i* observations. The order statistic medians are derived elsewhere [3], and represent a theoretical normal distribution.

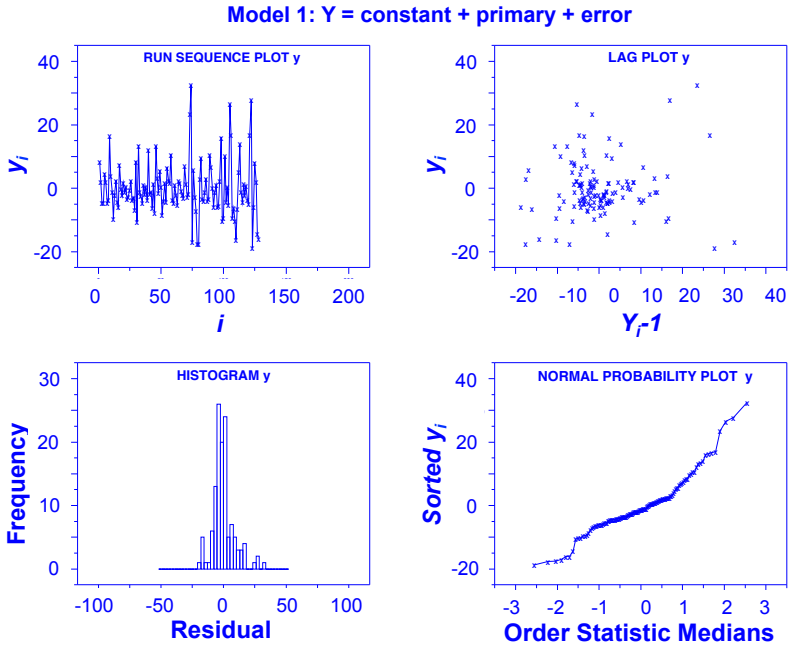

Figure A3.6b: 4-Plot for Model 1. The residual standard deviation is 9.209.

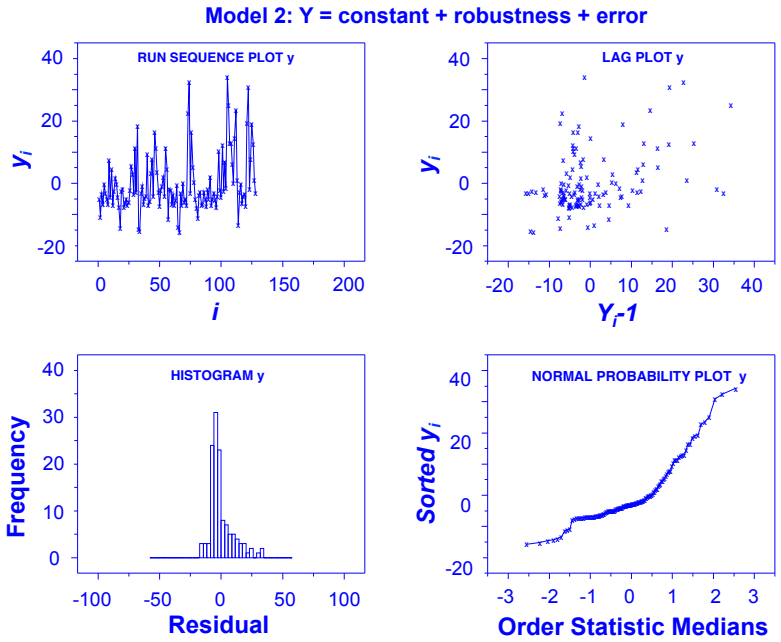

Figure A3.6c. 4-Plot for Model 2. The residual standard deviation is 9.910.

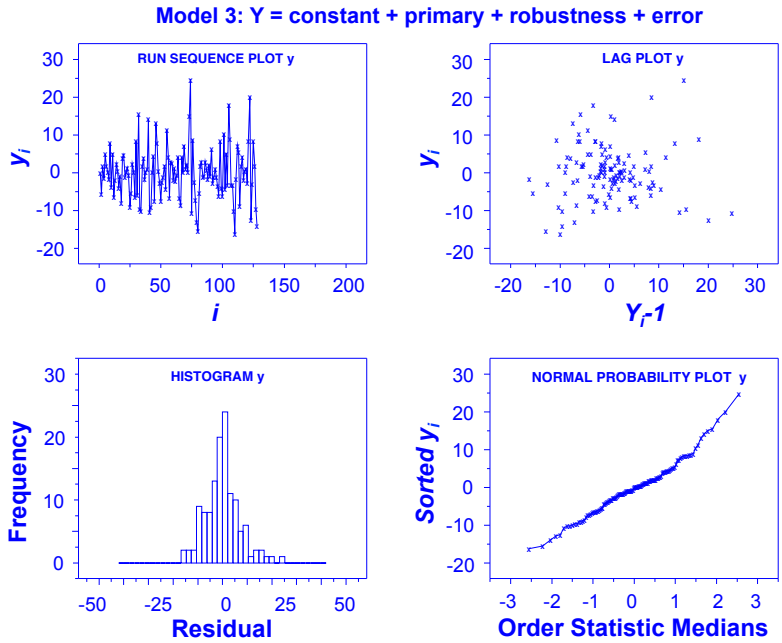

Figure A3.6d. 4-Plot for Model 3. The residual standard deviation is 7.692.

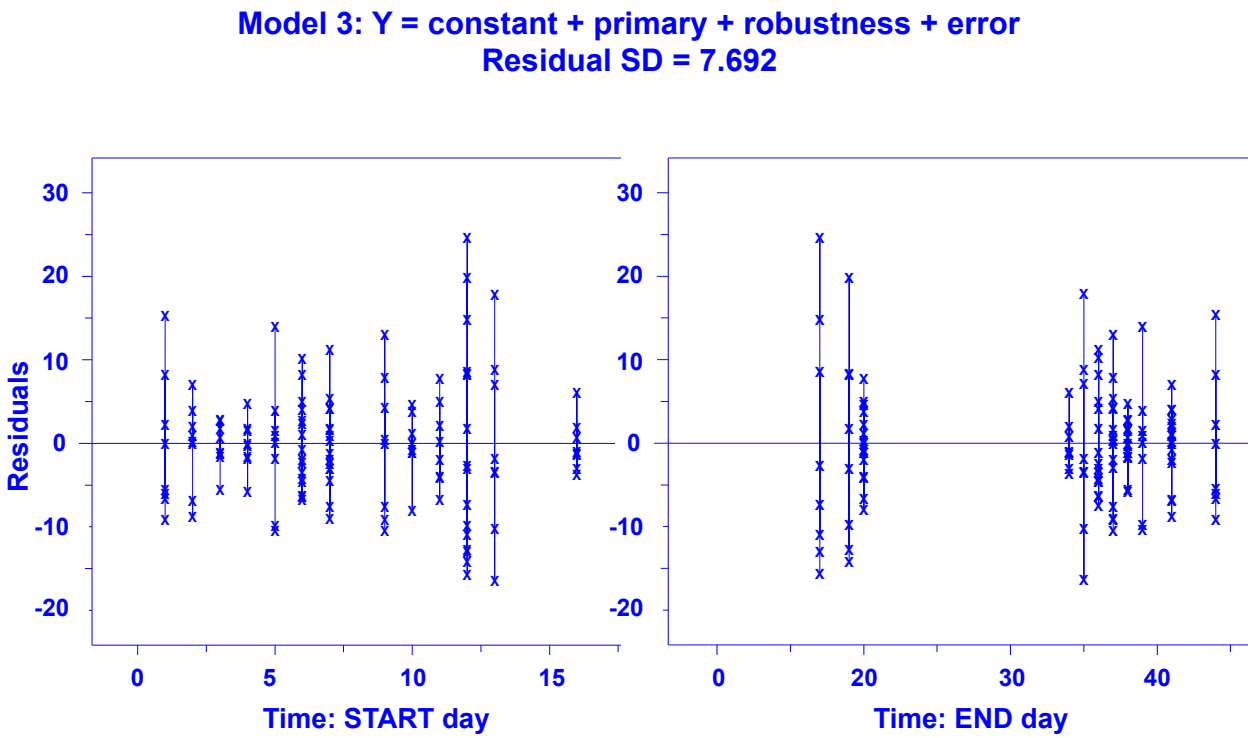

Figure A3.6e. The residuals of the data set using Model 3 are plotted against the "start" and "end" days, representing the day in which the first and second replicates were performed, respectively.

APPENDIX 3.7: THE SCATTER PLOT

Scatter plots [1] are a simple way to isolate location changes, variation changes, and outliers, observations that can sometimes be missed in more advanced quantitative or graphical methodologies [1, 2]. The Scatter Plot shown in Figure 1 concludes that the most important factor affecting the molar mass response is buffer concentration (X5), due to its greatest difference in response when changing factor settings from (-) to (+); the next most important factors were cross flow and injection volume. The least important is ramp time.

The plot also revealed an in the buffer (-) setting, which would greatly reduce the importance of buffer concentration. However, from the literature it is generally accepted that buffer concentration (specifically, ionic strength), is very influential in separation, recovery, and aggregation behavior of humic substances [4-6]. While buffer composition is also an important consideration, NH_4NO_3 was fixed in order to determine relative influence of other primary/instruental factors and for ease of completing a large number of samples. In order to retain design balance, the outlier was not simply removed, but instead replaced with the global average for all mean MM values, with the assumption that it would minimize any bias of local means.

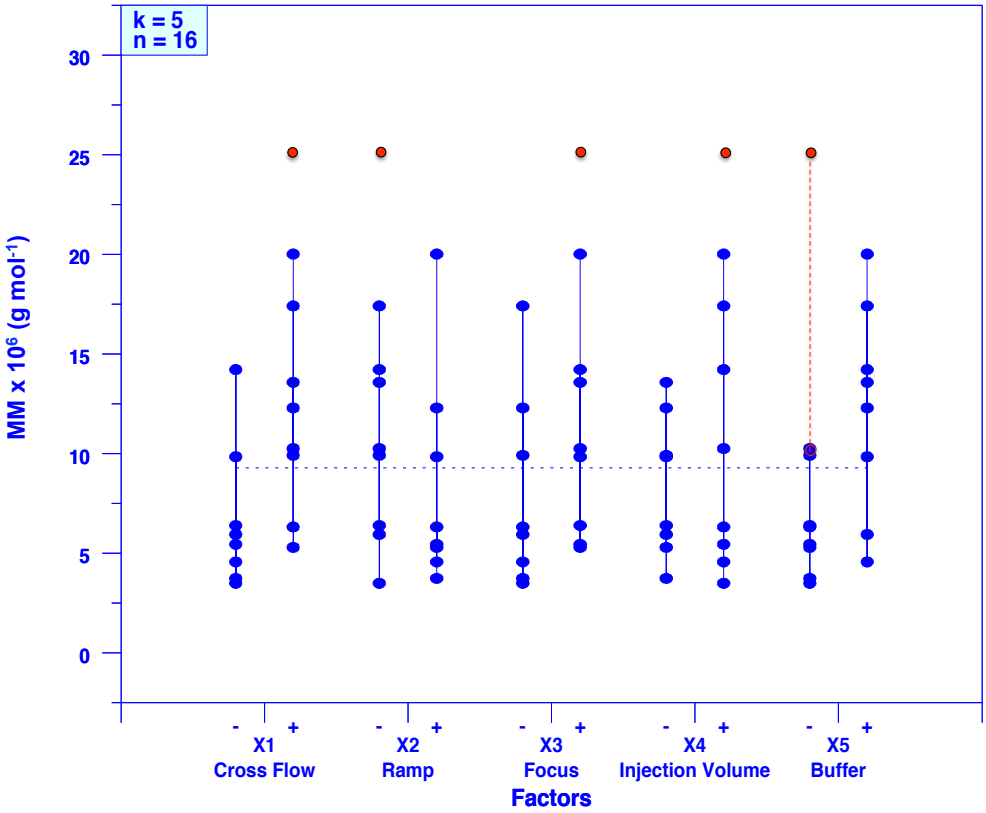

Appendix 3.7: Scatter plot. The vertical axis represents the mean of both average MM measurements from replicated data points for each combination of primary/instrumental factors. Red points represent an identified outlier, which was replaced for subsequent analysis with the global mean (indicated by dashed line) to maintain design balance.

APPENDIX 3.8: THE INTERACTION EFFECTS MATRIX PLOT

The interaction effects matrix plot includes both main effects and 2-factor interactions to expand our exploration of the ranked list and best settings for each of the *k* factors. The interaction effects matrix is shown below, where (since all plots have the same vertical axis scale) the line slope is an indication of effect importance [1]: the steeper the slope—the more important the factor. The effects from the main effects plot re-appear here along the diagonal, but this plot also incorporates effects due to 2-term interactions. Based on the effect slope, the top ranked effects (in decreasing order of importance) is buffer concentration, cross flow, focus flow, and the cross flow x buffer concentration interaction.

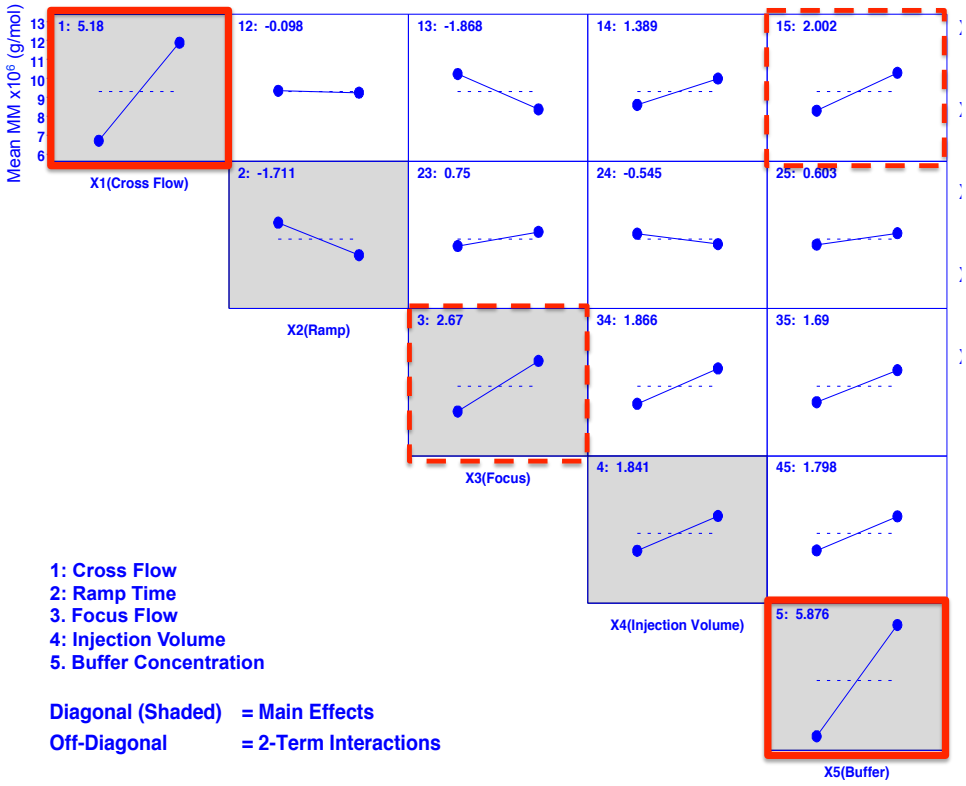

Appendix 3.8: Interaction effects matrix. The diagonal shows mean plots for the *k* main factors, and 2-factor interactions are displayed in the off-diagonal plots. The vertical axes display the mean response for each factor setting and 2-factor interaction—all on a common scale. The horizontal axis holds settings within each factor or interaction. The legend includes the least-squares-estimate for each factor or interaction, with magnitude proportional to importance. The two most important factors (X5, X1) are shown in the bold solid boxes, and the next most important factor (X3) and interaction (X1X5) are shown in the bold dashed boxes. Note again that due to the nature of the orthogonal fractional factorial design that was chosen for this study, none of these 5+10 = 15 factor effect estimates are confounded with one another.

APPENDIX 3.9: THE ABSOLUTE EFFECTS PLOT

The absolute effects plot is given below, and ranks the most important factors as buffer concentration, cross flow, focus flow, and a cross flow/buffer concentration 2-factor interaction (X1234 = X5, X1, X3, and X234 = X1X5). This agrees with the conclusions made with main effects plot and interaction effects matrix. Further, the absolute effects plot suggests that both buffer concentration and cross flow are significant, whereas the remaining effects are not.

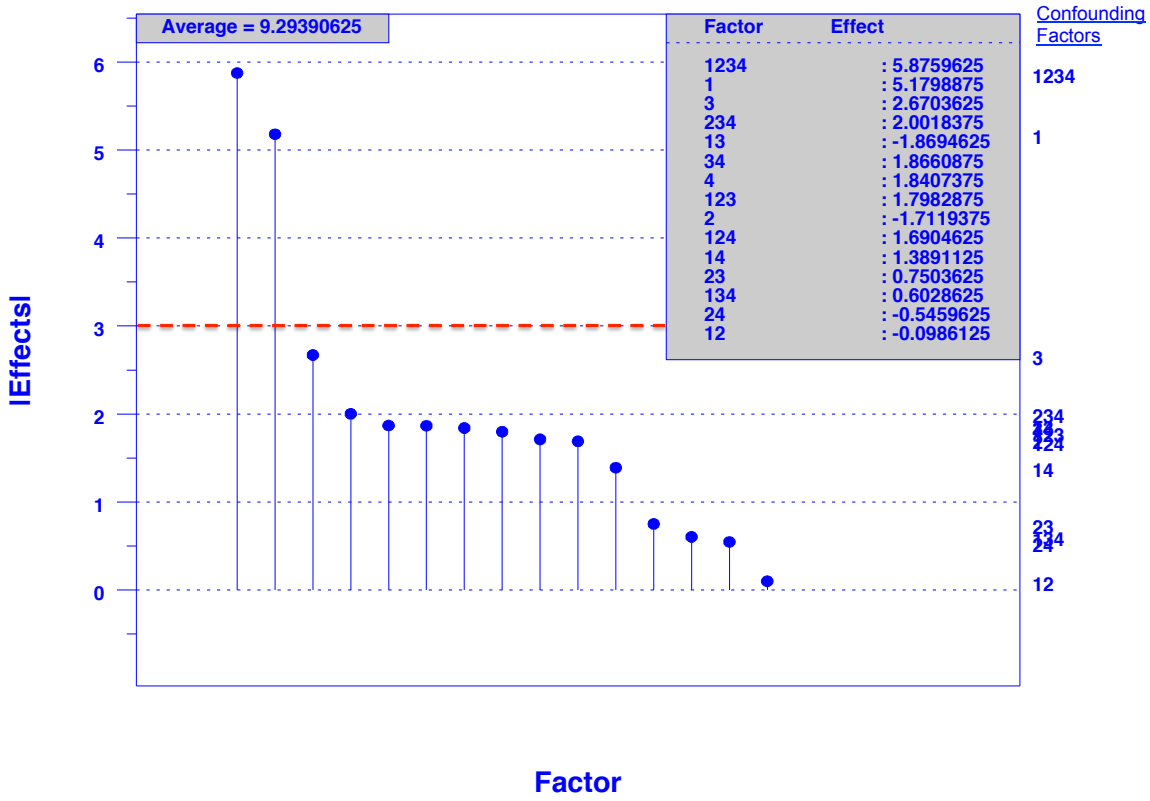

Appendix 3.9: Absolute effects plot. The vertical axis lists the ordered absolute value of the estimated effects for each factor and interactions. The horizontal axis is the factor or interaction identification, with the ranked effects given in order of magnitude. The confounding structure for fractional factorial designs is provided, and the upper right table lists the ranked least squares effect estimates. The ranked list of factors and interactions is (X1234 = X5, X1, X3, X234 = X1X5). The dashed red line indicates the division between significant and non-significant factors.

APPENDIX 3.10: REPLICATION ANALYSIS

A replication analysis matrices showing replication relative to time is given below. It is important to note that there does not appear to be any significant instrument drift, as variability between replicates seems to be a consequence of factor settings and random noise. This suggests that some combination of robustness/environmental factors, or in this case, water quality characteristics, result in more sample variability and therefore less consistent analysis. The increase in replication variability appears to coincide with the previous conclusions of ranked factor settings. The trends yielding better separation with decreasing cross flow, buffer concentration are conserved in the ranked primary/instrumental factor settings, and higher NOM concentrations is well represented in the ranked robustness/environmental factor settings. This is especially important to keep in mind when running characterized environmental samples, as it requires more care and rigor to ensure the quality of any results reported. Further, it brings consistency into question, particularly in the case of comparing results between systems or laboratories.

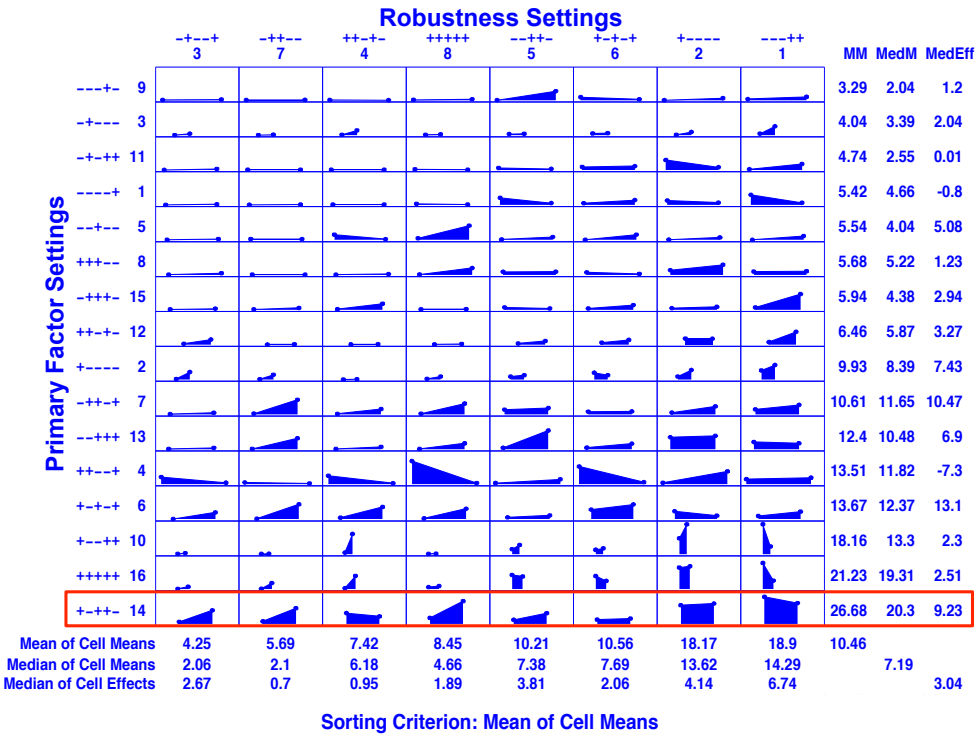

Appendix 3.10: Replication analysis matrix showing replicated factor settings relative to time. The horizontal axis is time (day 1-50), and the vertical axis is measured MM. The red box indicates the outlier identified in Appendix 2.7. The plots are sorted according to the mean of cell means. The median of cell means and cell effects are also given.

APPENDIX 4.1: STATISTICAL CALCULATIONS FOR LINEAR REGRESSION SLOPE COMPARISONS

	Ag^+, no membrane	AgNP, no membrane	AgNP, membrane	AgNP, membrane + focusing
n	6	6	6	6
b	5190.784405	5838.469693	5437.044231	3327.368637
y-intercept	635.0075963	9.51460987	-292.3078937	361.8264558
R^2	0.992431251	0.99573523	0.99657595	0.993210688
$S_{y,x}$	1050.400691	885.3909996	738.4785653	637.4605255
S_x	1.794881612	1.794881612	1.794881612	1.794881612
S_b	261.7183589	220.604462	183.9996868	158.8299817
$S_{b1\text{-}b2}$			287.2667983	243.0696358
t			1.397395957	8.679305365
df			6	6
alpha			0.05	0.05
p-value			0.211783749	0.000129105
significant?			NO	YES
				(YES if p-value < alpha)

n = number of observations, *b* = slope, $S_{y,x}$ = standard error of the estimate, S_x = standard deviation of x, S_b = standard error of the slope, p-value = t-distribution test statistic for 2-tailed value, *df* = degrees of freedom, t = t-distribution, alpha = 95% confidence interval

APPENDIX 4.2: THE NATURAL ISOTROPIC RATIO OF $^{107}Ag/^{109}Ag$

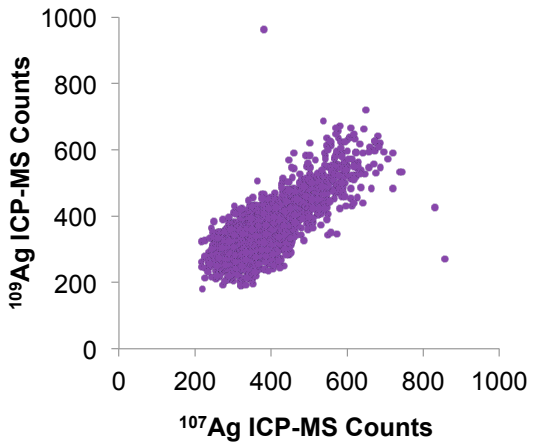

Appendix 4.2: The natural isotropic ratio of $^{107}Ag/^{109}Ag$ is near 1:1 for a raw lake water sample.

APPENDIX 4.3 NOM FLUORESCENCE QUENCHING

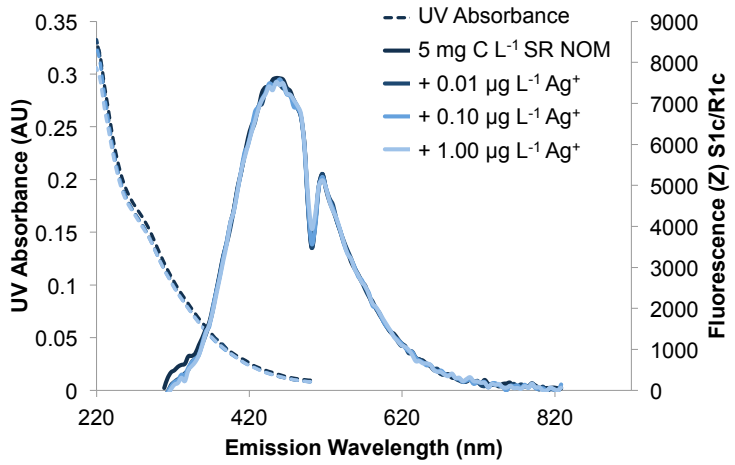

Appendix 4.3a: NOM fluorescence quenching of 5 mg C L^{-1} SR NOM with addition of increasing concentrations of Ag^{+}. Samples equilibrated 1 hour after addition of Ag^{+} prior to analysis. Excitation wavelength 250 nm, 1 second integration time.

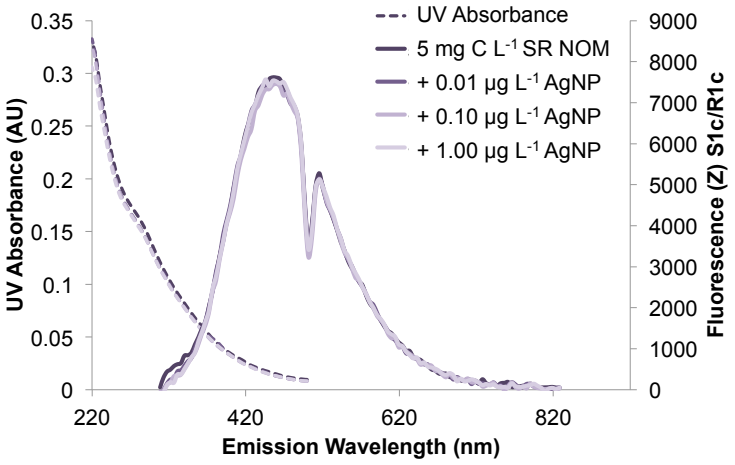

Appendix 4.3b: NOM fluorescence quenching of 5 mg C L^{-1} SR NOM with addition of increasing concentrations of AgNP. Samples equilibrated 1 hour after addition of AgNP prior to analysis. Excitation wavelength 250 nm, 1 second integration time.

REFERENCES

1. National Institute of Standards and Technology An EDA Approach to Experimental Design. *NIST/SEMATECH e-Handbook of Statistical Methods* **2013,** Accessed *2014,* http://www.itl.nist.gov/div898/handbook/pri/section5/pri59.htm

2. Anonymous Sensitivity Analysis of MesoNet, In *Study of Proposed Internet Congestion Control Mechanisms,* Mills, K.M., Filliben, J.J., Cho, D.Y., Schwartz, E. and Genin, D., Eds.; U.S. Government Printing Office: Washington, D.C., 2010; pp. 71-135.

3. National Institute of Standards and Technology Process Modeling. *NIST/SEMATECH e-Handbook of Statistical Methods* **2013,** Accessed *2015,* http://www.itl.nist.gov/div898/handbook/pmd/pmd.htm

4. Benincasa, M.; Cartoni, G.; Imperia, N. Effects of ionic strength and electrolyte composition on the aggregation of fractionated humic substances studied by flow field-flow fractionation. *J. Sep. Sci.* **2002,** *25,* 405-415.

5. Manh Thang, N.; Geckeis, H.; Kim, J.I.; Beck, H.P. Application of the flow field flow fractionation (FFFF) to the characterization of aquatic humic colloids: evaluation and optimization of the method. *Colloids Surf. A- Physicochem. Eng. Aspects* **2001,** *181,* 289-301.

6. Dubascoux, S.; Von Der Kammer, F.; Le Hecho, I.; Gautier, M.P.; Lespes, G. Optimisation of asymmetrical flow field flow fractionation for environmental nanoparticles separation. *J. Chromatogr. A* **2008,** *1206,* 160-165.